Neutron Imaging of Metal Hydride Systems

Dissertation
zur Erlangung des Doktorgrades
an der Fakultät für Mathematik, Informatik und Naturwissenschaften
Fachbereich Physik
der Universität Hamburg

vorgelegt von
Stefan Börries

Hamburg
2017

Gutachter:	Prof. Dr. Andreas Schreyer Prof. Dr. Thomas Klassen
Zusammensetzung der Prüfungskommission:	Prof. Dr. Andreas Schreyer Prof. Dr. Thomas Klassen Prof. Dr. Andreas Stierle Prof. Dr. Christian Schroer Prof. Dr. Daniela Pfannkuche
Vorsitzender der Prüfungskommission:	Prof. Dr. Daniela Pfannkuche
Datum der Disputation:	27.10.2017
Vorsitzende des Fach-Promotionsausschusses PHYSIK:	Prof. Dr. Wolfgang Hansen
Leiter des Fachbereichs PHYSIK:	Prof. Dr. Michael Potthoff
Dekan der Fakultät MIN:	Prof. Dr. Heinrich Graener

Eidesstattliche Versicherung / Declaration on oath

Hiermit versichere ich an Eides statt, die vorliegende Dissertationsschrift selbst verfasst und keine anderen als die angegebenen Hilfsmittel und Quellen benutzt zu haben. Die eingereichte schriftliche Fassung entspricht der auf dem elektronischen Speichermedium.
Die Dissertation wurde in der vorgelegten oder einer ähnlichen Form nicht schon einmal in einem früheren Promotionsverfahren angenommen oder als ungenügend beurteilt.

Hamburg, den 04.04.2017

Stefan Börries

Abstract

Among the different possibilities to store hydrogen, solid-state hydrogen storage in nano-crystalline metal hydrides offers highest volumetric densities combined with a high degree of safety. For an optimized scale-up of materials aiming at future industrial applications, a precise knowledge of the spatial distribution of hydrogen inside the metal hydride is essential. The method of choice for the investigation of the time and spatial resolved hydrogen distribution is Neutron Imaging due to the high neutron-hydrogen interaction cross section. During this work, new methods for the characterization possibilities of metal hydride systems using Neutron Imaging have been developed. For solid-state metal hydrides, a technique for a reliable quantitative, time-resolved investigation of the hydrogen distribution has been introduced. In combination with multi-correlation analysis, it allows for the determination of relevant driving forces for the reaction kinetics in solid metal hydride beds. For metal hydrides containing liquid phases, methods for the investigation of material transport and structure evolution have been developed. Among the use of fission neutrons for the analysis of scaled-up systems, cold Neutron Imaging combined with isotope labeling allows for the investigation of fundamental material properties of liquid phases within a solid framework due to the simultaneous access to spatial resolution and phase sensitiveness. Developed methods have been applied to two promising representatives for the different metal hydride classes. The solid-solid system sodium alanate has been analyzed by in-situ Neutron Radiography and a multi-correlation analysis has been performed to reveal the interaction of temperature, material packing density and reaction kinetics. Additionally, the liquid-solid system $LiBH_4$-MgH_2, a so-called Reactive Hydride Composite, has been analyzed both by fission Neutron Imaging as well as cold Neutron Imaging in combination with isotope labeling of the liquid phase $LiBH_4$. New insights into material transport, structural changes and phase separation have been derived. The results highlight the great potential of quantitative Neutron Imaging for fundamental research on metal hydride systems as well as for optimization of scaled-up systems with respect to future application.

Zusammenfassung

Unter den verschiedenen existierenden Möglichkeiten zur Speicherung von Wasserstoff bietet die Verwendung von nanokristallinen Metall-Hydriden die höchsten volumetrischen Speicherdichten bei gleichzeitig hoher Gefahrensicherheit. Für eine optimale Skalierung geeigneter Metall-Hydride mit dem Ziel einer zukünftigen, industriellen Anwendung, ist eine präzise Kenntnis der räumlichen Verteilung des Wasserstoffs im Inneren des Materials essentiell. Durch die starke Wechselwirkung von Neutronen und Wasserstoff ist Bildgebung mit Neutronen für die zeitaufgelöste Darstellung und Analyse der räumlichen Verteilung von Wasserstoff die Methode der Wahl. Im Rahmen dieser Arbeit wurden hierfür neue Analyse-Methoden unter Verwendung einer Bildgebung mit Neutronen entwickelt. Für feste Metall-Hydride wurde eine neue Methode zur zuverlässigen, zeitaufgelösten Untersuchung der räumlichen Verteilung von Wasserstoff eingeführt. In Verbindung mit einer Multi-Korrelations-Analyse erlaubt sie die Ermittlung relevanter, treibender Kräfte der Reaktionskinetik in festen Metall-Hydriden. Für Metall-Hydride mit einer flüssigen Phase wurden Verfahren für die Untersuchung von Materialtransport und Strukturveränderungen entwickelt. Während Spaltneutronen zur Untersuchung von hoch-skalierten Systemen benutzt wurden, erlaubt die Verwendung von kalten Neutronen in Verbindung mit der gezielten Markierung von Isotopen die gleichzeitige Kenntnis über Phase und entsprechende räumliche Verteilung und ermöglicht damit die Analyse fundamentaler Eigenschaften der flüssigen Phase in Umgebung einer festen Matrix. Die im Rahmen der Arbeit entwickelten Methoden wurden auf zwei vielversprechende Metall-Hydride angewendet. Als Referenz-System für ein festes Metall-Hydrid wurde Natriumaluminiumhydrid mithilfe von zeitaufgelöster Bildgebung mit Neutronen charakterisiert. Um die Wechselwirkung des Temperaturfeldes, der Material-Packungsdichte sowie der Reaktionskinetik zu untersuchen, wurde eine Multi-Korrelationsanalyse durchgeführt. Darüber hinaus wurde das System $LiBH_4$-MgH_2, ein sogenanntes 'Reactive Hydride Composite', als Beispiel für eine Kombination von fester und flüssiger Phase analysiert. Hierfür erfolgte der Einsatz von Bildgebung mit Spaltneutronen und auch mit kalten Neutronen und gleichzeitiger Isotopenmarkierung der flüssigen Phase $LiBH_4$. Dadurch konnten neue Einblicke in den Materialtransport, die Strukturveränderungen und Phasenseparation in flüssig-fest Phasenmischungen erzielt werden. Insgesamt heben die Ergebnisse das große Potenzial quantitativer Bildgebung mit Neutronen für sowohl fundamentale Untersuchungen an Metall-Hydriden als auch für die Optimierung von hoch-skalierten Systemen hervor, hier insbesondere im Zusammenhang mit dem Ziel einer zukünftigen Anwendung.

Contents

Chapter 1

Introduction

With respect to the worlds increasing energy demand and challenges of a potential climate change there is a strong need for a new energy carrier and its corresponding storage [7]. Hydrogen is widely agreed on as a promising candidate [104, 130] due to its high gravimetric energy density of 119.9 MJ/kg. Additionally, there is the possibility for the establishment of a hydrogen economy including its generation using so-called 'renewable' energy resources (e.g. wind and solar energy), storage and consumption in both stationary and mobile applications [31]. However, a drawback is the low volumetric density of hydrogen at standard conditions for pressure and temperature. Hence, the increase of volumetric density is the main target of existing hydrogen storage techniques, which mainly separate into pressurized and liquid storage and the storage in metal hydrides. The first is most commonly used, with pressures reaching up to 700 bar for automotive applications [59]. The main drawbacks are the technical efforts required for a safe high-pressure storage of hydrogen and the inflexible, rigid constrain to cylindrical tank vessels. Liquid hydrogen storage needs very low temperatures (e.g. 20 K at 1 bar) which is accompanied by a high energy demand for cooling. The third option is the storage of hydrogen in metal hydrides, which offers the highest volumetric densities [105] This is referred to in literature as solid-state hydrogen storage. In addition to high volumetric capacities, metal hydrides provide a safe and often reversible storage. When in contact with hydrogen, many metals and compounds have the ability to bond hydrogen, either in the interstitial sites of the lattice or by nucleation and growth of a new lattice structure and phase. The reaction with hydrogen is simply controlled via pressure and temperature. For interstitial hydrides, the required temperatures of operation are low, which is the reason why they are also referred to as 'room temperature' hydrides, e.g. $LaNi_5H_6$. A drawback of metal hydrides and in particular interstitial hydrides is their poor gravimetric hydrogen capacity of typically below 2 wt.%, where the latter is expressed as the amount of

stored hydrogen normalized by the raw-material mass. Current research aims at the improvement of gravimetric capacity, combined with low temperature of operation, low pressures (< 100 bar) and fast kinetics. This resulted in the development of complex hydrides (e.g. $NaAlH_4$) or compositions of two hydrides (e.g. $2LiBH_4$-MgH_2). A lot of fundamental research on materials was done on the tailoring of reaction enthalpies and kinetics by use of appropriate additives [34, 36]. However, with respect to application the investigation and optimization of scaled-up metal hydride systems and storage tanks is indispensable. For a comprehensive knowledge about mechanisms and to address the respective design challenges, this requires an appropriate characterization technique - Neutron Imaging. Due to its high sensitivity towards hydrogen and the relative translucency of the metallic tanks shell, Neutron Imaging provides unique insights into the distribution of hydrogen inside the metal hydride bed in situ, and has the potential to reveal the dominant driving forces and rate-limiting steps in these complex systems.

Chapter 2

Theoretical background

In the following sections the theoretical background of Neutron Imaging is given, mainly adapted from *Neutron Imaging and Applications* by Ian S. Anderson et al. [61] as relevant for this work.

The existence of the 'neutron' was proven in 1932 by Chadwick [28]. Its fundamental properties are listed in table 2.1. Due to its mass, it exhibits a de Broglie

Table 2.1: Fundamental properties of neutrons

Mass m_n	Charge	Spin	Magnetic moment
$1.6749 \cdot 10^{-27}$ kg$\approx$ 1 u	0	1/2	-9.662$\cdot$ 10^{-27} J$\cdot$ T^{-1}

wavelength in the order of atomic distances, which makes it sensitive for the characteristic length scales of condensed matter. The relation between neutron energy and its wavelength is given according as

$$\begin{aligned} \lambda &= \frac{h}{m_n \cdot v} \\ E &= \frac{1}{2} m_n \cdot v^2 \end{aligned} \tag{2.1}$$

where λ is the de Broglie wavelength of the neutron with mass m_n and velocity v, h is the Planck's constant. The neutron energy range is classified as given in table 2.2 according to [110, 27]. Since a neutron carries no charge and its mass is significantly higher than an electron mass, the relevant interaction is with the nuclear potential of the penetrated matter. For thermal neutron energies the wavelength is large in comparison to the range of nuclear forces (in the order of femtometers), hence the scattered waves are spherical symmetric and the total scattering cross section is given

Table 2.2: Classification of neutron energies according to [110, 27].

Notation	Energy [meV]	Velocity [m/s]	λ [nm]
Cold	1	437	0.9
Thermal	25	2187	0.18
Epithermal	1000	13832	0.029
Fast/Fission	$1{\cdot}10^{9}$	$14{\cdot}10^{6}$	$2.86{\cdot}10^{-5}$

by

$$\sigma_{tot} = 4\pi b^2 \tag{2.2}$$

with the scattering length b. The latter is derived experimentally due to the lack of a proper theory [112]. The cross section has the unit *barn*, with 1 b = 10^{-24} cm^2. A strong variation of the total cross section among different isotopes and energies exists. The most prominent example for the cross section difference of two isotopes is probably the one of hydrogen and deuterium, which is about 82.3 b to 7.6 b for thermal neutrons [29]. The energy dependency of cross sections[1] is visualized in Figure 2.1 [4]. For

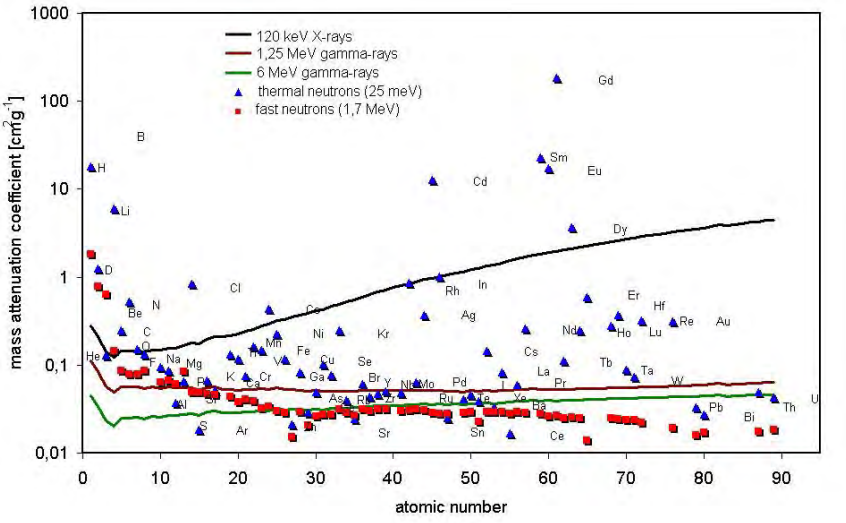

Figure 2.1: Comparison of mass attenuation coefficients for X-rays, γ-rays, thermal and fast neutrons, taken from Bücherl et al. [4].

reasons of better comparison, the mass attenuation coefficients are shown for X-rays and high energy γ-rays as well. As visible, attenuation coefficients for fast neutrons and X,γ-rays are approximately complementary and correlated to the atomic number. In contrast, attenuation coefficients for thermal neutrons vary strongly with the atomic

[1] To be more precise, the Figure shows the total attenuation coefficients normalized to the element mass. For the attenuation coefficient see section 2.1.1.2.

number, originating from variation of the absorption cross section (see section 2.1.1.2). However, the great advantage of neutrons over X-rays is their ability to penetrate elements of high atomic number. In particular, metals are easily penetrated while the interaction with hydrogen is relatively high.

2.1 Neutron Imaging

Neutron Imaging is the superordinate for both Neutron Radiography and Neutron Tomography. The latter is in fact a combination of several Neutron Radiography measurements and is described in section 2.1.2. While a number of measurement techniques and characterization methods are based on the detection and study of the scattered signal, classical Imaging techniques in general[2] are based on the measurement of the beam transmission **through** the sample. These techniques are further described in the following.

2.1.1 Neutron Radiography

The general setup of Neutron Radiography is schematically shown in Figure 2.2 for an exemplary Neutron Radiography of a hydrogen storage tank. The different steps are

- Generation of the neutron beam by the neutron source
- Neutron-sample interaction and projection of corresponding volume element on the detection unit
- Detection of the transmitted neutron beam

These steps are successively elucidated in more detail in the next chapters.

2.1.1.1 Neutron Source

For the generation of a neutron flux sufficient for scattering or imaging experiments two different types of sources are available: reactor sources and accelerator-based sources. The flux of neutrons is defined as the number of neutrons per cm^2 and second.

Reactor sources

The production of neutrons by nuclear research reactor sources are based on the neutron induced fission process of Uranium-235, illustrated in Figure 2.3. Here, a fission of Uranium-235 is induced by an incoming neutron, resulting in the creation of two lighter nuclei and additional neutrons. Typically, one to two neutrons per fission

[2]Independent of the probe, e.g. X-rays or neutrons.

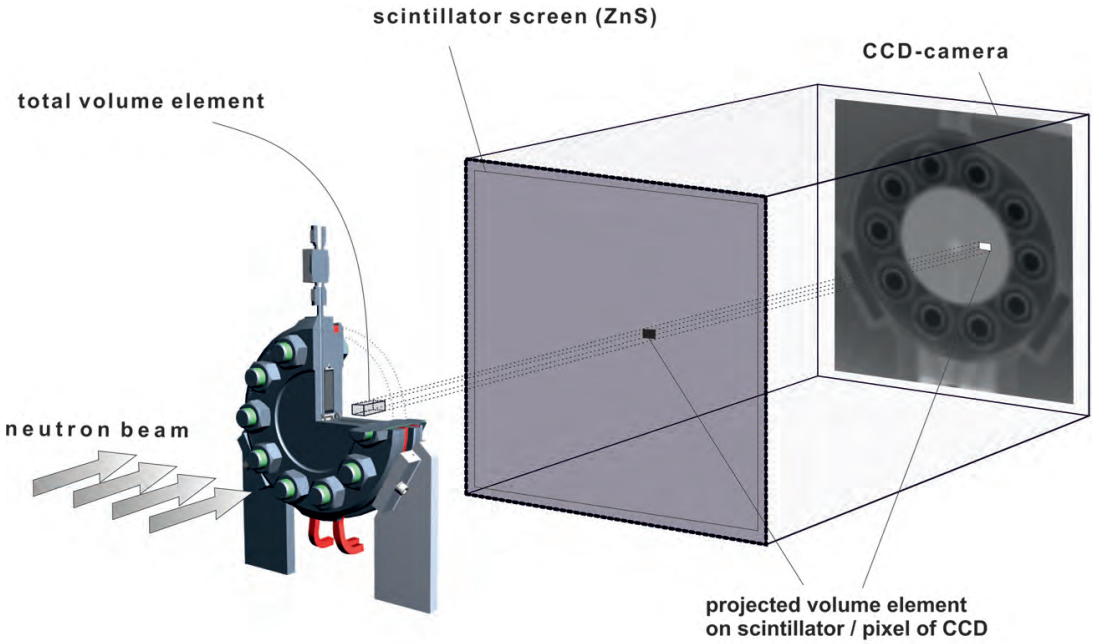

Figure 2.2: Schematic standard setup for Neutron Radiography. The total volume element of neutron-sample interaction is projected onto the scintillator screen (for fission neutrons in this case, ZnS) where the transmitted neutron beam intensity is converted into optical light and imaged by a CCD camera.

reaction can be used for research purposes, the others are either lost or necessary for sustaining the chain reaction [61]. The fission reaction itself is accompanied by a large amount of energy release in terms of heat. However, in contrast to power reactors, research reactor designs are optimized for high resulting neutron flux. After the fission process, the generated neutrons are 'fast' according to table 2.2 with energies in the MeV range and have to be slowed down by a moderator in order to sustain the chain reaction and facilitate a scientific use. This 'thermalization' process is achieved by multiple scattering interactions of neutrons and moderator material, leading to a thermal equilibrium. Most commonly, light or heavy water are used as moderators due their high moderating efficiency[3] [113]. Before neutrons are directed via beamtubes and neutron guides to the target instrument/beamline, they are potentially further moderated to lower energies in a so-called 'cold neutron source' by use of liquid hydrogen or deuterium [47]. The current most powerful research reactors in terms of flux are the FRM II at MLZ in Germany, the HFR at ILL in France and the HFIR at ORNL in the USA.

[3]The high moderation power of hydrogen is due the large elastic scattering cross section. The main advantage of heavy water is its lower absorption cross section, allowing for a less compact reactor core design.

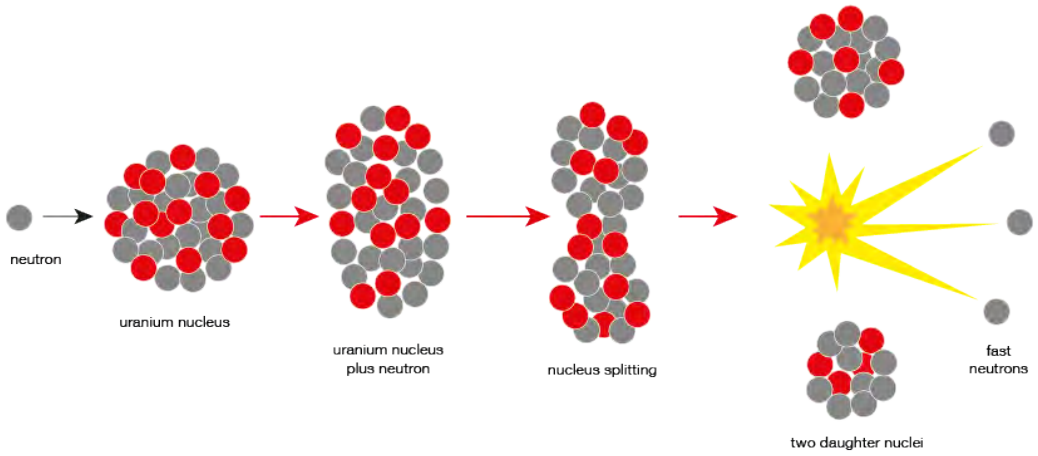

Figure 2.3: Schematic principle of neutron fission reaction for U-235, induced by a thermal neutron; Figure taken from [2].

Accelerator-based sources

The second concept for high-flux generation of neutrons is nuclear spallation, where a target is hit by high-energy protons. The latter are of energies in the order of GeV and are generated by proton accelerators. The number of neutrons released by spallation is significantly higher (factor in the order of 5 [98]) and they cover a large energy range from 10^{-2}-10^{2} MeV, peaked in the range of MeV (2 MeV for Tungsten targets [98]). The used target materials are most commonly Mercury or Tungsten and most sources are pulsed except for the SINQ at PSI in Switzerland. Moderation of the incident 'spalled' neutrons is achieved by liquid hydrogen or liquid methane. The challenge in spallation source design is the minimization of beam loss and heat dissipation [43]. In case of pulsed-sources the heat can dissipate in the pulse intervals, allowing for high power and neutron flux pulses. Additionally, an energy-resolved spectrum is supplied by the different traveling times corresponding to neutron velocities. As a consequence and due to safety issues related to research reactor operation, the current development is focusing on future spallation sources like e.g. the European Spallation Source (ESS) in Lund, Sweden.

2.1.1.2 Neutron-Sample Interaction

Neutrons are guided within beam tubes to the target instrument. For the design of neutron guides, beam tubes and collimator the reader is referred to the various text books, eg. [121]. The transmitted neutron beam intensity I measured by the detector

is described by Lambert Beer's law. With x being the neutron beam direction, it is

$$I = \int_0^E f(E')\gamma(E') \exp^{-\int \mu(E',x)dx} dE' \tag{2.3}$$

with $f(E)$ the spectrum of the incident polychromatic neutron beam, $\gamma(E)$ the detector efficiency, μ the total macroscopic attenuation coefficient. The initial intensity without the sample, I_0, is then given by

$$I_0 = \int_0^E f(E')\gamma(E')dE' \tag{2.4}$$

For a finite sample thickness, as visualized in Figure 2.2, the attenuation by a single element in a distinct volume V (in the figure it is denoted as the 'total' volume element) is defined as

$$\Omega = \mu \cdot d = \frac{m}{V \cdot M} \cdot N_A \cdot \sigma \cdot d = \frac{m}{A} \cdot \frac{N_A}{M} \cdot \sigma = \rho_A \cdot \frac{N_A}{M} \cdot \sigma \tag{2.5}$$

where m is the sample mass, M its molar mass, N_A Avogadro's constant and $\rho_A = m/A$ the area density. The quantity σ is the total microscopic attenuation coefficient. It sums the different types of neutron-matter interactions and can primarily be separated into a total scattering, σ_s and an absorption cross section, σ_a, part

$$\sigma = \sigma_s + \sigma_a \tag{2.6}$$

The absorption cross section , σ_a, describes the true neutron capture process. It depends on the explicit composition of the nucleus and varies significantly among different isotopes, exhibiting a strong energy dependency. In the framework of this thesis, absorption cross sections are generally not taken into consideration except for their particular use in section 5.3.2.

The scattering cross section , σ_s, can be further subdivided into elastic and inelastic scattering interactions and each even further into coherent and incoherent contributions. The elastic coherent scattering carries the structural information on the locations of the nuclei in the lattice. For crystalline materials this is used for structural investigations by 'diffraction' studies. Elastic incoherent scattering is the sum of the individual elastic scattering contributions from single nuclei. The largest incoherent scattering cross section is the one of hydrogen, H-1 [29]. Inelastic scattering contributions are rather small, conveying information on collective excitations in the case of coherent inelastic scattering (e.g. phonon excitations) or on excitation of single

particles/nuclei in case of incoherent inelastic scattering (e.g. diffusion).
All these interactions contribute to the incident neutron beam attenuation. For studies on metal hydrides the elastic incoherent scattering of hydrogen is most dominant, except for use of highly absorbing isotopes as Li-6 and B-10 (section 5.3.2).

Coming back to the schematic drawing in Figure 2.2, in the typical case there is presence of multiple elements within the penetrated volume V. Then, the total attenuation is just the accumulation of attenuations by different isotopes

$$\Omega_{tot} = \sum_{i}^{N} \Omega_i \tag{2.7}$$

where N equals the absolute number of isotopes inside the volume.

Deviations from Beer's law

The ideal Beer's law description for the beam attenuation by neutron-sample interaction is potentially violated in real Neutron Imaging setups. For interaction with hydrogen the beam attenuation is dominated by the large elastic incoherent scattering cross section, as mentioned above. However, scattered neutrons are not necessarily out of the beam or not being detected, depending on the sample-detector distance or the effect of multiple scattering. Hence, effects of scattering potentially perturb ideal Beer's-type dependency of incident and transmitted neutron beam. An additional effect originates from the initial energy distribution of the beam: Due to the energy-dependent interaction probability with the penetrated sample the total beam attenuation changes with increasing penetration depth. This is known as the effect of beam hardening[4] [22]. Both effects of scattering and beam hardening are investigated and discussed comprehensively within this work in sections 5.2.1 and 5.3.2.1.

2.1.1.3 Neutron Detector systems and image generation

For quantitative Neutron Imaging the detection is a process of conversion of neutrons and projection onto a discrete array of pixels with intensities proportional to the registered neutron intensity. Within this framework, an image is denoted as the 2D spatial distribution of neutron intensities. For fast digital processing of images, charge-coupled device (CCD) cameras are used and the measured or counted intensity is discretized by use of gray values. Accompanied by the use of CCD cameras there is a necessity for conversion of neutrons into optical light, which is realized by a scintillator

[4]For presence of high amounts of hydrogen in the sample, the latter can also act as kind of a moderator, softening the spectrum due to elastic collision instead of hardening it.

screen. Additional components are a 45°front surface mirror after the scintillator to prevent radiation damage of the camera by γ-rays or even neutrons. Moreover, a focusing lens system can be used to vary the spatial resolution. The typical setup is given by scintillator, mirror, lens system and CCD-camera [56, 92, 103]. In Figure 2.2 only the scintillator screen and the CCD-camera are shown for reasons of simplicity. The scintillator material depends on the neutron energy: for fast neutrons e.g. ZnS embedded in propylen is used [25]. The detection mechanism is based on proton-recoil by the incoming neutron beam and ionization of ZnS, with photon release on relaxation [70]. For thermal and cold neutrons a thin layer of e.g. Li-6F:ZnS is used [111]. The highly absorbing component (Li-6) is used to produce charged particles by a neutron capture reaction, which then ionizes a scintillator composite material (ZnS) and optical light is generated within the relaxation process.
Considering the influence of the detector system itself, the finally derived gray value or intensity of a pixel within an image is given by

$$I^{\star} = C^{\star} \cdot I + I_D \tag{2.8}$$

where $C^{\star}$ is a proportionality factor of the detector system, I is the original neutron beam intensity after the sample transmission and I_D is the dark current of the detector [61]. The incident beam intensity is measured without sample in the beam path, the corresponding image is denoted by the flat field in the following chapters. The dark current is measured without the beam itself, its corresponding image is referred to as the dark image. Accordingly, for a negligible energy dependency total attenuation is derived by

$$\Omega = -ln\left(\frac{I - I_D}{I_0 - I_D}\right) \tag{2.9}$$

where $I = I^{\star}$ is denoted as the measured neutron beam intensity for the following chapters of this thesis.

2.1.1.4 Spatial resolution

The resulting spatial resolution in an image depends on different parameters. Primarily, there is the pixel array of the CCD camera itself and the scintillator screen that is projected onto it. By using optical systems the size of the focused section of the scintillator can be changed and therewith the pixel resolution. Nowadays, the pixel array of CCD cameras range typically from 1024×1024 to 2048×2048 pixel. However, the final effective resolution in the image depends on additional parameters like geometrical unsharpness, scintillator thickness as well as scattering influences. The first is known as the L/D ratio and is solely given by geometry as shown in Figure 2.4.

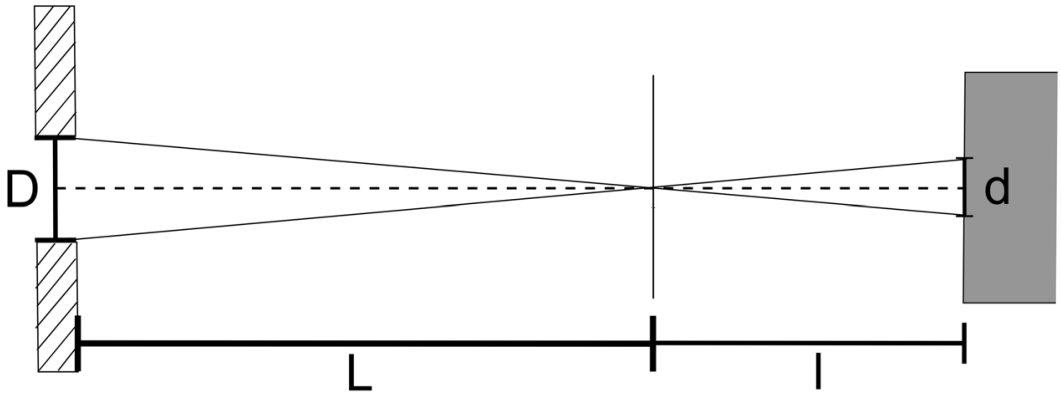

Figure 2.4: Principle of the L/D criterion: A point is broadened by d for sample-detector distance l, assuming a virtual source of width D and distance L to the sample.

Assuming a virtual source on the left side with thickness D, a point at a distance L is enlarged by d for l being the point (sample)-detector distance. Hence, it is

$$L/D = l/d \tag{2.10}$$

Accordingly, to increase the spatial resolution the sample-detector distance has to be minimized. By collimation of the neutron beam, the virtual source width D at the end of the collimator can be reduced, further increasing the spatial resolution. Since high L/D ratios are usually accompanied by a low neutron flux, measurements are a compromise of beam intensity and spatial resolution [61]. Additional blurring and unsharpness is caused by the effect of scattered neutrons superimposing the transmitted neutron beam, which is in particular present for strong incoherent scattering contributions, e.g. by hydrogen. Additionally, the scintillator thickness reduces the spatial resolution. Since the conversion rate and therewith detection efficiency are positively correlated to the scintillator thickness, it is again a compromise between spatial resolution and image intensity.

The effective spatial resolution can be quantified by determination of the Edge Spread Function of the system [118]. If an edge object with the edge in parallel to the beam direction is imaged, the edge is transferred to a step function in case of an ideal imaging system. However, in real system the transition is broadened as expression of the limited spatial resolution. This broadening is described by the Edge Spread function, from which several derivations can be calculated for quantification of the spatial resolution. In appendix A.1.1 further information is given on the comparison of different functions for the calculation of the spatial resolution.

2.1.1.5 In situ Neutron Radiography

The sequential acquisition of Neutron Radiography images for the analysis of time-resolved processes is denoted as in situ Neutron Radiography. The total time between subsequent images is the sum of exposure time (image acquisition time) and the time necessary for data-processing and storage. The optimal exposure time is a compromise of fast image acquisition, spatial resolution and corresponding quality of the derived images as discussed in the section above. If the time-dependency can be assigned to a single element or contribution of the total attenuation coefficient, it can be separated into

$$\mu_{tot}(x, y, z, t) = \mu_C(x, y, z) + \mu_{TD}(x, y, z, t) \tag{2.11}$$

with a time-constant part, $\mu_c(x, y, z)$ and time-dependent part, $\mu_{TD}(x, y, z, t)$. Considering only the projection on one pixel in terms of the time-dependent beam attenuation, the difference attenuation in the time interval $t - t_0$ is given by

$$\Delta\Omega(t) = \Omega_{TD}(t) - \Omega_{TD}(t_0) = -ln\left(\frac{I(t) - I_D}{I(t_0) - I_D}\right) \tag{2.12}$$

and simply the logarithmic ratio of dark image corrected intensities at t and t_0.

2.1.2 Neutron Tomography

The second method addressed by the superordinate Neutron Imaging is Neutron Tomography. It is a combination of several two-dimensional Neutron Radiography measurements, which allows for a three-dimensional reconstruction of the projection data set and gives access to the three-dimensional total attenuation coefficient. The following has been adopted from Kak and Slaney [68]. Let $\mu(x, y)$ be the two-dimensional total attenuation coefficient of an object with (x, y) spanning a plane in parallel to the projection direction. The attenuation of a neutron beam propagating along a line A through the sample is described by the total integrated attenuation coefficient along this line - a one-dimensional projection of the attenuation coefficient. The line A can be parametrized by two variables (θ, t) as shown in the left part of Figure 2.5, with its parametrization given by

$$x \cdot cos(\theta) + y \cdot sin(\theta) = t \tag{2.13}$$

The projection is then expressed by the line integral

$$P_\theta(t) = \int_{line} \mu(x, y)ds \tag{2.14}$$

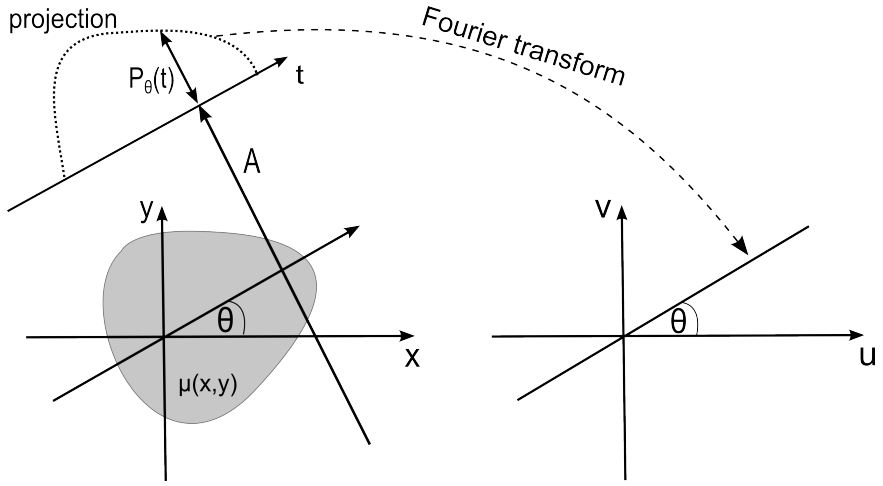

Figure 2.5: Left: Projections $P_\theta(t)$ of the total attenuation coefficient $\mu(x, y)$ defined by line integrals along the line A, defined by the parameters θ and t. Right: Principle of *Fourier slice theorem*, according to which the Fourier transform of projection $P_\theta(t)$ corresponds to a line through the origin of the frequency domain (u, v) of the Fourier transform of the attenuation coefficient. Adapted from Kak and Slaney [68].

which can be rewritten so that

$$P_\theta(t) = \int_{-\inf}^{\inf} \int_{-\inf}^{\inf} \mu(x, y) \cdot \delta\left(x \cdot cos(\theta) + y \cdot sin(\theta) - t\right) dxdy \tag{2.15}$$

The as defined transformation of $\mu(x, y)$ is called the *Radon transform* of $\mu(x, y)$. For Tomography data sets the Radon transform is also denoted as *sinogram*, since a full 2π rotation of θ transforms the projection of a point onto a sinusoidal line in the (θ, t) reference system. A full projection of a finite sample object is derived by a combination of several line integrals for constant rotation angle θ, assuming a parallel projection[5] The two-dimensional Fourier transform of the attenuation coefficient is given by

$$F(u, v) = \int_{-\inf}^{\inf} \int_{-\inf}^{\inf} \mu(x, y) \cdot \exp^{-i2\pi(ux+vy)} dxdy \tag{2.16}$$

whereas for a projection at constant angle θ the corresponding one-dimensional Fourier transform is given by

$$S_\theta(\omega) = \int_{-\inf}^{inf} P_\theta(t) \cdot \exp^{-j2\pi\omega t} dt \tag{2.17}$$

According to the *Fourier slice theorem* the one-dimensional Fourier transform of a projection is equal to values of $F(u, v)$ along a line through the origin, as visualized

[5]This, however, requires a negligible beam divergence, which usually a valid assumption for most imaging beamline.

in right part of Figure 2.5. This line is defined by a rotation of the u-axis by angle θ:

$$P_\theta(\omega) = F(\omega, \theta) = F(\omega\ cos(\theta), \omega\ sin(\theta) \tag{2.18}$$

with $u = w\cos(\theta), v = w\sin(\theta)$. Thus, Fourier transforms of projections of the attenuation coefficient reveal the values of $F(u, v)$ along lines defined by θ. Accordingly, the original attenuation coefficient can be reconstructed from the projection data by inverse Fourier transform. The algorithm commonly implemented for attenuation coefficient reconstruction is the filtered back-projection algorithm (for derivation, see [68])

$$\mu(x, y) = \int_0^\pi \int_{\inf}^{\inf} S_\theta(\omega)\, |\omega| \exp^{j2\pi\omega t}\, d\omega d\theta \tag{2.19}$$

where $|\omega|$ is a frequency filter and the integration over ω is the 'back-projection'. The quality of reconstruction depends on the number of different projections at corresponding angles θ. According to Kak and Slaney [68] the optimal number of projections is defined by

$$N_\theta = \frac{\pi}{2} \cdot N_s \tag{2.20}$$

where N_θ is the number of equally distributed projection angles in the range of 0°-180°and N_s is the number of pixels necessary for an image of the sample. Hence, for a typical Tomography experiment the number of pixels that represent the object to be imaged determine the number of necesary roational angles. The reconstruction for every projection in the (x, y)-plane results in a (x, y)-slice. Including the 3rd dimension, z, gives a stack of slices, representing the full three-dimensional attenuation coefficient.

2.2 Metal-hydride based hydrogen storage

From the overall large field of metal hydrides, the following sections are limited to a short introduction into the properties and fundamentals of hydrogen absorption by metal hydrides that are relevant in the framework of Neutron Imaging analyses performed within this work. For further reading there are a number of text books, e.g. [58] or [7], that the interested reader is referred to. The following is based on *Hydrogen as Future Energy Carrier* [7]. In general, a hydrogen absorption process starts with the emergence of a physisorbed state characterized by an attractive Van-der-Waals interaction force between a hydrogen molecule and the metal surface. Further approaching the metal surface, the molecule is dissociated and hydrogen metal bonds are formed in the chemisorbed state. Next to chemisorption is the transition into subsurface layers and diffusion of hydrogen in the host metal. The thermodynamic features of a proceeding reaction are schematically given in Figure 2.6. It shows the aspects of

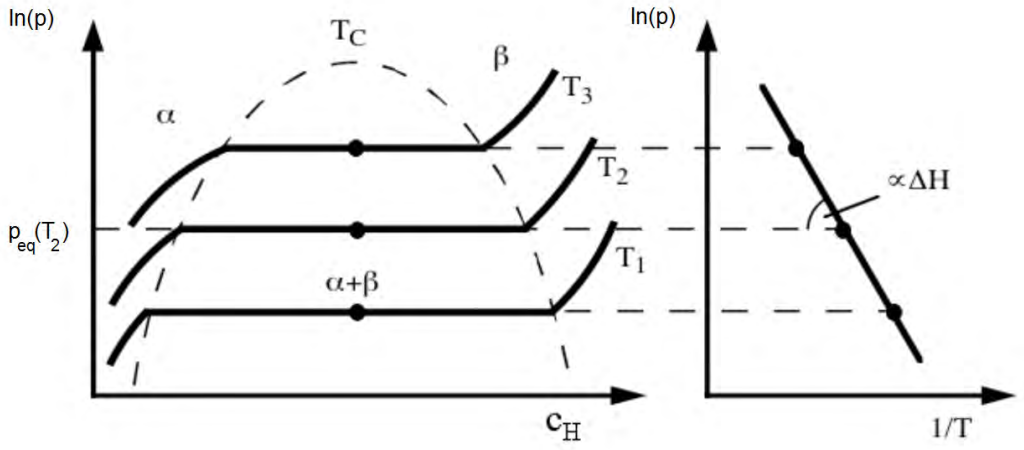

Figure 2.6: Schematic principle of pressure concentration isotherms (left) with according van't Hoff plot (right), adapted from [35].

pressure-composition isotherms in the left part, where the logarithmic hydrogen gas pressure depending on the concentration of hydrogen in the metal (denoted by c_H) is shown for different isotherms. For low concentrations the metal and hydrogen form a solid solution, denoted as the α-phase. For a given temperature, the concentration of hydrogen in solid solution is further increased by increase of pressure. At a certain pressure level, hydrogen-hydrogen interaction inside the metal becomes relevant and nucleation and growth of the hydride phase is induced [105]. For the coexistence of solid solution (α) and hydride phase (β) the isotherms in Figure 2.6 show a flat plateau, reaching until the maximal hydrogen content for the specific temperature is reached

in the pure β-phase. Further increase of hydrogen concentration can only be achieved by pressure increase and emergence of solid solution of hydrogen in the β-phase. With increase of temperature the plateau range is reduced, it vanishes for the critical temperature T_C, above which separation into the two different α and β-phase is no longer possible. Temperature and equilibrium pressure of a corresponding plateau are used for calculation of the formation enthalpy of the metal hydride according to the van't Hoff equation

$$\frac{1}{2} \cdot \ln\left(\frac{p}{p_0}\right) = \frac{\Delta H}{RT} - \frac{\Delta S}{R} \tag{2.21}$$

where R is the universal gas constant, ΔH the enthalpy and ΔS the corresponding entropy of formation. In the case of two or more hydride forming metals, multiple plateaus can occur [58]. In the right part of Figure 2.6 the van't Hoff plot of the left pressure-composition isotherms is shown. The line defines the plateau pressure for the two-phase equilibrium of the α and β-phases depending on the inverse temperature. It states that ab- or desorption of hydrogen is controlled by change of temperature or pressure: starting from equilibrium for a given temperature and pressure, absorption of metal hydride phase is ensured by pressure increase at constant temperature and vice versa. This thermodynamic mechanism represents the driving force for reaction of all metal hydride systems and corresponding storage tanks.

2.2.1 Sodium alanate - $NaAlH_4$

In addition to this thermodynamic considerations, kinetic barriers for the respective thermodynamically more stable state have to be taken into account. This may hinder thermodynamically favored reactions. In some cases, a hydride may release hydrogen upon heating, but may neither re-absorb hydrogen nor form the initial hydride again. Reaction barriers need to be overcome and respective measures need to be applied. Bogdanovic and Schwickardi have shown that the complex metal hydride sodium alanate can successfully store and release hydrogen reversibly, if $TiCl_3$ is added [14]. This is one of the few examples of hydrides so far that combine moderate temperature of operation and rather high capacity of 5.5 wt.%. Due to its promising properties for application purpose, it has been subject to a number of research studies. The absorption of hydrogen takes place with a two-step reaction

$$\mathrm{NaH} + \mathrm{Al} + \frac{3}{2}\,\mathrm{H_2} \rightleftharpoons \frac{1}{3}\mathrm{Na_3AlH_6} + \frac{2}{3}\mathrm{Al} + \mathrm{H_2} \rightleftharpoons \mathrm{NaAlH_4} \tag{2.22}$$

evolving from the initial state to a hexa-alanate state and finally to tetra-alanate. The apparent pressure-temperature conditions for the existence of the three phases are shown in Figure 2.7. Starting from the desorbed state, the hydrogen storage

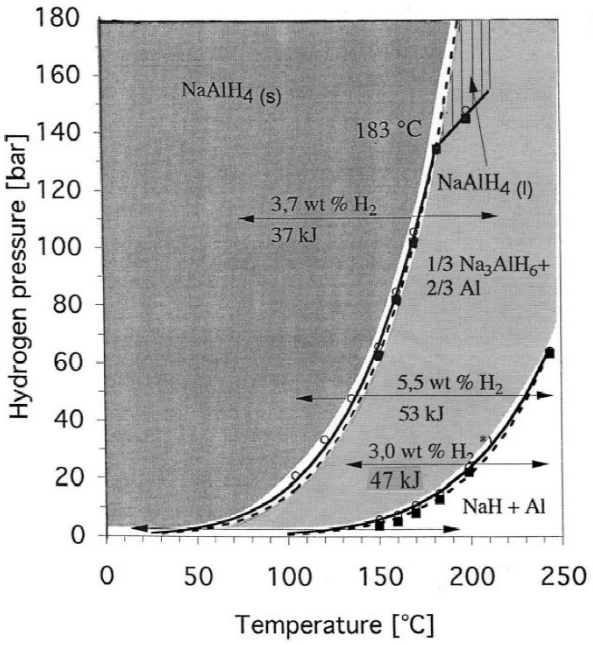

Figure 2.7: Pressure-temperature phase diagram for sodium alanate with added $TiCl_3$, taken from Bogdanovic et al. [12].

capacity for the first absorption step is 3.0 wt.%, followed by additional 3.7 wt.% for the evolution from the hexa to the tetra state. For improvement of heat transfer and volumetric density, the loose powder has been compacted to pellets and studies on the effect of compaction have been carried out [115, 77, 126] confirming an increased thermal conductivity. Both powder and pellets show good cyclability [13, 115].
The handling of a scaled-up production of raw NaH-Al-0.05$TiCl_3$ has been proven by e.g. Eigen et al. [37], showing a suitability of sodium alanate for application in scale-up storage systems and tanks. For this reason, several studies on large sample size as well as storage tank studies have been carried out by Donald L. Anton and others [81, 82, 128]. Though all of them report a good scalability, studies are limited to loose powder beds. However, for scaled-up storage system based on compacts, the capacity is significantly reduced to 4 wt.% as reported by Bellosta von Colbe et al. [127], the reason for this is has not been clarified yet.

2.2.2 Reactive Hydride Composite - Li-RHC

Vajo et al. and Barkhordarian et al. introduced the concept of 'Reactive Hydride Composites' (RHC) [122, 9, 8], where two complex hydrides (one e.g. a borohydride, the other e.g. Magnesium Hydride) react exothermally during dehydrogenation and thus lower the overall reaction enthalpy of the system. During the reaction of borohy-

drides with MgH_2, MgB_2 is formed and reversibility was shown for the $LiBH_4$-MgH_2 system [20, 90]. The $LiBH_4$-MgH_2-RHC[6] system is of particular interest due to its high theoretical hydrogen storage capacity of 11.5 wt.% and low reaction enthalpy of 40.5 kJ/mol(H_2) with an equilibrium pressure of 1 bar at 225 °C [122]. The absorption takes place in a one-step reaction

$$2\,LiH + MgB_2 + 4\,H_2 \rightleftharpoons 2\,LiBH_4 + MgH_2 \tag{2.23}$$

while the desorption is found to be a two step reaction with initial decomposition of Magnesium Hydride followed by destabilization of $LiBH_4$ and formation of MgB_2 and LiH. For reversibility the formation of MgB_2 during dehydrogenation is considered to be crucial, according to Bösenberg et al. and Vajo et al. it depends on the applied hydrogen back pressure [91, 20, 122]. The reaction kinetics can be significantly increased with simultaneous lowering of ab- as well as desorption temperatures by use of additives, e.g VCl_3 and $TiCl_3$ [20, 19, 33, 65, 18]. Still, strong kinetic constrains are presesent, causing elevated temperatures of operation. Hence, typical conditions for absorptions are temperatures of 350 °C at a pressures of 50 bar respectively 400 °C at 3-5 bar for desorption. For these conditions, it shall be noted that $LiBH_4$ is present in the liquid phase due to its melting point at about 275 °C. Concerning the cycling stability, a significant capacity loss is reportet during cycling even for small sample sizes [65]. Compaction of material has been performed by Jepsen et al. to increase thermal conductivity and reversibility with encouraging results [66].
Scale-up of material is so far reported only by Jepsen for loose powder material, where an increased degradation of capacity was observed during cycling [65]. Within a current project, Bor4Store [117], a scale-up of Li-RHC and its combined use with a solid oxide fuel cell is investigated.

[6] In the following it will be denoted as Li-RHC for reasons of simplification.

Chapter 3

Neutron Imaging of metal hydrides - state of the art and scope of work

In the following a brief summary of the evolution of Neutron Imaging for the investigation of hydrogen storage materials is given, followed by a description of the state of the art of the technique and the present limits for the investigation of metal hydride based storage systems. Finally, the scope of this work is presented, subdivided into method development and their application on two promising metal hydride systems.

3.1 Characterization of storage systems by Neutron Imaging - state of the art

The use of metal hydrides for commercial hydrogen storage needs the transfer from lab-scale, basic scientific investigations to the study of scaled-up and application related systems. To tailor materials towards their theoretical capacity and towards application, there is a strong need for the possibility to investigate the hydrogenation process in operando. This enables a potential identification of the rate limiting steps and helps to overcome the slow kinetics that may be associated with them. By 'classical' measurement techniques, the thermodynamic quantities pressure and temperature inside the metal hydride bed and the hydrogen flow are measured to determine the systems overall kinetics. Doing so, the total sample amount is averaged and no investigation of the spatial distribution of hydrogen inside the material is possible. That is why only hypotheses can be stated for observed deviations from theoretical or lab-scale capacities and kinetics as it is the case in [127, 65]. Powerful scattering techniques

like in situ diffraction studies, SANS, USANS or complementary X-ray techniques [94] are not applicable due to the large sample size and surrounding tank hull material, minimizing the beam transmission in particular for X-ray studies. A solution and comprehensive analysis tool is Neutron Imaging. Already in early 2000 the first successful Neutron Imaging experiments on the distribution of hydrogen in Mg_2Ni samples have been reported [99, 100]. However, investigation possibilities were limited due to the use of imaging plate detector techniques [83], which did not allow for a simple processing of data. With development of imaging instrumentation, referring to both hardware in terms of CCD cameras and software in terms of data processing and image reconstruction packages, the potential of in situ investigations increased significantly. Against this background, in-situ Neutron Imaging has been identified as an extremely suitable and effective method for the characterization of hydrogen storage systems.[49, 63, 93, 94] Due to the high neutron cross section of hydrogen in comparison to other elements, the in situ study of hydrogen distribution inside the metal hydride becomes possible. While first works have been based on the qualitative analysis only, studying macroscopic structure deformations due to pressure application or cycling of material, there is a growing interest in a quantitative analysis for precise determination of the explicit distribution of hydrogen in the metal hydride [49, 63, 93, 94, 99]. Fundamental Beer's law and the ratio of images of one ab- or desorption sequence is used for the investigation of the hydrogen distribution according to equations 2.5 and 2.9 in section 2.1.1 .
For investigation of the 3D material structure, Neutron Tomography (NCT) has been proven to give unique insights into the 3D distribution of hydrogen [94, 63, 55]. While mostly limited to ex-situ studies due to the relatively long overall acquisition time for a full set of projection images, recently there has been shown the possibility of real-time NCT by use of projection angles according to the Golden Ratio [131] .

Neutron Imaging - methodical limits

Still, a major drawback concerning quantitative data evaluation is the uncertainty of the effective macroscopic neutron attenuation coefficient for hydrogen [63] according to equation 2.5. It depends on the sample detector distance in terms of the influence of scattering, the neutron beam spectrum and profile and in case of thermal or cold neutron spectra also on potential Bragg scattering [102, 114, 15] by structures of the metal hydride material and beam hardening effects [74, 107]. So far, either literature values for the cross section of hydrogen or calibration measurements using water are used, both causing uncertainties in quantification of data [63, 93]. For in situ Neutron Radiography, the amount of hydrogen is determined according to the attenuation difference of subsequent images and a reference image in combination with the explicit

macroscopic attenuation coefficient of hydrogen as described above. The normalization to the underlying raw material to derive the wt.%-distribution is so far only possible if the exact bed geometry and distribution of material mass is known or assumed a priori [49, 108]. Thus, a method is missing to determine the material distribution within the measurement, independently of the metal hydride bed geometry, in order to correlate the distribution of hydrogen to the raw material distribution. Furthermore, current studies on Neutron Imaging of metal hydride materials are limited to a sole 'image' of the hydrogen distribution, not taking into account relevant driving forces like e.g. temperature or material packing density. Thus, so far there exists no possibility to distinguish between influences of single driving forces on the overall reaction and the distribution of hydrogen. This is a major methodical limit for the use of Neutron Imaging for metal hydride systems.

Neutron Imaging - material investigation limits

Concerning the investigation of metal hydride materials and the results gained from Neutron Imaging studies, current research is well below the full potential of the method: qualitative, ex-situ investigations have strong limitations and quantitative in situ studies have been limited to interstitial hydrides only. Until now, no promising or potential materials for application have been investigated by quantitative Neutron Imaging. Additional, quantitative studies have been limited to small samples sizes since scale-up material investigation require storage tanks or sample cells in particular designed for the use of Neutron Imaging.

3.2 Scope of work

Apart from the introduction of experimental specifications and methods, this thesis can in general be subdivided into two parts: first, new methods are developed for the investigation of metal hydride systems by means of Neutron Imaging. In the second part, the developed methods are applied to two promising systems with respect to future application of metal hydride based hydrogen storage: sodium alanate and the Lithium-based reactive hydride composite. In the following a short overview on the two parts is given.

1. The method development covers both in situ Neutron Radiography as well as Neutron Tomography. A new approach for data quantification in solid-state metal hydride systems is presented. It is based on the combination of intrinsic thermodynamic quantities and nuclear physics theory, overcoming the above mentioned limits of the use of the neutron-hydrogen interaction cross section

and corresponding absolute attenuation coefficient. In this context, a method for scattering field analysis and its correction is developed. A technique to correlate Neutron Imaging data and additional macroscopic fields like temperature and material packing density is developed, which gives a first-time access to the interdependency of driving forces in metal hydride systems or complex systems in general. Within that framework, a new method is developed for the determination of a quasi-continuous temperature field of scaled-up metal hydride beds by means of IR-Thermography. The second part of method development refers in particular to the analysis of metal hydride systems with presence of liquid phases. A general method is developed for identification of material transfer and estimation of the amount of mass transport, independent of sample size and neutron energy spectrum. Furthermore, a new concept is introduced for Neutron Imaging: isotope labeling in combination with a cold neutron spectrum aiming at a unique characterization of highly absorbing phases like $LiBH_4$ for lab-scale sample sizes with micrometer resolution. The effect of beam hardening and consequences for data quantification are clarified.

2. The developed methods are applied to two metal hydride systems: Methods for solid-state metal hydride systems are applied to a scaled-up sodium alanate pellet. Therewith, a quantitative Neutron Imaging study on a scaled-up complex hydride is performed. The introduced new methods for data quantification, scattering correction and, most important, correlation analysis by combination of multiple macroscopic fields for temperature, material packing density and hydrogen distribution are applied for the fist time in order to study the interdependency of the corresponding driving forces temperature field and material packing density. Methods for the analysis of solid-liquid phase mixtures are applied to the Li-RHC system, both with macroscopic and microscopic resolution by choice of fission respectively cold neutron energy spectra. Within this context, an absorption process for a scaled-up pellet is investigated both by in situ Neutron Radiography as well as Neutron Tomography to study both the time-resolved hydrogen distribution as well as the 3D material structure. The developed methods for detection of material transfer are applied to investigate the long-range mobility of $LiBH_4$ in the system. Isotope labeling is applied on lab-scale Li-RHC samples and material transfer of the liquid phase is studied in detail with respect to phase separation and clustering. By combination of spatial resolution and phase sensitiveness, the distribution and dynamics of a highly absorbing phase, $LiBH_4$, is followed throughout the reaction.

Finally, perspectives are given in terms of future method development and application of developed methods. Furthermore, a complementary use of neutrons and x-Ray imaging for addressing multi-scale problem is shown. The impact of new methods developed within this work and observed results as well as conclusions for investigated materials are summarized.

Chapter 4

Experimental and methods

4.1 Beamline setups

The performed measurements within this work have been carried out at two different Imaging instruments at the research reactor FRM II at MLZ in Garching near to Munich. For the investigation of scaled-up samples the fission Neutron Imaging instrument NECTAR was used, respectively the cold Neutron Imaging instrument ANTARES for the study of lab-scale samples. Both beamlines are briefly introduced in the following, including the instrument setups for the performed measurements.

4.1.1 NECTAR - fission neutron imaging

The Neutron Imaging beamline NECTAR at FRM II is the only instrument available for user services in Europe providing a fission neutron spectrum [25], which makes it especially suitable for the investigation of scaled-up samples due to lowered overall neutron interaction cross sections and accordingly a high transmittivity as shown in Figure 2.1 in section 2. In the left part of Figure 4.1 a schematic drawing of the beamline is shown. The instrument consists of two parts, where the first measurement station, MEDAPP, is a neutron therapy facility and the second station is the Imaging station. The generation of the fission neutron spectrum is done by use of a converter plate that is placed within the moderator at the entry of the beam tube, consisting of uranium silicide with 93% U-235. Fission neutrons are guided within a beam tube to the instrument. A permanent filter consisting of 1 cm B_4C and 1 cm lead is used for reduction of thermal neutrons as well as for reduction of γ-radiation. Before reaching the collimator, the neutrons pass a bench of additional available filters. The typical filter set used for Neutron Imaging is a combination of iron and borated PE as well as cadmium layers and lead [25, 21], which leads to a spectrum at the instrument as

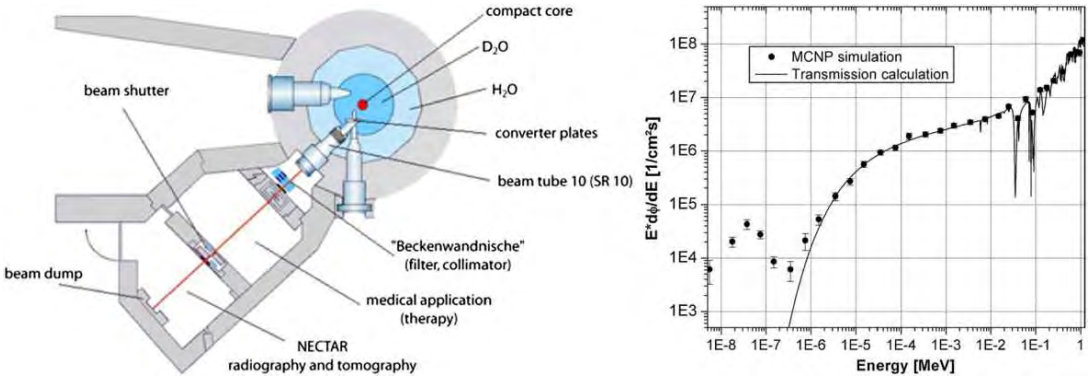

Figure 4.1: Schematic overview of the NECTAR beamline, taken from [24] and fission neutron spectrum using a standard filter setup; taken from [25].

shown in the right part of Figure 4.1. The small thermal peak is due to the influence of moderation in the guide [21]. The spectrum is peaked at 1.8 MeV with an average neutron energy of 1.1 MeV. In the frame of this work, the filter setup was changed for higher suppression of the gamma background and a filter of 10 cm of lead was used instead. A change of the energy spectrum with respect to the one shown in the right part of Figure 4.1 was not further considered. The collimator opening resulted in a L/D ratio of about 75. The scintillator is ZnS embedded in polypropylene using proton recoil induced fluorescence of ZnS as conversion reaction. The described setup is denoted as the standard setup for the following chapters. The acquisition of images was performed with a CCD-ANDOR DV-434BU camera with a pixel array of 1024 $\times$ 1024 at a pixel size of 293 μm. For the reduction of influence by image artifacts caused by radiation directly hitting the detector, a filtering algorithm for fission Neutron Imaging was applied in combination with an additional median filtering of the image data.[84]

4.1.2 ANTARES - cold neutron imaging

For investigation of lab-scale samples at micrometer resolution measurements have been performed at the ANTARES Neutron Imaging instrument [106]. In the left part of Figure 4.2 a schematic drawing of the beamline is shown. The measurement position is in chamber 2, the energy spectrum at ANTARES is given in the right part of the Figure. It is a cold spectrum peaked at about 1.6 Å. For the measurements a pinhole of 18 mm was used, leading to an L/D ratio of 800. The precise adjustment of the beam shape in order to match it to the sample geometry is done by a beam limiter. Two different detector setups have been used:
For short exposure times and high time-resolution of in situ process monitoring a LiF-

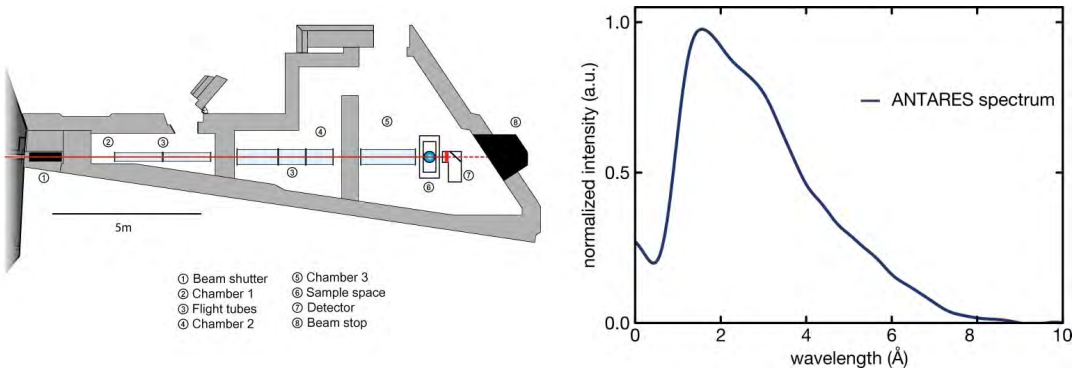

Figure 4.2: Left: Instrument setup of the cold Neutron Imaging instrument ANTARES at FRM II, taken from [106]. Right: Cold neutron energy spectrum at ANTARES, Figure modified from [1].

ZnS scintillator has been used with thickness of 200 μm, offering a field of view of 150 $\times$ 150 mm. The acquisition of images is performed with a CCD-ANDOR cooled camera with pixel array of 2048 $\times$ 2048 at a pixel size of 73.2 μm. Ex situ studies have been performed with a high resolution setup with a Gadolinium Oxysulfide (Gd_2O_2S) scintillator of 10 μm thickness, offering a field of view of 40 $\times$ 40 mm. With the same camera, a pixel size of 20.6 μm is derived by use of an optical lens system.

4.1.3 Neutron Tomography data reconstruction

The acquired projection data sets of Neutron Tomography studies are first filtered for so-called white spots (saturated pixel originating from e.g. γ-ray impact) by use of an adaptive filter (e.g. 'Despeckle' within *ImageJ* [95]) and then reconstructed with use of commercially available software, *Octopus* [26], and a filtered back-projection algorithm. The reconstructed slice data is then visualized by either *VGStudio MAX* [48], ImageJ, *MATLAB* [62] or *ParaView* [6]. For a volume data visualization, one element of the mesh is referred to as a so-called *voxel* with a macroscopic attenuation coefficient μ scaled by [1/cm].

4.2 Loading station and storage tank systems

In the following, design and experimental details of the used loading station for sorption experiments as well as storage tanks respectively sample cells are given.

4.2.1 Loading station

The hydrogen loading station used within this work allows for in-situ monitoring and control of absorption and desorption measurements. In appendix A.2 a schematic drawing of the setup is shown and more detailed information is given. The hydrogen flow is controlled by a mass flow controller (MFC). The standard setup and procedure for an absorption experiment is as follows:
An external hydrogen pressure bottle is attached to an input valve at the loading station with a reservoir pressure at least 3 bar above the maximal target pressure in the tank to ensure a sufficient pressure gradient necessary for operation of the mass flow controller. At the output valve, a tube connection to the storage tank containing the metal hydride is attached. The storage tank is heated to the target temperature for the absorption process and a controlled hydrogen flow to the storage tank is set. Thermodynamic quantities hydrogen flow, pressure and temperature at the storage tank are recorded. This allows for determination of the absorbed hydrogen content by a kind of continuity equation: hydrogen passing the MFC is either in gaseous phase or absorbed by the metal hydride. Hence, it is

$$n(H_2)_{abs}(t) = \int_{t_0}^{t} f_{H_2}(t')dt' - \frac{p(t)}{R}\left(\frac{V_{Tank}}{T_{Tank}} + \frac{V_p}{T_p}\right) \tag{4.1}$$

where $f_{H_2}(t) = dn/dt$ is the hydrogen flow (unit $\mathrm{ml}_n/\mathrm{min}$), $p(t)$ is the time-dependent hydrogen gas pressure, V_{Tank} the effective free storage tank volume and T_{Tank} the corresponding temperature inside the storage tank. V_p is the pipe volume from the MFC to the storage tank and T_p the corresponding temperature. The pipe volume is dead volume and can be reduced by e.g. use of PEEK capillaries with 2 mm inner diameter as connection tubes. The effective free tank volume is the remaining free volume in the tank containing the metal hydride. Due to the porosity in the metal hydride bed depending on its material packing density, it is not simply the difference of empty tank volume and corresponding macroscopic metal hydride volume, but has to be calculated by means of a calibration measurement. For that, the pressure inside the storage tank containing the metal hydride is increased by continuous hydrogen flow monitored by the MFC. Measurements are done at room temperature to ensure isothermal conditions for both tank and pipe volume, the maximal pressure has to be chosen according to the used metal hydride to prevent any absorption by the metal hydride. The effective volume is then given by

$$V_{Tank} = \frac{1}{dp/dt} \cdot f_{H_2} \cdot R \cdot T - V_p \tag{4.2}$$

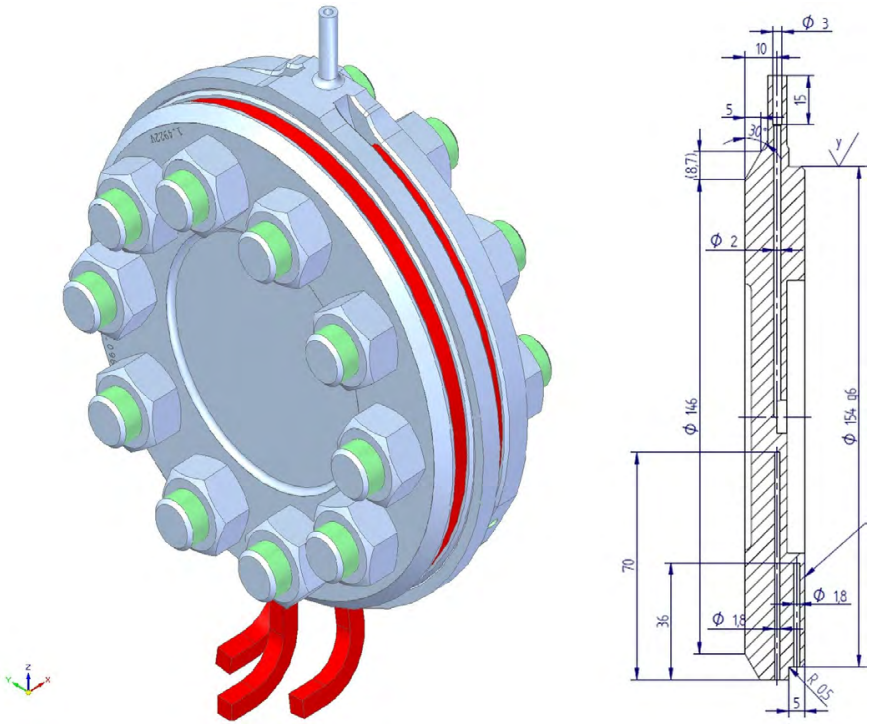

Figure 4.3: Left: Volume view of the FlexiStore tank without thermal insulation. The heating cartridges are colored in red. The upper cylindrical part is the connection for the hydrogen supply line. Right: Technical drawing of the side cross section of the tank bottom body part with hydrogen supply line (vertical, from top to the center) and boreholes for thermocouples (vertical, starting from the bottom part).

where dp/dt is the pressure increase. The pipe volume is determined in full analogy but with disconnected storage tank.

4.2.2 Hydrogen storage tank FlexiStore

For measurements of scaled-up metal hydride pellets and powder a storage tank in particular designed for in situ Neutron Radiography was constructed, in the following referred to as 'FlexiStore'. It is made of steel EN 1.4922 and offers a large temperature and pressure range of operation, namely T_{max} = 400 °C at maximal pressure of 150 bar. The tank model is shown in the left part of Figure 4.3. It is composed of two bodies for a simple exchange of samples and a leakage free connection of the two body halfs is ensured by a seal. The type of the latter depends on the target temperature: for temperatures of up to 200 °C, a polymer-based FFKM O-ring is used while for higher temperatures a silver-coated, spring-loaded metal-based (Inconel 718) C-ring is used. Heating cartridges are attached to the outer body providing a total heating power of 2000 W. The center area contains the metal hydride material, it is of reduced

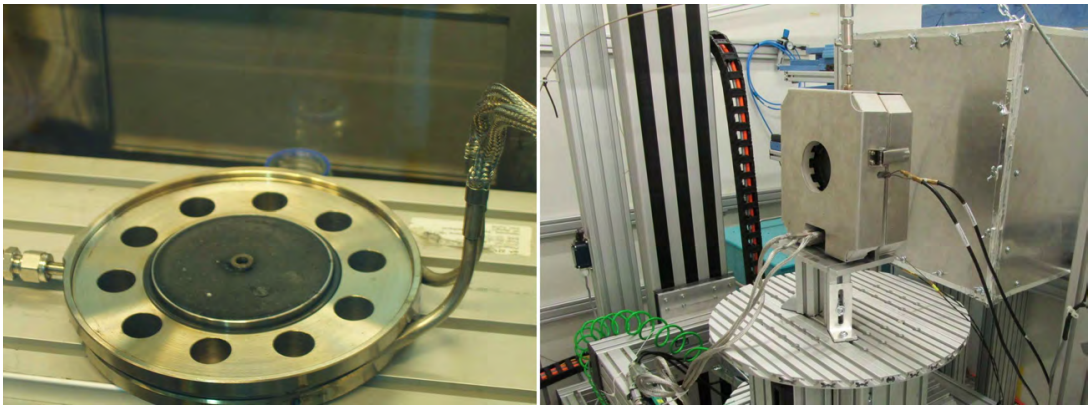

Figure 4.4: Left: Bottom body part of FlexiStore, filled with a sodium alanate pellet. Right: Complete FlexiStore setup with attached thermal insulation, hydrogen supply and thermocouples before an in situ Neuron Radiography measurment at NECTAR. The tank is mounted on the rotational unit in front of the scintillator.

wall thickness of in total 24 mm for sufficient neutron beam transmission. The volume of this area is about 60 ml and exhibits a cylindrical symmetry with 80 mm diameter and 11 mm depth. A technical drawing of the side cross section of the bottom body part is shown in the right part of Figure 4.3. The vertical inlet reaching from the top to the center is the hydrogen supply line. The inlets from the bottom to the lower inner volume boundary respectively to the center are inlets for thermocouples. In the center the wall-thickness is reduced for attachement of a sinter metal filter to prevent a blocking of valves by metal hydride powder. For homogenization of the temperature field a thermal insulation can be attached, with an opening in the center tank area. The bottom body part containing a metal hydride pellet is shown in the left part of Figure 4.4. An additional spacing ring is applied to prevent direct contact of metal hydride powder and the sealing ring. The cylindrical part in the center as visible in the Figure is the as-mentioned sinter metal filter. Due to the tank wall thickness and steel material the use of thermal or cold neutron spectra is limited. The FlexiStore tank is in particular suitable for scaled-up samples and measurements at instruments providing fission neutron spectra like NECTAR. The measurement setup is exemplary shown in the right part of Figure 4.4 with the FlexiStore tank and attached thermal insulation, heating and thermocouples placed in front of the scintillator at NECTAR.

4.2.3 Small sample cell

For measurements of lab-scale samples and use of thermal or cold neutron spectra including both in-situ Neutron Radiography as well as Neutron Tomography a sample cell was designed exhibiting a rotational symmetry with the rotational axis perpen-

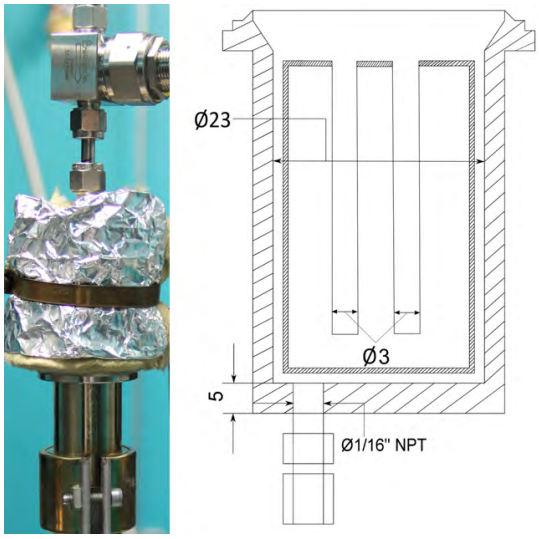

Figure 4.5: Left: Photograph of the small sample cell at the ANTARES beamline with attached thermal insulation (top, covered in aluminum foil) and nozzle heater (bottom). Right: Schematic drawing of the sample cell, quantities are scaled in mm. The outer body is of stainless steel 1.4401, the sample is carried by an aluminum insert body (finely shaded). From the bottom part a thermocouple is attached for measurement of temperature and control of the heating power.

dicular to the beam direction. This allows for homogeneous wall thickness during a Neutron Tomography measurement and hence a constant influence by the sample cell material. For the latter stainless steel of quality 1.4401 was chosen so that the whole sample cell could be designed out of *Swagelok* [30] standard parts except for a few components. The sealing is ensured by standard *Swagelok* VCR Fitting. A photo of the mounted cell is shown in the left part of Figure 4.5. At the bottom part a nozzle heater is attached with a total heating power of 245 W. Above is the sample cell element carrying the inner free volume and the metal hydride material. At the upper part a thermal insulation is used to homogenize the temperature field. The sample cell is designed for maximal temperatures of 450 °C at a pressure of 75 bar. A schematic drawing is given in the right part of Figure 4.5. In the inner free volume an aluminum body with a diameter of 23 mm is inserted (finely shaded), the metal hydride material is placed within the two boreholes of 3 mm diameter each. Aluminum is used for reasons of its good thermal conductivity and its low total neutron attenuation coefficient. At the bottom of the aluminum insert a thermocouple is attached for monitoring of temperature changes during the reaction as well as control of the heating power.

4.2.4 Metal hydride material

The raw components of the metal hydride material used within this work have been purchased by Sigma Aldrich and Alfa Aesar. Unless otherwise described, raw materials have been pretreated by ball milling, where an attritor mill [116] with milling time of 10 h and a planetary ball mill [116] with 5 h milling time and a ball to powder ratio of 10:1 have been used for scaled-up materials measured at NECTAR (sections 5.4, 5.5.1). A high-energy SPEX mill has been used for lab-scale material amounts measured at ANTARES (section 5.5.2) with milling time of 5 h and ball to powder ratio of 10:1. In all cases, steel balls have been used. For powder compaction a manual press with maximal weight of 200 tons was used. To prevent the oxidation of the samples all treatment and processing of materials was performed within a glove box with impurity levels of $\leq$ 10 ppm (O_2, H_2O).

4.3 Infrared-Thermography

In the following the basic setup for Infrared-Thermography measurements is introduced, which has been developed for measurements of the temperature field on the tank surface to approximate the corresponding temperature field within the metal hydride.
For a black body radiator the emitted heat radiation is described by the Stefan Boltzmann law with the radiation power solely depending on the temperature of the radiator. For real bodies, a correction parameter is introduced with the emissivity ϵ that is dependent of the surface material. Thus, the radiation power is

$$P^\star = \epsilon \cdot \sigma_B \cdot A \cdot T^4$$

with the emissivity $\epsilon \in [0,1]$, σ_B the Stefan Boltzmann constant and A the radiator surface. The aim of Infrared-Thermography (IRT) is the determination of an object temperature based upon the measured heat radiation of the objects surface. If the transmission through the object to be measured as well as the interaction with the transmitted medium (usually normal atmosphere) can be neglected, the total radiation power normalized to the surface, P_T, that reaches the IR detector is

$$P_T = \epsilon \cdot \sigma_B \cdot T_O^4 + (1 - \epsilon) \cdot \sigma_B \cdot T_E^4 \tag{4.3}$$

where T_O is the object temperature. The second summand is the reflected radiation with T_E the effective temperature of the environment. A high emissivity reduces a perturbation by the environment and enhances the measurement accuracy. Metals

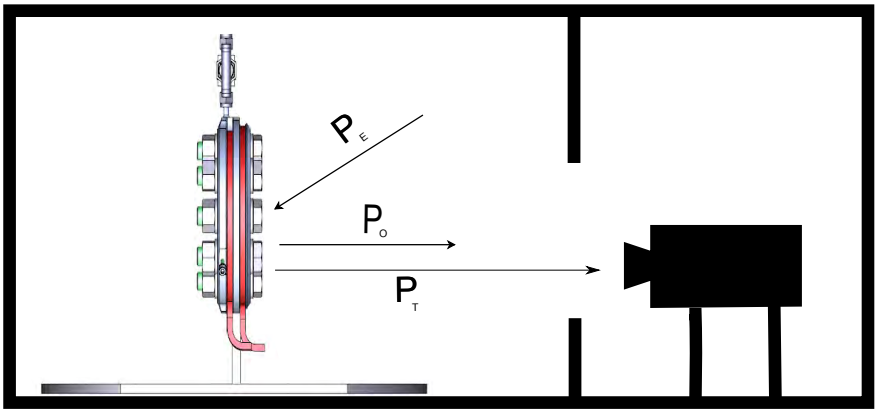

Figure 4.6: Schematic drawing of the IR-Thermography setup. The sample to be measured and the IR camera are covered by a coated box for approximation of a closed system and reduction of potential perturbation by the environment (P_E). The radiation power P_O is generated by the sample. The IR camera measured the total radiation power P_T according to equation 4.3.

typically have a low emissivity but are most commonly used as storage tank hull materials Thus, a direct measurement of the tank surface by IRT is limited and a coating is necessary. For reasons of practical feasibility and large temperature range of operation, black varnish has been used for surface coating, with the layer thickness limited to a few micrometer to limit influences of the varnish on the temperature field. The emissivity of the varnish was determined to $\epsilon = 0.941 \pm 0.004$ by use of a calibration measurement[1]. The setup for IR-Thermography is schematically shown in Figure 4.6 with labels according to equation 4.3. For further reduction of environmental influence an IRT station has been set up, enclosed by a box coated with black varnish for derivation of a closed system approximating a black body behavior. The distance d between the storage tank and the IR-camera depends on the used optics. Within this work, a FLIR A305sc IR-camera is used with a pixel array of 320 x 240 pixels at a maximal frame rate of 9 Hz. The minimum focal distance is 0.4 m, which is the tank-

[1]For determination of the emissivity of the varnish, a thermocouple is attached to the tank surface in direct contact to the varnish. Simultaneously to the temperature measurement, which serves as a reference, the varnish temperature is derived by IR-Thermography, starting with a default emissivity value. The correct emissivity of the varnish refers to an emissivity, for which the two measured temperature values equal each other.

camera distance used for the measurements here. IRT measurements of the storage tank surface are performed after reaching the steady state temperature of the storage tank with attached thermal insulation to exclude effects of the heating process.

Chapter 5

Results and Discussion

This chapter is subdivided into two parts: In the first two sections new methods for the characterization of metal hydride systems (scaled-up and lab-scale) are developed and described in detail, while section 5.2 concentrates on the general quantification of data and correlation analyses. Section 5.3 focuses in particular on investigation possibilities for solid-liquid system compositions. It is pointed out, that methods developed here are not limited to a special class of hydrides but are valid for a broad field of storage systems in general. In the framework of method development, a comprehensive software package has been designed an built in MATLAB for a semi-automatic run of routines and analyses. Within the last sections this software package is used for the application of developed methods on two different, complex metal hydride systems in order to show the tremendous potential of Neutron Imaging on characterization and optimization of metal hydride systems.

5.1 Temperature field by IR-Thermography

The temperature field in Sievert's machines or other lab-scale instruments is assumed to be approximately isothermal and hence measured by a single thermocouple close to the sample. However, in scaled-up metal hydride beds and corresponding storage tanks the temperature field is much more complex, and thus also its determination. Most commonly, an array of temperature sensors distributed over the metal hydride bed or the tank wall is used for determination of discrete temperatures values (e.g. [65, 80]). The latter are then used to derive a rough estimation of the temperature field. However, this bears uncertainties due to possible changes of material structure (e.g. by channel formation [94]) and is accompanied by a high experimental effort since a large sensor array is necessary for a sufficient data point density. Furthermore, a direct contact of temperature sensors and metal hydride bed limits the possible bed

design and gives constraints to the tank geometry.
The measurement of the tank surface temperature by IRT has the advantage of a quasi-continuous field and a simple measurement setup. The measurement itself is indirect and contactless. In the following, the difference of the tank surface temperature field derived by IRT and the corresponding field by an internal thermocouple array is investigated.

5.1.1 Experimental setup and measurement process

As a tank model system the FlexiStore tank is used, the coating of surface and the general IRT setup is described in section 4.3. An IRT image of the storage tank is exemplarily given in Figure 5.1. In the left part an overview of the total storage tank

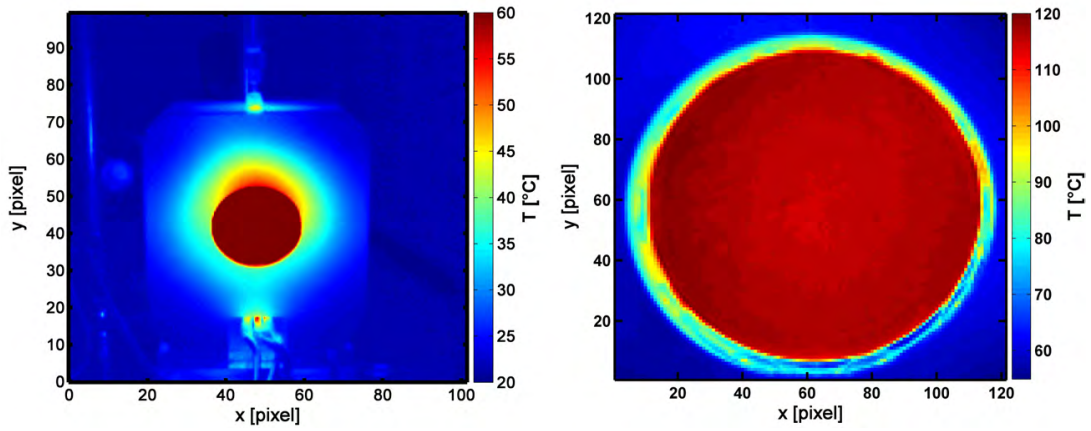

Figure 5.1: Left: IR-Thermography image of the whole FlexiStore tank. The dark red pellet area in the center has temperatures T > 60 °C which exceeds the contrast interval for the overview image. Right: Temperature field of the pellet in thermal equilibrium as the region of interest.

including the thermal insulation is shown. The dark red pellet area in the center exhibits temperatures $T > 60$ °C, which exceeds the contrast interval for the overview image. The right part of the Figure shows the temperature field of the pellet in thermal equilibrium as the region of interest. In the following, the analysis is limited to this region of interest. The temperature inside the tank vessel was determined by using an array of in total 16 thermocouples. For practical feasibility, a steel body was used as a test phantom instead of a metal hydride pellet and the internal array of thermocouples was subdivided into 8 points equally distributed on each of two circles for inner and outer diameter as schematically shown in Figure B.1 in appendix B.1. The ex situ temperature after reaching the thermal equilibrium was measured and interpolated to a quasi-continuous field for target temperatures of 125 °C, 165 °C, 350 °C and 400 °C

corresponding to ab- and desorption temperatures of sodium alanate respectively Li-RHC, the metal hydride systems of interest for this work. The exact procedure is described in appendix B.1. Additionally, a temperature field of the tank surface was acquired by IRT for each of the target temperatures.

5.1.2 Results and discussion

The difference of steady-state temperature fields derived by IRT and the internal sensor array is shown in Figure 5.2 for the different target temperatures. As visible, the

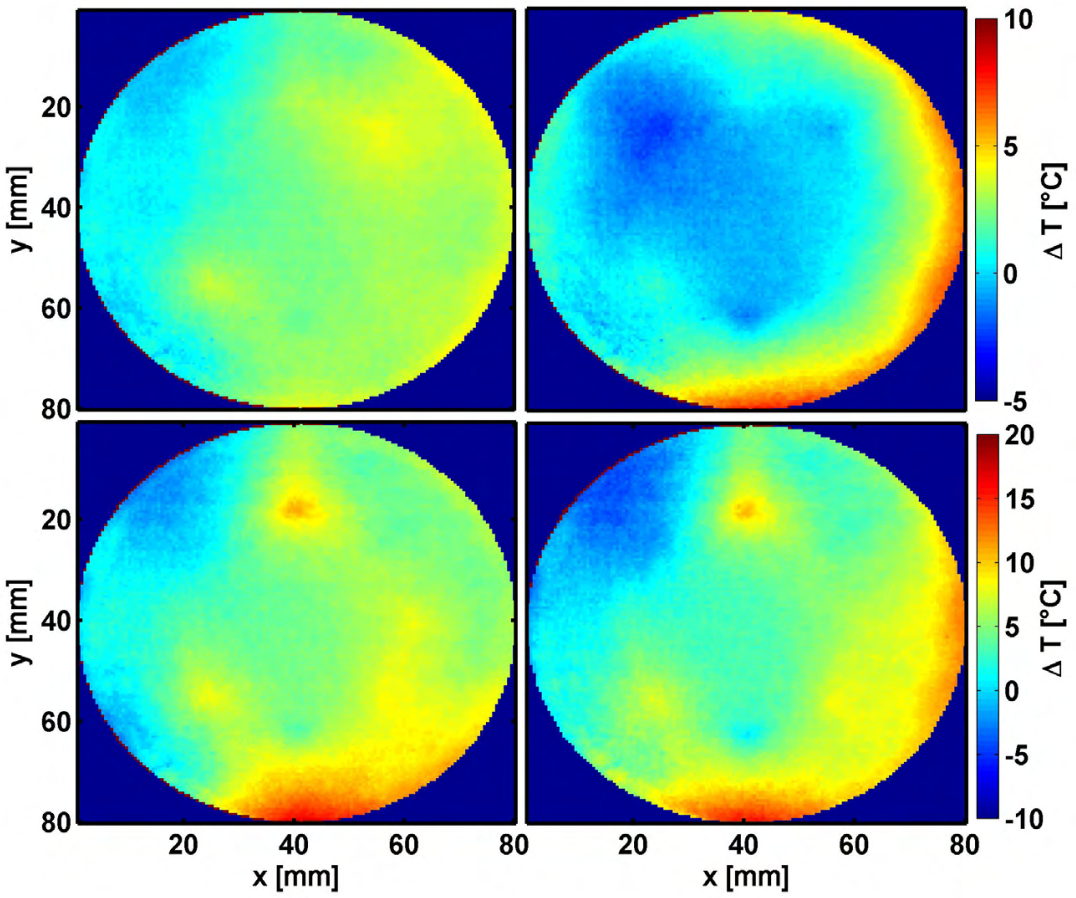

Figure 5.2: Steady-state temperature differences of tank surface temperatures determined by IR-Thermography and interpolated internal tank temperatures derived by a thermocouple array. The absolute equilibrium temperatures are 125 °C (upper left), 165 °C (upper right), 350 °C (lower left) and 400 °C (lower right).

difference between the IRT image on the tank surface and the internal temperature field is non-significant. Absolute differences are correlated to the absolute target temperature. Still, even for the highest temperature of 400 °C, temperature differences

are maximum 15 °C. The discrete spot visible at (x,y)-position of about (40,20) mm in the lower images is probably due to an incorrect measurement procedure for this data-pair and related to the explicit procedure (see appendix B.1). Thus, it is not further considered. In general, the temperature distribution is rather homogeneous with less than 30 K difference over the whole tank for a target temperature of 400 °C. However, some distinct cooler and hotter areas as compared to the average can be recognized. At the left and in particular upper left tank area, ΔT is found to be negative. When moving to the lower right boundary, the difference is inverted and temperatures measured at the tank surface by IRT are even higher than corresponding internal temperatures. This effect must be caused by the explicit distribution of heating power of the FlexiStore tank. The heating cartridges are attached at the outer perimeter of the tank vessel, not fully covering the latter. Thus, a heat flow is possible, directed from the highest heating power input to the temperature sink, causing an internal negative temperature gradient from the temperature source (the upper left area) to the sink (the lower right area). On the tank surface, the heat input is different due to the location of the heating cartridge. Additionally, there is potential influence of the coating itself due to its thermal conductivity, which needs to be investigated further. Still, the temperature differences are small and the temperature field inside the storage tank is in good agreement with the corresponding field on the tank surface derived by IRT. Thus, the temperature of the metal hydride bed in thermal equilibrium can be approximated by IRT, which gives for the first time access to a quasi-continuous temperature field. Though a sufficient contact of metal hydride bed and tank wall is required and the tank geometry should exhibit a plane and thin surface like in the FlexiStore design, the introduced method is believed to be equivalent or at least complementary[1] to classical measurements by single thermocouples due to the simple and contactless measurement and the access to a quasi-continuous field. Moreover, due to the indirect measurement principle there are no constraints to the metal hydride bed geometry. In addition to the encouraging results for equilibrium temperature fields, IRT offers a high potential for in situ temperature field characterization as well, which is discussed in more detail in the perspectives and outlook in section 7.1.1.

[1] The advantage or disadvantage depends on the explicit tank design. In vessel geometries like the FlexiStore where a large plane tank surface with good contact of tank and metal hydride material an accordingly good heat transfer is provided, IRT is superior.

5.2 Development of evaluation methods for Neutron Imaging data

In the following new methods for the quantitative analysis of hydrogen distributions in solid-phase metal hydrides are developed, based on a combination of thermodynamic quantities and nuclear physics theory and the concept of macroscopic attenuation. In preparation for that the scattering field is investigated and a simple way to consider its influence on the measured intensity distribution is shown. Some of the methods developed in this thesis and their application on the sodium alanate system as shown in section 5.4 have already been published prior to this thesis [17, 16].

5.2.1 Scattering and beam attenuation by hydrogen

As already described in section 2.1.1.2, the consideration of scattering influences is important due to the high incoherent scattering cross section of hydrogen relative to other elements for all relevant neutron energies, reaching from fission to cold neutron spectra.
In general, for an in situ investigation of a hydrogenation of a metal-hydride by ideal NR, the total attenuation coefficient Ω_{tot} of equation 2.3 is 4-dimensional as shown in equation 2.11 in section 2.1.1: the 3 dimensional information is related to the spatial information of the material distribution and the additional dimension is a time-dependency due to the absorption of hydrogen by the metal hydride. Instead of considering the additional energy dependency of the attenuation coefficient related to the energy spectrum of the instrument an averaged attenuation is used for reduction of complexity. For taking a ratio as it is described in equation 5.2 and using large propagation distances between sample and detector, spectral shifts in the projected volume of the metal hydride that are caused by moderation or beam hardening can be neglected in first approximation. This is discussed later on. If the attenuation by the material can be assumed to be constant in time referred to the pixel area, the attenuation coefficient separates into a material and a hydrogen contribution

$$\mu_{tot}(r,t) = \mu_M(r) + \mu_{H_2}(r,t) \tag{5.1}$$

where only the latter carries the time-dependent information. This assumption is crucial to the separation of contributions and the following equation 5.2. Its validity is analyzed later on. It is stressed again, that the total time-constant attenuation is the sum of attenuations by the metal hydride material itself as well as any enclosing tank or sample cell material. Considering the projection of the sample volume element

according to Figure 2.2 in section 2.1.1, the attenuation by hydrogen within the time interval $t - t_0$ is given as the logarithmic ratio of intensities at the corresponding time steps according to equation 2.12

$$\Delta\Omega(t) = \Omega_{H_2}(t) - \Omega_{H_2}(t_0) = -ln\left(\frac{I(t)}{I(t_0)}\right) \tag{5.2}$$

Here, $I(t)$ is the measured intensity at t during the absorption process and $I(t_0)$ is the reference image of the material distribution before the hydrogen uptake. All images are corrected by a dark field measurement.

Contemporaneous to the evolution of $\Delta\Omega$, a time-dependent scattering field is emerging due to the high incoherent scattering cross section of hydrogen in comparison to other elements. The scattering field in total leads to an increased background intensity. In first approximation this background intensity is assumed to be spatially constant on the detector plane for large neutron propagation distances from the sample to the detector. In general, an effect of scattering can be denoted as a perturbation of the ideal Beer's law with almost no spatial dependency for propagation distances above 10 cm, which was shown in particular for fission neutrons in [109]. Thus, the perturbation is assumed to be spatially invariant, but time-dependent due to the increasing amount of hydrogen during the sorption process. It is

$$I(r,t) = I_0 \cdot exp(-\Omega(r,t)) + I_{sc}(t) \tag{5.3}$$

Here, $I_{sc}(t)$ denotes the scattering background for a given initial beam intensity[2]. Accordingly, the time evolution of the scattering contribution can be investigated by taking the difference of $I(t) - I(t_0)$ in areas for a time constant attenuation, assuming a time-constant distribution of the initial beam intensity.

The measurements were performed at the instrument NECTAR, described in section 4.1.1. Two setups have been used: a pellet with mass of 50.1 g of desorbed sodium alanate ($NaH+Al+0.05TiCl_3$) stored inside the FlexiStore tank has been investigated with a CCD readout frequency of 5MHz and a total time between two succeeding images of 252 s. Additionally, about the threefold amount of the same material, 147.5 g, stored in a tank made of aluminum has been studied, tank specifications are given in appendix A.3. For the latter tank study, a less collimated beam was used for reduction of exposure time in combination with a readout frequency of 1MHz. In total,

[2]It is remarked, that this formalism does only hold for a given, specific flat field I_0. For generalization, I_{sc} can be introduced as the flat field modulated by a scattering parameter $b = I_{sc}/I_0$, which will be discussed later on.

the time between two succeeding images is 138 s. In this second setup an additional filter was installed in the beamline setup consisting of 1cm of $B_4C(50\%)$ embedded in epoxy. In order to avoid a strong scattering influence, the distance between the sample and the detector was set to 15 cm for both setups. To correlate the beam attenuation caused by hydrogen absorption with its corresponding amount inside the metal hydride material, the hydrogen flow from an external gas supply to the sample was measured by a mass flow controller as described in the section 4.2.1. Additionally, the temperature and pressure at the sample inside the two storage tanks were recorded. These thermodynamic quantities allow for the calculation of the amount of absorbed hydrogen by the metal hydride material according to equation 4.1 in section 4.2.1. By time-synchronization to the image acquisition, each image can be allocated to the respective amount of absorbed hydrogen. The performed absorption was the first absorption after manufacture of the raw material. As an initial pressure application is known to cause a macroscopic structure deformation for loose powder [94, 128], the metal hydride material in both storage tanks was pre-compacted using a manual press so that the cylindrical symmetry of the metal hydride bed is preserved. During the absorption process, the material structure can be assumed to remain macroscopically stable as well: for compacts of sodium alanate, the volumetric expansion within the first absorption is negligible, since it is below 3% in radial dimension according to studies by Lozano et al. [77]. Moreover, no significant change of the material's diameter was observed by NR during the measurement. The change in axial direction is less important as the beam attenuation is integrated for a projected volume element. Additionally, according to Lozano et al. the expansion in the axial direction is as well less than 3%.

5.2.1.1 Time-dependent scattering component

In Figure 5.3, Neutron Radiography images of the hydride material enclosed by the two tanks are shown. The measured intensity was corrected for the dark image and normalized by the flat field. In the left part of the Figure, the FlexiStore tank is shown storing the pellet of mass 50.1 g. The gaseous amount of hydrogen in the remaining free volume in projection direction of the pellet inside the tank is negligible, it is lower than 3% of the absorbed amount of hydrogen by the material. In the lower part of the figure the second setup is shown with the pellet of mass 147.5 g inside the aluminum tank. The remaining free gas volume inside the tank in projection direction of the pellet is 27% and has to be taken into account, in contrast to the FlexiStore setup. Both pellets are cylindrical with an inner diameter of 11 mm and an outer diameter of 77 mm, the thickness is 11 mm (steel tank setup) and 25.5 mm (aluminum tank

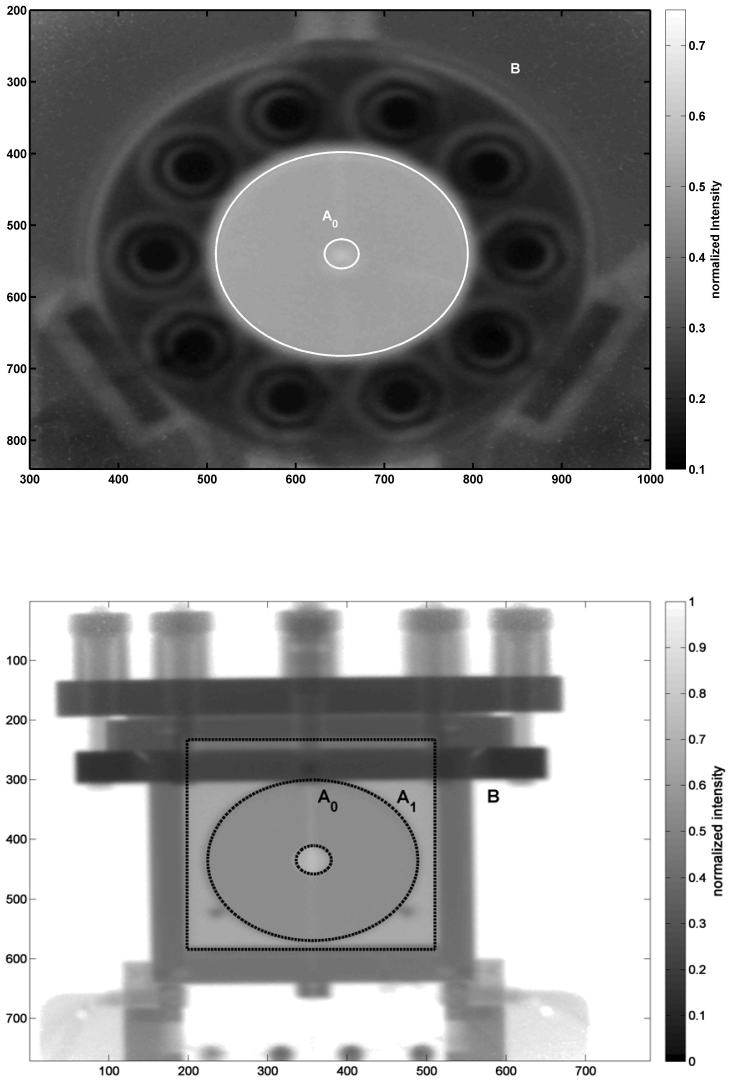

Figure 5.3: Radiography images of the two investigated storage tanks filled with metal hydride material. In the upper part an amount of 50.1 g of desorbed material is stored inside the FlexiStore tank and 147.5 g of material are stored inside the tank made of aluminum. The areas marked with circles are the projected volumes containing the metal hydride material, denoted by A_0. In the remaining area the attenuation is time independent, it is denoted by B. Area A_1 in the lower part corresponds to free gas volume inside the aluminum tank.

setup), respectively.

The projected volume inside an image containing the metal hydride material is enclosed by the white (FlexiStore) respectively black (aluminum tank setup) circles and denoted by A_0. The attenuation in A_0 is time-dependent due to the absorption of hydrogen by the metal hydride. In case of the aluminum tank there is additional free hydrogen gas volume inside the tank. Hence the attenuation in this area, which is denoted by A_1, is time dependent as well. The amount of gaseous hydrogen is correlated to the pressure inside the tank vessel. Outside these areas, denoted by B for both setups, the attenuation is caused only by the tank material and therefore constant in time. For every image the intensities within sections taken out of area B are averaged and the difference to a reference image at t_0 is calculated. As the attenuation by the tank material is assumed to be constant in time, any change within the difference $I(t) - I(t_0)$ in area B is directly assigned to a change of the scattering contribution. This is the time-dependent part of the total scattering intensity as introduced in equation 5.3. The difference is taken in order to be sensitive to small changes in the measured intensity. The correlation of the time-dependent scattering intensity to the amount of hydrogen in the projected volume containing the pellet is shown in Figure 5.4. The amount of hydrogen is normalized to the pellet area to derive an average amount of hydrogen inside the projected pellet volume, denoted by the subscript V. The evolution of the scattering intensity for the steel tank setup is shown in the left part of the image. Up to an amount of about $\mathrm{n(H_2)}_V = 0.006$ mol/cm^2 the time-dependent scattering intensity increases linearly with the hydrogen content. This is exactly what is expected for a time-dependent scattering originating from hydrogen uptake. With further uptake of hydrogen there is no linear dependency any more, the curve converges into a plateau. Interestingly, the transition at $\mathrm{n(H_2)}_V = 0.006$ mol/cm^2 is distinct and equals the beginning of the second absorption step according to the two reactions steps of sodium alanate according to equation 2.22 in section 2.2.1, as it is visible in the inset of Figure 5.4. The inset is a kinetic plot, showing the absorbed amount of hydrogen inside the projected pellet volume, $n(H_2)_V$, as a function of time and normalized by the pellet area. The time evolution is generic for systems undergoing two reaction steps as it is the case for sodium alanate: the final phase, tetra-alanate, is separated from the first phase, hexa-alanate, by the slow increase of $n(H_2)_V$ from t$\approx$ 100 min to t$\approx$ 270 min. After that, the increase of the slope indicates the beginning of the 2nd reaction step and the formation of the tetra-alanate phase. This coincides with the transition observed for the scattering intensity evolution. It is not clear, whether this transition is caused by any structure-related transformation correlated with the reaction steps or whether it

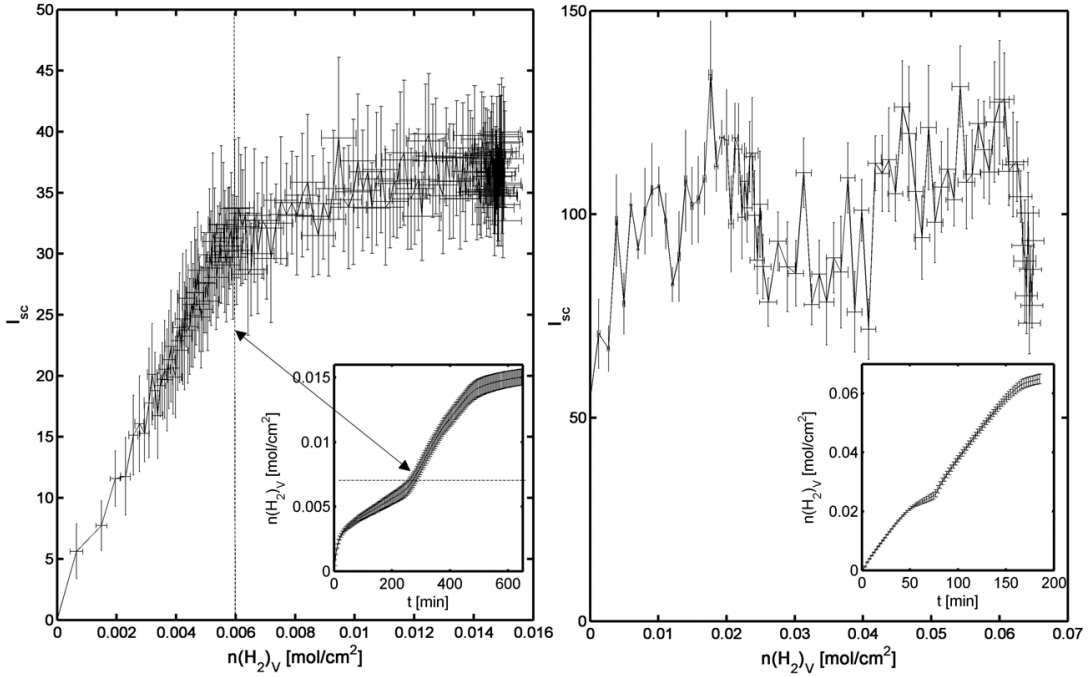

Figure 5.4: Evolution of the time-dependent scattering intensity in area B with the amount of hydrogen inside a projected volume element for the steel tank setup (left) and the aluminum tank setup (right). The insets show the time evolution of the amount of hydrogen in the projected pellet volume, normalized by pellet area.

is at random and caused by multiple scattering. The formation of the tetra-alanate phase includes the formation of a new lattice structure. A change of the scattering intensity measured in area B that is caused by this structural change should then be only due to the thermal part of the energy spectrum of NECTAR [25], which allows for the appropriate angular distribution of scattered neutrons to be detected in B. However, according to the measurement principle of the ZnS scintillator embedded in propylene there should be no sensitivity towards energies below typical electronic binding energies (several eV) for the hydrogen atoms, as recoiled protons are necessary for a luminescence of the ZnS [132]. Consequently, the scattering intensity evolution measured in area B should not contain any information related to structural changes. However, for multiple scattering the transition should be more continuous and smooth than the one measured in Figure 5.4 as the angular distribution for scattering by an ensemble of particles is given by a probability distribution. In case of multiple scattering also the existing amount of hydrogen in the sodium hydride as part of the reference image at t_0 has to be considered[3]. The emergence of multiple scattering would then

[3]In the desorbed state, there is presence of hydrogen within NaH.

be related to a total amount of 0.016 mol/cm^2.
The different setup in case of the aluminum tank with about the threefold pellet mass is used to clarify whether the change of slope is related to structural changes or caused by the emergence of multiple scattering due to the increasing amount of hydrogen in the projected volume element. In analogy to the procedure described above for the lower mass pellet, the evolution of scattering intensity correlated to the amount of hydrogen inside the projected pellet volume is shown in the right part of Figure 5.4. In contrast to the FlexiStore setup with 50.1 g of material, the scattering intensity shows no linear correlation to the hydrogen content in the projected volume at all. There is a distinct increase of the intensity observed already for the first images at the beginning of the absorption process followed by an oscillatory behavior around an average intensity of approximately 100 counts. In the lower right inset the time evolution of the hydrogen content in the projected pellet volume is shown. The structural change of the metal hydride with emergence of the hexa-alanate phase starts at approximately 0.025 mol/cm^2. There is no correlation to the evolution of the measured scattering intensity. This clearly indicates that an emergence of multiple scattering is the reason for the transition observed in the steel tank setup with less amount of material! Considering again the initial amount of hydrogen in the pellet with 145.5 g of material, already within the reference image there is 0.028 mol/cm^2 of hydrogen inside the projected volume. Accordingly and if the different tank geometries are neglected, the multiple scattering regime is already present at $t = t_0$ for the aluminum tank setup. The initial increase of the scattering intensity is most probable due to the amount of gaseous hydrogen in the free volume inside the tank according to area A_1 of Figure 5.3. The absolute number of counts measured is influenced by the different tank geometries, the different initial beam intensities and collimator setups and therefore rather complex. However, in this case only the evolution of the intensity correlated to the amount of hydrogen in the projected pellet volume was needed to clarify the influence of multiple scattering on the measured scattering intensity field. The fluctuations in intensity are due to fluctuations of the initial beam intensity. The oscillating signal visible in the right part of Figure 5.4 is most probable originating from an oscillating initial beam intensity as well, which is not yet understood but might be due to end of lifetime of the converter plate for generation of the fission neutron spectrum. As part of the interaction process of fission neutrons and hydrogen, which is predominantly elastic scattering, the scattering intensity measured within area B is determined by moderated neutrons. Depending on the number of scattering events, moderation can result in a decrease over several magnitudes in energy [97]. However, the distribution of the time-dependent scattering field is broad and shows no radial dependency as it

is expected due to the large sample-detector distance. Therefore it is valid to assume that the energy spectrum of neutrons detected in area B is almost the same as in area A_0, especially with emergence of multiple scattering as this is accompanied by a broadening of the angular distribution of scattered neutrons towards 4π. Thus, the measured intensities can be used to correct all Radiography images for the effect of time-dependent scattering by subtracting the scattering intensity given in Figure 5.4 from the corresponding image.

5.2.1.2 Correlation of hydrogen content and beam attenuation

While area B of Figure 5.3 was used to determine the scattering field intensity and to correct for time-dependent scattering, area A_0 is used for the investigation of the correlation between the attenuation by hydrogen and the corresponding amount of absorbed hydrogen inside the projected pellet volume. To calculate an average atten-

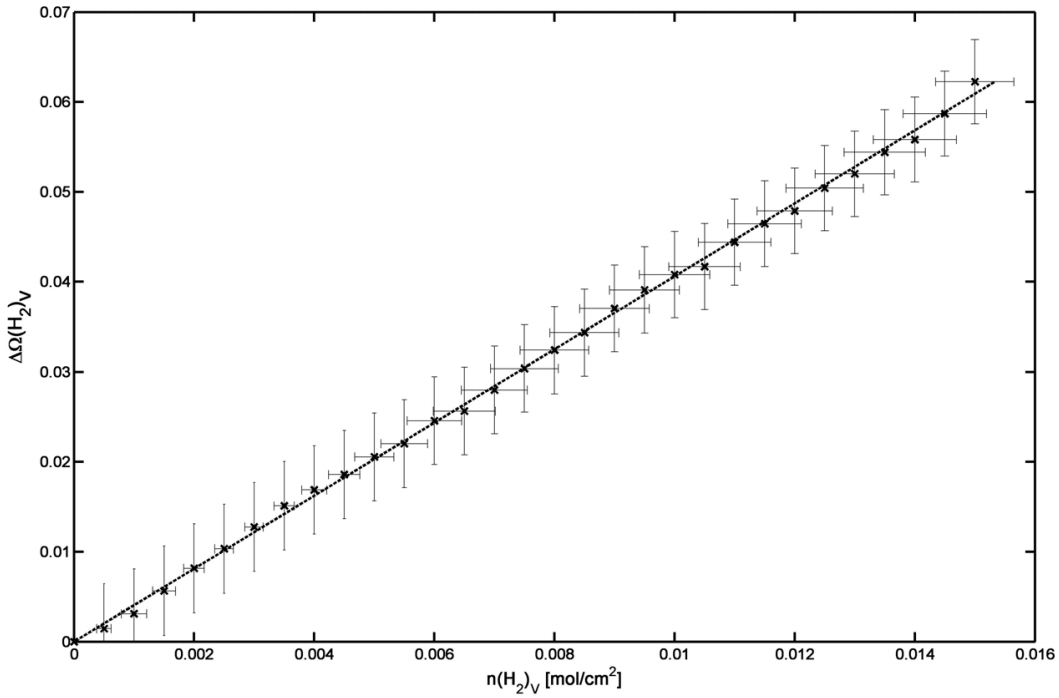

Figure 5.5: Correlation of the attenuation by hydrogen, $\Delta\Omega$, and the amount of absorbed hydrogen inside a projected volume element for the pellet, $n(H_2)_V$, for the steel tank setup. Additionally, the linear fit is plotted.

uation, the $\Delta\Omega_i$ of each pixel i inside A_0 are calculated according to equation 5.2 and averaged. By that, $\Delta\Omega$ is independent of local fluctuations of the amount of stored hydrogen. Its correlation to the amount of absorbed hydrogen in a projected volume element of the metal hydride, $n(H_2)_V$, is shown in Figure 5.5. The dependency is

linear, $\Delta\Omega = c \cdot n(H_2)$, with a proportionality factor of c = 4.0 ± 0.15 cm^2 mol^{-1}. This linearity is in agreement with the energy spectrum of neutrons at NECTAR [25], according to which the flux has its maximum in the MeV regime. At these energies there should be no sensitivity towards material structures but towards nuclear potentials, which are the single hydrogen nuclei in this case. The same correlation is shown for the aluminum tank setup in Figure 5.6. The attenuation derived according

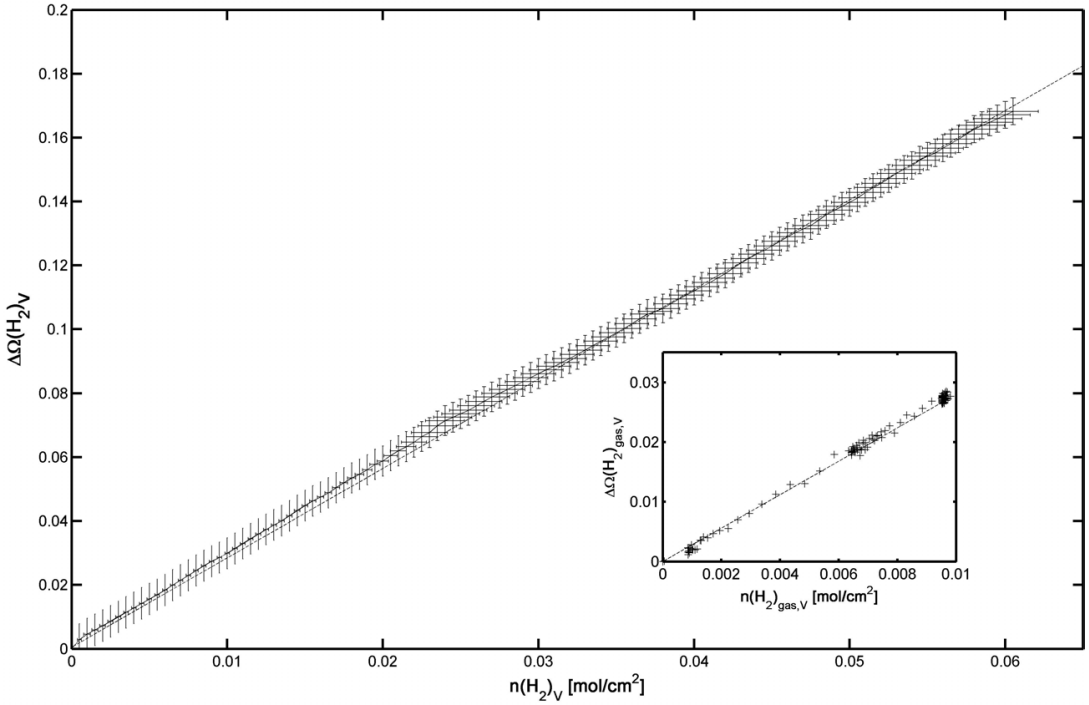

Figure 5.6: Correlation of the attenuation by hydrogen, $\Delta\Omega$, and the amount of absorbed hydrogen inside a projected volume element for the pellet, $n(H_2)_V$, for the aluminum tank setup. Additionally, the linear fit is plotted. The inset shows the analogue correlation for the gaseous amount of hydrogen.

to equation 5.2 contains both the attenuation by the absorbed hydrogen as well as the attenuation by gaseous hydrogen in the free volume of the total projection of the pellet volume. Since area A_1 represents the free volume inside the aluminum tank, it is used to investigate the correlation of the amount of gaseous hydrogen inside a projected free volume element and the corresponding neutron beam attenuation. This is shown in the inset of Figure 5.6, a linear correlation is observed with a proportionality factor of c = 2.8 ± 0.2 cm^2 mol^{-1}. Thus, the influence of the attenuation by gaseous hydrogen can be corrected with known tank geometry to derive only the attenuation by the absorbed amount of hydrogen in a projected volume element. This is shown as the main plot in Figure 5.6. The correlation is again linear with the same proportionality

factor of c = 2.80 ± 0.03 cm^2 mol^{-1} as it was the case for the attenuation by gaseous hydrogen. For both investigated setups, which differ significantly in terms of the total amount of stored hydrogen as well as in terms of geometry and tank materials, a linear correlation of absorbed hydrogen in a projected volume element and the beam attenuation by interaction with hydrogen was found. This shows that even for larger amounts of samples the ideal Beer's law can be assumed correctly which is important for a quantitative determination of the hydrogen distribution. However, the slope between the steel tank setup and the aluminum setup was found to differ significantly. A reason might be the different initial energy spectrum due to the additional 1 cm filter of $B_4C(50\%)$ embedded in epoxy. Spectral simulations analogously to the ones performed by Breitkreutz et al. [21] for the changed setup revealed a hardening of the spectrum with an average energy of $\bar{E} = 2.1\ MeV$ instead of $\bar{E} = 1.8\ MeV$ as for the steel setup. This directly lowers the interaction probability of hydrogen nuclei and incoming neutrons due to the energy dependency of the cross section for hydrogen [29]. Accordingly, a logarithmic ratio of two images according to equation 5.2 leads to a changed slope for the linear correlation. This shows that the explicit beamline setup, which determines the spectrum, has a strong impact on the explicit correlation. The interaction between fission neutrons and the hydrogen nuclei is predominantly elastic scattering which leads to a moderation of neutrons that are scattered at hydrogen nuclei, in particular inside volume containing the metal hydride material. During the absorption process these moderated neutrons are measured as time-dependent scattering intensity as investigated in the beginning, leading to an increased background intensity. Due to the lower interaction probability of MeV-neutrons with the hydrogen nuclei the energy spectrum of neutrons measured in the detector area corresponding to the projected pellet volume is expected to be shifted to higher energies. This spectral shift to higher energies is known as 'beam hardening' [22] and would perturb a linear correlation of attenuation by hydrogen and normalized amount of hydrogen content. However, since a linear correlation was found for both setups effects of beam hardening can be neglected for an amount of hydrogen inside a projected volume element up to at least 0.09 mol cm^{-2}. This value originates from the initial amount of hydrogen inside a projected volume for the reference image of the 145.5 g-pellet, 0.028 mol cm^{-2}, added to the corresponding final amount of absorbed hydrogen of 0.062 mol cm^{-2} according to Figure 5.6. Thus, though the image formation process is quite complex including the processes and perturbations mentioned above, the linear correlation and, by implication, simple Beer's law is robust for large propagation distances.

5.2.1.3 Time constant scattering influence

In addition to the time-dependent scattering influence caused by an increasing amount of hydrogen inside the storage tank during the absorption process there is an additional time-independent scattering intensity contribution by the metal hydride material itself and the storage tank components that contributes to the total scattering field given by equation 5.3. This scattering contribution could as well affect and distort the measured intensity distribution and therewith investigated quantities. To clarify, whether the linear correlation that was found in Figure 5.5 is influenced by a time-constant scattering field, again a spatially constant scattering intensity I_{sc} on the detector plane is assumed due to the large propagation distance as it was done for equation 5.3, but this time it is set as time-constant. Using this, the attenuation difference for time steps t_0 and t according to equation 5.2 becomes

$$\Delta\Omega^{\star}(t) = -ln\left(\frac{\exp^{-\Omega(t)} + \frac{I_{SC}}{I_0}}{\exp^{\Omega(-t_0)} + \frac{I_{SC}}{I_0}}\right)$$

In the following, $b = I_{SC}/I_0$ is introduced as a scattering parameter defined by the ratio of scattering and flat field intensity. Therewith

$$\Delta\Omega^{\star}(t) = \Delta\Omega(t) - \left[ln\left(1 + b \cdot \exp^{\Omega(t)}\right) - ln\left(1 + b \cdot \exp^{\Omega(t_0)}\right)\right] \tag{5.4}$$

The quantity $\Delta\Omega(t)$ is the ideal attenuation difference without any influence of scattering. The parenthetical term on the right is a perturbation of this ideal attenuation due to scattering contributions. If the latter are considered to be small, the perturbation can be expressed as a Taylor series and simplifies to

$$\Delta\Omega^{\star}(t) = \Delta\Omega(t) \cdot \left(1 - b \cdot \exp^{\Omega(t_0)}\right) \tag{5.5}$$

This is based on the assumption that $b \cdot \exp^{\Omega(t)} \ll 1$ and $\Delta\Omega \ll 1$. In ideal NR, attenuation difference and amount of hydrogen are directly proportional, given by definition of the macroscopic attenuation (see equation 2.5). It is

$$\Delta\Omega(t) = \Omega(t) - \Omega(t_0) = -ln\left(\frac{I(t) - I_D}{I_{t_0} - I_D}\right) = c \cdot \Delta n(H_2)(t) \tag{5.6}$$

with the dark field intensity I_D and $\Delta n(H_2)(t) = n(H_2)(t) - n(H_2(t_0))$ and the proportionality constant c according to equation 2.5. More precisely, it carries among

others the microscopic cross section of hydrogen:

$$c = \frac{2 \cdot N_A \cdot \sigma_H}{A} \tag{5.7}$$

The factor of 2 is due to a calculation with molecular hydrogen. From equation 5.5 the following relation is derived for the attenuation difference by hydrogen under the influence of small, time-invariant scattering fields:

$$\Delta\Omega^\star(t) = c^\star \cdot \Delta n(H_2)(t), \qquad c^\star = c \cdot \left(1 - b \cdot \exp^{\Omega(t_0)}\right) \tag{5.8}$$

Thus, it can be concluded that for small scattering contributions fulfilling the above given conditions a linear correlation of beam attenuation difference and the total amount of hydrogen[4] is preserved. The proportionality constant, $c^\star$, is reduced to the ideal case. Thus, within a correlation plot like it is shown in Figures 5.5 and 5.6 the same overall evolution is derived but with a reduced slope. For high scattering fields a linear correlation does not hold due to a decreasing slope for higher amounts of hydrogen according to equation 5.4. However, it is essential that a linear correlation of the attenuation by hydrogen and the amount of absorbed hydrogen is invariant to small scattering influences in the way that only the explicit slope is changed, but not the entire type of a linear correlation. According to Figure 5.6 a first approximation of a lower limit can be derived, for which the amount of hydrogen in the projected volume and corresponding scattering influences do not affect this linear correlation. Starting from an absorbed amount of 0.05 mol cm^{-2}, a distinct linear correlation is found for the remaining data range. Considering an initial amount of hydrogen of 0.028 mol cm^{-2} already present in the initial reference image, a lower limit of about 0.08 mol cm^{-2} of hydrogen is derived. A linear correlation facilitates a quantitative investigation of the hydrogen distribution within the metal hydride bed, which will be described in detail in the next section.

It is emphasized, that given results are based on the fission neutron spectrum at NECTAR. However, the introduced methods for scattering investigation and correlation of beam attenuation and hydrogen amount are valid for all type of neutron energy spectra. Still, for use of thermal and in particular cold neutron spectra there are significant differences due to the energy dependency of overall attenuation coefficients for the corresponding energy range: In particular, the time-dependent scattering field is expected to be more complex due to potential effects of bragg scattering [102]: All chemisorption driven metal hydrides undergo a change of the crystalline structure during hydrogenation, thus the microscopic cross section carries a time dependency

[4] It is remarked again that the latter is the total amount within the projected volume.

related to this structural change. Additionally, the absolute cross sections are significantly higher and therewith the scattering field is enhanced in comparison to the one observed in Figure 5.4.

5.2.2 Combination of Thermodynamics & Nuclear Physics Theory: Normalization method

With the combination of thermodynamic quantities and macroscopic attenuation a simple way was introduced for the study of the correlation between the beam attenuation by hydrogen and the corresponding hydrogen content. This can be realized with low experimental effort, since the thermodynamic quantities pressure, temperature and hydrogen flow are sufficient for the calculation of the evolution of the hydrogen absorption.
So far, for quantification of data and determination of the spatial and time-resolved hydrogen distribution the microscopic cross section σ is used to calculate the mass of hydrogen assigned to the measured intensity of one pixel, according to the formalism for the attenuation coefficient μ as given in equation 2.5. The major problem is that the latter explicitly depends on the individual instrument setup at the beamline including sample detector distance, neutron energy spectrum and sample composition and corresponding scattering field. For the scattering field the effect of both time-dependent and time-invariant scattering effects was shown in the previous sections, where the time-invariant effect changes the proportionality constant in case of a linear correlation. This can be understood as a change of the effective attenuation coefficient, causing deviations from literature-based values! Additionally, there is a potential influence by the crystalline structure of the material for use of thermal and cold neutrons. This is explicitly used in Bragg-edge Imaging and discussed already in the previous section. Hitherto, these effects are neglected and literature values for hydrogen or values derived by calibration measurements with water are used instead.[63, 93] This is clearly not optimal for a precise quantitative investigation. A unique but simple method to overcome this problem is to use a combination of thermodynamic quantities and nuclear physics formalism for the macroscopic attenuation coefficient, which determines the measured intensity in Neutron Imaging. The following is not limited to a fission neutron spectrum as used here, but also valid for thermal and cold neutrons. During the hydrogen absorption experiment the thermodynamic quantities pressure and temperature and additionally the hydrogen flow into the tank volume allow for a ready calculation of the absorbed amount of hydrogen by means of a kind of continuity equation as described by equation 4.1 in section 4.2 . In case of a linear correlation of

beam attenuation by hydrogen and corresponding amount of hydrogen it is

$$\Delta\Omega(t) = c \cdot n(H_2)(t)$$

according to equation 5.6, where the reference amount, $n(H_2)(t_0)$, has been set to zero per definition. In fact, both $\Delta\Omega(t)$ and $n(H_2)(t)$ are not continuous but discrete. Their time-resolution is given by the time interval between subsequent Neutron Radiography images. For every image, the following condition for normalization is defined

$$\acute{C} \cdot \sum_{i=1}^{N} \Delta\Omega_i(t) = n(H_2)(t) \tag{5.9}$$

where N is the number of pixels and $\Delta\Omega_i$ is the attenuation difference in pixel i. This defines the normalization constant, $\acute{C}$, and therewith each image pixel i of an image at time step t can be assigned to the corresponding amount of absorbed hydrogen by

$$n(H_2)_i = \acute{C} \cdot \Delta\Omega_i(t) \tag{5.10}$$

By that, the spatial and time-resolved, quantified distribution of hydrogen within the metal hydride bed is derived. It is stressed, that it solely relies on a linear correlation of attenuation by hydrogen and corresponding hydrogen content in the sample volume, but **not** on the absolute attenuation coefficient and is therewith more precise and robust against varying experimental setups! Still, a basic assumption is the time-constant material amount within the resolution of one pixel area, excluding material transfer. In case of the latter the reader is referred to section 5.3.

5.2.3 Material distribution

While the in situ image data of the hydrogen absorption process is used for the determination of the time and spatial-resolved, quantitative hydrogen distribution as shown in the above section, a reference image at t_0 corresponding to the desorbed state of the material before the start of the absorption process can be used to calculate the distribution of material amount and material packing density. In full analogy to the normalization condition for the hydrogen distribution according to equation 5.9, the corresponding condition for the material distribution is

$$\acute{C} \cdot \sum_{i=1}^{N} \Omega_{i,mat} = m_{tot} \tag{5.11}$$

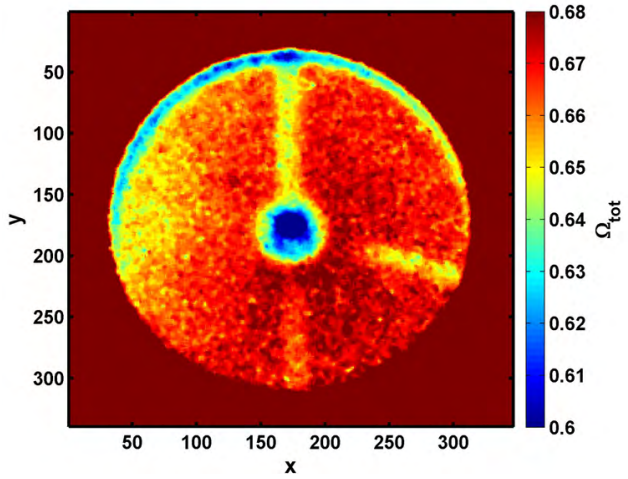

Figure 5.7: Distribution of total attenuation for the FlexiStore setup with the metal hydride pellet for visualization of geometry effects of the storage tank/ sample cell.

where m_{tot} is the total metal hydride mass and $\Omega_{i,mat}$ is the attenuation caused solely by the metal hydride material within pixel i of the reference image. As for the derivation of the hydrogen content distribution, a linear correlation of material amount and corresponding attenuation by material, Ω_{mat}, is a necessary condition for a valid normalization, its validity has to be ensured a priori. In addition, in case of multi-component metal hydride systems a homogeneous spatial distribution of material components has to be assumed, which can be achieved by ball-milling as part of the sample preparation process. The attenuation distribution of a reference image is exemplary shown in Figure 5.7 for the FlexiStore setup and a metal hydride pellet. The color-coding indicated by the colorbar is chosen in the way that only the region of interest, the metal hydride pellet, is visible. The outer area, colored in dark red, corresponds to the attenuation by the FlexiStore tank only and refers to area B according to the upper part of Figure 5.3. The total attenuation shown in Figure 5.7 is a superposition of attenuations by tank, Ω_{Tank}, and metal hydride material, Ω_{MH}

$$\Omega_{tot}(x,y) = \Omega_{Tank}(x,y) + \Omega_{MH}(x,y) \tag{5.12}$$

Ω_{MH} is the quantity of interest, necessary for normalization and derivation of material distribution. Ω_{Tank} is homogeneous and exhibits a spatial dependency due to reduced wall thicknesses for temperature sensors and hydrogen inlet as shown in the technical drawing in Figure 4.3 in section 4.2. These effects are visible in Figure 5.7 by reduced attenuation, where the vertical lines correspond to the hydrogen supply line (upper line) and temperature sensor (lower line), respectively. The line at about 109°from

the top (4 o' clock position) corresponds to an additional borehole for temperature monitoring. The area of reduced attenuation in the center is due to a reduced wall thickness for the sinter metal filter. The correction of Ω_{tot} by Ω_{Tank} according to equation 5.11 for derivation of the attenuation by the metal hydride material depends on the explicit tank geometry. In the following two correction procedures are presented for the most common tank geometry effects.

5.2.3.1 Correction of tank geometry influences

The correction procedures are shown exemplary for the FlexiStore tank but are readily transferable to other storage tank designs or sample holders. In general, geometry effects in terms of their profile are either step functions or curvatures, where for the latter only cylindrical symmetries are considered.

Cylinder geometries

In the upper left part of Figure 5.8 a section of Figure 5.7 is shown referring to the varying wall thickness at about 109°. In the upper right part the corresponding profile

$$P_i = 1/N \sum_{j=1}^{N} \Omega_{tot,i,j} \tag{5.13}$$

is given for averaged y-positions (indicated by index j), where the image has been rotated to turn the edge into a vertical position to allow for a readily calculation of profiles. The notation is changed from continuous to discrete i, j to consider the array representation of the image data. According to the technical drawing of FlexiStore (see Figure 4.3) the variation of wall thickness exhibits a cylindrical symmetry with the rotational axis being perpendicular to the projection direction. Thus, in ideal case the profile should be of the form $P_i = 2 \cdot \sqrt{r^2 - (i - i_c)^2}$, with r the radius corresponding to cylindrical symmetry. However, a broadening and clear deviation from the ideal case is observed. The reason is geometrical unsharpness and blurring due to the limited resolution of the instrument as described in section 2.1.1.4. A reference attenuation, Ω_r is defined by the left and right boundary of the profile, corresponding to a volume with constant wall thickness. In the lower left part of Figure 5.8 the difference of profile attenuation and reference is shown with $\Omega_C = P_i - \Omega_r$. The curve is fitted by a Gaussian and the fit curve is used for correction of the total attenuation by wall thickness variation

$$\Omega^{\star}_{tot,i,j} = \Omega_{tot,i,j} + A \cdot \exp^{-\left(\frac{i-i_c}{\sigma}\right)^2};$$

where parameters A, i_c and σ are derived by fitting. The corrected attenuation is

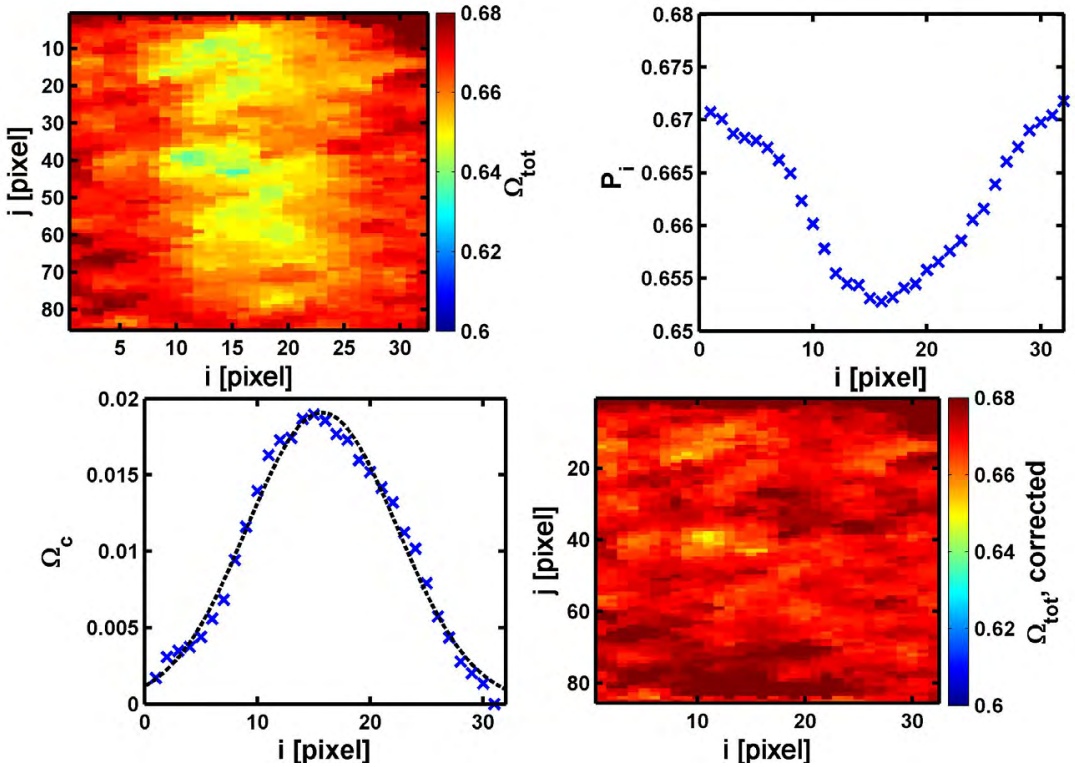

Figure 5.8: Correction principle for cylinder geometries. Upper left: Total attenuation image rotated counterclockwise by 109°for the determination of the effect of wall thickness reduction caused by the borehole for a thermocouple. Upper right: Corresponding averaged profile plot according to equation 5.13. Lower left: Profile of attenuation difference $\Omega_c = P_i - \Omega_r$ and Gaussian fit. Lower Right: Corrected total attenuation image.

shown in the lower right part of Figure 5.8. The distribution of attenuation by the material is well preserved. It is remarked, that in case of a better spatial resolution the broadening is reduced and an approximation of profiles by Gaussian is no longer valid. A combination of Gaussian and theoretical profile has to be used instead with the limit of the theoretical profile for high spatial resolutions. The latter has to be considered for use of thermal and cold neutrons, for fission neutron spectra the approximation by Gaussian is sufficient.

Step geometries

In addition to cylinder geometries and profiles, tank vessels or sample cells often exhibit step functions. Again, the FlexiStore tank is taken as an example in the following. Here, the center wall thickness reduction for the sinter metal filter is a step function, exhibiting a radial symmetry in the projection. The center section of the to-

tal attenuation is shown in the upper left part of Figure 5.9. Due to image broadening effects caused by the spatial resolution of the instrument the distinct edge is transfered into a broadened transition from higher to lower wall thickness. This is shown by profile plots in the upper right part of Figure 5.9. Each profile plot is derived from

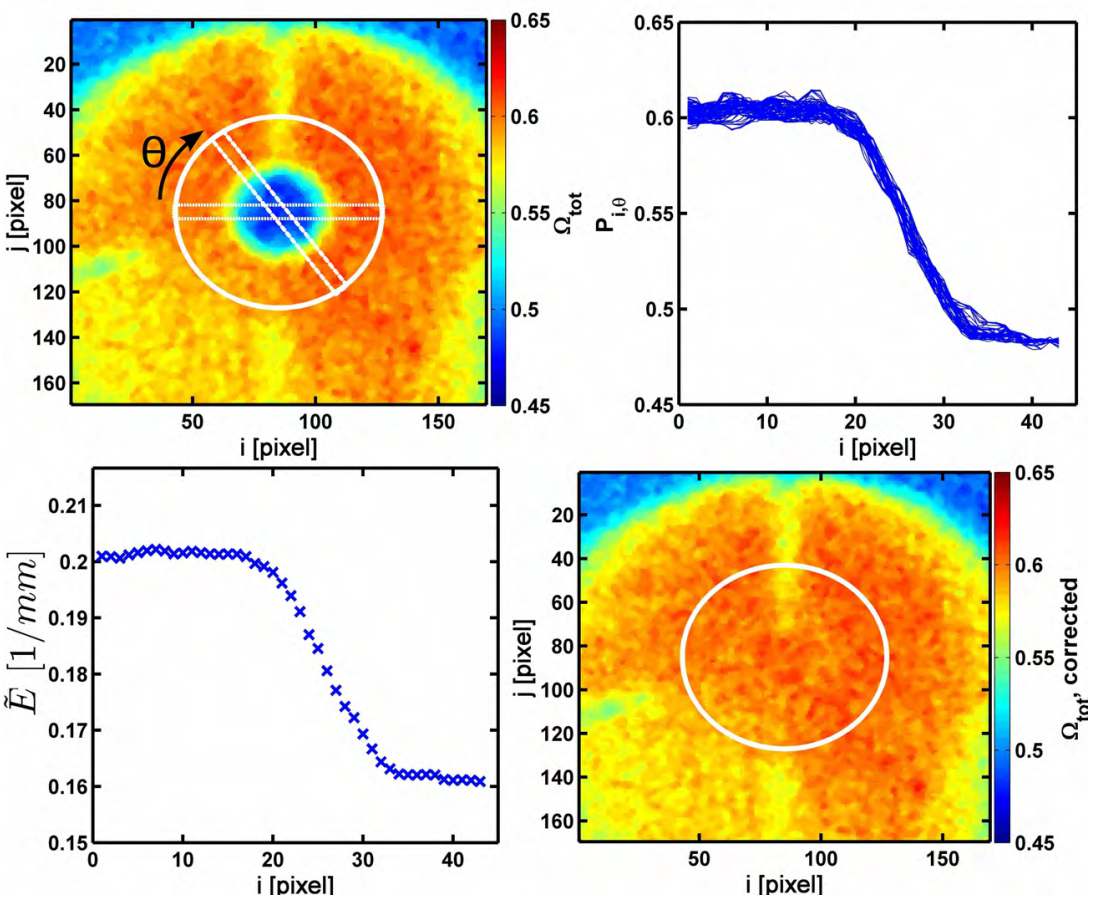

Figure 5.9: Correction principle for step geometries. Upper left: Total attenuation and effect of wall thickness reduction in the center of FlexiStore. Iteratively, profiles are calculated for various rotation angles θ. Upper right: Evolution of calculated profiles for different rotation angles. Lower left: Averaged normalized edge profile according to equation 5.14. Lower right: Corrected total attenuation image.

a rectangle for fixed angle θ as visualized in the upper left part of the Figure. The rectangle height is finite and an averaged profile of the rectangular subsection is calculated according to equation 5.13 from the left boundary to the center. Subsequently, the image is rotated by θ and the procedure is iterated for a full 2π rotation to increase data statistics. The edge broadening is described by the Edge-Spread function as introduced in section 2.1.1.4 and in appendix A.1.1. As visible, all profiles corresponding to different rotation angles exhibit the same curvature, fluctuations are due

to image artifacts. For correction of edge geometries, the edge profiles are averaged and normalized by the geometric step height in wall thickness, h_T,

$$\tilde{E} = \frac{1}{N_p \cdot h_T} \cdot \sum_{l=1}^{N_p} P_{i,\theta_l} \tag{5.14}$$

where the average of N_p rectangular profiles is used for reasons of increased data statistics. The as-derived spread function is shown in the lower left part of Figure 5.9. A normalization by the edge-height generalizes the edge profile and has to be calculated only once for a definite sample-detector distance and energy spectrum[5]. By use of the radial symmetry of the edge step, the normalized profile, $\tilde{E}$, is extrapolated to 2D. As reference attenuation for the constant tank wall thickness the averaged left hand boundary of edge profiles in the upper right part of Figure 5.9 is used in analogy to the procedure performed for cylindrical geometries in the above paragraph. Then, the tank step geometry effect is corrected by

$$\Omega^{\star}_{tot,i,j} = \Omega_{tot,i,j} + \left(h_T \cdot \mathbb{1} - \tilde{E}_{2D}(i,j)\right)$$

The resulting attenuation is shown in the lower right part of Figure 5.9, where the distribution of attenuation by the material is well preserved.

Final correction and normalization for derivation of the material distribution

After correction of as described geometric effects the resulting attenuation by the tank material is constant and homogeneous. It is determined from a reference area containing no metal hydride material or from an empty-tank reference measurement. Subsequently, it can be corrected by simple subtraction according to equation 5.12 to derive the distribution of attenuation by the metal hydride material only. This sets the basis for a valid normalization and calculation of the quantitative material amount in pixel i

$$m_i = \acute{C} \cdot \Omega_{i,mat} \tag{5.15}$$

with $\acute{C}$ defined by equation 5.11. The quantity m_i is the amount of material in a projected volume element corresponding to image pixel i. In case that the exact shape or geometry of the metal hydride bed is known, the packing density can be calculated readily with given pixel size, p_s. For a pellet with its base area perpendicular to the projection direction as it is the case for the standard setup of FlexiStore, the material

[5]This is under the assumption, that effects of multiple scattering and beam hardening, causing a different edge spread, can be neglected.

packing density is simply

$$\rho_i = \frac{m_i}{p_s^2 \cdot d} \tag{5.16}$$

where d is the thickness of the pellet. The spatial distribution of material packing densities allows for analysis of potential inhomogeneties and enables an optimization of compaction process routes.

5.2.4 In-situ hydrogen distribution

In the previous sections methods have been introduced to calculate the time and spatial-resolved, quantitative hydrogen distribution as well as the spatial distribution of material amount or packing density. For determination of the weight-normalized hydrogen content distribution, the two quantities are combined and the normalized, absorbed hydrogen content in pixel i at time t is given by

$$\tilde{n}(H_2)(t)_i = \frac{2 * n(H_2)(t)_i}{m_i} \tag{5.17}$$

with $n(H_2)(i)(t)$ and m_i according to equations 5.10 and 5.16. In the following, the necessary steps to derive the normalized hydrogen content distribution are summarized:

1. The absorption process of a metal hydride material is measured in-situ by Neutron Radiography. In addition to the image data acquisition, the thermodynamic quantities pressure, temperature of the metal hydride bed and hydrogen absorption flow are recorded to allow for a calculation of the time-resolved amount of absorbed hydrogen.

2. The image data is corrected for the dark image and normalized to the flat field.

3. The scattering field is investigated, a correction of time-dependent scattering and and analysis of the correlation of the attenuation by hydrogen and the corresponding hydrogen content in the projected volume is performed.

4. In case of linear correlation a normalization of the attenuation by hydrogen to the corresponding total absorbed hydrogen amount is performed.

5. Tank geometry effects are corected using a reference image, referring to a material distribution in the desorbed state before the absorption process.

6. In case of linear correlation of attenuation by material and corresponding material amount, a normalization to the total metal hydride mass is carried out.

7. The combination of hydrogen and material distribution results in the time and spatial-resolved, quantitative distribution of the hydrogen content.

It is remarked, that the procedure shown here for an absorption holds in full analogy also for a desorption process. Furthermore, the methods of normalization are not limited to Neutron Radiography studies, but are as well valid for Neutron Tomography data sets.

5.2.5 Correlation analysis - multiple-field approach

Hitherto introduced analyses possibilities are limited to the above described evolution of the hydrogen content distribution. However, to explore the full potential of in-situ Neutron Radiography, investigations have to be taken beyond the sole image data. That includes, in fact, a combination of the unique spatial distribution of hydrogen and additional macroscopic fields that exhibit the same spatial information. For the case of metal-hydride based hydrogen storage, the relevant quantities for scaled-up samples are the temperature field and the material packing density. While the former is assumed to be isothermal for lab-scale sample sizes in e.g. Sievert's machines, it is more complex for scaled-up samples, significantly affecting reaction kinetics. The material distribution or packing density is known to significantly influence reaction rates [80]. However, the time-resolved interdependence of these different driving forces has not been investigated. So far there exists no possibility to distinguish between influences of single driving forces on the overall reaction or material performance. This is a major drawback for the optimization of scaled-up systems! In the following, a way is presented to overcome this problem by combination of multiple macroscopic fields. Within this work, it was already shown that IR-Thermography allows for determination of quasi-continuous temperature fields of metal hydride beds based on tank surface measurements as introduced in section 4.3. Furthermore, within the framework of method development for quantitative image data analysis according to the above section, a way for determination of the material distribution or material packing density has been introduced. In the following, only the term material packing density is used, without loss of generality. In case of non-uniform metal hydride bed geometries the methods developed in the following are valid as well. The three macrsocopic fields - hydrogen content, material packing density, temperature distribution - are combined to allow for a correlation analysis of the corresponding quantities $n(H_2), \rho$ and T.

5.2.5.1 Multi-Correlation (3D)

After determination of packing density, temperature field and time-resolved hydrogen distribution as shown previously, the three macroscopic fields are given as exemplary

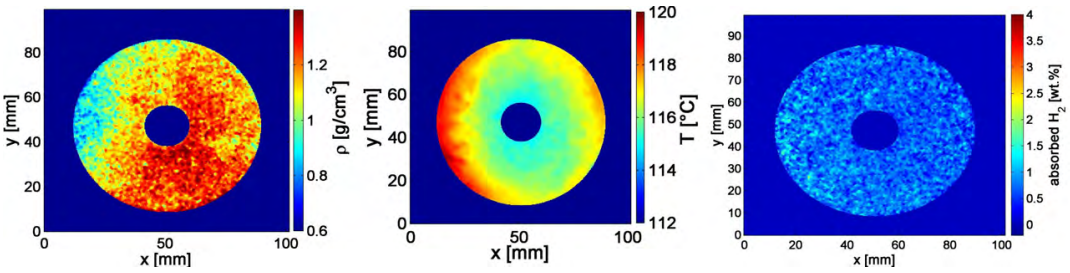

Figure 5.10: Accessible macroscopic fields: material packing density (left), temperature field (center) and normalized hydrogen distribution image (right).

shown in Figure 5.10. These fields are taken from the method application to sodium alanate in section 5.4 and are shown here just for illustration purpose, the results for the material are discussed in the corresponding section 5.4.5. In the upper part of Figure 5.11 a section of the three macroscopic fields is shown for the time step t, where only the hydrogen distribution to the right carries a time-dependency. Both packing density as well as temperature field are assumed to be time-invariant. For the temperature, this first approximation is valid if the maximal reaction rate and therewith the release of reaction enthalpy rate is limited by a controlled hydrogen flow. It will further be discussed in section 5.4 for the application of methods to the scaled-up sodium alanate system. At time step t, one pixel p_i of an image carries a data triplet consisting of its hydrogen content, specific temperature and material packing density. It is denoted by $[n(H_2)_i, T_i, \rho_i]$. The last two quantities are fixed and the average hydrogen amount is calculated for every pixel of an image matching the tuple $[T_\alpha, \rho_\beta]$, which results in

$$\langle n(H_2)\rangle_{\alpha,\beta} = \frac{\sum_{i=1}^{N} n(H_2)_i \cdot \delta_{T_i,T_\alpha} \cdot \delta_{\rho_i,\rho_\beta}}{\sum_{i=1}^{N} \delta_{T_i,T_\alpha} \cdot \delta_{\rho_i,\rho_\beta}} \tag{5.18}$$

where N is the total number of pixels corresponding to the metal hydride material and the $\delta_{i,j}$ are Kronecker deltas. The quantity $\langle n(H_2)\rangle$ is the averaged hydrogen content of pixel $p_{\alpha,\beta}$ in a so-called 'multi-correlation map'. The formation principle for the latter is schematically shown in Figure 5.11 where the hydrogen distribution data is combined with information regarding the temperature field as well as the material packing density distribution for a specific pixel p_i of the corresponding image. The exemplary pixel is framed inside each image. The derived triple $[n(H_2)_i, T_i, \rho_i]$ contributes to one pixel of the multi-correlation map, where packing density and temperature determine the abscissa respectively ordinate position and the amount of absorbed hydrogen contributes to its average for the specific $[T_\alpha, \rho_\beta]$-tuple. This denotes a transformation from real to correlation space, the spatial information is lost within a multi-correlation

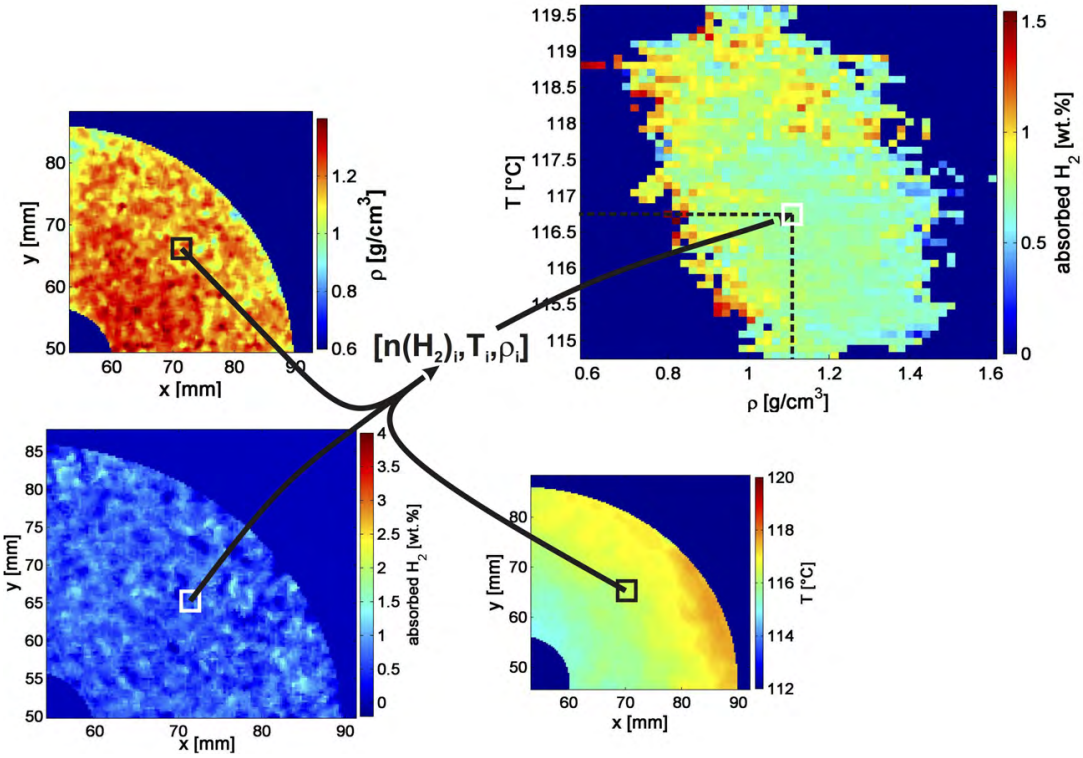

Figure 5.11: Schematic illustration of the transformation from real to correlation space for multi-correlation analyses. Pixel information for material packing density (upper left), hydrogen distribution (lower left) and temperature field (lower right) are combined within the triple $[n(H_2)_i, T_i, \rho_i]$ to derive one element of the multi-correlation map shown in the upper right.

map. As a consequence, the consistency of correlations for different regions inside the image has to be ensured, which is done by calculation of corresponding maps for data frequency and standard deviation as shown in the end of this subsection. In the present case of a time-constant material packing density and temperature field the only time-dependent quantity is the hydrogen distribution image. Performing the transformation for every existing $[T_\alpha, \rho_\beta]$-combination for every hydrogen distribution image, a time-resolved multi-correlation map of hydrogen content, temperature and material packing density is derived. For reason of sufficient data statistics, discrete intervals instead of continuous values are used for T_α, ρ_β. As a result of this binning, several pixels are matching a $[T_\alpha, \rho_\beta]$ tuple and the hydrogen content in equation 5.18 is an averaged quantity. The shape of these correlation maps is defined by existing tuples $[T_\alpha, \rho_\beta]$ and therefore depends on the explicit spatial distribution of temperature field and material packing density for the investigated metal hydride sample.

With the as-given definition of multi-correlation maps, the interdependency of quan-

tities can directly be resolved, where gradients of averaged hydrogen content indicate a present correlation.

- If gradients are inclined by $\pm$ 45°, the influence of the given temperature field and the material packing density is equal. If the axis labeling is in ascending order as it is in Figure 5.11, gradients exhibiting a positive slope indicate a positive correlation and therewith an increased hydrogen content for increasing temperature and material packing density and vice versa.

- A deviation of gradient orientation from $\pm$ 45°indicates a predominant influence of one quantity. In case of reduced slopes the influence of packing density is more pronounced and vice versa.

- In the limit of purely vertical or horizontal orientation there is exclusive presence of 2D correlation and non-significance of one quantity.

- In case of non-significant gradients or high fluctuation over time no general interdependency of driving forces (macroscopic fields) can be stated.

It is remarked that correlations resolved by this method solely depend on inhomogeneities that are present for the studied metal hydride with explicit temperature field and material packing density. Thus, correlations always have to be considered against this background, they might change for different conditions of temperature and packing density. Though binning is applied and pixel matching a $[T_\alpha, \rho_\beta]$ tuple are averaged, still the reliability for poor data statistics is low. This typically affects in particular the boundary of correlation maps, but might be important for large areas as well. To resolve the data statistics distribution, a frequency distribution on the correlation map morphology as well as standard deviation distribution has to be considered. The frequency distribution is given by the number of pixel corresponding to a distinct $[T_\alpha, \rho_\beta]$ under the chosen binning

$$f_{\alpha,\beta} = \sum_{i=1}^{N} \delta_{T_i,T_\alpha} \cdot \delta_{\rho_i,\rho_\beta} \tag{5.19}$$

The standard deviation distribution is given with use of equation 5.18 and the above defined frequency $f_{\alpha,\beta}$ by

$$std_{\alpha,\beta} = \sqrt{\frac{1}{f_{\alpha,\beta}} \sum_{i=1}^{N} \Big(n(H_2)_i - \langle n(H_2) \rangle_{\alpha,\beta} \Big)^2 \cdot \delta_{T_i,T_\alpha} \cdot \delta_{\rho_i,\rho_\beta}} \tag{5.20}$$

An increase of intervals (increase of binning) reduces the correlation map dimension and typically decreases values of standard deviation. As in real space imaging, the optimal binning is a compromise between resolution and data statistics. It is remarked, that if standard deviation maps reveal a high fluctuation of hydrogen amounts for different tuple $[T_\alpha, \rho_\beta]$ though presence of sufficient data point frequency, the correlations for triplets originating of different image regions are not consistent and no general conclusion concerning the type of correlation between temperature, material packing density and hydrogen content can be drawn.
In case that multi-correlation maps exhibit vertical or horizontal gradients, the data set can be reduced to derive a 2D correlation map which is shown in the following.

5.2.5.2 2D-Correlation

If the influence of one quantity (field) can be neglected, the full field dataset can be visualized without the necessity of averaging as performed in equation 5.18. Hence, a tuple $[q, n(H_2)]$ corresponds to a pixel within a 2D correlation map, where one tuple element is the normalized hydrogen content, the other, denoted by q, is either the temperature or the corresponding material packing density. The 2D-correlation map is then given by

$$c_{\alpha,\beta} = \sum_{i=1}^{N} \delta_{n(H_2)_i, n(H_2)_\alpha} \cdot \delta_{q_i, q_\beta} \tag{5.21}$$

where it is spanned by intervals of $n(H_2)$ and q with α, β indexing a pixel of the 2D-correlation map. Due to the time-resolution of the hydrogen content distribution, the 2D-correlation map carries a time dependency as well. Two general cases of corrleations are visualized in Figure 5.12. Here, the left part of the Figure shows an uncorrelated dataset for quantities $q1, q2$. The presence of correlation is then indicated by formation of order as can be seen in the right part of the Figure. The degree of order determines the significance of correlation. An as shown inclination indicates a linear correlation. In that case, the correlation can be quantified by the Pearson correlation coefficient which is defined by

$$r_{n(H_2),q} = \frac{\sum_{i=1}^{N} (n(H_2)_i - \langle n(H_2) \rangle)(q_i - \langle q \rangle)}{\sqrt{\sum_{i=1}^{N} (n(H_2)_i - \langle n(H_2) \rangle)^2 \sum_{i=1}^{N} (q_i - \langle q \rangle)^2}} \tag{5.22}$$

It is stressed again, that the determination of the 2D-correlation map is necessary to confirm the presence of a linear correlation **before** its quantification.

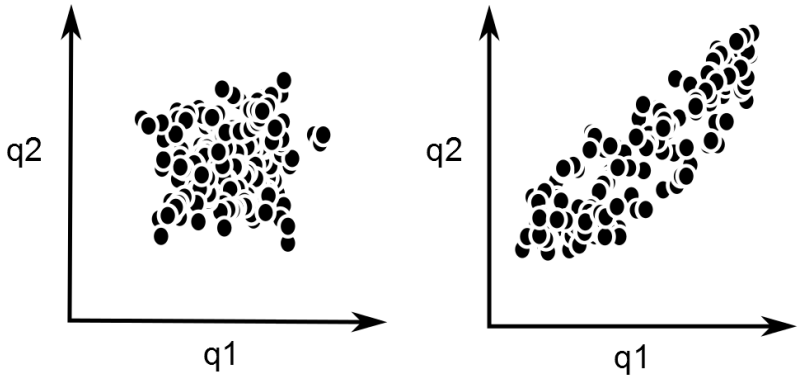

Figure 5.12: Cases of 2D correlation for variables $q1, q2$: uncorrelated (left) and linear correlated (right).

5.3 Development of analysis methods for systems with liquid phases

Within in the previous sections, the developed methods include a normalization of the attenuation difference between an image at t and a reference image at t_0 to assign a hydrogen content to every pixel. Against this background, the basic assumption for quantification of the hydrogen distribution in the metal hydride is that the initial material distribution stays constant during the sorption reaction. Consequently, any change between the images can be exclusively assigned to the interaction with hydrogen in the projected volume element, hence to an absorption in case of $\Delta\Omega > 0$ or to a desorption vice versa. For solid-state metal hydride systems this approximation holds well[6] However, the situation is fundamentally different for metal hydrides containing a combination of liquid and solid phase, as the case in e.g. Li-RHC for standard temperatures of ab- and desorption. In the following, methods for the analysis of solid-liquid metal hydride systems are developed using Li-RHC as a model system.

[6]Differences are mainly due to the volumetric increase in case of initial cycling of compacts, so that measurements should be done either for first-time absorptions or after several cycles, when the expansion is negligible.

5.3.1 Indication of material transfer

In general, in case of material transfer of the liquid phase within the solid throughout the reaction and measurement, a spatial invariance of material distribution does no longer hold. The change in attenuation of one pixel $p_{i,j}$ between two images is now driven by a superposition of two time-depending quantities: the amount of moving $LiBH_4$ and the amount of hydrogen absorbed in the projected volume defined by pixel $p_{i,j}$[7]. It is

$$\Delta\Omega_{i,j} = \Delta\Omega(H_2)_{i,j} + \Delta\Omega(LiBH_4)_{i,j} = c_1\Delta m(H_2)_{i,j} + c_2\Delta m(LiBH_4)_{i,j} \tag{5.23}$$

, where c_1 and c_2 are proportionality constants according to equation 2.5. Again, the Δ refers to the time interval $\Delta t = t - t_0$ between the two images at t and t_0. During an absorption process, the first summand is monotonously increasing while the second is varying since the liquid phase can both disperse or accumulate within $p_{i,j}$. From that it is not possible to separate these two quantities, since only the superposition $\Delta\Omega$ can be accessed. However, detection and estimation of material transfer is possible by an indirect approach using the following boundary condition: The maximal possible normalized hydrogen content equals the maximum theoretical capacity of the material, which is well defined by the stoichiometry of the final composition in the absorbed state. To make use of this boundary condition, the standard normalization procedure is performed to derive the hydrogen content in each pixel as shown in the previous sections, ignoring the above shown superposition and potential influence of material transfer. Thus, the derived distribution of hydrogen in the material is a pseudo-distribution, since every change in attenuation is assigned to absorption of hydrogen only. Hence, a material transfer can be identified if

$$\exists p_{i,j} : wt(p_{i,j}) > wt_{max} \tag{5.24}$$

where $wt(p_{i,j})$ is the weight-normalized hydrogen content of pixel $p_{i,j}$ in the pseudo distribution according to equation 5.17[8] in section 5.2.4 and wt_{max} is the maximal possible hydrogen content of the system. The maximal amount of hydrogen is given by the initial amount of material according to the reference image and the maximal theoretical capacity of the material

$$m(p_{i,j})_{H_2,max} = m(p_{i,j})_0 \cdot wt_{max} \tag{5.25}$$

[7]For reason of simplicity the formalism for the case of an absorption is shown. The desorption is in full analogy.

[8]Here, wt instead of $\tilde{n}(H_2)$ is used.

In the ideal case, the threshold for identification of material transfer is given by the theoretical capacity according to equation 5.24. However, real systems rarely reach their theoretical capacity. Thus, a more practical threshold for the material can be set according to empirical capacities derived from lab-scale measurements (e.g. Sievert's based) or literature.

5.3.1.1 Estimation of motion distance by selective binning

Since the change of attenuation according to equation 5.23 is based on the projected volume defined, the pixel area can be used to estimate a lower limit for the material transfer distance: Any motion of the liquid phase inside the projected volume area is not resolved, since it is

$$\Delta\Omega(LiBH_4)_{i,j} = c_2 \cdot \Delta m = c_2 \cdot \int_{V_p} \Delta m' \quad dV$$

where $\Delta m'$ is the difference of mass fields from t and t_0 and V_p is the projected volume defined by the pixel area. Consequently, changes inside this volume equal out due to conservation of mass. By that, a variation of the pixel size allows for a change of resolution with respect to material transfer. If at a given pixel size p_s the condition according to equation 5.24 is fulfilled and a material transfer is identified, the pixel size is enlarged by binning up to a pixel size $p_s^\star$, for which the following condition is fulfilled:

$$\max\left(wt(p_{i,j})\right) \approx wt_{max} \tag{5.26}$$

where the set (i, j) defines the sample area. This is visualized in Figure 5.13 by a static, rectangular binning, where for pixel size $p_s^\star$ the motion is limited to the corresponding pixel area and not resolved. The estimated motion distance is then derived by

$$M_d \approx p_s^\star - p_s$$

In the limit of one pixel covering the total sample area the correlation of attenuation by hydrogen and hydrogen content is derived as shown in section 5.2.1.2. Since at this resolution any change in attenuation is originating of the absorption of hydrogen, the general correlation is not affected and the normalization procedure is valid in case of a linear correlation.

A static and rectangular binning as visualized in the left part of Figure 5.14 is the simplest but most inaccurate estimation of M_d, since it does not account for the specific

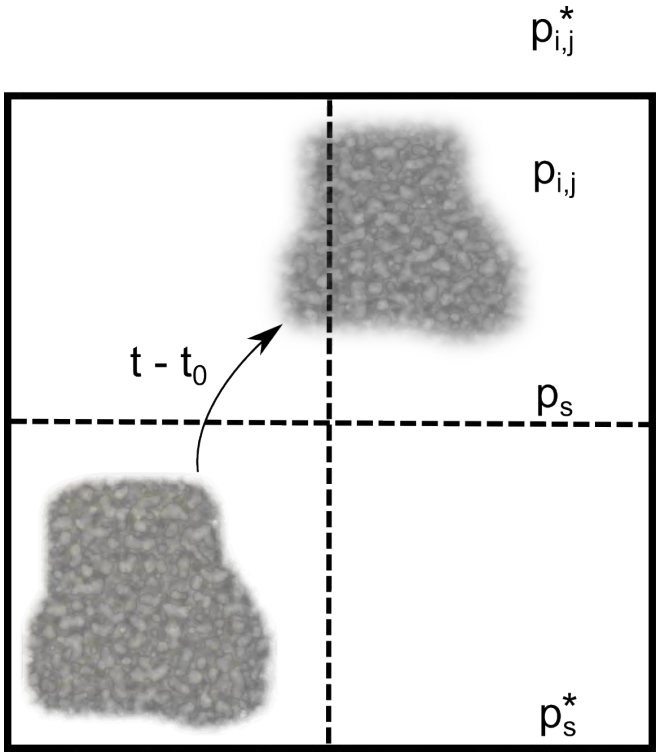

Figure 5.13: Effect of static, rectangular binning on the identification of material motion between time interval t and t_0, where motion is implied from the lower left pixel to pixel $p_{i,j}$. At pixel size p_s (visualized by dotted lines), motion can be identified while at (2x2) binning with corresponding pixel size of $p_s^\star$ (solid outer boundary) the motion is in the inside of pixel $p_{i,j}$ and not detected.

shape of the area that is formed by pixels fulfilling condition 5.24[9]. The darkened area in the Figure corresponds to a clustering of pixels with $wt(p_{i,j}) > wt_{max}$ at an unbinned pixel size according to the dotted lines, denoted by p_s. The shadowed and enlarged area is the area that originally hosted the moved material. For this static, rectangular binning (the origin is set on the upper left edge), a pixel size of $p_s^\star$ and a corresponding pixel area defined by the solid outer boundary line is necessary to reach the condition given in 5.26. The according motion distance $M_d = p_s^\star$ is significantly overestimating the true motion distance for the given setup. To this respect, a selective binning is proposed that takes this specific shape into account.

A pixel in this selective binning is initially defined in the way that it encloses the center area of a hydrogen pseudo content. In the following, binning is then enlarged according to the initial binning shape by ensuring an equidistant boundary difference of

[9]The motion of a liquid phase is induced by a driving force. Thus, a clustering or accumulation in a contiguous area can be assumed.

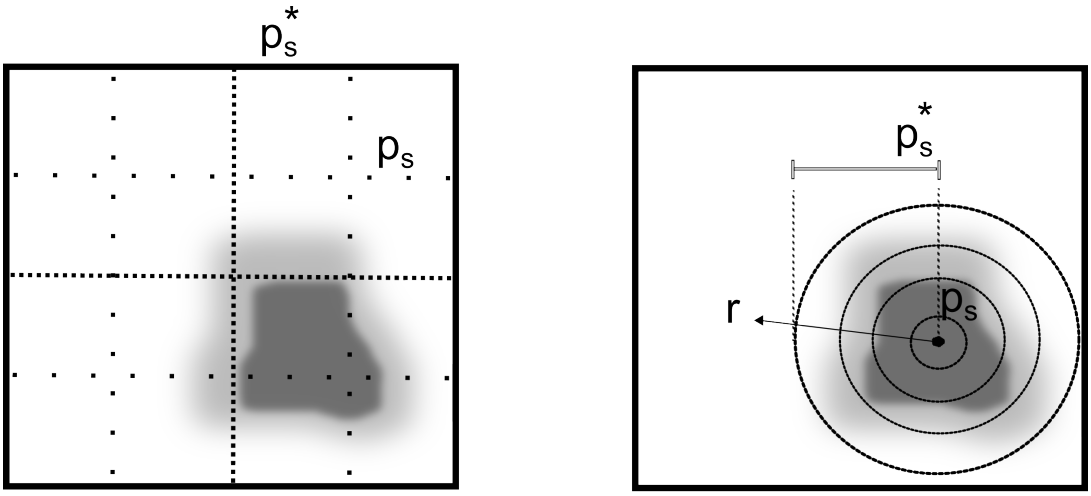

Figure 5.14: Comparison of static (left) and selective binning (right, shown exemplary for radial binning) for a cluster of pixel owing $wt(p_{i,j}) > wt_{max}$ (shown as darkened area) as result of a material motion from shadowed background.

old and new binning area[10]. This is an iterative process until the normalized hydrogen content in each redefined pixel is below or equal to its respective maximum according to equation 5.26. The boundary difference is the estimated material motion distance. The application of selective binning is visualized in the right part of Figure 5.14, where the initial pixel area of material motion is approximated by a circle with radius r_0 (denoted in the Figure by p_s). Hence, the outer boundary of binning areas and redefined pixels are circles and M_d is defined by the radius difference $r - r_0$ with r chosen in the way that condition 5.26 is fulfilled. This gives $M_d = p_s^\star$ since for the radius $r = p_s^\star$ the material transfer takes place in the inside of the corresponding circular pixel area. Compared to the static, rectangular binning in the left part of Figure 5.14 the estimation of the motion distance by selective binning is much more precise.

5.3.1.2 Estimation of material mass involved in material transfer

Besides the above described estimation for the material transfer distance, the boundary condition formulated in 5.25 allows for an estimation of the material mass involved in this transfer as well. For $LiBH_4$ as liquid phase in the system, the dominant interaction cross section for a fission neutron spectrum in the total attenuation of $LiBH_4$ is the one

[10]It is remarked, that redefined pixels according to this procedure are not necessarily of symmetric shape.

by hydrogen[11]. Thus, the excessive mass of hydrogen in a pixel can be calculated by using the maximal mass of absorbed hydrogen that is given by the maximal theoretical hydrogen content and the reference mass according to equation 5.25. It is

$$m(p_{i,j})_{exc} = wt(p_{i,j}) \cdot m(p_{i,j})_0 - m(p_{i,j})_{H_2,max} \tag{5.27}$$

Hence, the total mass of hydrogen that is involved in material transfer is estimated to

$$m_{mov} = \sum_{i,j} m(p_{i,j})_{exc} \cdot \Theta\left(m(p_{i,j})_{exc}\right) \tag{5.28}$$

where Θ is the Heaviside step function. From that the mass of the corresponding $LiBH_4$ can be calculated. In case that the composition of the liquid phase is different and the attenuation of other elements than hydrogen cannot be neglected, a calibration measurement for the liquid phase is necessary to determine its attenuation normalized by area density. Subsequently, the material mass can be calculated from the excessive attenuation in analogy to equation 5.27. The estimated mass is again a lower limit, since the starting point (the source) of material transfer cannot be resolved.

5.3.2 Isotope labeling

The investigation possibilities shown in the previous chapters are based on the changes of the total attenuation within a projected volume element between subsequent images (in situ NR) or within the ratio of two Tomography data sets (ex situ NCT). For the presence of only one time-depending quantity, which is hydrogen in most cases, this allows for a precise investigation of its distribution inside the host metal hydride material. However, the analysis of systems containing two or more time-depending quantities is limited, as it is not possible to assign the changes of attenuation to a specific quantity or material species. This is shown in the previous section, where an indirect assignment can be performed making use of the maximal theoretical capacity of the system to be investigated. In the following, a method will be introduced which allows to address a specific species in a multiphase system in order to study its distribution and dynamics.

Due to the interaction of neutrons with the nuclei of the penetrated material there exists a strong dependency of the interaction cross section on the explicit configuration of the nucleus as already introduced in the theoretical section in the beginning of this work. Accordingly, some elements show a tremendous difference of the total interaction cross section among their different isotopes. This 'isotope effect' is widely

[11] For use of a thermal or cold spectrum the effect of high absorption cross section by isotopes like Li and B has to be considered. This is explained in detail in the following section.

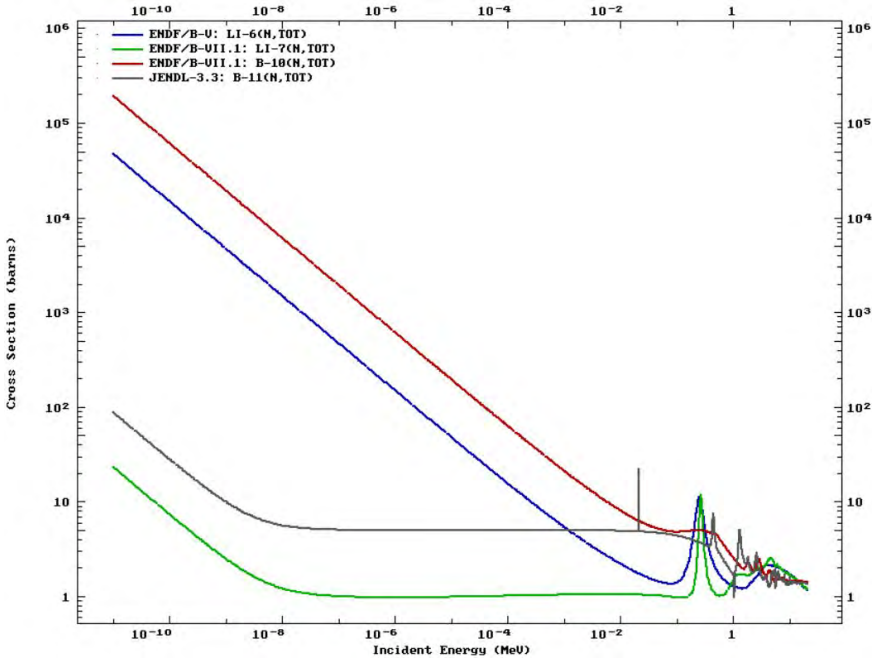

Figure 5.15: Total cross sections of Li-6, Li-7, B-10 and B-11 as a function of neutron energy. The data is used from ENDF data base [42].

used, both within the neutron scattering and the NI community, either for reduction of the elastic incoherent scattering contributions by H-1 hydrogen or to explicitly label hydrogen in the sample (e.g. [57, 79]). An even higher difference in neutron absorption cross section exists for the two elements Lithium and Boron and their isotopes Li-6, Li-7 respectively B-10 and B-11. The absorption cross section as a function of neutron energy is shown in Figure 5.15, it was derived from the Evaluated Nuclear Data File (ENDF) [29, 42]. In addition to the strong energy dependency in the absorption cross section for the shown isotopes Li-6 and B-10, they show a high absorption cross section in the thermal and cold neutron energy regime. This is as well listed in table 5.1 for a neutron energy of 25 meV in combination with the natural abundance for the different isotopes of Li and B. A total neutron beam attenuation within a system containing

Table 5.1: Isotopes of Lithium and Boron and their corresponding total neutron interaction cross section. The plot is generated based on data of Evaluated Nuclear Data File [42, 29]

Isotope	nat. abundance [%]	σ_{tot} (25 meV) [b]
Li-6	7,4	937
Li-7	92,6	1
B-10	19,9	3849
B-11	80,1	5

Lithium or/and especially Boron is dominated by the attenuation by these two elements, which enables a unique analysis of their distribution or dynamics in the overall system. This is of particular interest for the investigation of metal hydride materials as many promising systems contain either Boron, Lithium or even both of them. In this manner, the Reactive Hydride Composite $2LiBH_4$-MgH_2 bears a high investigation potential since the $LiBH_4$-phase contains both highly absorbing elements Li and B. Additionally, this phase is in the liquid state during an absorption or desorption process, which gives additional dynamics to the whole system and makes it highly interesting from the materials science point of view. Thus, the following methods and investigations will be shown for the $2LiBH_4$-MgH_2 system, but can be readily generalized to every other metal hydride systems containing a significant difference in cross section for the different isotopes of one or more of its elements.
In order to 'mark' the $LiBH_4$ phase by using the isotope effect so that its behavior during a reaction can be studied, samples with at least two different isotope compositions have to be compared. In this way, a change or motion of the $LiBH_4$ phase should be visible in both samples by a change of attenuation. If the ratio of attenuations is in agreement with the ratio of attenuations for the different isotope compositions, the corresponding change, motion or material can be identified as $LiBH_4$. It is pointed out, that within a single isotope composition this is not possible since the measured total beam attenuation is an accumulation of the interaction of all elements within the corresponding projected volume element. In particular, a significant perturbation is due to the beam attenuation by hydrogen in case of absorption or release of hydrogen. Since the measured beam attenuation Ω in an experiment depends on a large variety of parameters as described in the theoretical background section, the attenuation by $LiBH_4$ needs to be calibrated for different isotope compositions. For that an aluminum block is used, drilled with 5 holes of 3,5 mm diameter each. These wholes are filled with $LiBH_4$-MgH_2-$0.025TiCl_3$ powder with different weight ratios of isotope compositions. In the following, the natural isotope composition of $LiBH_4$ will be denoted as $LiBH_4$ and the corresponding $LiBH_4$-MgH_2-$0.025TiCl_3$ system as Li-RHC. The low absorbing isotope composition of Li-7B-$11H_4$ will be denoted as $LiBH_{4,iso}$, the corresponding $LiBH_4$-MgH_2-$0.025TiCl_3$ system as Li-RHC_{iso}. $LiBH_{4,iso}$ was purchased from Katchem with purities of $B-11 > 99,8\%$ and $Li-7 > 99,8\%$. The mixtures of the two systems are given in the table below: For better statistics, 5 Neutron Radiography images have been combined by means of a median filtering. Image acquisition was performed with an exposure time of 22 s with the high resolution setup. A $(2x2)$ binning has been applied, resulting in a pixel size of 51.2 μm. The corresponding attenuation image is shown in 5.16, the positions of the different mixtures in the image

Table 5.2: Mixtures of Li-RHC$_{iso}$ and Li-RHC.

Position	Iso : Nat	amount Li-RHC$_{iso}$	amount Li-RHC	Mass [g]
1	0:1	0	1	0.022
2	2:1	2/3	1/3	0,044
3	1:1	1/2	1/2	0,043
4	1:2	1/3	2/3	0,044
5	1:0	1	0	0,064

are listed in the first column of table 5.2. The highly absorbing sample with natural

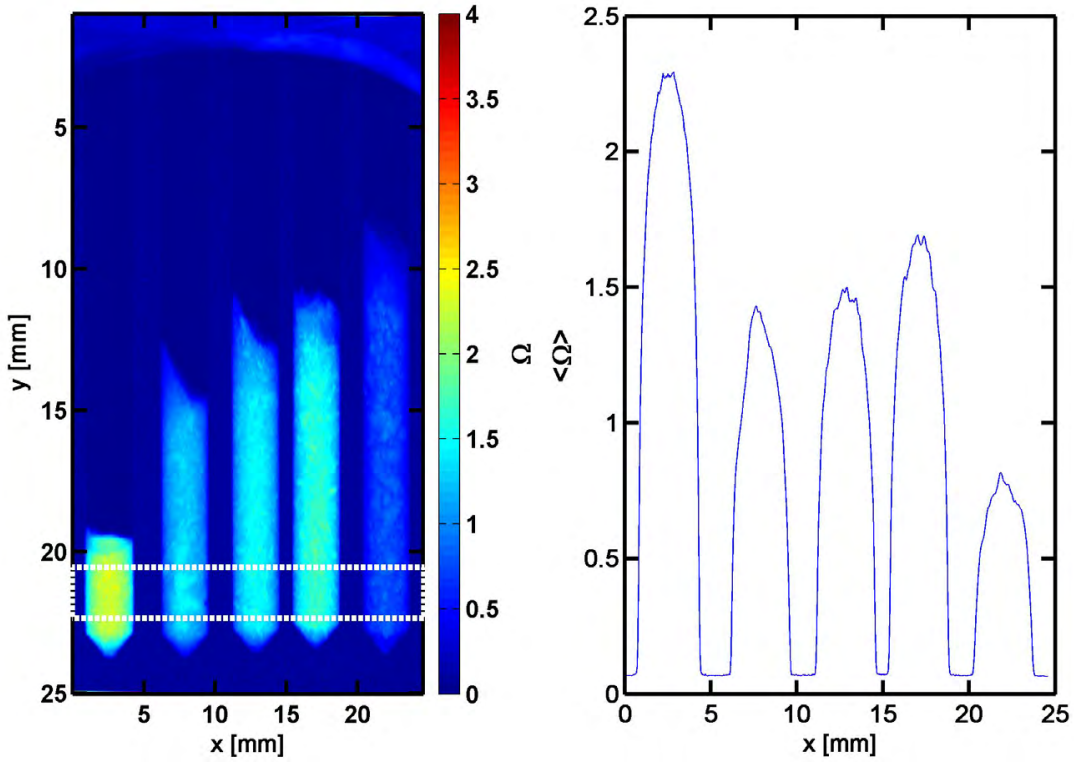

Figure 5.16: Left: Attenuation of different mixtures of natural and isotope Li-RHC positioned according to table 5.2 with the marked area used for the profile plot. Right: Profile plot of the marked area along the x-direction showing $< \Omega > (x)$.

composition is shown to the left, the low absorbing, isotopically enriched sample is shown to the right. In between the samples are positioned in ascending order with respect to their amount of high absorbing isotopes from left to right. The quantity of interest is the beam attenuation that is caused by the $LiBH_4$-phase. The measured beam attenuation, Ω_{tot}, that is given in Figure 5.16 is the sum of attenuations by the different materials inside a projected volume element. The attenuation by the additive $TiCl_3$ is neglected due to the small amount of substance in the mixtures. Thus, to

derive the attenuation by $LiBH_4$ the other contributions have to be subtracted:

$$\Omega_{LiBH_4} = \Omega_{tot} - (\Omega_{holder} + \Omega_{MgH_2} + \Omega_{Li-RHC_{iso}})$$

where Ω_{holder} is the attenuation by the sample holder made of $AlMg_3$. It is determined by a reference area above the sample. In the theoretical background chapter it was described that the attenuation caused by an element is determined by the number of atoms within a projected volume V element according to

$$\Omega = \mu \cdot d = \frac{m}{V} \cdot N_A \cdot \sigma \cdot d = \frac{m}{A} \cdot N_A \cdot \sigma = \rho_A \cdot N_A \cdot \sigma$$

with area density $\rho_A = m/A$. Thus, in ideal Neutron Radiography the normalized attenuation

$$\tilde{\Omega} = \frac{\Omega}{\rho_A} \tag{5.29}$$

is constant and allows to calculate the material mass in a projected volume element for a corresponding average attenuation and area:

$$m = \frac{< \Omega > \cdot A}{< \tilde{\Omega} >} \tag{5.30}$$

This can be used vice versa to correct the total attenuation by the influence of MgH_2 and Li-RHC_{iso}:

$$\tilde{\Omega}_{LiBH_4} = \Omega_{tot} - \left(\rho_{A,MgH_2} \cdot \tilde{\Omega}_{MgH_2} + \rho_{A,Li_RHC_{iso}} \cdot \tilde{\Omega}_{Li-RHC_{iso}}\right) \tag{5.31}$$

The area densities for Magnesium Hydride and Li-RHC_{iso} can be calculated using their pure sample compositions. A homogeneous spatial distribution of the compounds is assumed (no clustering!), thus the corresponding area A is the total sample area, which is defined by a simple threshold

$$A = \sum_{i=1}^{N} p_s^2 \cdot \Theta\left(\Omega_i - \Omega_E\right)$$

with p_s being the pixel size and Ω_E being the standard deviation of the background attenuation (noise) after correction of the sample holder, it is determined to 0.021. The normalized attenuation Li-RHC_{iso} is directly derived from the sample at position 5, the one for Magnesium Hydride is derived from a pure MgH_2 pellet serving as a reference sample (see appendix B.2.1). For the former it is $\tilde{\Omega}_{Li-RHC_{iso}} = 4.36\ cm^2/g$, for the latter $\tilde{\Omega}_{MgH_2} = 2.2\ cm^2/g$. The validity of considering a constant normalized attenuation is checked within the next section and in appendix B.2.1, respectively.

In ideal Neutron Imaging the attenuation can be averaged for each sample and corrections according to equation 5.31 can be performed using average area densities for Magnesium Hydride and Li-RHC$_{iso}$. Finally, a linear correlation of Ω_{LiBH_4} and the corresponding area density would be derived, with a specific area density for each of the five mixtures.

5.3.2.1 Beam hardening effect and evolution of normalized attenuation

However, in real Neutron Imaging there are perturbations by mainly scattering and beam hardening [12] which cause a deviation from the linear correlation. Thus, the explicit correlation of $\Omega(\rho_A)$ for the given instrumental setup has to be analyzed. Due to the cylindrical symmetry of the boreholes in the aluminum sample holder the sample mass area density varies along the x-axis. Each sample area is subdivided into a set of areas in which the average attenuation as well as the area density is calculated. It is assumed that the area density of the powder is homogeneous and the different elements and material compounds are homogeneously distributed inside the sample volume. Consequently, the mass fraction m_f within a subarea defined by an x-interval $x \in [x_0, x_0 + \Delta x]$ is given as follows

$$m_f = \frac{2}{r^2 \cdot \pi} \int_{x_0}^{x_0+\Delta x} \sqrt{r^2 - (x' - x_c)^2} \quad dx'$$

where r is the radius of the borehole [13] and x_c is the x-position of the sample center. By this, the area densities of $LiBH_4$, Magnesium Hydride as well as Li-RHC$_{iso}$ can be calculated and the averaged as well as normalized attenuation by $LiBH_4$ is derived for the subarea. Each sample is divided into 11 subareas, the corresponding correlation of attenuation and area density is shown in the left part of Figure 5.17. A strong deviation from a linear correlation is observed, starting already at low area densities of 0.015 g/cm^2. The data points until $\rho_A = 0.075$ g/cm^2 originate from samples with different mixtures of Li-RHC and Li-RHC$_{iso}$, the last data point with area density of 0.13 g/cm^2 is derived from a pellet of Li-RHC[14]. Since the increase in attenuation is dampened

[12] By use of a monochromatic beam the effect of beam hardening can be reduced [119], depending on the energy resolution of the selector. However, this is accompanied by a significant loss of beam intensity. For in-operando measurements of reactions and processes of highly attenuating elements like Boron, Li, hydrogen, etc. or steel sample holders like storage tanks with low transmittivity, a monochromatic instrument mode is often not suitable.

[13] Since the sample fills the whole borehole, the radius of the latter equals the sample radius.

[14] The pellet is of 70 mg mass, with diameter of 8 mm. A Neutron Radiography image was aquired with the pellet stored in vertical position inside an aluminum cell to ensure a constant are density in the projection image.

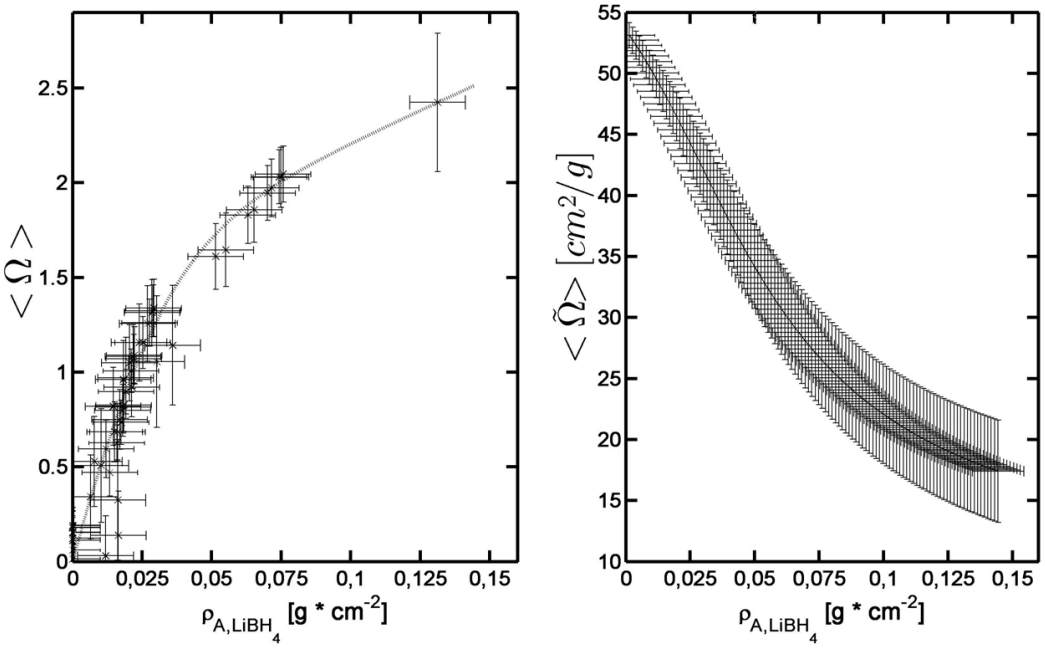

Figure 5.17: Left: Correlation of attenuation by $LiBH_4$ and corresponding area density, fitted by the bimodal energy model according to equation 5.32. Right: Evolution of the normalized attenuation, $\tilde{\Omega} = \Omega/\rho_A$, as a function of the area density of $LiBH_4$.

with increasing area density of high absorbing isotopes Li-6 and B-10, the effect of non-linearity can be explained by a beam hardening of the polychromatic neutron energy spectrum. Due to the strong energy dependence of the neutron interaction cross sections for the isotopes B-10 and Li-6 as shown in Figure 5.15, the interaction probability for low-energy neutrons is increased and vice versa. Consequently, the neutron energy spectrum of the polychromatic beam is hardened when penetrating the sample. More precisely, the dominant energy dependency for Li-6 and B-10 is carried by their respective neutron absorption cross section. In addition, the influence of the elastic scattering cross section of hydrogen is energy-dependent as well, which is shown in appendix B.2.1. Thus, there is a contribution to the beam hardening effect by hydrogen, even though it is less pronounced due to the significantly lower cross section value. As a consequence of beam hardening, the linear correlation of the measured attenuation and the area density is lost as visible in Figure 5.17. This phenomenon is widely known and studied in X-ray-Tomography [32, 39, 23]. Comparably little number of studies is found for the same effect in the Neutron Imaging community [15]. In this context, most of the correction algorithms have been developed within

[15] A search publication database search via 'Web of Science' gives only 22 entries for beam hardening in NI, but 670 for X-ray Imaging (request of 14.12.2015)

the X-ray community. The majority of them is based on hardware filtering [64] to sharpen the energy spectrum before an interaction with the sample or linearization [54]. For both, a physical model for the correction algorithm is missing. The best approach in this regard is the so-called 'bimodal energy model', introduced by Van de Casteele and Van Dyck in 2002 [124, 123]. It assumes two dominant energies $E_{1,2}$ in the spectrum with corresponding attenuation coefficients μ_1 and μ_2, holding $\mu_1 > \mu_2$. By that equation 2.3 becomes

$$\frac{I}{I_0} = \frac{\sum_{i=1}^{2} C_i \cdot \exp^{-\mu_i d}}{\sum_{i=1}^{2} C_i}$$

where $C_i = f(E_i)\gamma(E_i)$. Defining the ratio $\alpha = C_1/C_2$ and using the expression for the area density according to equation 2.5 the following expression for the attenuation[16] based on the area density is derived:

$$\Omega(\rho_A) = -ln\left(\frac{I}{I_0}\right) = \rho_A \cdot \eta_1 + ln\left(\frac{1+\alpha}{1+\alpha\exp^{-(\eta_1-\eta_2)\rho_A}}\right) \tag{5.32}$$

where $\eta_i = \sigma(E_i) \cdot N_A/M$.

The non-linear increase of the attenuation is converging into a linear correlation for large thicknesses or high area densities, in which the attenuation is determined by the second and higher energy E_2. Although the reduction of a polychromatic spectrum to only two relevant energies is a rough approximation, the resulting function fits wells to experimentally derived beam hardening curves [125]. The shown model is valid for a single element or material, for a multi-component system the beam hardening function has to be corrected in principle for every single phase inside the system. However, since the dominant cross sections are given by the highly absorbing isotopes B-10 and Li-6, the investigation of an effective attenuation for the $LiBH_4$ phase as shown in the left part of Figure 5.17 is sufficient. The model derived in equation 5.32 is used to fit the experimental data for varying $\rho_{A,LiBH_4}$, the analytical fit function is plotted as a dotted line in Figure 5.17. As can be seen, the bimodal energy model fits well to the experimental data, the determined fit parameter are listed in table 5.3. Without draw-

Table 5.3: Fit parameter according to the 'bimodal energy model'-fit of attenuation correlated to area density.

η_1 [b/kg]	η_2 [b/kg]	α
66 ± 6	7 ± 2	3.7 ± 0.8

[16]The attenuation here is simply denoted as logarithmic ratio of dark image corrected intensities, $\Omega = -ln\,(I/I_0)$.

ing quantitative conclusions about the underlying energy modes and their relation to the real polychromatic spectrum, the qualitative ratio of η_1 and η_2 is reasonable with respect to the strong energy dependency of the Li-6 and B-10 isotopes. Due to the effect of beam hardening the normalized attenuation is a function of the area density. This is shown in the right part of Figure 5.17. For $\rho_A \approx 0$ the correlation should be linear in the left part of the figure for small attenuation densities, resulting in a plateau for the normalized attenuation in the right part of the Figure in agreement with the analytical function according to equation 5.32. A further increase of the area density is accompanied by a decrease of the normalized attenuation due to the beam hardening effect. In the natural isotope composition of $LiBH_4$ the influence of beam hardening on the beam attenuation is strongly pronounced and is significant for even small area densities of $\rho_A = 0.005$ g/cm^2. Still, the analytical function can be used to calculate the material mass inside a pixel (in Neutron Radiography) or voxel (in Neutron Tomography) within any Li-RHC-system.

From the pure Li-RHC$_{iso}$ sample in the total right position in Figure 5.16 the normalized attenuation for $LiBH_{4,iso}$ is calculated. In contrast to the mixtures containing natural Li-RHC, the whole sample volume is averaged since the normalized attenuation shows no significant dependency to the corresponding area density of $LiBH_{4,iso}$ in agreement with the results found for MgH_2 as shown in appendix B.2.1 for low area densities. This is due to the fact that for $LiBH_{4,iso}$ and MgH_2 the dominant attenuation is originating from the cross section of hydrogen as shown in Figures 5.15 and B.3. The correction of the influence of Magnesium Hydride is performed in analogy to the procedure described above using equation 5.31. Thus, the normalized attenuation for $LiBH_{4,iso}$ is calculated to

$$< \tilde{\Omega} >_{LiBH_{4,iso}} = 7.85 \left[\frac{cm^2}{g} \right] \tag{5.33}$$

The ratio of the normalized attenuations of natural $LiBH_4$ and isotopically enriched $LiBH_{4,iso}$, which is again a function of the area density of natural $LiBH_4$, is defined as:

$$\tilde{r} = \frac{< \tilde{\Omega} >_{LiBH_4}}{< \tilde{\Omega} >_{LiBH_{4,iso}}} \tag{5.34}$$

Its evolution with area density for natural $LiBH_4$ is shown in Figure 5.18. The ratio shows strong differences depending on the respective area density: For small ρ_A values a maximal ratio of $\tilde{r} = 6.8 \pm 0.8$ is found. For highest ρ_A of the natural sample of Figure 5.16 (total left position) this ratio is reduced to 3.5 ± 0.8. For the identification

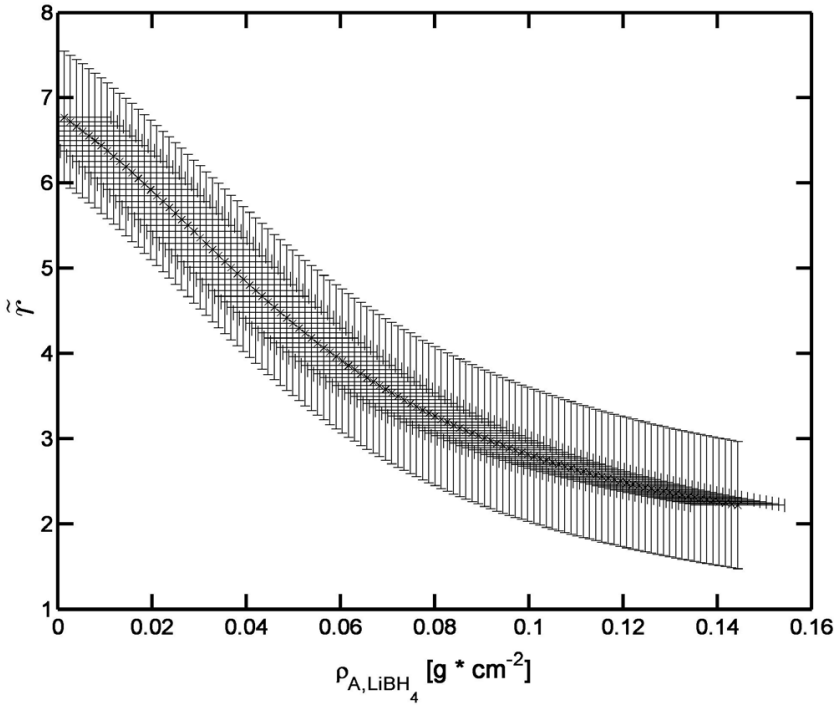

Figure 5.18: Evolution of the ratio of normalized attenuation of $LiBH_4$ and $LiBH_{4,iso}$, $\tilde{r}$, depending on the area density of $LiBH_4$.

of $LiBH_4$ and calculation of masses this has to be considered, which is described in the following.

5.3.2.2 Identification and mass estimation of $LiBH_4$ in multi-compound systems

As already described, knowledge of the normalized attenuation as a function of the area density allows for the calculation of mass of $LiBH_4$ according to equation 5.30. This is in particular useful for a tomographic dataset and mass estimation in arbitrary volumes of interest or even single voxel sets. Since a Neutron Tomography dataset consists of a combination of several Neutron Radiographies in which the total volume area of the sample in the field of view is projected, it is the total area density of a projection that determines the attenuation and influence of beam hardening. According to the calibration curve in the left part of Figure 5.17 the total area density is given by the measured attenuation in the projected sample volume. Hence, this total area density determines the normalized attenuation based on the calibration curve in the right part of the same Figure. For a mono-phase sample of $LiBH_4$ with unknown material mass, the latter can be directly calculated using $< \tilde{\Omega} > (\rho_{A,tot})$, where $\rho_{A,tot}$

is the area density of a Neutron Radiography of the sample.

In general, the system of interest does not consist of such a mono-phase, but is a mixture of multiple compounds like in the system that is investigated here, the Li-RHC. Though a priori the spatial distribution of phases can be assumed to be homogeneous with respect to the pixel resolution of 20.06 μm after ball milling [133, 5], the distribution of phases after chemical reactions like hydrogenation is not known. In particular, since the $LiBH_4$-phase is in the liquid state during hydrogenation this introduces a high dynamics into the system and might lead to a clustering, motion or separation of phases. There are two methods to identify such a phase and estimate its mass:

- The induction of a motion or change of $LiBH_4$ is caused by a driving force. It has to be assumed that the induced motion or change can be exclusively assigned to $LiBH_4$. A possible driving force is the temperature, causing a solidification or melting of $LiBH_4$ and corresponding changes in the total sample. It is pointed out, that this way of phase identification is indirect and a comparison of a priori and a posteriori states is necessary. Following the assumption that a detected change between two data sets that refer to two different states of the system can be assigned solely to $LiBH_4$, the mass of $LiBH_4$ can be calculated in the way described above using the normalized attenuation. This method is not limited to samples of different isotope contents but can be applied on any system. It is in full analogy to the method developed for the quantification of the hydrogen distribution in solid state metal hydride systems as introduced in section 5.2.1.2. However, the use of two identical samples except for their isotope composition - Li-RHC and Li-RHC$_{iso}$ - gives some advantages: Due to the high absorption cross section for Li-6 and B-10, any change of the $LiBH_4$ in the natural composition is especially pronounced. Additionally, the behavior of the phase (e.g. motion, clustering) should not depend on the explicit isotope composition. Thus, a comparison of Li-RHC and Li-RHC$_{iso}$ should reflect the ratio $\tilde{r}$ for the correct area density. This introduces the second method, namely the

- direct identification of $LiBH_4$ by comparison of Li-RHC and Li-RHC$_{iso}$. If the ratio of attenuations of the two samples in any volume or region of interest is in agreement with $\tilde{r}$ for the total area density of the natural composition of $LiBH_4$, the material inside the area can be identified as $LiBH_4$. Again, the corresponding material mass can then be calculated by use of the normalized attenuation.

The last method is exclusively enabled by use of the isotope contrast for Lithium and Boron. It is a powerful and unique investigation tool for the $LiBH_4$-MgH_2 system

in terms of the identification of phase separation, clustering and material motion originating from the $LiBH_4$-phase. It is stressed, that the method of isotope labeling combines phase sensitiveness and spatial resolution! The method introduced here is not limited to Li-RHC, the approach can be used in general for any metal hydride systems containing Lithium and/or Boron or other elements with isotopes of different interaction cross sections.

5.4 Applications - sodium alanate

Several studies have been carried out on sodium alanate to reveal fundamentals and mechanisms of the sorption reaction. Due to the moderate temperature regime of operation and relatively high hydrogen capacity, it has as well been subject to several scale-up studies (e.g. [128, 81] (see section 2.2.1) and can be ideally treated as model system for first-time application of developed methods within the previous section. Though there is general agreement on the high potential of sodium alanate systems for scale-up and application, there has never been a direct, quantitative study of time-resolved hydrogen distribution nor a correlation to macroscopic fields of temperature and material packing density. In the following subsections the high impact and investigation depth of in-situ Neutron Radiography investigations are shown, starting with qualitative analysis but revealing its full potential in the time-resolved quantitative analysis and correlation studies. Excessive use of the methods that were introduced and described in section 5.2 for the investigation of solid-state metal hydride systems will be made.

5.4.1 Experimental and measurement setup

Both desorbed-state sodium alanate powder and pellet in composition $NaH + Al + 0.05TiCl_3$ have been studied within the FlexiStore tank at the fission Neutron Imaging instrument NECTAR at FRM II. For loose powder, a material amount of 30 g respectively 50 g for the pellet was used. The latter was of 77 mm outer diameter, 12 mm inner diameter and 10.5 mm thickness. For both measurement configurations, a sinter metal filter was placed in the center of the tank to prevent a potential blocking of valves by powder particles. A hydrogen absorption experiment was performed at a temperature of 125 °C for reasons of comparability to other scale-up studies [127]. Additionally, it is reported to be a suitable temperature for $TiCl_3$-doped sodium alanate [128, 101]. The external heating was applied 1 h before the measurement to ensure thermal equilibrium. The starting pressure was 1 bar followed by a quasi-instantaneous increase to 35 bar within a time interval less than 1 s. A further increase of the hydrogen pressure up to a maximum of 100 bar was controlled by a mass flow controller with the flow set to 50 ml_n/min to match reaction kinetics to the image exposure time. During the measurement the thermodynamic quantities pressure and temperature inside the tank volume as well as the hydrogen flow were recorded. Simultaneously to the hydrogen absorption process, an in situ Neutron Radiography measurement has been performed using the standard instrumental setup as described in section 4.1.1. The total time between two succeeding images was 252 s. In order to avoid a significant perturbation

by scattered neutrons with respect to section 5.2.1, the sample detector distance was set to 15 cm.

5.4.2 Qualitative Neutron Imaging - material structure changes

Focusing on the region of interest, which is the pixel area representing the metal hydride material, already qualitative Neutron Imaging results reveal information about the influence of a quasi-instantaneous pressure increase on the macroscopic material structure. In Figure 5.19 the left column shows the material distribution in terms of the measured intensity normalized by the flat field and corrected for the dark image for loose powder before application of hydrogen pressure (top) and after (bottom) the pressure increase from 1 to 35 bar within a short time interval of about 1 s. Initially the powder is homogeneously distributed, except for a free volume in the upper part that originates from vibrations during transport and densification by gravitation. As

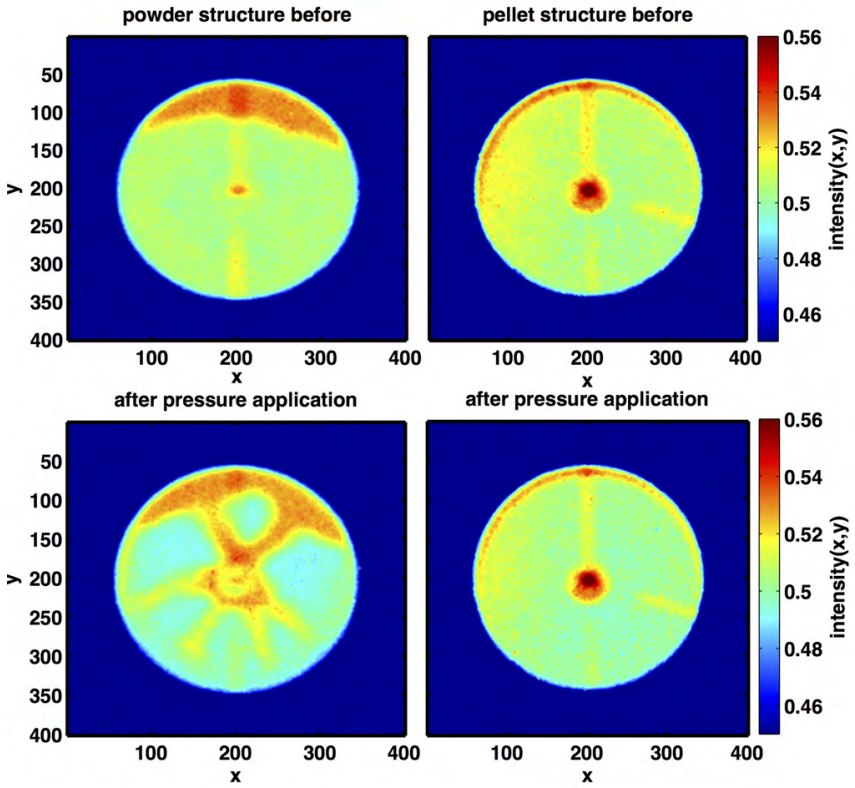

Figure 5.19: Intensity distribution normalized to the flat field and corrected for the dark image according to equation (1) for loose powder (left column) and pellet (right column). Top: material distribution before H_2 pressure increase; Bottom: after pressure increase.

visible in the lower left image, a pressure induced compaction and radial channel structures have formed due to the centered hydrogen inlet in accordance with the results found for a different tank design.[94, 128]. The position of the hydrogen inlet in combination with the initial material distribution and possible packing density differences seem to determine the complex structure after quasi-instantaneous pressure increase. These changes in macroscopic structure limit an efficient design of the raw material distribution, e.g. in terms of a contact to the tank hull to ensure an optimal heat transfer and management. In case of the pellet (right column of Figure 5.19) the macroscopic structure is stable and remains almost unchanged during hydrogen uptake. In addition to an increased volumetric efficiency compared to loose powder it allows for the tailoring of macroscopic raw material distributions with respect to the tank geometry to ensure an optimal contact between tank and metal hydride bed for maximum thermal conduction as mentioned above. Due to these superior properties, the further characterization focusses on pellets in the following.

5.4.3 Temperature field

The steady state temperature field is derived by IR-Thermography (IRT) of the Flex-iStore tank for the desorbed state and a flow of 50 ml_n/min. At this low hydrogen flow, significant effects of the reaction enthalpy on the measured temperature field can be neglected. The measurement procedure and setup is described in section 4.3. According to the results given in section 5.1 the temperature field derived by IRT is in good agreement with the internal temperature field of the metal hydride and serves as appropriate approximation. The derived temperature field on the tank surface is shown in Figure 5.20. It is cropped to the region of interest, showing only the tank surface area that corresponds to the metal hydride pellet. As visible, the temperature field is rather homogeneous with maximum temperatures of 119 °C at the left pellet area and lowest temperatures of about 115 °C near to the hole in the pellet center as well as at the lower pellet area. Maximum temperature differences are determined to 5 °C and are originating from a non-homogeneous heating power input from the the heating cartridges.

5.4.4 Material packing density distribution

In metal hydride based hydrogen storage the relevant quantity is the gravimetric hydrogen content [wt.%] of the hydride, which is the amount of stored hydrogen normalized to the raw material mass. Hence, for the quantitative characterization of the hydrogen distribution the raw material mass corresponding to each pixel is necessary. It can be derived from the reference image at t_0 before starting the absorption measurement

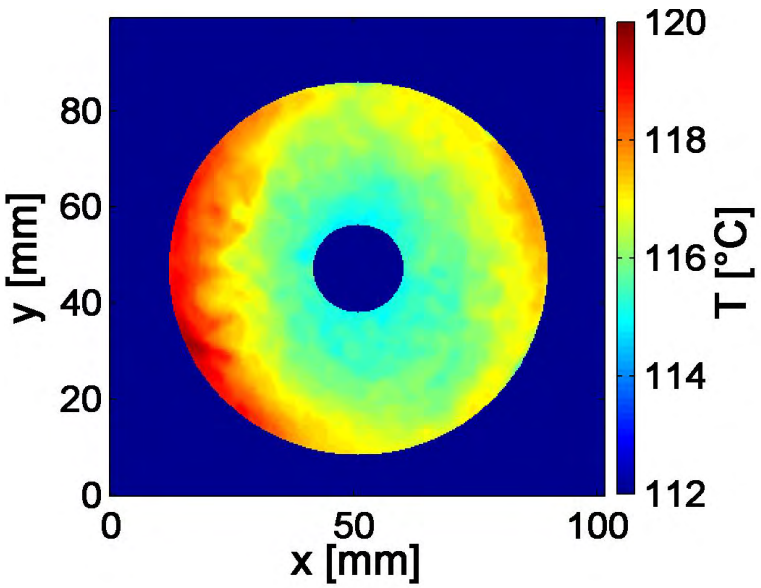

Figure 5.20: Approximated steady-state temperature field for the sodium alanate pellet, derived by IR-Thermography.

as described in detail in section 5.2.3. In the left part of Figure 5.21 the raw data of

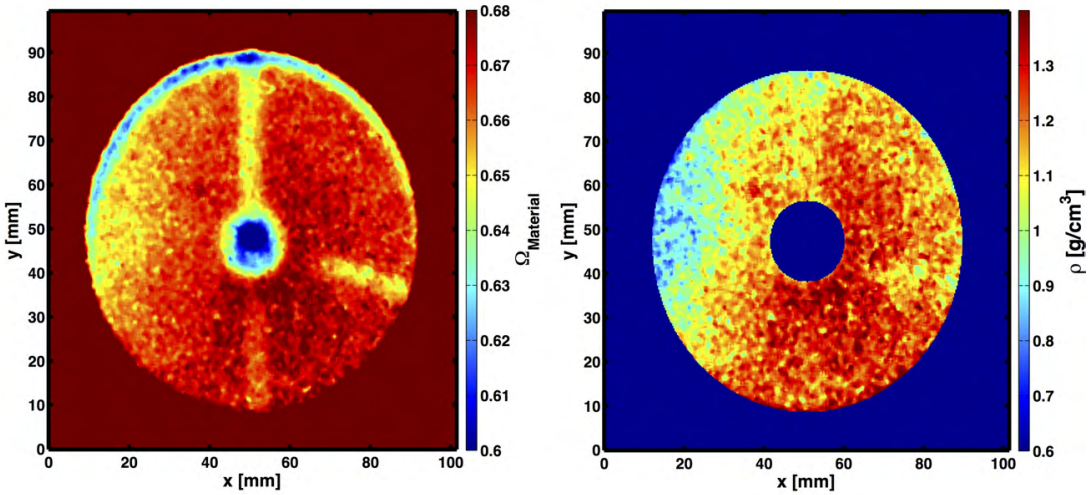

Figure 5.21: Attenuation distribution of a reference image normalized for flat field and corrected for dark image (left). Material packing density distribution after correction of influences by the sample environment and after normalization procedure (right).

the reference image is shown, normalized for the flat field and corrected for the dark image. The lines visible in the image correspond to temperature sensors inside the tank hull to record the temperature. As the intensity measured by one pixel is the total projected volume of the sample object which is the sample environment consist-

ing of tank hull, temperature sensors and the pellet (see the illustration of the total projected volume in Figure 2.2), the image has to be corrected for the influence of any quantity except for the metal hydride material. If the geometry of the storage tank is known, the correction can be readily performed (see section 5.2.3.1). Since the inner pellet diameter fits to the wall thickness reduction in the centre for the sinter-metal filter, a correction is not necessary. The effects of inlets for temperature sensors and hydrogen supply are corrected by Gaussian as shown in section 5.2.3.1 for cylindrical geometries. Subsequently to correction of tank geometry effects, the pellet is selected as a region of interest and a logarithm is applied to get the distribution of the macroscopic neutron beam attenuation by the raw metal hydride material in the desorbed state (see left part of Figure 5.21). The quantitative material distribution is calculated according to section 5.2.3 by normalization of material's attenuation to the total material amount. A sufficiently homogeneous distribution of NaH, Al and the additive in the overall pellet is assumed after ball milling treatment (see experimental section 4.2.4). According to studies by Bücherl and L.v. Gostomski the neutron beam attenuation at NECTAR correlates linearly to the material mass of the present components, thus the normalization procedure is valid [24][17]. After compaction, the pellet has a homogeneous thickness of 10.5 mm, allowing for the calculation of the material packing density according to equation 5.16, which is shown in the right part of Figure 5.21. The packing density is visualized by pseudo colors. A density gradient is apparent with minimal density (approx. 0.8-0.9 g/cm^3) in the left part and a maximum density (approx. 1.3-1.4 g/cm^3) in the lower right part near the hydrogen supply line in the center, which is masked in the image. These large differences in the packing density originate from the combination of a non-homogeneous bulk density of the loose powder inside the press matrix before compaction.

5.4.5 Time resolved hydrogen distribution and correlation studies - multiple field analysis

In situ Neutron Radiography data is combined with thermodynamic data from the tank and metal-hydride to derive the quantitative, time and spatial-resolved hydrogen distribution within the pellet. For that, the procedure introduced in section 5.2.2 is applied. When taking the logarithm of the ratio of an image at t and a reference image at t_0 to derive the attenuation difference by hydrogen according to equation 5.2, the

[17] In fact, for the fission neutron spectrum at NECTAR the attenuation caused by desorbed state metal hydride is dominated by the interaction cross section of hydrogen that is present in sodium hydride. Attenuation by sodium, aluminum and the additive is negligible. The linear correlation of attenuation by hydrogen and the corresponding amount of the substance has already been verified for the NECTAR spectrum in section 5.2.1.2.

effect of the gaseous amount of hydrogen in a projected pixel volume is equal or lower than 3 % of the corresponding amount absorbed by the metal hydride[18] and neglected in the following. Any effect of material transfer as described in section 5.3.1 by means of the expansion of material can be neglected: for sodium alanate pellets, the volumetric expansion within the first absorption is below 3 % in radial dimension [77]. Additionally, no significant change of the material's diameter was observed during the measurement. A change in axial direction does not have to be taken into account as the beam attenuation is integrated over the full projected volume.

After the normalization procedure for the calculation of the hydrogen distribution, the data set is combined with the material packing density for derivation of the gravimetric hydrogen content distribution as described in section 5.2.4. This distribution is shown exemplary for three images at time steps t = 77, 265 and 519 min in Figure 5.22 (lower part) together with the evolution of the overall hydrogen content in the metal hydride (upper part of the figure) derived by thermodynamic data according to equation 4.1 in section 4.2.1. The plot shows the typical two-step absorption reaction for the complex hydride sodium alanate, evolving from the initial state to a hexa-alanate state and finally to tetra-alanate [12] according to equation 2.22 in section 2.2.1. The formation of the tetra-alanate phase in this absorption process starts at t $\approx$ 265 min. The three time steps, for which the absorbed hydrogen distribution is shown in the lower part of Figure 5.22, are marked by circles. The images demonstrate the main advantage of in-situ Neutron Imaging, namely the analysis possibility of the spatial, temporal and quantitative resolved hydrogen distribution within the metal hydride simultaneously, which is scaled by pseudo colors for each image. Up to the beginning of the 2nd phase, hydrogen seems to be homogeneously distributed within the material. However, in the last of the three images shown in Figure 5.22, corresponding to the end of the absorption process, an increased concentration of hydrogen in the left part of the pellet is visible, indicating a spatial difference in the kinetics. The region of increased hydrogen content matches the region of maximal temperature by external applied heating (see Figure 5.20, right) as well as regions for lowest material packing density (see Figure 5.21, right). Temperature and material packing density are known to have a significant impact on the sorption behavior of metal hydrides in general and so it is for the complex hydride sodium alanate.[12, 76] However, so far there has been no possibility to investigate the interdependency of these different driving forces. With the method of combination of macroscopic fields in terms of a multi-correlation study as introduced in section 5.2.5 it is possible to resolve the impact of the two different driving forces. At time step t, one pixel p_i carries a data triplet consisting

[18] This is due to the fact that the pellet occupies almost all free volume inside the tank.

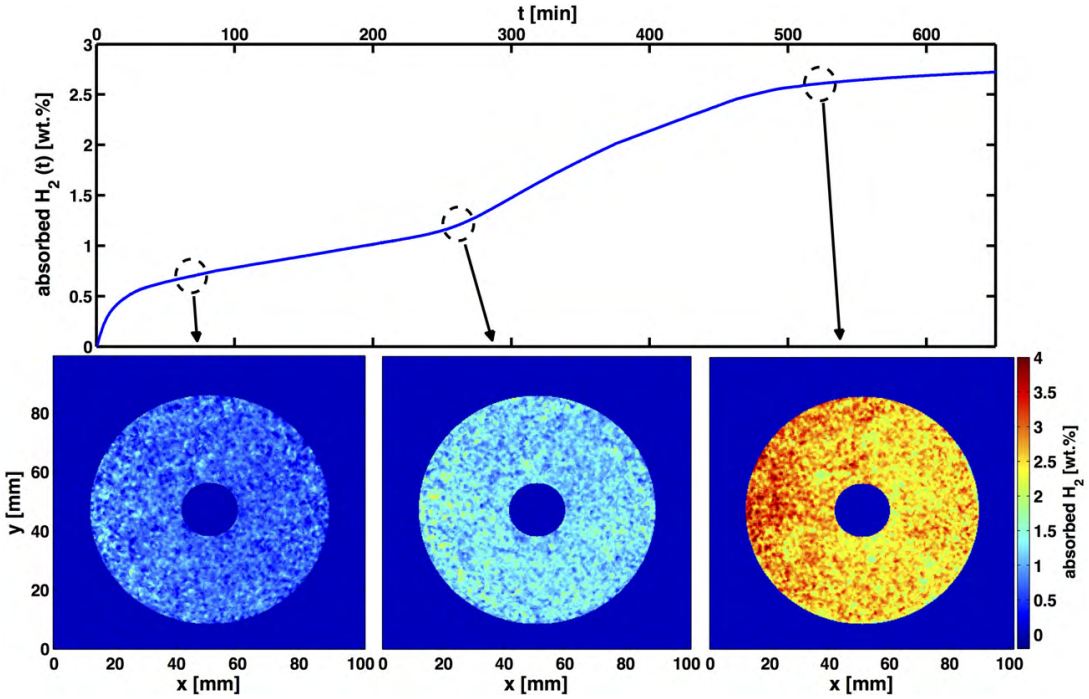

Figure 5.22: Time evolution of absorbed hydrogen (top) with quantitative, spatially resolved hydrogen distribution in the material (bottom) for selected time steps, indicated by dashed circles in the overall time evolution image.

of its hydrogen content, specific temperature and material packing density. The triple $[n(H_2)_i, T_i, \rho_i]$ contributes to one pixel of the multi-correlation map according to equation 5.18, where packing density and temperature determine the abscissa respectively ordinate position and the amount of absorbed hydrogen contributes to the average for the corresponding $[T_\alpha, \rho_\beta]$ pixel of the multi-correlation map. Doing so for every hydrogen distribution image a time-resolved multi-correlation map of hydrogen content, temperature and material packing density is derived. Multi-correlation maps for 6 selected time steps (t = 60, 144, 248, 290, 415 and 623 min) are shown in Figure 5.23. For reason of sufficient statistics discrete intervals instead of continuous values are used for T_α, ρ_β. Interval widths of 0.021 g/cm^3 have been chosen for ρ_β and 0.1 °C for T_α, respectively. On the x-coordinate the material packing density is plotted, on the y-coordinate the temperature field. The average hydrogen content is scaled by pseudo colors. For the beginning of the hydrogen absorption (t = 60 min, see also Figure 5.22) there is no significant correlation in conformity with the first image showing the spatial hydrogen distribution. With a further proceeding hydrogen absorption (maps for t = 144, , 290 min), the highest hydrogen contents are found at the left boundary line of the multi-correlation map, e.g. for $T \approx 115.5$ °C and $\rho \approx 0.95$ g/cm^3 in the lower

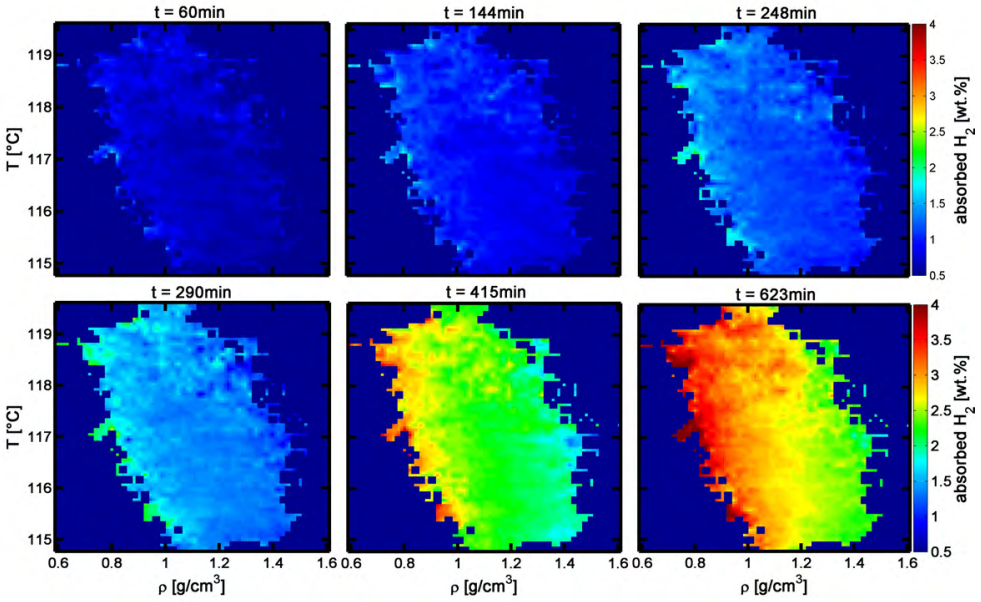

Figure 5.23: Multi-correlation maps for correlation of temperature T, material packing density ρ and average hydrogen content (as color bar) for different time steps (t = 60, 144,. . . , 623 min).

left image of Figure 5.23 (for t = 290 min). In this area, data statistics is low since only a few pixel fulfill the required condition for temperature and packing density, which is shown in Figure 5.24. In the left part the frequency distribution of existing tuple $[T_\alpha, \rho_\beta]$ is shown. It is determined by the explicit temperature field and material packing density distribution for this experimental study. The highest frequencies and accordingly best data statistics are found in the lower area for $\rho \in [1, 1.4]$ g/cm^3 and $T \in [115, 117]$ °C. At the boundary areas as well as in the upper area, statistics is particularly low with high fluctuation of data for contributing pixels as indicated by the standard deviation map shown in the right part of the Figure. Consequently, effects observed in these areas are less significant and conclusions have to be drawn carefully.

In addition to the influence of data statistics, a neighborhood effect might be the reason for these discrete spots. Indeed, if transformed back to real space, the left boundary of the correlation map corresponds to regions near to the left pellet area, where highest kinetics are measured. Neighborhood effects might be e.g. the heat transfer from a reaction spot during formation of the hydride phase to adjacent areas, enhancing the reaction in the local neighborhood. This could also be observed for the interstitial hydride $LaNi_5$ by use of Neutron Imaging [49, 63]. Additionally, the reaction and evolution of a new phase is accompanied by structural changes and

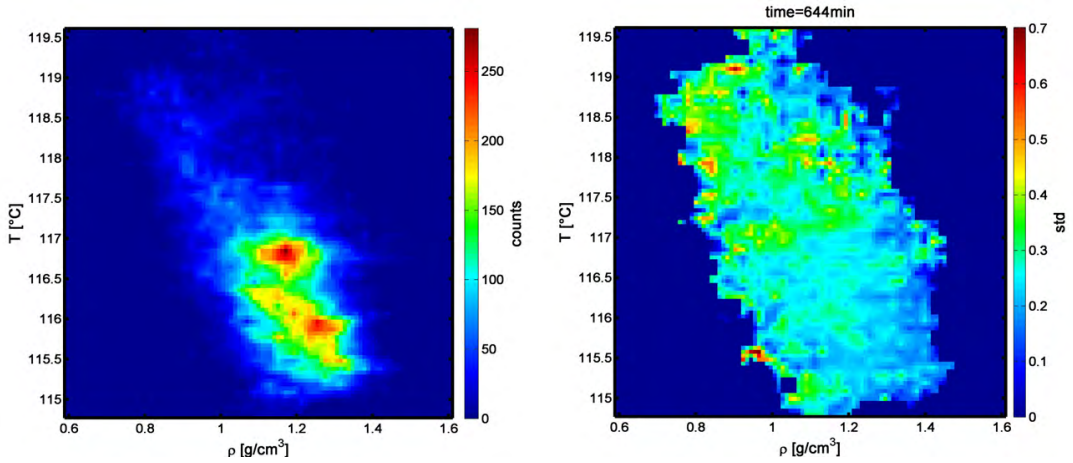

Figure 5.24: Left: Frequency distribution of existing tuple $[T_\alpha, \rho_\beta]$ for the same binning as used for the calculation of multi-correlation maps. Right: Corresponding distribution of the standard deviation, exemplary for t = 644 min.

motion of reactants on the nano or atomic scale, which also influences local neighborhoods. Besides these spots for lower temperatures that are most probably caused boundary effects and statistical fluctuations, there additionally seem to be higher hydrogen contents for temperatures above T = 117 °C. Moving further along the time axis of Figure 5.22 and entering the 2nd and final tetra-alanate phase, a clearly visible correlation between hydrogen content/kinetics and material packing density is forming (Figure 5.23, t = 415 min, 623 min), indicated by the emergence of vertical orientated, color-coded transitions between different hydrogen contents and horizontal gradients. A significant influence of the temperature deviations in the pellet of maximum 5 °C on the kinetics could not be observed. Under the applied conditions, reaction kinetics is dominated by the material packing density distribution as indicated by the multi-correlation study. Furthermore, the correlation is found to be negative. Thus, an increased inner porosity inside the metal hydride and between particles enhances reaction kinetics and vice versa.

5.4.5.1 2D-correlation

To further distinguish and more precisely investigate the influence of both, temperature and material packing density, the data of multi-correlation maps is used for a 2D-correlation analysis according to section 5.2.5.2, which is the $n(H_2)-T$ or $n(H_2)-\rho$ correlation. With respect to the strong influence of packing density especially for advanced absorption stages a small interval ($\rho \in$ [1.1-1.3] g/cm^3) is chosen to study the influence of the temperature field only. Within this range, effects of material packing

density variations are negligible: elements (pixel) exist for almost every $[\rho, T]$-tuple of the subset of the multi-correlation space defined by the above ρ interval. Additionally, for this interval the best statistics is found by means of a high frequency of pixel matching tuples $[\rho, T]$. Resulting 2D-correlation maps are shown in the upper left part of Figure 5.25 exemplary for t = 135 min, which is within the first absorption step, and for the end of the measurement at t = 644 min (lower left part of Figure 5.25). Here, the x-coordinate is the temperature and the y-coordinate refers to the hydrogen

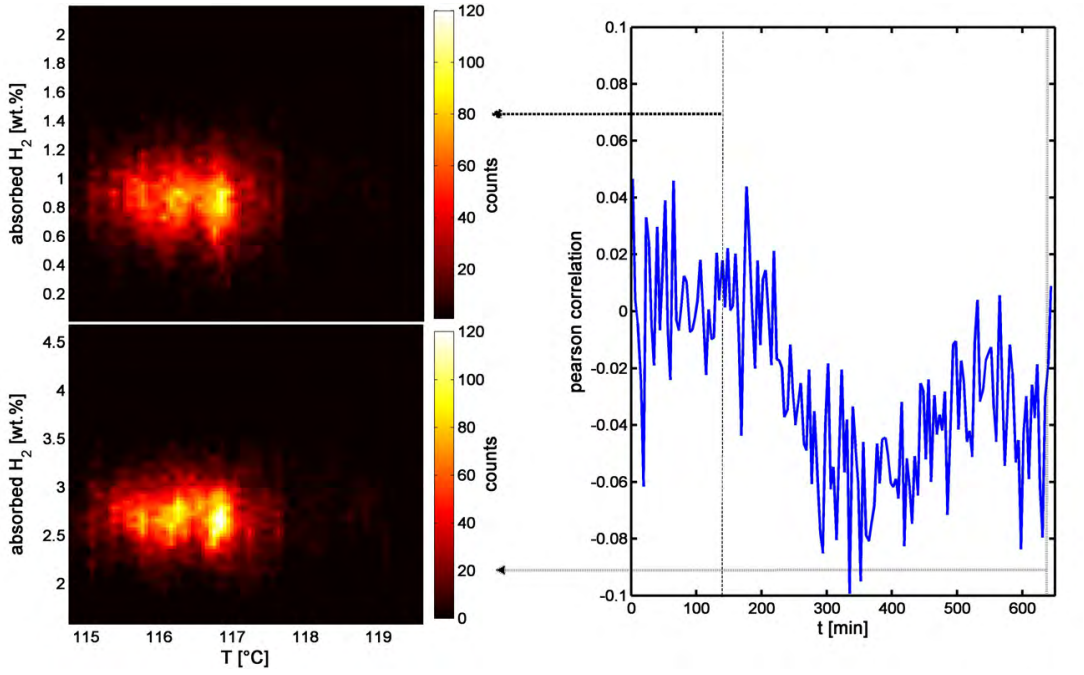

Figure 5.25: Left: Correlation maps at selected time steps for correlation of the temperature and hydrogen content. Right: Time evolution of the Pearson correlation coefficient.

content. The frequency of pixels matching the specific tuple $[T, n(H_2)]$ is scaled by pseudo colors. As can be seen by the 2D-correlation map, there exists no significant correlation between temperature and hydrogen content/kinetics, though this is indicated by the upper part ($T > 117.5$ °C) in the corresponding multi-correlation map in Figure 5.23 for the same time step. This disagreement is due to low frequencies for tuples of high temperatures and low or medium material packing density. Since the 2D-correlation reveals a linear correlation, the time evolution of the Pearson correlation coefficient can be calculated by use of equation 5.22, which allows to quantify the correlation of interest [87]. In the right part of Figure 5.25 the time evolution of the Pearson correlation coefficient for all existing $[T, n(H_2)]$-tuples is shown, the absolute values are below 0.1. According to the classification introduced by Evans,

the correlation is very weak, confirming a non-significant impact of the temperature field on the kinetics [40]. Although a decrease of the correlation coefficient is visible, it is not significant. Still, the investigation of the temperature effect is limited by means of the low statistics for $T > 117$ °C and medium or low densities. For that reason, a complex correlation especially pronounced for higher temperatures cannot be investigated nor stated. An analogue 2D-correlation study is performed for material packing density and hydrogen content. The whole set of existing $[\rho, n(H_2)]$-tuples is used assuming a negligibility of the temperature influence as implied by the previous results. 2D-correlation maps are shown in the left of Figure 5.26 for the same time steps as before (t = 135 min, upper left, t = 644 min, lower left). The time evolu-

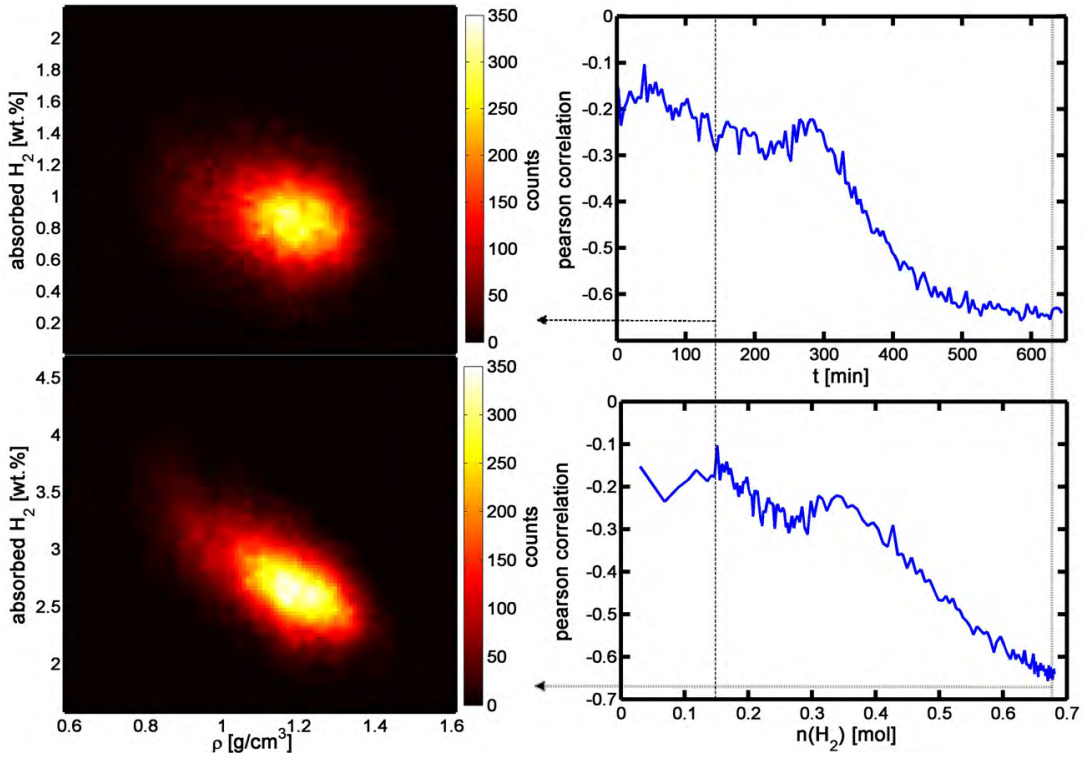

Figure 5.26: Left: Correlation maps at selected time steps for the correlation of material packing density and hydrogen content. Upper right: Time evolution of the Pearson correlation coefficient. Lower right: Correlation of Pearson correlation coefficient and hydrogen content.

tion of the Pearson correlation coefficient is shown on the right. A linear correlation between material packing density and hydrogen content or reaction kinetics is found, indicated by the initial broad distribution of $[\rho, n(H_2)]$-tuple frequencies turning into an ellipse for proceeding absorption. The Pearson's correlation coefficient is negative and the slope of its evolution is especially pronounced at t $\approx$ 280 min, which almost

coincides with the beginning of the second absorption process (see upper right part of Figure 5.26). This means that an increased material packing density results in lower reaction kinetics. However, the plot of the Pearson's correlation coefficient against the absorbed amount of hydrogen reveals a non-trivial $\rho - n(H_2)$ correlation, shown in the lower right part of Figure 5.26. Despite the underlying noise two different regimes can be observed: i) a weak negative correlation reaching into the second absorption step in concordance with multi-correlation maps for t = 144,..., 290 min and ii) an increased and significant negative correlation for the second phase. The correlation is still present and strongest pronounced for the absorbed hydrogen amount evolving into a plateau (Figure 5.22), indicating the end of the absorption process. Ex situ studies on smaller amounts of material confirm a reduced kinetics with increased material packing density and vice versa [66, 77]. However, the reason for this dependency is still not fully understood: A possible explanation is, that the material compaction influences the particle arrangement and induces reorganization with preferential orientation perpendicular to the compaction direction. The inner porosity is reduced, resulting in an increased barrier for the nucleation and growth of the hydride phase that has a lower density than the raw material. However, the reaction enthalpy for the formation of the hydride phase is 47 kJ $mol^{-1}(H_2)$ for absorption to the hexa-phase and 37 kJ/mol_{H_2} for the final tetra-phase and should be much higher than the energy needed for a volumetric increase.[12] Still, an effect of free volume could in principle explain the evolution shown in Figure 5.26. Initially, inner porosity exists since densities after compaction are well below the theoretical bulk density of 2.07 g/cm^3. Therefore, the most probable explanation is hindered or limited permeation of hydrogen[66, 129]. The initial less pronounced correlation could again be explained by inner porosity inside the sample, enabling permeation of hydrogen among the particle interfaces. During the reaction the emergence of the hydride phase causes a reduction of free volume due to its lower density of 1.24 g/cm^3 for the final $NaAlH_4$. This leads to a blocking of pores and channels and consequently to a reduced permeation. Reduction of permeation and the need for splitting of hydrogen molecules for diffusion through the solid increases the overall diffusion lengths and reduces kinetics.

5.4.6 Conclusions from in situ NR studies for solid state MH systems

From the measurement and results described and discussed in the above sections the following conclusions for storage system based on sodium alanate can be drawn and additionally some general features concerning solid-state, scaled-up metal hydrides and their investigation possibilities using Neutron Radiography are derived.

Initial pressure application leads to significant changes of the initial macroscopic material structure for loose powder beds. The porosity of the bed is reduced and a compaction is observed due to the pressure surge, where the resulting structure is influenced by the position of the hydrogen supply line as well as the explicit powder bed distribution. For design of the metal hydride bed geometry in terms of optimal heat transfer between material and tank an as observed channel structure is not optimal. Best bed design in terms of heat transfer and stability of geometry is derived by compaction and use of pellets. For in-situ resolution of structure changes of metal hydride beds already qualitative in situ Neutron Radiography is sufficient. For solid-state metal hydride systems the results derived here from correlation studies are in conformity with reports from literature, stating a highly significant, negative correlation of material packing density and absorption kinetics. By quantitative, time-resolved correlation analysis the derived time evolution of correlation indicates a transition from permeation to diffusion probably depending on the remaining free pore volume. The optimal metal hydride bed design is a compromise of bed structure stability and robustness against pressure surges, high volumetric densities and optimal kinetics. Since there is a tendency towards a self organized density of compacts during cycling as reported in [77], the compaction process should be performed in the way that the maximal theoretical density in absorbed state is not exceeded. This allows for a optimal bed design in terms of volumetric density, structure stability and kinetics. Moreover, the material packing density distribution can be derived by a single quantitative Neutron Radiography. For scaled-up pellets, the homogeneity of bulk powder density inside the press matrix is important to allow for a homogeneous absorption process. Against this background, Neutron Radiography can serve as a tool for optimization of metal hydride compaction processes. For sodium alanate, the effect of temperature field variations of about ± 3 °C were found to have no significant influence on reaction kinetics. Hence, the focus for tank and metal hydride bed design is on the optimization of material packing density distribution and heat transfer from metal hydride to the tank.

In general, in situ Neutron Radiography with use of methods for quantification and multiple field analysis as applied above was shown to be a highly powerful method for in operando investigation of scaled-up metal hydride beds. It is so far the only method that is capable of spatially resolving the hydrogen distribution inside the metal hydride bed! Furthermore, the use of fission neutron spectra allows for the analysis of even large metal hydride beds and covering tank vessels.

5.5 Applications - Li-RHC

In contrast to $NaAlH_4$, the Li-RHC system exhibits a liquid phase for the absorbed state because the temperatures typically used for absorption and desorption are well above the melting point of $LiBH_4$. A presence of the liquid state dramatically changes material and structure properties as will be shown in this section. Additionally, the analysis differs in comparison to a solid system, allowing for a detection of material transfer in the system using the methods introduced in section 5.3. In the first part, the analysis of a scaled-up pellet of $LiBH_4$ is examplarily presented to show the investigation potential for scaled-up storage systems. In the second part the resolution is increased from millimeter to micrometer and the $LiBH_4$ phase is studied in particular, making intensive use of isotope labeling introduced in section 5.3.2.

5.5.1 Li-RHC storage system

5.5.1.1 Experimental and measurement setup

A pellet of 60 mm diameter, 23.27 g mass, 6.4 mm thickness and an initial density of $\rho = 1.14$ g/cm^3 was analyzed by in-situ Neutron Radiography to study the time-resolved absorption process of the Li-RHC system with liquid $LiBH_4$ phase. To additionally reveal the 3D-material structure, a Neutron Tomography analysis was performed. It is remarked, that there is no effect of neutron absorption by isotopes B-10 and Li-6 due to the fission neutron spectrum of the NECTAR instrument (see Figure 5.15 in section 5.3.2). To investigate a potential phase separation, the pellet was cycled 7 times beforehand. Starting from the desorbed state, the hydrogen absorption process was investigated by in situ Neutron Radiography. In contrast to the investigation of the scaled-up sodium alanate system the exposure time could be reduced to 120 s due to a new instrument software, allowing for a better time-resolution of in-operando processes. The pellet is stored within the FlexiStore storage tank. The standard measurement setup for in-situ investigation of metal hydrides is used as introduced in section 4.1.1, except for an additional 1 cm B_4C filter embedded in epoxy that was also used for the investigation of scattering effects in section 5.2.1 for the aluminum tank setup. Absorption was performed at a temperature of T = 355 °C with a controlled hydrogen flow of 200 ml_n/min into the tank volume up to a pressure of 70 bar. In the left part of Figure 5.27 a Neutron Radiography image of the storage tank is shown for a qualitative overview. The intensity is normalized by the flat field and corrected for the dark image. The area of interest is the tank center region where the metal hydride pellet is located. This is shown in more detail in the right part of the Figure by the distribution of the total beam attenuation, Ω, scaled by pseudo colors.

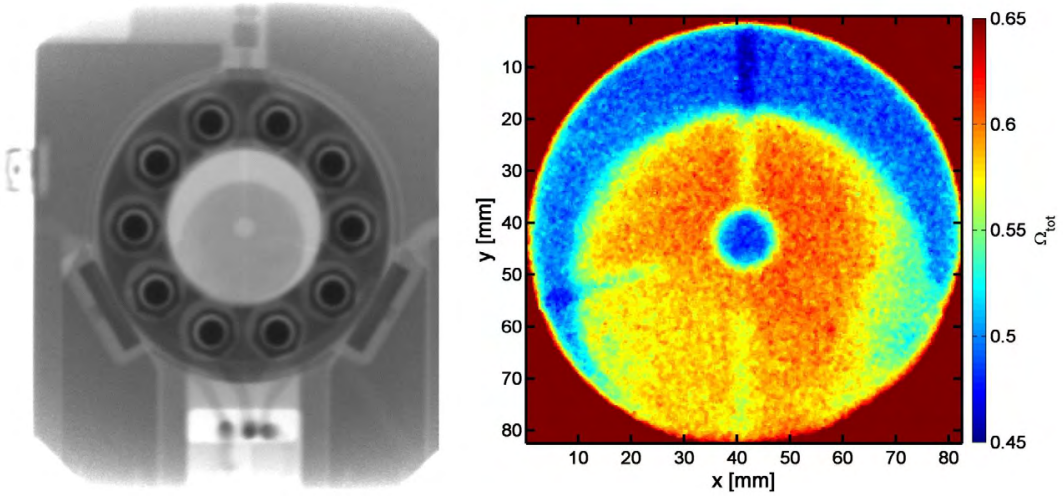

Figure 5.27: Left: Neutron Radiography of a 60 mm Li-RHC pellet inside the FlexiStore tank, the intensity is scaled in gray values. Right: Total attenuation image derived from a region of interest showing the metal hydride pellet, scaled by pseudocolors. The blue color above the pellet corresponds to free volume inside the tank due to a reduced pellet diameter.

Due to a reduced pellet diameter of 60 mm there is a significant void volume inside the tank, corresponding to absolute beam attenuations of about $\frac{1}{2}$. The attenuation contrast in terms of bright lines corresponds to the hydrogen supply line and temperature sensors, respectively. The circular center contrast is due to the indentation for the sinter metal filter and the accordingly reduced tank wall thickness. As for the presence of a sinter metal filter with direct material contact a phase separation was observed [65], measurements are performed without any filter material. To prevent a potential blocking of the hydrogen supply line by $LiBH_4$, the pellet is enclosed within an aluminum jacket with a thickness of about 1 mm. Its contribution to the overall beam attenuation is non-significant and it is neglected for the following analysis. A reaction of $LiBH_4$ with the aluminum jacket was not observed.

5.5.1.2 Material packing density and temperature field

In contrast to the 77 mm diameter pellet in case of the sodium alanate study in section 5.4 the pellet here has no inner diameter. Hence, for a correct normalization procedure according to equation 5.11 in section 5.2.3 to derive the material distribution and packing density, the effect of non-homogeneous wall thickness has to be corrected. In contrast to the cylindrical symmetry of insets for temperature sensors and hydrogen supply, the wall thickness variation in the center exhibits a step function in the projection image. Consequently, a fit of the attenuation variation and a

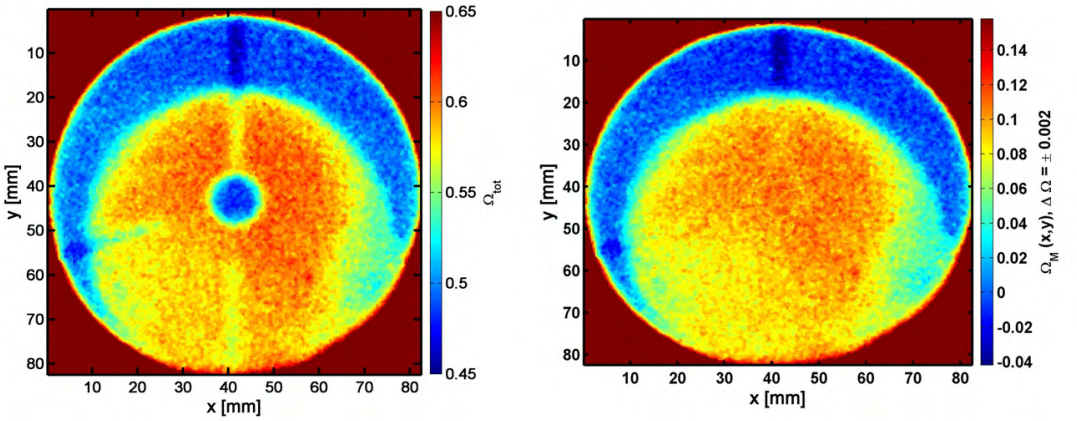

Figure 5.28: Left: Total attenuation distribution of an uncorrected reference image, the attenuation is scaled by pseudo colors. Right: Attenuation by material after correction of tank geometry effects and subtraction of tank background attenuation.

corresponding correction by Gaussian is not possible. Instead, the edge profile itself is used as described in section 5.2.3.1 for step geometries. Effects of temperature sensors and hydrogen supply are corrected by Gaussian fits as described in the first part of section 5.2.3.1. Additionally, the plain tank background is corrected as well as shown in section 5.2.3.1. In the right part of Figure 5.28 the resulting material attenuation distribution after tank geometry corrections is shown in addition to the total, uncorrected attenuation image in the left part of the Figure. Areas which are corrected by both, Edge Spread and Gaussian functions, are well embedded into the neighboring areas. At the right pellet boundary a low attenuation by the material is observed which is tantamount to a highly porous structure. Additionally, the pellet boundary deviates from purely radial symmetry in this area, indicating a partial, slight macroscopic structure loss. This will be discussed later on. For reasons of simplicity, this area is not considered within the normalization procedure for the calculation of the material distribution. The latter is derived as described in detail within section 5.2.3 and visualized in the left part of Figure 5.29. Here, the material packing density is calculated based on the assumption of an unchanged pellet depth, keeping its initial value of 6.4 mm. Accordingly, packing densities represent an upper limit since an expansion of the material during cycling is highly likely. Still, the relative distribution of packing density is correct and significant inhomogeneities are observed. Highest densities are found in the upper pellet part of about 1.3-1.4 g/cm^3. As already mentioned, at the right pellet boundary the densities are approximately halved with about 0.7 g/cm^3, indicating a highly porous structure. In the lower right area moderate densities of about 1-1.1 g/cm^3 are found. For this area also the lowest temperatures are observed

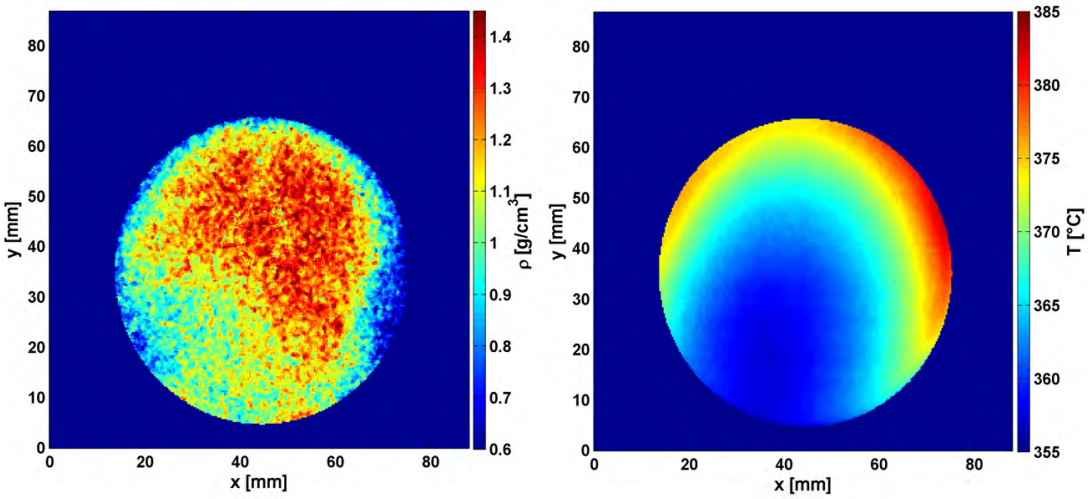

Figure 5.29: Left: Distribution of material packing density based on the assumption of homogeneous pellet depth of 6.4 mm. The density is scaled by pseudo colors. Right: Approximation of the steady state temperature field of the Li-RHC pellet derived by IR-Thermography of the tank surface.

for an equilibrium temperature field as shown in the right part of Figure 5.29. As described in section 4.3 the temperature field is acquired by an IR-Thermography measurement of the steady-state temperature field on the tank surface. The temperature field is cropped to the region of interest, namely the metal hydride pellet. As in the case for sodium alanate the influence of the reaction enthalpy corresponding to the absorption of hydrogen is low due to the limited flow of hydrogen for reasons of time resolution. Thus and against the background of high measurement accuracy as shown in section 5.1, the temperature field on the tank surface is assumed to be a good approximation for the temperature field within the metal hydride bed. Due to the non-homogeneous heating setup the temperature field shows significant temperature gradients and spatial differences. Lowest temperatures are found in the lower pellet area with T$\in$ [356-358] °C while highest temperature are found at the right boundary of the pellet with T $\approx$ 380 °C, corresponding to highly porous packing densities. The maximum temperature gradient is about 0.8 K/mm. In contrast to the sodium alanate study, where the temperature field was homogeneous and no effects on kinetics and hydrogen distribution have been observed (section 5.4.5), a significant influence of the temperature field on the absorption process and distribution of hydrogen is expected for the Li-RHC system.

5.5.1.3 Time resolved hydrogen distribution - material motion

By using the thermodynamic quantities temperature and pressure the normalized hydrogen content is calculated according to equation 4.1 in section 4.2.1. Its time evolution is shown in the left part of Figure 5.30 together with the hydrogen pressure evolution. After about 4 h the absorption converges into a plateau, with a corresponding hydrogen content of about 7.9 wt.%. The theoretical maximal capacity for the system composition is 11.2 wt.%. Hence, the deviation is about 30 %, which is also reported for other scaled-up storage systems as reported by Jepsen [65]. The beam attenuation difference due to the absorption of hydrogen is calculated as shown in section 5.2.1. Its correlation to the amount of absorbed hydrogen, normalized by the pellet area is given in the right part of Figure 5.30. A linear correlation with a proportionality constant of 2.8±0.1 cm^2/mol is observed, which is in perfect agreement with the correlation derived for sodium alanate inside the aluminum tank for the same instrument setup[19] as shown in Figure 5.6, section 5.2.1.2. Thus, the time and spatially resolved hydrogen distribution is derived by the normalization procedure according to section 5.2.2 by combination of thermodynamic quantities and beam attenuation difference. Using the material packing density distribution given in Figure 5.29 the time-resolved, normalized hydrogen content distribution is calculated. It is shown in

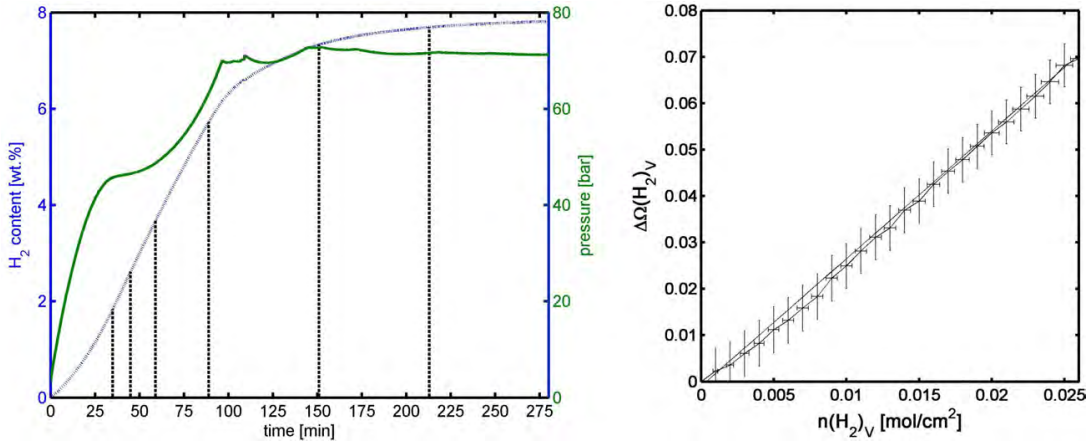

Figure 5.30: Left: Time evolution of normalized hydrogen content (left y-axis) and pressure (right y-axis) for the absorption process of the scaled-up Li-RHC pellet. The vertical lines correspond to selected time steps for hydrogen distribution images (Figure 5.31) and multi-correlation maps (Figure 5.33). Right: Correlation of the total attenuation by hydrogen ($\Delta\Omega(n(H_2)_V)$) and absorbed amount of hydrogen, normalized by area. The linear regression is shown additionally as a straight line plot.

[19] In contrast to the standard instrument setup, an additional B_4C filter was used as in the case of the aluminum tank study in section 5.2.1.2.)

Figure 5.31 for selected time steps of t = [35,45,59,89,151,213] min. The time steps are

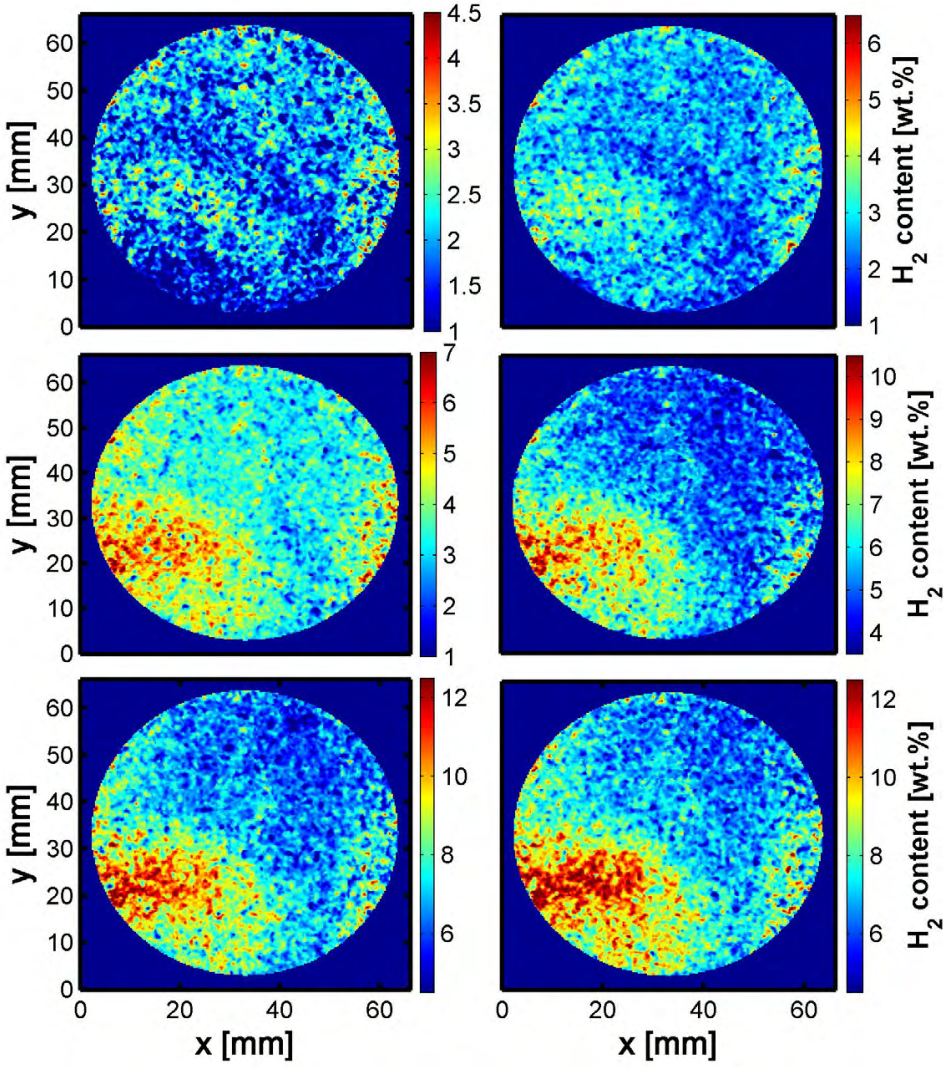

Figure 5.31: Normalized hydrogen distribution inside the pellet shown for time steps of t = [35,45,59,89,151,213] min (starting in the upper left, ascending row-wise) according to the vertical lines in the left part of Figure 5.30.

indicated in the overall hydrogen content evolution in Figure 5.30 by vertical, dashed lines. The corresponding sequence of the spatial hydrogen distribution in Figure 5.31 is row-wise from left to right, the first time step for t = 35 min is visualized in the upper left. Here, a rather homogeneous distribution of hydrogen within the metal hydride bed is observed. Still, the content is enhanced at the right pellet boundary corresponding to lower packing densities. With proceeding absorption there is an evolution of a distinct hydrogen concentration spot in the lower left pellet area. For the time step t = 151 min hydrogen contents are derived that are above the theoretical

maximum! Taking into account that the difference attenuation by hydrogen averaged over the whole pellet volume according to Figure 5.30 is linear, observed phenomena of high hydrogen contents are **not** due to a failure of the normalization procedure. Instead, the only possible explanation is a violation of the basic assumption of a constant material distribution according to equation 5.1 in section 5.2.1 and therewith the evidence of material transder in the system! Thus, the calculated hydrogen contents are pseudo-contents since there is a superposition of attenuation changes caused by hydrogen absorption and material transfer. Concerning the latter, there is in principal the possibility of combined material transfer of $LiBH_4$ and MgH_2, LiH or MgB_2. However, there is no visible macroscopic structure loss by deformation of the pellet since it still exhibits a radial symmetry in the acquired projection images. Accordingly, in the following the detected material transfer is assumed to be exclusively due to material transfer of the only liquid phase present - $LiBH_4$. When the absorption reaction converges into a plateau and quasi-equilibrium[20], the effect of material transfer is still present as indicated by persisting pseudo-contents in the last image of Figure 5.31.
With use of methods developed in section 5.3.1 the motion distance and involved material mass can be estimated. For calculation of the motion distance, a selective binning as visualized in Figure 5.14 is used. For the present study, a radial binning with its origin at the hydrogen pseudo-content spot is used, shown in the left part of Figure 5.32. The binning radius is enlarged until condition 5.26 is fulfilled and no pixel is present with corresponding hydrogen content higher than the theoretical maximum. The derived radius and pixel size directly depends on the maximal theoretical hydrogen content. The theoretical maximum for the sample composition investigated here is 11.2 wt.%, which corresponds to a binning radius and therewith to a motion distance of 5 mm. However, Li-RHC systems under real experimental conditions so far never reached their theoretical capacity. For lab-scale samples with an amount of several mg there are deviations of about 10-20 % reported in literature. Even worse, for scaled-up systems the deviation is reported to be about 30 % for 6× cycled powder samples [65]. To consider this broad range of system capacities, in the right part of Figure 5.32 motion distances for different realistic hydrogen content maxima are shown. For low content maxima of 9.5-10 wt.% the observed motion of $LiBH_4$ and phase separation might already partially be the reason and therewith these motion distances are less probable. However, it can be concluded that the motion distance is at least 5 mm, which corresponds to the maximal theoretical system capacity. Still,

[20]Since at given conditions for temperature and pressure the purely absorbed state with full conversion of components is thermodynamically favored, reaction rates have to be seen against the background of $\lim_{t\to\infty}$, in which full conversion should be reached and which demarks the true equilibrium. Hence, there are kinetic barriers that lead to the plateau in Figure 5.30, which is therewith a quasi-equilibrium.

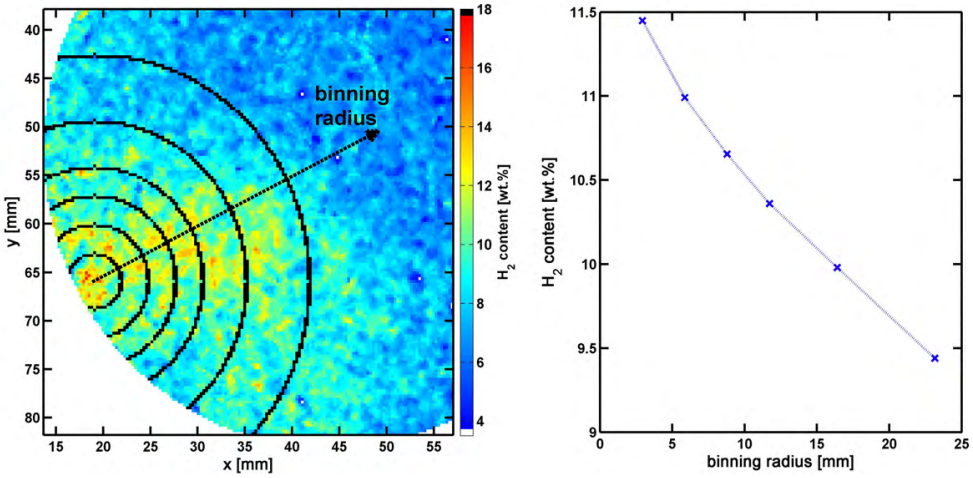

Figure 5.32: Selective binning for estimation of the motion distance. Left: Different radii of radial binning with origin at the pseudo hydrogen concentration spot at the pellet boundary. Right: Normalized hydrogen content for the binned area and corresponding estimated motion distance. The data points correspond to the different binning radii in the left part of the Figure.

this represents the lower limit since the origin of motion is not known and cannot be addressed. Based on these considerations, a larger motion distance is highly likely.
In addition, it is possible to estimate the amount of material that is involved in motion by use of equations 5.27 and 5.28. The attenuation by Lithium and Boron can be neglected for the fission neutron energy spectrum at NECTAR and therewith the excess mass of hydrogen given by equation 5.28 directly gives the corresponding amount of $LiBH_4$ contributing to motion:

$$m_{LiBH_4,mov} = \frac{m_{mov}}{r_{H_2,LiBH_4}} \tag{5.35}$$

where $r_{H_2,LiBH_4} = 0.185$ is the mass ratio of hydrogen and $LiBH_4$. Calculated quantities are listed in table 5.4. As does the motion distance, the amount of material depends on the assumed maximal theoretical hydrogen content. The quantities shown in Figure 5.32 are used again for mass estimation. In the last column of table 5.4 the ratio of the total mass of $LiBH_4$ in the sample and the mass of $LiBH_4$ contributing to motion is given. Depending on the assumed maximal theoretical hydrogen content, about 0.4-2.3 % of the total formed $LiBH_4$ is involved in motion. Again, this represents the lower limit due to the limited spatial resolution. For the correlation of material packing density, temperature field and hydrogen content a multi-correlation analysis is performed as introduced in section 5.2.5. It is shown in Figure 5.33 for the

Table 5.4: Estimated material amount of $LiBH_4$ involved in motion, $m_{LiBH_4,mov}$, ratio of moving $LiBH_4$ to the total mass of $LiBH_4$ in the sample for different maximal hydrogen contents, $wt.\%_{max}$.

$wt.\%_{max}$	$m_{LiBH_4,mov}$ [mg]	$\frac{m_{LiBH_4,mov}}{m_{LiBH_4,tot}}$ [%]
11.2	36	0.4
10.99	46	0.5
10.65	65	0.8
10.35	88	1.0
9.45	196	2.3

same time steps that where selected for the hydrogen content evolution according to Figures 5.30 and 5.31. The time series is sequenced row-wise, starting from the upper

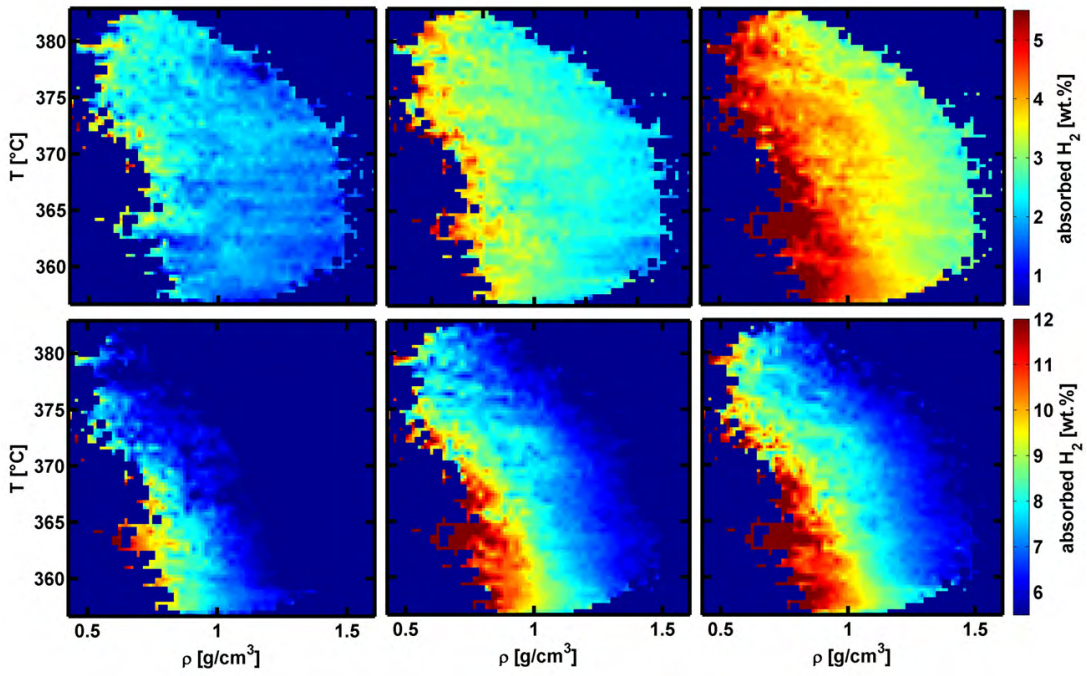

Figure 5.33: Multi-correlation maps of temperature, material packing density and average normalized hydrogen content (scaled by pseudo colors) for selected time-steps of t = [35,45,59,89,151,213] min (starting in the upper left, ascending row-wise) according to the vertical lines in the left part of Figure 5.30

.

left image. In the beginning of the absorption process a correlation as already known from the absorption of solid sodium alanate according to Figure 5.23 in section 5.4.5 is observed. Kinetics is enhanced for areas of lowest packing density, corresponding to the left boundary lines of the correlation map. In contrast to the sodium alanate

study, the temperature field gradient is significant and kinetics is positively correlated to the temperature. Accordingly, highest hydrogen contents are observed in the upper left area of the first correlation map in Figure 5.33. With further proceeding absorption, correlations change: correlation maps 2 and 3 show a transition towards an enhanced hydrogen content for packing densities of $\rho \in$ [0.75-0.95] g/cm^3. Transition lines for different hydrogen contents are not vertical as in the case of the sodium alanate study (compare Figure 5.23, section 5.4.5) but inclined, seemingly indicating a negative correlation of temperature and hydrogen content. However, the results have to be interpreted considering a transfer of material from which the following working hypothesis can be drawn: With initial forming of $LiBH_4$ in the right pellet boundary area corresponding to high temperatures and low material packing densities and further proceeding absorption, the liquid phase is attracted by a solid matrix framework that provides the ideal porosity to allow for surface energy minimization and wetting, assuming a good wettability of $LiBH_4$ on the solid compounds MgH_2, MgB_2 and LiH. The driving force for material transfer are capillary forces. For high packing densities the amount of wetting fluid is low with respect to the solid matrix material amount due to the low provided porosity. The optimal packing density is derived as the one where attraction points of motion are observed in the multi-correlation map in Figure 5.33, which is as mentioned $\rho \in$ [0.75-0.95] g/cm^3. A probable source of material transfer is the right pellet boundary area with low porosity and high temperature. The latter enhances mobility of the liquid due to the correlation of diffusion and temperature according to Fick's law [41] and the temperature dependency of viscosity [96]. This might be the reason for the low hydrogen content in this area with further proceeding absorption. As a consequence of the liquid phase present in the Li-RHC system, the standard and reasonable correlation as it was derived in section 5.4.5 for purely solid system compositions like sodium alanate is no longer valid! To investigate the 3D structure of the hydrogen distribution and to clarify, whether high hydrogen pseudo-contents are due to possible surface effects a combined Neutron Tomography study is performed, which is shown in the following.

5.5.1.4 Combined Neutron Tomography - 3D structure

Before performing an in-situ absorption study a Neutron Tomography investigation of the desorbed state was carried out to derive the 3D material distribution and packing density. After the absorption process, again a Tomography analysis is performed. Both studies have been performed at room temperature without thermal insulation at a hydrogen pressure of 2 bar. The same measurement parameters have been used for both Tomography measurements for reasons of comparability. In total, for each

Tomography 375 projections have been acquired with corresponding projection angles distributed over 360°at an exposure time of 120 s. The sample position is kept unchanged between the two measurements and no effect of thermal expansion has to be considered due to the ex-situ, room-temperature state of the system in de- and absorbed state. Hence, projection data sets can be combined directly and the ratio of intensity distributions[21] for the ab- and desorbed state is computed for every projection step. This "new" projection data is then reconstructed using the software OCTOPUS [26] to derive the attenuation difference caused by hydrogen absorption. This is shown in Figure 5.34, where in the left part an overview image is plotted for reconstructed data corresponding to the desorbed state. The volume data is clipped to

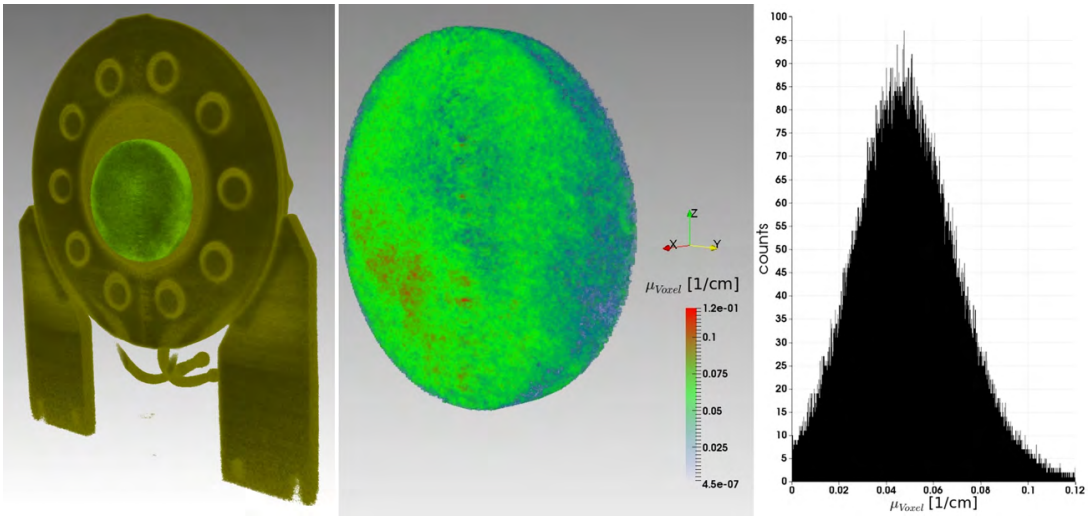

Figure 5.34: Left: Overview image of reconstructed data of the desorbed state showing the tank geometry. The latter is clipped to visualize the metal hydride pellet in the tank center. Visualization of data was done with *VGStudio Max* [48]. The center image shows the spatial distribution of voxel attenuation coefficients for the pellet region of interest of the combined data set, it is quantitatively scaled by pseudo colors. Right: Corresponding histogram with voxel attenuations.

visualize the inner part of the FlexiStore tank containing the metal hydride pellet. In the center part of the Figure the pellet is selected as region of interest. Here, the distribution of voxel attenuation coefficients, μ_{Voxel} of the reconstructed combined data set is shown, representing the spatial distribution of the attenuation by hydrogen. The right part of the Figure shows the corresponding histogram, with voxel attenuations sorted into 2^{16} equally distributed bins $\in [0,\mu_{max}]$. For quantification of the hydrogen content distribution, the procedure is in full analogy to the 2D-case carried out before. A normalization procedure as introduced in section 5.2.2 is performed, but extended

[21] The intensity distributions are normalized by the flat field and corrected for the dark image.

to 3D with the sum covering all voxels instead of pixels. Referring to Figure 5.34, the normalization constant is the quotient of the total amount of absorbed hydrogen and accumulated histogram according to equation 5.9. The normalization method is valid since the correlation of the attenuation difference by hydrogen and the corresponding amount of substance was proven to be linear as shown in Figure 5.30. For the hydrogen content in each voxel normalized by the corresponding material mass, an analogue normalization is done for the desorbed state data set by use of the total pellet mass, again in full analogy to the 2D case with summing here over 3D voxel data instead. The resulting quantitative distribution of hydrogen contents is visualized in Figure 5.35. In the left part, the total pellet volume is shown. As indicated

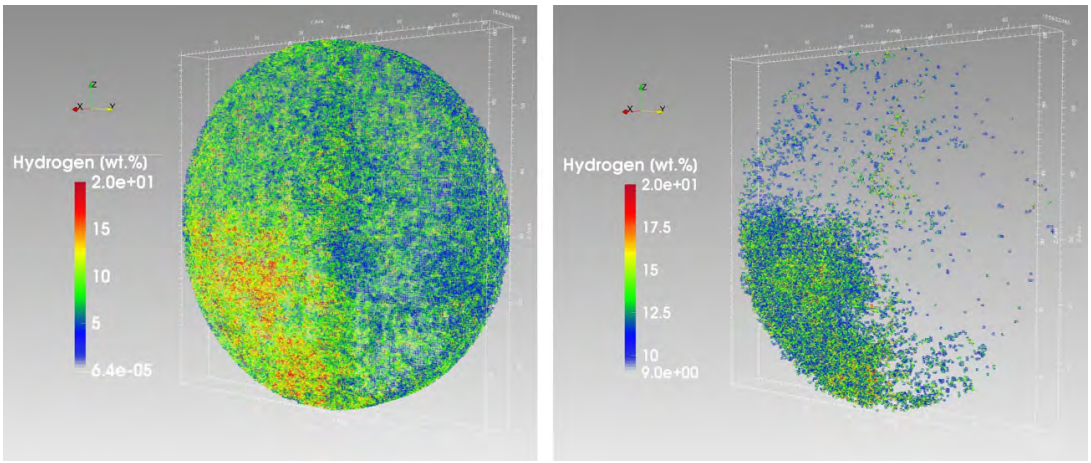

Figure 5.35: Volume data set for the spatial distribution of the normalized hydrogen content, scaled by pseudo-colors. Left: Full volume data set. Right: Applied threshold, showing only voxels with a corresponding normalized hydrogen content $\geq$ 9 wt.%.

by the colorbar, the hydrogen content reaches values up to 20 wt.% that are located in the lower left pellet area. In the remaining area, values are significantly lower. In good agreement with results from in-situ Neutron Radiography, lowest hydrogen contents are observed at the right pellet boundary. Thus, a combined Tomography analysis of ab- and desorbed state confirms a motion of material by the presence of hydrogen pseudo-contents higher than the maximal theoretic capacity! In the right part of Figure 5.35, the volume data set is thresholded to exclusively derive the spatial distribution of hydrogen contents equal or higher than 9 wt.%. As visible, the location of voxels is predominantly in the as mentioned lower left pellet volume, indicating no limitation to the surface. Single, isolated voxels that are spread over the whole pellet volume are corresponding to artifacts due to the low contrast in the combined projection data set. However, a more accurate investigation of the axial and radial distribution can be derived by an analysis of xz-slices for different y positions, where

x is the projection direction in parallel to the neutron beam. This is shown in Figure 5.36 for 6 slices at different x-positions. The viewing direction is along the negative

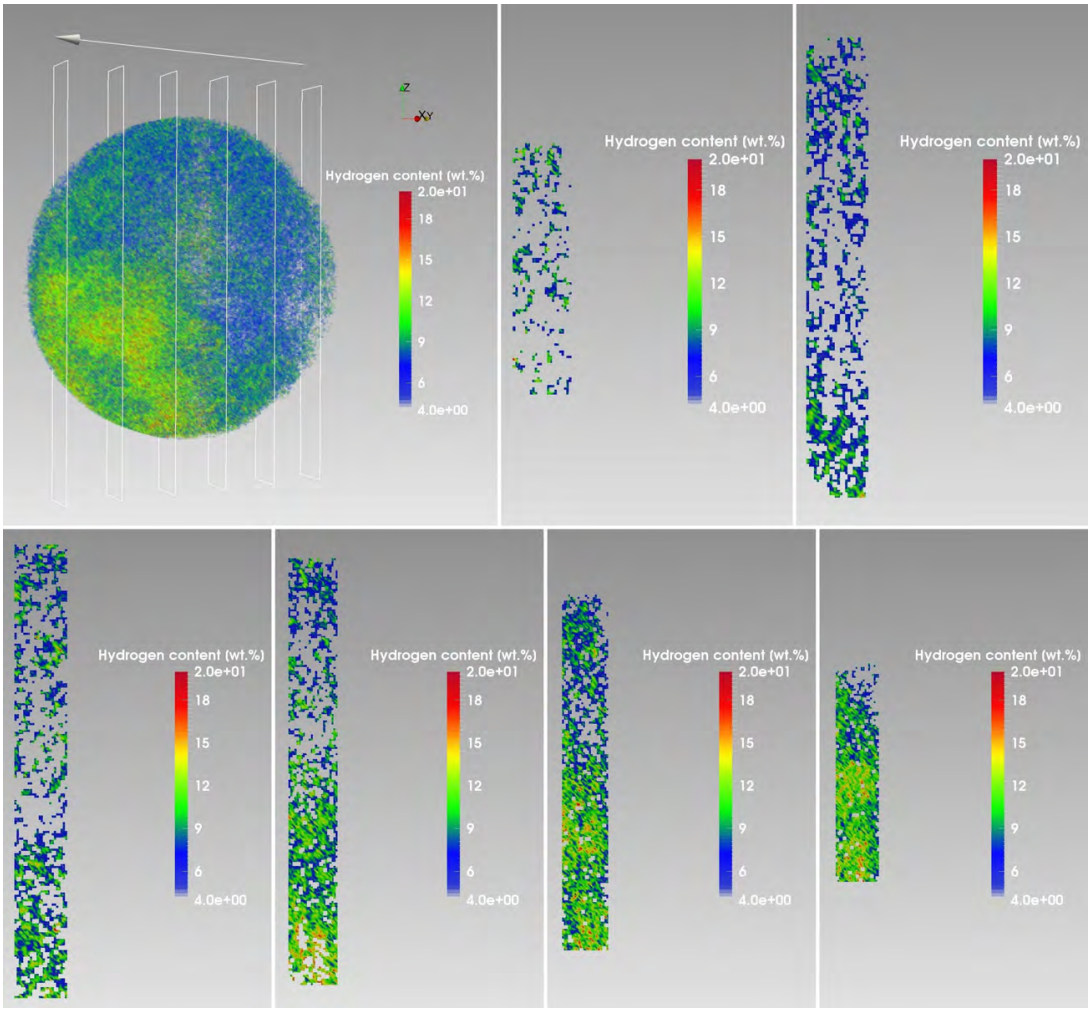

Figure 5.36: Distribution of the normalized hydrogen content in (x,z)-slices. The upper left image shows the volume data set of the pellet, with (x,z)-slices for different y-positions indicated by the white rectangles. The slice data is shown starting from the upper middle, ascending row-wise in the sequence indicated by the arrow within the overview image.

y-axis and the sequence of slices is indicated by the arrow in the overview image to the upper left. The first slice is given in the middle of the upper row and the following slices are sequenced row-wise. The concentration spot of hydrogen contents in the lower left pellet volume is again clearly visible in slices 3 to 6. Quantitative values are most frequent in the range of 12-14 wt.%, being slightly higher than in case of the in-situ Radiography study. Additionally, distinct spots of hydrogen contents of about 18 wt.% are observed, in particular for the last two slices corresponding to the left pel-

let boundary. Still, there is general agreement of 2D projection and 3D Tomography data. The absolute, quantitative differences are discussed again in section 5.5.3. As the main benefit from slice data analysis, it can be proven that pseudo-content spots are not due to surface effects since a rather homogeneous distribution in axial (x-) direction is derived. From that it can be deduced that the directed mass transport by motion of $LiBH_4$ towards the lower left pellet boundary is equally distributed in axial pellet direction. This is in good agreement with the formulated working hypothesis, in which capillary forces are causing a motion of liquid $LiBH_4$ to minimize the surface energy by wetting of the solid matrix framework. From the time evolution of the hydrogen content in Figure 5.31 and multi-correlation analysis in Figure 5.33 it can be concluded that high pseudo-contents of hydrogen are due to a directed motion of $LiBH_4$ towards a material packing density of $\rho \in [0.75\text{-}0.95]$ g/cm^3. This density seems to provide the best porous framework for agglomeration and wetting, thus attracting mass transport of $LiBH_4$. The distribution of the material packing density in the pellet is essentially determined by the compaction process itself. It is in first approximation homogeneous in the axis that is perpendicular to the compaction direction, which is the axial pellet direction in this case. Accordingly, a homogeneous distribution of $LiBH_4$ along the axial pellet direction is expected since it exhibits the same packing density and provides the same porous framework. This is well confirmed by results derived by slice analysis as shown in Figure 5.36 as discussed above. Based on the results of both, in-situ Neutron Radiography as well ex-situ Neutron Tomography, the following mechanism for the absorption process of scaled-up Li-RHC compacts is proposed:

1. With beginning of the absorption the system composition is predominantly pure solid state, therewith the correlation of material packing density and reaction kinetics is the same as for the solid-solid sodium alanate system and it can be stated in general for solid-solid systems: lower packing density and increased porosity enhances reaction kinetics. Possible reasons have been already worked out in section 5.4 and refer to increased hydrogen diffusion and, most important, permeation rates. Additionally, there is a positive correlation of kinetics and temperature, where the latter contributed to e.g. enhanced diffusion and permeation rates as well.

2. With further proceeding absorption the amount of liquid $LiBH_4$-phase is continuously increasing, accompanied by an induced motion that is driven by capillary forces present for the porous solid framework due to surface energy minimization and wetting of solid phases. The wettability is assumed to be good since no macroscopic expulsion of liquid phase is observed. The present porous frame-

work in the pellet is inversely related to the material packing density that is defined by the compaction pressure during pellet manufacture. Capillary forces are as well inversely correlated to pore diameters [11, 53] and therewith areas of maximal attraction are areas of highest packing density. However, the total amount that can accumulate within these areas is limited.

3. Ongoing absorption and further increasing amount of liquid $LiBH_4$ lead to a partial expulsion of excess $LiBH_4$ out of areas with high packing densities. The optimal porous framework that provides best compromise of free volume and capillarity is determined to exhibit a packing density range of $\rho \in [0.75\text{-}0.95]$ g/cm^3. This is reasonable since it coincides with the maximal theoretical packing density of the absorbed state, which is 0.83 g/cm^3 for the given system composition based on solid material compounds.

4. In the final absorption state an accumulation of $LiBH_4$ is observed at as-mentioned packing densities. Due to the compaction process the packing densities are homogeneous in the direction perpendicular to the compaction direction. Accordingly, $LiBH_4$ is distributed homogeneously in the axial pellet direction.

Most important is that motion of $LiBH_4$ during the absorption process occurs over long distances of at least 5 mm and affects at least about 1 % of the total material. The material transport within the pellet is expression of a long-range phase separation process. The reversibility of material transfer during the desorption reaction is questionable due to the long-range motion distances. The observed phase separation is probably the reason for the degradation of capacity over cycling as reported by Jepsen [65]. Though material transfer and liquid phase are present, no macroscopic structure loss is observed, except for the small shape-deviation at the highly porous area briefly described in the beginning. Thus, after the initial compaction process the solid compounds consisting most dominantly of Magnesium Hydride seem to form a stable framework during the sorption processes, still providing a sufficient porosity to allow for agglomeration and motion of liquid $LiBH_4$.

With evidence of phase separation and mass transport by motion of $LiBH_4$ on a macroscopic dimension, there is a strong need for a more detailed analysis on the fundamental aspects of motion of $LiBH_4$, its phase transition and effects due to melting. This is done in a detailed and intensive manner in the following section.

5.5.2 Mobility of $LiBH_4$ in $LiBH_4$-MgH_2

For a precise investigation of the fundamental properties and dynamics of liquid $LiBH_4$ within the solid phase there is the need for higher spatial resolution and in particular the need for a phase sensitiveness towards the $LiBH_4$ phase. The spatial resolution that can be achieved by use of fission neutron spectra is limited to the order of mm and is thus not sufficient. An increase of resolution to the order of micrometer is possible by a change of the neutron energy spectrum to the cold regime, which is provided by the ANTARES instrument as described in section 4.1.2. Considering the required phase sensitivity, the method of isotope labeling that was developed in section 5.3.2 can be applied. In the following sections a comprehensive study on $LiBH_4$ and its distribution and motion inside the solid matrix is carried out. The combination of spatial resolution and phase sensitiveness reveals fascinating new insights into the fundamental properties of the Li-RHC system, heavily impacting also strategies for future scale-up in terms of application.

5.5.2.1 Experimental and measurement setup

To ensure sufficient neutron beam transmission and data statistics, the mixture 1:1 of $LiBH_4$ and MgH_2 is used instead of the normal 2:1 mixture that was used for the study of the scaled-up system above. The potential effects of the changed composition are discussed later on. The samples are placed in the aluminum inset within the small cell sample holder as described in section 4.2.3. Due to potential effects of compaction and in order to focus on the fundamental interactions, loose powder samples are used. To study explicitly the dynamics of the $LiBH_4$ phase, isotope labeling of this phase is used. This method is introduced and explained in detail in section 5.3.2 with the natural composition of $LiBH_4$ containing the highly absorbing isotopes Li-6 and B-10. The investigations were performed at the ANTARES instrument at FRM II to provide the necessary cold neutron spectrum [120]. To get the best compromise between spatial and time resolution the standard setup with pixel size of 73.2 μm is used, the exact specifications are given in section 4.1.2. The exposure time for each Neutron Radiography is 26 s. In Figure 5.37 the sample setup at the instrument is shown where the sample cell with the attached thermal insulation and nozzle heater is positioned in front of the LiF-ZnS scintillator (shiny, in the left part of the Figure). In front of the sample a Boron rubber is placed with an opening matching the relevant sample field of view. This is to prevent a CCD camera pixel overflow corresponding to the flat field region for long exposure times.

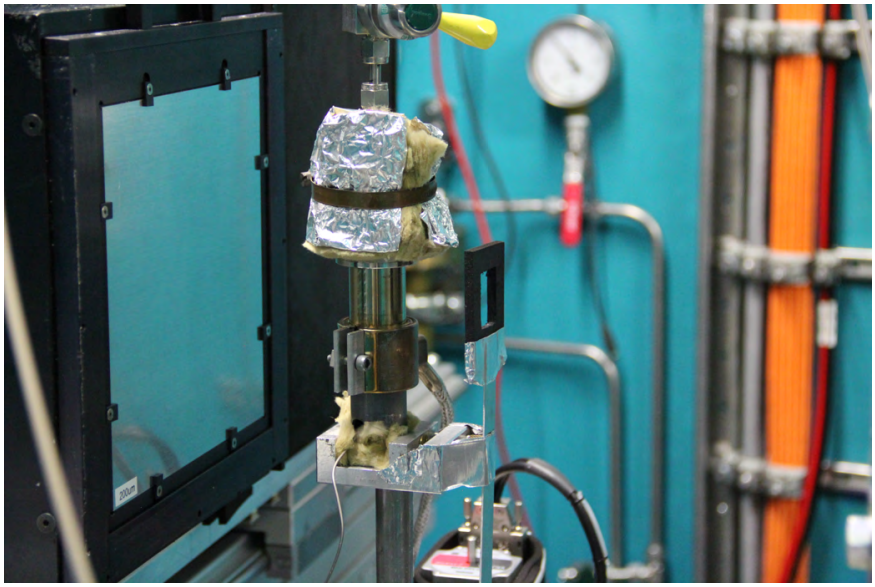

Figure 5.37: Measurement setup for the small cell at the ANTARES instrument, showing the sample with attached nozzle heater and thermal insulation in front of the scintillator unit (to the left). Additionally a black Boron rubber is used to prevent a CCD camera pixel overflow for long exposure times.

5.5.2.2 Initial liquefaction of $LiBH_4$

In first stage, the effect of initial liquefaction of $LiBH_4$ on the material structure of the total composite is investigated. The material packing distribution of the as-prepared sample is shown in the total attenuation image in the total left of Figure 5.38. The natural composition with highly absorbing Li-6 and B-10 is in the left part of the sample holder, to the right is the isotope composition. The structure is typical for a loose powder bulk density with low packing density, which is given in table 5.5. The attenuation image was calculated from a Neutron Radiography at conditions corresponding to the solid phase of $LiBH_4$, namely at a pressure of 13 bar and a temperature of 200 °C. To induce liquefaction of $LiBH_4$, the temperature was increased to 350 °C and the pressure was kept constant. At a temperature of T = 275 °C Lithium Borohydride starts to

Table 5.5: Parameters for loose powder samples investigated by the isotope-labeling technique and effect of first liquefaction of $LiBH_4$ on the macroscopic powder density.

	Li-RHC	Li-RHC$_{iso}$
mass [mg]	75 ± 0.1	45 ± 0.1
ρ_{Powder} - initial $[g/cm^3]$	0.58 ± 0.02	0.39 ± 0.03
ρ_{Powder} - liq $[g/cm^3]$	n.a.	0.5
density increase by phase transition [%]	n.a.	30 ± 17

melt. This change of structure affects the total macroscopic structure of the composite, visualized in the middle and in the right image of Figure 5.38. The middle image shows the sample with $LiBH_4$ in liquid phase and after the changes of material structure, when the equilibrium is reached. In the right part a difference image is shown, the data set of the Radiography after liquefaction is subtracted from the dataset before liquefaction. The intensity of the attenuation difference, $\Delta\Omega_{tot}$, is scaled by pseudo colors. Values corresponding to $\Delta\Omega_{tot} < 0$ refer to a reduced attenuation in the system with liquid $LiBH_4$, which indicates a reduction of the material amount in this area. Hence, the material packing density is reduced as well. Vice versa, $\Delta\Omega_{tot} > 0$ refers to an increase of the material amount. Thus, the material packing density is increased for the corresponding area. The difference image indicates an increased packing in the main and center part of the sample, which is both due to radial contraction as well as due to contraction in height. The latter is most significant as can be seen by the pseudo coloring for $\Delta\Omega_{tot}$. In case of the natural composition (the left of the two samples) the change of material packing density or area density in case of a projection like it is here is much stronger pronounced than in case of the isotope-sample, as it is indicated by the difference data set in Figure 5.38. Accordingly, changes in attenuation on the top of the sample are more significant for the natural composition. From the difference image it can be stated that liquefaction of $LiBH_4$ induces a transformation of the overall macroscopic material structure. Within the framework of this change, the material packing density is significantly increased, which is estimated in table 5.5 by the absolute attenuation image after liquefaction. As visible in the difference image, there is a difference between Li-RHC and Li-RHC$_{iso}$ in terms of the structural change induced by liquefaction. The volume change of the Li-RHC$_{iso}$ sample is symmetric, since after liquefaction it still has a cylindrical symmetry. For the natural composition, a non-symmetric change is observed in the difference image with a kink visible in the difference data set at an y-position of about 8 mm, where the pillar is tilted differently above and below this kink. For Li-RHC$_{iso}$, the density increase is estimated to 30$\pm$17 %. The large measurement uncertainty originates from a reduction of the sample diameter that cannot be determined precisely with the given pixel resolution. Due to the non-symmetric sample boundary for the natural composition, the density increase cannot be quantified. Still, the overall density increase is lower than for the isotope-sample due to the higher initial powder density [22]

According to the difference image, the liquid $LiBH_4$ phase is not macroscopically separated from the Magnesium Hydride along the vertical axis since there is no evidence of a vertical gradient in the attenuation difference, $\Delta\Omega_{tot}$. Due to the rotational sym-

[22]The differences in initial powder packing density are due to different treatments during filling, e.g. by applied shaking to accumulate the powder in the sample holder bottom.

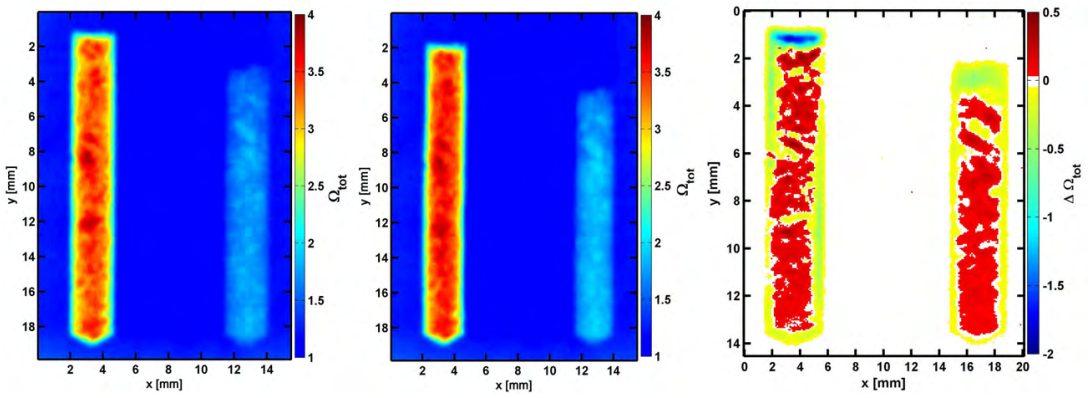

Figure 5.38: Left: Total attenuation of the natural sample composition with highly absorbing isotopes Li-6 and B-10 (left) and isotopically enriched composition (right) before the initial liquefaction of $LiBH_4$. Samples are stored within the small sample cell according to section 4.2.3. Middle: The analogue to the left, but after liquefaction of $LiBH_4$. Right: Difference attenuation image (liquid-solid).

metry of the sample cell, it is not possible to resolve or investigate a phase separation in the plane with its normal perpendicular to the projection direction. For that, a Neutron Tomography analysis is necessary, which is shown in the following sections. Due to the time-resolved imaging data the time interval of the sintering process during liquefaction of $LiBH_4$ can be derived. It is estimated to $\Delta t = 182 \pm 13$ s, after which no further changes in material structure are observed and equilibrium is assumed. Since the resolution is limited by the pixel size, any changes occurring on a scale smaller than the pixel size of 73.2 μm are not detected and the estimated sintering process time has to be interpreted as a lower limit. In addition to the change of material structure there is an additional change in attenuation by thermal expansion of the sample holder cell, which is estimated to 1.5±0.15 mm.

From the analysis of initial liquefaction of the $LiBH_4$ the following conclusions can be drawn:
Starting from an as-prepared powder bulk density, the first liquefaction of $LiBH_4$ results in a significant change of the overall macroscopic material structure accompanied by a denisfication of the material. Hence, the process can be described by liquid phase sintering [46], where by liquefaction of $LiBH_4$ and wetting of solid Magnesium Hydride particles capillary forces emerge that cause a densification of the system [69]. Porosity reduction is driven by minimization of surface energy [69]. Densification shows no preferential orientation except for a shrinking in z-direction due to the influence of gravity, as the sample volume is reduced in all spatial directions. Still, there seems to

be a dependency of the a posteriori structure on the explicit initial distribution of particles and agglomerates since a difference was found for the two investigated samples. This agrees with literature, where the amount of densification and the magnitude of rearrangement of structure depends on the size and shape of particles, as well as on the distribution of pores [67, 73]. Since the initial packing densities of natural and isotope composition samples differ significantly (see table 5.5), the different structures after sintering are reasonable. On time domain, sintering was found to reach equilibrium after already approximately 180 s. However, though there is presence of a liquid phase and a high degree of material transfer, no evidence of expulsion of the liquid phase is observed in the simple projection images derived by Neutron Radiography within the investigated time interval (Figure 5.38). This is in well agreement with the observed densification and confirms the process of sintering, which assumes a good wettability of the solid to allow for the emergence of capillary forces. A bad wettability and a corresponding high contact angle between liquid phase and solid would counteract densification [60, 86] and cause a macroscopic phase separation in height due to the lower density of the liquid phase, which is not observed. Consequently, the identification of sintering also indicates a good or sufficient wettablility of the Magnesium Hydride phase.
The observed densification as a result of sintering has important consequences for the development and design of hydrogen storage tanks: the initial volume occupied by loose powder filling will decrease significantly already after the first absorption, changing the material structure and reducing the interface area of metal hydride material and tank surface. This causes a reduced heat transfer and accordingly a worse overall performance of the storage system, since poor heat transfer of storage medium and surrounding tank material is one of the main hurdles for tank optimization [78].

5.5.2.3 Liquid state - clustering

Using isotope labeling in combination with Neutron Tomography analysis, it is possible to resolve the structure of $LiBH_4$ in the total sample composition in all spatial dimensions. This gives rise to a fundamental investigation of material properties, as shown in the following sections. Surprisingly, isotope labeling of highly absorbing isotopes has not yet been used in the Neutron Imaging community.

The starting point of investigation is the state of equilibrium after sintering of the material as described in the previous section. Therefore, a Neutron Tomography analysis has to be performed for the characterization of the liquid state, since the phase transformation in terms of solidification of $LiBH_4$ potentially changes the structure

(for that, see the following sections). To ensure a stable liquid state of $LiBH_4$, pressure and temperature are set to 15.5 bar respectively 357 °C according to conditions for the absorbed state of Li-RHC as given by its van't Hoff plot [75]. The temperature is controlled based on data given by the temperature sensor at the bottom of the aluminum fitting inside the sample cell as described in section 4.2.3. To resolve the full 3D material structure after initial sintering of $LiBH_4$, a Neutron Tomography analysis is performed. For that, the hydrogen supply has to be disconnected from the sample cell to allow a precise angular motion of the sample holder on the rotational axis. Though the material structure was found to have reached equilibrium, there is still a potential material transfer within a voxel since the determination of equilibrium is based on in-situ Neutron Radiography, averaging out an undirected motion inside the material in the projected volume. To minimize resulting motion artifacts in the reconstructed slices of the Tomography data set, the total time for a Tomography run has to be minimized. Consequently, the number of acquired projection images is below the Nyquist criterion, it was set to 375 for this study. In fact, this is a compromise between the influence by artifacts originating of motion and undersampling, since both negatively effect the quality of the reconstructed data [10]. The exposure time is t_{exp} = 26 s at a pixel size of 0.074 mm. Including the detector inherent time between two images and the adjustment of rotation angles a Tomography run was performed within 220 min. Within this time interval, temperature fluctuations were less than 1.5 °C so that effects on the structure or thermal expansion of the sample are negligible. The image processing and data reconstruction was standardized and done with the OCTOPUS software. It is briefly described in the appendix A.4. In the left part of Figure 5.39 an overview of the reconstructed and visualized data of the samples with natural and isotope composition is given in terms of the attenuation coefficient colored in gray values. The shown data was reduced to the volume of interest, the sample volumes, and thresholded to correct for voxels with an attenuation coefficient corresponding to the free gas volume inside and above the metal hydride powder. Thresholding involves a calculation of the attenuation coefficient for the sample environment, μ_E, which is dominated by gaseous hydrogen (since the sample volume is pressurized to ensure thermodynamic conditions appropriate for the absorbed state) and determined to μ_E = 0.5 1/cm[23]. In the left part of Figure 5.39 the sample with the natural composition is shown in the front, the back part shows the isotope sample. To show both samples simultaneously in one image, the gray values for the attenuation coefficient of each sample are scaled differently. Thus, no quantitative conclusions concerning the attenuation coefficient can be drawn from this overview image. Still, a first surface

[23]The threshold is derived from a reference area above the main sample volume for pure attenuation by gaseous hydrogen.

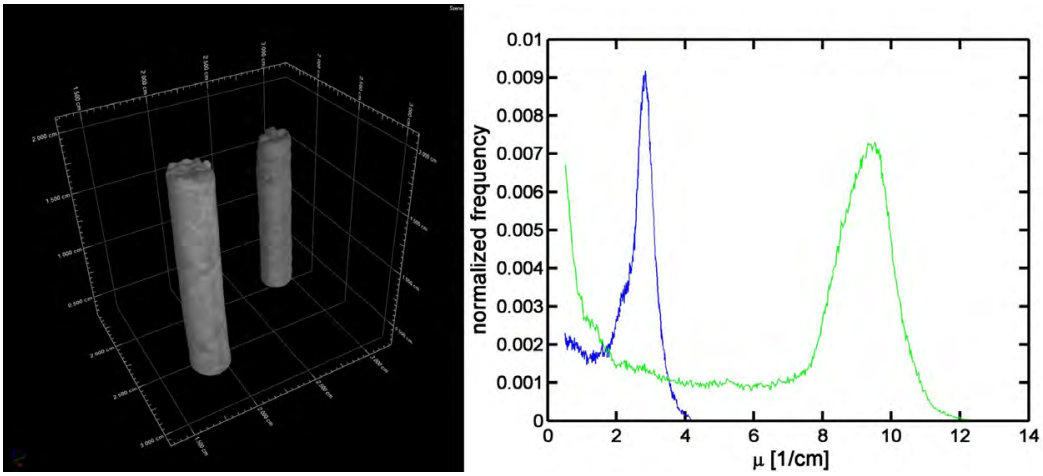

Figure 5.39: Left: Volume data set of attenuation coefficients for natural (front) and isotope (back) composition for the liquid state of $LiBH_4$ (T > 275 °C), derived by Neutron Tomography analysis. For simultaneous visualization of both sample compositions voxel for the two data set have been scaled individually by gray values. Right: Histogram of attenuation coefficients for the two sample compositions. The frequency is normalized by the absolute number of contributing voxel. The blue curve refers to the isotope sample, the green to the natural composition, respectively.

comparison is possible: Though approximately half of the total sample amount is in the liquid state and liquefaction of $LiBH_4$ caused a clear change of the macroscopic material structure (compare Figure 5.38), the top surface of the material is not smooth and plane but structured. This indicates a present MgH_2 structure, acting as a stabilizing matrix for the liquid phase which is in agreement with the results found for the sintering process from the 2D projection images, where a separation of phases could not be observed, hinting to a stabilizing Magnesium Hydride matrix. Still, surface structures differ less than 0.5 mm, which is the result of an initial homogeneity of material compounds MgH_2 and $LiBH_4$ achieved by material preparation in terms of high-energy ball milling. It can be assumed that the initial distribution of material compounds highly determines the structure after sintering as already stressed in the above section. Thus, the material preparation route becomes in particular important for the case of scaled-up storage systems.

The right part of Figure 5.39 shows histogram plots of the natural (colored in green) and the isotope composition (blue) for the frequency distribution of the attenuation coefficient of the whole sample volume. The attenuation coefficients are sorted into 512 equally spaced bins. The environmental threshold, μ_E, sets the left boundary to 0.5 cm^{-1}. The frequency values are normalized to the number of relevant voxels in

the sample, N, that is given by

$$N = \sum_{i=1}^{N_{tot}} \Theta\left(\mu_i - \mu_E\right)$$

, where N_{tot} is the total number of voxels in the volume of interest and μ_i is the attenuation coefficient of voxel v_i. The distribution of attenuation coefficients for the natural composition is shifted to higher values due to the highly absorbing isotopes Li-6 and B-10 in agreement with results of section 5.3.2. The average attenuation of the natural composition is determined to $< \mu >_{Li-RHC} = 6.69$ cm^{-1}, for the isotope composition it is $< \mu >_{Li-RHC_{iso}} = 2.35$ cm^{-1}. For the natural composition there is a significant frequency increase at the left boundary, which cannot be observed for the isotope composition. The reason might be an increased environmental attenuation coefficient, which will be discussed later on.

The full access to the 3D material structure that is given after reconstruction allows for a comprehensive analysis of the structure inside the material and gives unique insights into the sample composition in the liquid state after sintering, which is shown in the following. By processing the data set in terms of setting a threshold for the attenuation coefficient, μ_T, only voxels with a corresponding attenuation higher than the chosen threshold are visualized. If this is applied on the natural composition data set for the right flank of the attenuation coefficient distribution according to the right part of Figure 5.39, only highly attenuating voxels of the total volume are selected, which represent a high amount of $LiBH_4$ in the voxel composition. By that, concentration spots of the liquid phase within the sample can be visualized. This is shown qualitatively in Figure 5.40 for both the natural, highly absorbing composition (left part) and the isotope composition (right). The reference coordinate system is the lab coordinate system with x and z-axis scaled in mm, the attenuation coefficient for each voxel is scaled by pseudo colors as indicated by the colorbar to the right of each image. The threshold for the natural composition is set to $\mu_T = 10.41$ cm^{-1} respectively $\mu_T = 3.33$ cm^{-1} for the isotope sample. At this stage, the threshold is chosen in the way to visualize exclusively areas of high attenuation. The explicit threshold levels are discussed in the next subsection. As can be seen in the left part of the Figure, voxels with high attenuation coefficients corresponding to material with high amount of $LiBH_4$ form cohesive volume elements. In the following, these volumes of high concentration of $LiBH_4$ are denoted as 'cluster' and the corresponding threshold as μ_{TC}. The clusters are in first approximation homogeneously distributed in height with no preferential orientation. This holds as well for the isotope composition in the right part of Figure 5.40, where the distribution of clusters qualitatively looks similar.

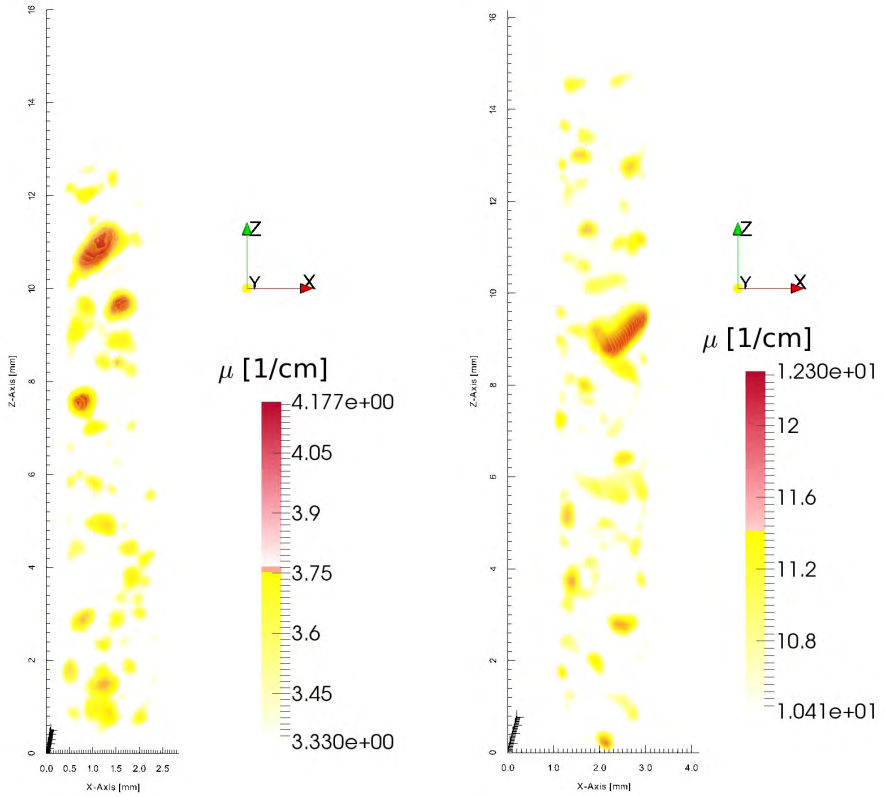

Figure 5.40: Cluster in the liquid state (temperature above 275 °C) revealed by thresholding of the data set. Left: Natural sample composition; visualization of voxels with attenuation coefficient $\geq \mu_T = 10.41$ cm^{-1}. Right: Isotope composition; visualization of voxels with attenuation coefficient $\geq \mu_T = 3.33$ cm^{-1}.

For the isotope composition the assignment of highly absorbing volume elements to a corresponding high concentration of $LiBH_4$ is not as distinct as for the natural composition sample: the difference in total attenuation between MgH_2 and $LiBH_4$ originates from incoherent scattering of hydrogen only. The contribution by metals Mg and Li is negligible, if isotope impurities in Li can be assumed to be non-significant.[24] Since the molar ratio of $LiBH_4$ and MgH_2 was chosen to 1:1 to ensure sufficient neutron beam transmission (as described in section 5.3.2), the attenuation of equi-molar $LiBH_4$ and MgH_2 differs only by a factor of 2. Additionally, the density of pure MgH_2 is approximately 2.2× higher than for $LiBH_4$. Thus, in case of clustering of pure Magnesium Hydride the expected total attenuation in a voxel is comparable to a corresponding pure $LiBH_4$. For the isotope composition sample, this makes it difficult to assign voxel

[24] In first approximation this is valid since the purchased isotopically enriched $LiBH_4$ has a purity of 99.8 % for Li-7. Furthermore, the amount of Li-6 in natural Li is only 7.4 %, which gives an effective, maximal impurity of 0.015 %.

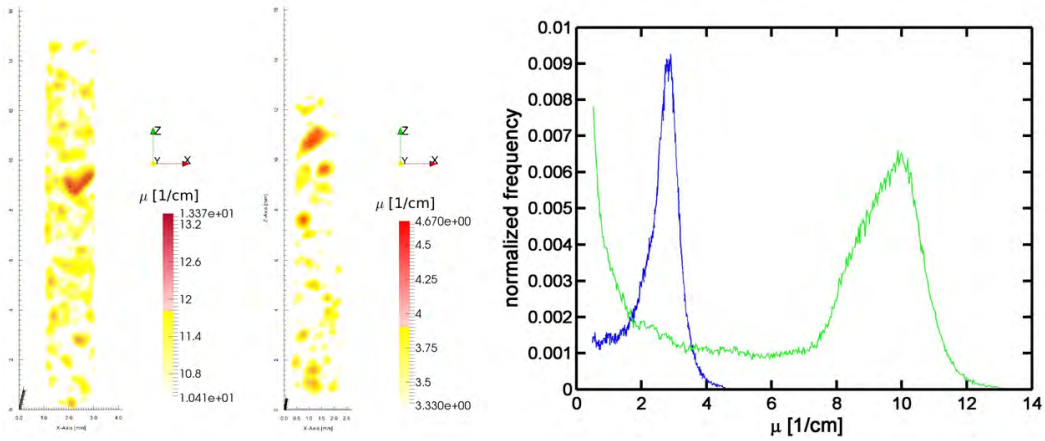

Figure 5.41: Cluster revealed by thresholding of the volume data in analogy to Figure 5.40, but for the solid state of $LiBH_4$ (temperature below 275 °C). Left: Natural sample composition; visualization of voxels with the attenuation coefficient $\geq \mu_T = 10.41$ cm^{-1}. Center: Isotope composition; visualization of voxels with the attenuation coefficient $\geq \mu_T = 3.33$ cm^{-1}. Right: Histogram of the full set of attenuation coefficients for the two sample compositions (no threshold exept for μ_E). The frequency is normalized by the absolute number of contributing voxel. The blue curve refers to the isotope sample, the green to the natural composition, respectively.

with corresponding high attenuation coefficient to a cluster of $LiBH_4$. The reason for clustering of the liquid phase and its spatial distribution is discussed later on.

To investigate the effect of solidification of $LiBH_4$ on the sample structure and the observed clustering, the temperature is reduced to 221.5 °C at a pressure of 13.1 bar.[25] This leads to a solidification of $LiBH_4$ at around 275 °C with the overall system still being in the absorbed state. The macroscopic density change of the total sample that is induced by solidification of $LiBH_4$ is estimated to about 4 % using the same techniques as for the study of the initial sintering. This is not further discussed here, details for macroscopic structure change due to solidification are given in appendix B.3. After reaching the thermal and structural equilibrium, again a Neutron Tomography study is performed with the same parameters as for the liquid state Tomography for reasons of comparability. Applying the same thresholds for the attenuation coefficient as for the liquid state, $\mu_{TC} = 10.41$ cm^{-1} (natural composition) respectively $\mu_{TC} = 3.33$ cm^{-1} (isotope composition), a similar clustering of $LiBH_4$ is observed, which is visualized in the left and middle part of Figure 5.41. In the right part the total histogram plot

[25] Since there is no connection to the hydrogen supply and a pressure loss due to leakage is negligible, the sample cell can be seen as a closed system. The reduction in pressure is directly caused by the temperature decrease.

of the frequency distribution of the attenuation coefficients for both natural (green) and isotope (blue) composition is shown. The number of bins is again 512, with an unchanged environmental threshold of $\mu_E = 0.5\ \mathrm{cm}^{-1}$. In comparison to the histogram for the liquid state shown in Figure 5.39, the right flank for both compositions is shifted to higher values for the attenuation coefficient.

5.5.2.4 Phase transition of $LiBH_4$ - density change & cluster determination

From this change of the histogram distributions it is possible to deduce a fundamental material property of $LiBH_4$: Since maximal values of the attenuation coefficient for the natural composition can directly be assigned to cluster of $LiBH_4$, the increase of attenuation is caused by a density increase of these cluster due to the solidification of $LiBH_4$. Thus, the phase transformation of $LiBH_4$ in terms of solidification is accompanied by an increase of material density and vice versa as it is a typical property of metals. Besides these qualitative results, it is also possible to quantitatively estimate density increase by solidification. To do so, the two Tomography data sets of liquid and solid state of $LiBH_4$ in the total mixture are compared. After reconstruction the distribution of attenuation coefficients is given, which is for a mixture of different compounds given as

$$\mu = \sum_i \frac{N_A}{M_i} \cdot \rho_i \cdot \sigma_i$$

which is already known from the theoretical section. In the case of a voxel containing only a mono-phase, which is assumed for voxel containing cluster of $LiBH_4$, the sum eliminates. Thus, the change of the attenuation coefficient is directly proportional to the change of density, which is the only non-constant quantity when comparing states before and after the phase transition. To be more precise, there is a potential, additional influence by the change of the elastic, coherent scattering cross section of $LiBH_4$ due to the emergence of a crystalline structure in case of solidification (Bragg scattering). Since the incoherent scattering cross section of hydrogen and in case of the natural composition especially the absorption cross section is dominant, the effect of potential Bragg scattering is neglected. Hence, it is

$$\rho_l = \rho_s \cdot \frac{< \mu_C >_l}{< \mu_C >_s}$$

where $\rho_{l,s}$ are the material densities and $< \mu_C >_{l,s}$ the averaged cluster attenuation coefficients of $LiBH_4$ in the liquid respectively solid state. The average cluster attenuation coefficient is a function of the chosen threshold for cluster determination, μ_{TC},

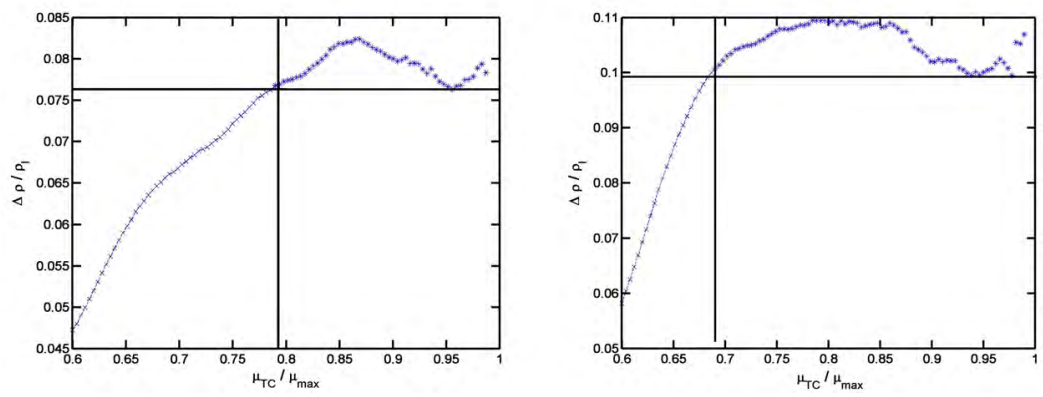

Figure 5.42: Evolution of the density change, $\Delta\rho/\rho_l$, depending on the cluster threshold ratio, μ_{TC}/μ_{max} for estimation of the density change of $LiBH_4$ corresponding to the phase transition (melting). Left: Natural composition. Right: Isotope composition. The assumed transition into a plateau is indicated by the two lines in the upper area.

and is derived by

$$< \mu_C >= \frac{\sum_{i=1}^{N} \mu_i \cdot \Theta\left(\mu_i - \mu_{TC}\right)}{\sum_{i=1}^{N} \Theta\left(\mu_i - \mu_{TC}\right)}$$

where μ_i is the attenuation coefficient of a voxel v_i within the sample volume. For low cluster thresholds, voxels contributing to the average cluster attenuation coefficient do not only contain $LiBH_4$ but Magnesium Hydride or pores as well. Since the latter are stable and undergo no phase transition for the conditions used in the two performed Tomography studies, the deduced density change is a pseudo density and underestimates the real density of pure $LiBH_4$. Thus, by continually increasing the cluster threshold, the pseudo density should converge to the real density. The evolution of the density change, $\Delta\rho/\rho_l = (\rho_s - \rho_l)/\rho_l$, depending on the cluster threshold is shown for both the natural (left) and isotope (right) sample composition in Figure 5.42. For real cluster with voxels containing only the mono-phase of $LiBH_4$, its solid state density is given by literature values, $\rho_s = 0.66$ g/cm^3 [134]. The cluster threshold is given as a relative quantity, it is normalized by the maximal attenuation coefficient of the solid state data set. As expected, the density change increases with normalized cluster threshold: starting from 0.6, it reaches a plateau at 0.8 with a corresponding density increase of 7.6 % for solidification in case of the natural composition. Going further on the abscissa, there is no more monotonic increase, the values fluctuate around an average of 7.9±0.25 %. The corresponding area in the plot is enclosed by the solid vertical and horizontal lines in the upper right area. The fluctuation is expression of measurement uncertainty and lower statistics for the right flank of the frequency

distribution of attenuation coefficients (see Figures 5.39 and 5.41). The convergence into a plateau agrees well with the theoretic considerations given before. Accordingly, for a normalized cluster threshold of 0.8, which corresponds to $\mu_{TC} = 10.74$ cm^{-1} for the solid state, voxels fulfilling these threshold condition can be assumed to contain purely $LiBH_4$[26]. Hence, the observed evolutions proves the existence of real cluster of pure $LiBH_4$, which where observed qualitatively in the upper section (Figures 5.40 and 5.41)! For the pure liquid phase in the natural composition sample, the solidification is accompanied by a density increase of 7.9±0.25 %. Accordingly, the liquid density is $\rho_l = 0.618\pm0.001$ g/cm^3. For the isotope composition in the right part of Figure 5.42, the general evolution is similar: starting again from a normalized attenuation of 0.6 and moving to higher values, the density change increases. However, it converges already at 0.69 to a density change of 10.5±0.25 %. The explicit normalized cluster threshold that denotes the transition into the plateau depends on the corresponding frequency distribution of attenuation coefficients as given in Figure 5.39 and 5.41. Therewith, it depends on the explicit material structure of the sample in terms of packing density, homogeneity of compounds and porosity. The derived density change for solidification is, however, of greater interest. With 10.5±0.25 % it is clearly higher than for the natural composition and though there is a significantly reduced distinguishability between Magnesium Hydride and $LiBH_4$, which should lead to a more complicated determination of $LiBH_4$ cluster as discussed in the upper paragraphs, the plateau in Figure 5.42 is distinct. The corresponding liquid density of $LiBH_4$ is $\rho_l = 0.603\pm0.001$ g/cm^3. In table 5.6 the derived values for the density change and absolute density of liquid $LiBH_4$ is summarized. The significant difference between

Table 5.6: Resulting liquid density of $LiBH_4$ and relative density change due to phase transition for both natural and isotope sample compositions.

	Li-RHC	Li-RHC$_{iso}$
ρ_l $\left[g/cm^3\right]$	0.618 ± 0.001	0.603 ± 0.001
$\Delta\rho/\rho_l$	0.079 ± 0.0025	0.105 ± 0.0025

the natural and the isotope composition can be explained by beam hardening and the results found in section 5.3.2: beam hardening leads to a deviation from the linear correlation of neutron beam attenuation and area density, which is shown for $LiBH_4$ in Figure 5.17. In particular, data points originating from the isotope mixture are not contributing to the plot, since it shows the area density for natural $LiBH_4$, only. In case of the isotope composition the beam attenuation originates mainly from the

[26]This statement is limited to the spatial resolution and measurement uncertainties. Though the existence of pores inside voxels denoted as cluster is possible, they still contain a predominant amount of $LiBH_4$.

incoherent scattering cross section of hydrogen as already discussed in the previous paragraphs. Accordingly, a beam hardening effect in case of the isotope powder composition for a maximal area density of 0.16 g/cm^2[27] is not significant. The proof is given indirectly by comparison with the beam hardening investigation of Magnesium Hydride, where no significant influence was found for area densities up to approximately 0.4 g/cm^2 (see appendix B.2.1). Consequently, an increase of material density as taking place by solidification of $LiBH_4$ results in an increase of area density, which is accompanied by a corresponding linear increase of the neutron beam attenuation. This is different in case of the natural composition sample. Here, a linear correlation does not hold any more as shown in Figure 5.17 for area densities higher than 0.005 g/cm^2. Thus, an increase of area density due to solidification is accompanied by a non-linear increase of neutron beam attenuation, which is especially pronounced in the right part of Figure 5.17 for the normalized attenuation. In case of the natural sample composition the maximal area density for $LiBH_4$ is about 0.077 g/cm^2, a further increase of area density leads to a significantly lower normalized area density and corresponding beam attenuation. Hence, the increase of beam attenuation for the natural composition is lower than for the isotope composition, which explains the lower density change derived for the natural composition. Additionally, solidification in case of the isotope composition is accompanied by a small macroscopic material packing density increase of approximately 4.2 %, which is not observed for the natural composition (as discussed in appendix B.3). Hence, there is still densification accompanied with solidification of $LiBH_4$. This will be discussed later on. Accordingly, an increase of the attenuation coefficient is partially caused by the reduction of porosity and mistakenly interpreted as change of pure $LiBH_4$ density due to solidification. It is stated that the reason for the higher density change observed for the isotope sample is a superposition of both effects: beam hardening and porosity reduction. Therewith, the density change derived from the natural composition represents the lower limit whereas the corresponding change derived from the isotope sample represents the upper limit:

$$\frac{\Delta\rho}{\rho_l} \in [0.0765, 0.1075]$$

Unfortunately, no study is reported in literature concerning the density of liquid $LiBH_4$. This is surprising against the background that it is a fundamental material property, relevant for material preparation, compaction and interpretation of results; in particular in the view of the fact that the temperature regime for both ab- and desorption of the Lithium-RHC corresponds to the liquid phase of $LiBH_4$. Apart from

[27] The maximal area density is calculated using the center of the sample (3 mm diameter) with a macroscopic material density of 0.52 g/cm^3 according to appendix B.3.

this fundamental material property the results shown above allow for a determination and proof of the existence of cluster that contain no other significant phase than $LiBH_4$ by use of the cluster attenuation threshold, μ_{TC}. In the following, this quantity will be used to comprehensively and quantitatively analyze the $LiBH_4$-clusters that are observed after melting of the liquid phase.

5.5.2.5 Sintering - macroscopic phase separation and multi-scale problem

In the following, the thresholds $\mu_{TC} = 10.7\ cm^{-1}$ and $\mu_{TC} = 3.74\ cm^{-1}$ for the natural respectively the isotope sample composition are used for the identification of voxels corresponding to cluster of $LiBH_4$ in the total sample volume.[28]

The analysis is limited to the natural sample composition due to the clear labeling of $LiBH_4$ by the highly absorbing isotopes of Li and B, so that influences of MgH_2 can be neglected. While a clustering for the liquid state is qualitatively distributed homogeneously in height and shows no ordering, which is again shown in the left part of Figure 5.43, this is different for the distance to center. The radial distribution of cluster of $LiBH_4$ is shown qualitatively in the right part of Figure 5.43 for the liquid state of the natural composition by a top view in negative z-direction for the same threshold for the attenuation coefficient as used for Figure 5.40, $\mu_{TC} = 10.41\ cm^{-1}$.[29] An ordering of cluster is visible, which are distributed at the boundary of the aluminum sample cell, sharing the same cylindrical rotational symmetry. In the center area of the sample no clustering of $LiBH_4$ can be observed! This is a surprising results since it shows the system in a state directly after melting of $LiBH_4$ and accompanied sintering of the liquid state of $LiBH_4$. For a quantitative analysis, a cluster attenuation threshold of $\mu_{TC} = 10.7\ cm^{-1}$ as described previously is used. Relevant cluster parameters like cluster volume and distance of centroid to center are derived by particle analysis performed with the ImageJ software, the exact procedure is shown in appendix B.4. It includes a thresholding using the above set cluster attenuation threshold in combination with a binarization of voxel identified as cluster or as being part of cluster. The histogram of the frequency of cluster volumes for the initial liquid state is given in the upper part of Figure 5.44, where the frequency of cluster volume is normalized to the absolute number of observed cluster. Cluster volumes are sorted into 50 equally spaced bins with binning width of $0.0193\ mm^3$. About half of the cluster in the liquid state are sorted into the first bin. Hence, their volume is equal or less than $0.0193\ mm^3$. Besides these small cluster there exist some with larger

[28] The thresholds for cluster attenuations correspond to a normalized cluster threshold of 0.8, which is originating from the natural composition according to Figure 5.42.

[29] This is slightly lower than the derived cluster threshold by Figure 5.42, $\mu_{TC} = 10.7\ cm^{-1}$, but chosen for a better visualization due to a higher amount of voxel fulfilling the threshold condition.

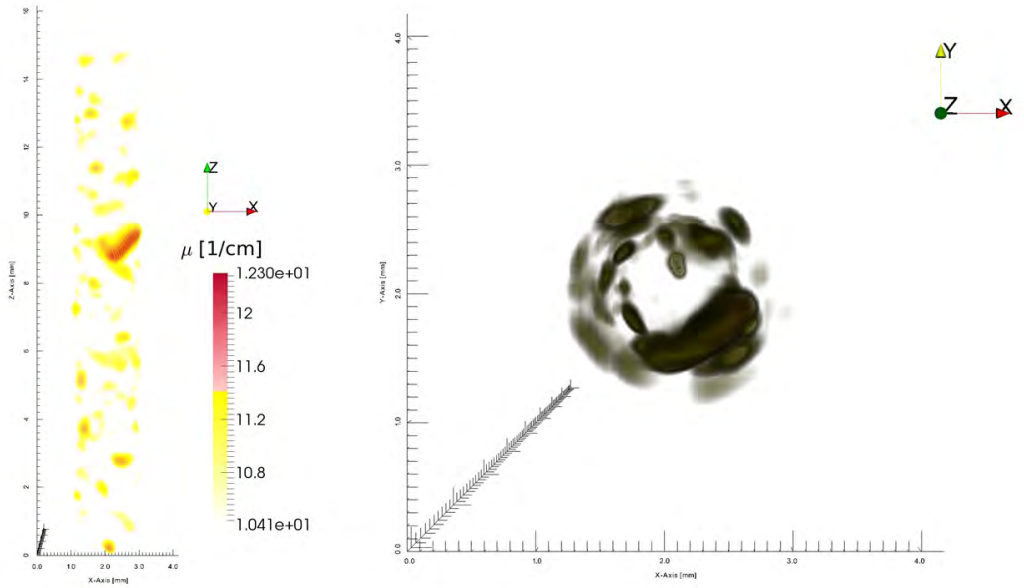

Figure 5.43: Left: Cluster distribution for the natural composition in the liquid state with applied threshold of $\mu_{TC} = 10.41$ cm^{-1}. Right: Top view in negative z-direction of the left image, revealing order and symmetry of cluster.

volume of up to 0.25 mm^3. The average cluster volume is determined to 0.03 mm^3. In the lower part of Figure 5.44 the histogram of distance of cluster centroids to sample center is shown, where the frequency is again normalized to the absolute number of cluster. The qualitative impression given by the top view in Figure 5.43 is confirmed by the histogram: the average distance of cluster centroids to the center is 0.91 mm, hence $LiBH_4$ is clustered at the outer sample boundary and has a rotational symmetry defined by the sample center axis.
The results of Neutron Tomography analysis of clustering for the liquid state of $LiBH_4$ in Li-RHC highly contribute to the understanding of the mechanism and effect of sintering, which is discussed in the following.

Before sintering is induced by liquefaction of $LiBH_4$ its distribution can be assumed to be homogeneous over the sample volume. If initial clustering is present, it is due to agglomerations of $LiBH_4$ in the loose powder bulk density that can occur even after milling procedure [38]. This initial clustering has no rotational symmetry but a random distribution. Increasing the temperature above the melting point of $LiBH_4$ at 275 °C causes a sintering of the solid material, Magnesium Hydride, in terms of a densification due to repacking of wetted particles, driven by capillary forces. This is in agreement with classical theory of liquid phase sintering [46] or supersolidus sintering

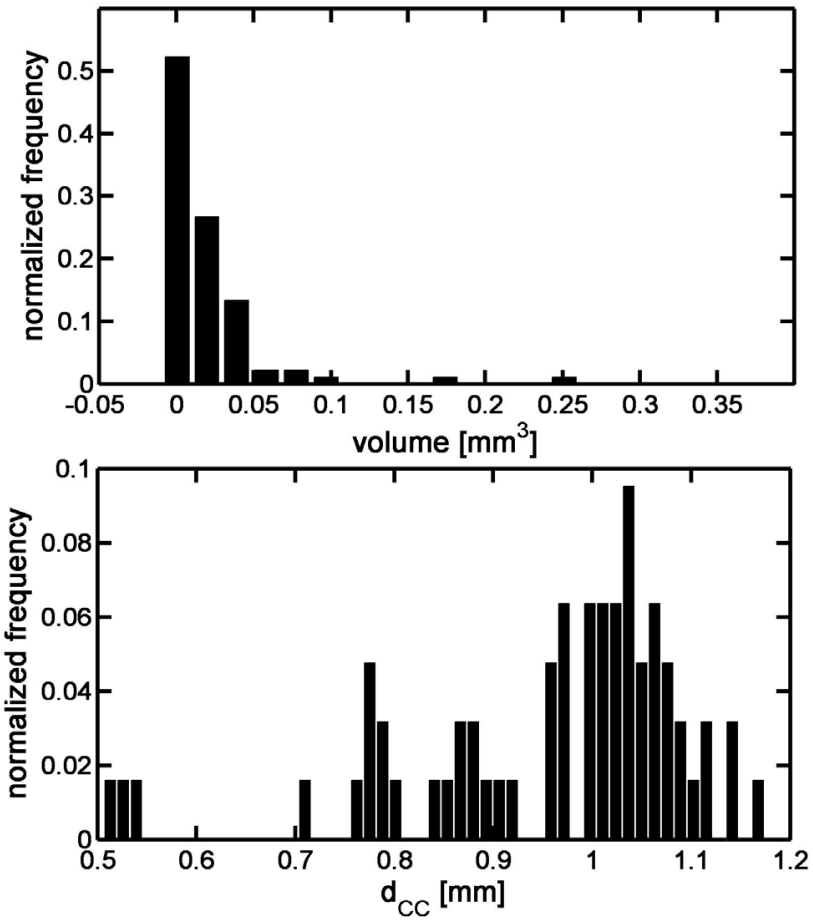

Figure 5.44: Top: Histogram of the frequency of cluster volumes for the natural sample composition in the liquid state for a binning of 50. Frequencies are normalized to the absolute number of cluster. Bottom: Histogram of the cluster centroid (center of gravity of a cluster) to sample center distances. Again, frequencies are normalized to the absolute number of clusters.

[45]. The latter comes closest to the a-priori state present in this case: after ball milling, particles can consist of both the solid as well as the melting phase. However, the amount of liquid is significantly different to typical sintering processes: In case of the system used here the molar ration of $LiBH_4$ and MgH_2 is 1:1. Since the density of $LiBH_4$ is less than half of the density of Magnesium Hydride, the volume ratio of liquid and solid material is higher than 2/3. For typical sintering processes aiming at high densification the liquid phase amount is about 30 % [44, 45]. Hence, in the Li-RHC system the volume amount of the liquid phase is approximately increased by a factor of 2! The high amount of liquid phase causes a rapid densification. This is in agreement with other results reported in literature, e.g. [72, 46]. Indeed, in Figure 5.38, 90 %

of the structure change is completed already after approximately 1 minute. Based on the results for clustering and according densification of the solid Magnesium Hydride matrix (Figures 5.38, 5.40, 5.44) a model for the sintering process is stated. It is schematically shown in Figure 5.45. The left part shows an exemplary composition of

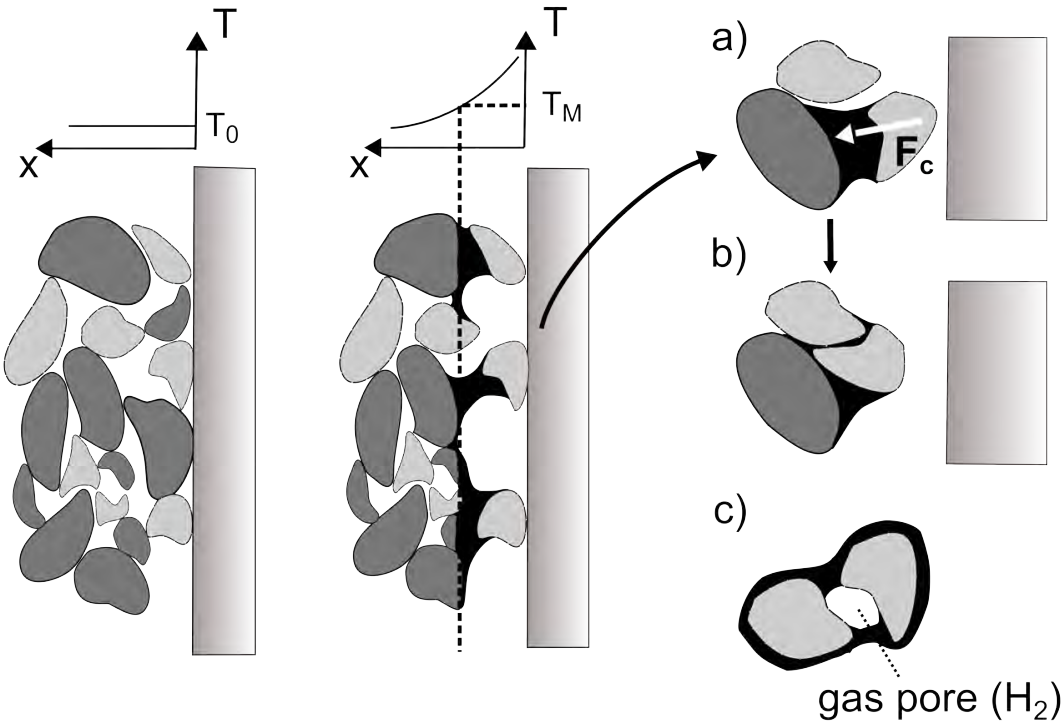

Figure 5.45: Developed model for densification during first-time liquefaction of $LiBH_4$. Left: Steady state at thermal equilibrium below the melting point with $LiBH_4$ in the solid state (phase is denoted by gray), the solid MgH_2 phase is marked light gray. Center: Temperature gradient inside the sample due to temperature increase above the melting point (T_M). The vertical line denotes the temperature boundary, to its right it is $T \geq T_M$. The liquid phase of $LiBH_4$ is shown in black, wetting the solid phase and a) inducing an effective motion of solid particles to the sample center, induced by capillary forces F_C, b) repacking of solid particles for optimal wetting and surface energy minimization, c) effect of containment of a hydrogen gas pore.

particles consisting of Magnesium Hydride and $LiBH_4$, where the latter is colored gray and the former is light gray. There is no ordering and the porosity between particles is in very good agreement with the low macroscopic density determined in the initial section. For reason of simplification, particles consist of a mono-phase only. The following is readily transferable to multi-phase particles as well. In the initial state the applied temperature field by external heating is well below the melting temperature of $LiBH_4$. Further, it is in equilibrium and shows no dependency on the distance to the

sample wall[30]. The latter is indicated by the continuous area in the right part. When the temperature is increased to induce a melting of $LiBH_4$ the temperature field shows a radial dependency with a decreasing temperature with increasing distance from the wall. This is due to the location of heating elements, which are placed at the outer part of the cylindrical sample cell as shown in section 4.2.3 and Figure 4.5. As a consequence of the radial temperature field, the melting of $LiBH_4$ starts at areas close the sample wall. This is shown in the middle image of Figure 5.45, where a quasi-static case is used for illustration. The melting point is indicated by T_M in the upper axes, corresponding to a radial distance indicated by the vertical dashed line. Starting from the sample wall to the right and moving further until this boundary line, $LiBH_4$ is in liquid state and colored black. On the left side of this line, the temperature is below the melting point and particles are solely in the solid state, providing a wettable surface area for $LiBH_4$.

The liquid state gives rise to mobility and structural changes of material composition. Solid Magnesium Hydride is wetted by $LiBH_4$ and capillary bridges arise between single solid particles in the right area and the solid surface at the boundary. Thus, capillary forces cause a displacement of single solid particles from the partially molten area towards the boundary line and therewith towards the sample center. This motion is accompanied by a rearrangement of particles to minimize surface and interfacial energy [46, 60], which is shown in a) of Figure 5.45. Here, the MgH_2 particle is increasing its distance to the cell wall, moving towards the solid area due to the capillary force F_C. Consequently, particles rearrange and a densified matrix is formed, in which the liquid phase is finely and dispersively distributed as shown in image b). With the temperature field evolving towards equilibrium, shifting the boundary line in the center image towards the sample center, the as described process continues: a densified solid matrix of MgH_2 is formed in the sample center, embedded in liquid $LiBH_4$. Still, it is not fully understood why the position of $LiBH_4$ clusters show a rotational symmetry with cluster oriented at the sample boundary as indicated by the analysis according to Figures 5.40, 5.44. A reason may be that particles and structures of the solid matrix are preferentially oriented towards the sample center even after equilibrium is reached and the sintering process is completed. Consequently, openings and large pores would be located at the outer boundary of the solid matrix and $LiBH_4$ could agglomerate and form clusters in these openings, resulting in the observed symmetry.

Accompanied by a full melting of $LiBH_4$ in the sample, the liquid-solid volume ratio converges to the as mentioned 2:1 ratio. For this volume ratio, a shape loss is reported in literature [44]. This is not the case in this study, since a reduction of the sample

[30]Since the sample holder has a rotational symmetry, this can be generalized to a non-radial dependency.

radius is observed according to Figure 5.38. A possible reason for this is the existence of gaseous pores in the sample due to the hydrogen pressure of 13 bar. During the densification process a trapping of pores might occur as illustrated in image c) in Figure 5.45, where the pore is trapped between the interface of two Magnesium Hydride particles. This contributes to a stabilization of the solid-matrix and overall sample structure, preventing a shape loss.
From that the solid matrix is proposed as being a mixture of densified MgH_2 particles including gaseous pores. It is penetrated by liquid $LiBH_4$, which shows cluster at the outer matrix boundary. The existence of a densified solid matrix that is penetrated by the liquid phase, where the latter is fine and dispersively distributed within the sample center area, is confirmed also by Figure 5.46. It shows the natural composition with two thresholds applied: $LiBH_4$ clusters[31] are defined by $\mu \in [\mu_{TC}, \mu_{max}]$ and are colored in blue as indicated by the colorbar, where the cluster attenuation threshold was already determined to $\mu_{TC} = 10.7$ cm^{-1}. The solid matrix forms the inner core and is defined by $\mu \in$ [7,9] cm^{-1}. By combination of isotope and natural samples the composition of the solid matrix can be partially resolved: for the isotope composition the maximal attenuation is 4.18 cm^{-1}, which is approximately the maximal attenuation of MgH_2 assuming a similar clustering for the isotope sample as indicated by Figure 5.41. Since attenuation coefficients for the solid matrix in the natural composition are up to 9 cm^{-1}, there has to be a contribution by highly attenuating $LiBH_4$. Consequently, the inner core colored in yellow in the Figure contains $LiBH_4$, distributed within the solid matrix. It is remarked that the analysis is limited to the spatial instrumental resolution with the lower limit given by the voxel size of $3.92 \cdot 10^{-4}$ mm^3. For this resolution, no clustering or gaseous pores are found within the solid matrix[32]. Still, it is highly likely that $LiBH_4$ is also occupying pores within the solid matrix, clustering on a lower dimension.

The results concerning the effect of liquefaction of $LiBH_4$ have a tremendous impact for the understanding of reaction mechanism and the material prospects for the future usage in hydrogen storage systems. A cluster emergence as a result of excess liquid phase due to the given molar ratio for the metal hydride system is nothing else than a phase separation of Magnesium Hydride and $LiBH_4$! The dimension of phase separation scales with the size of the sample, which leads to a macroscopic separation of phases, in particular for scaled-up systems. By that, the kinetic limitations observed for the system as given in the theoretical section are due to a multi-scale problem! In addition to kinetic limitations on the micro- or nanoscale that are tried

[31] It is remarked again, that 'cluster' is referred to voxel that contain solely $LiBH_4$. Thus, the results hihgly depend on the overall spatial resolution.
[32] For precise analysis probabilities of the solid matrix the reader is referred to section 7.1.3

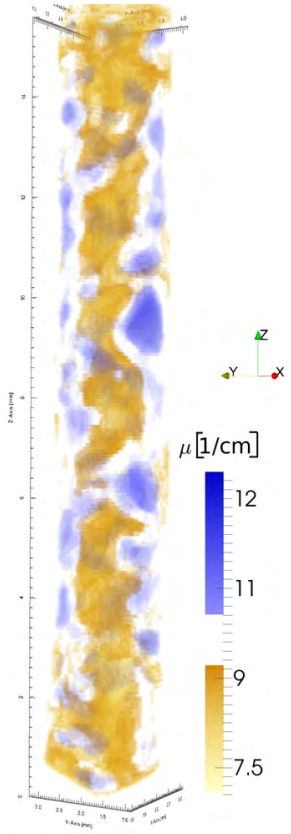

Figure 5.46: Volume data set of the natural composition in the liquid state with two applied threshold intervals: the solid matrix is defined by $\mu \in [7.5,9]$ cm^{-1} and colored in orange. $LiBH_4$ cluster are defined by $\mu \in [10.7,\max]$ cm^{-1} and colored in blue.

to be overcomed by additives, macroscopic phase separation is an additional, so far not considered issue. A large transport of material is necessary to complete sorption reactions. Even more, it is inherent in the system, since temperatures for absorption and desorption correspond to the liquid phase of $LiBH_4$, causing a high excess amount of the liquid phase in case of sintering.

The observed effect of phase separation might be the reason for observed incomplete reactions in literature. In fact, there is no evidence of above 90 % reaction completion reported in literature for the Li-RHC system. In addition to the phenomenon of phase separation, there might be another effect: Due to reduction of pores/cracks and defects during densification with accompanied MgH_2-MgH_2 interface occupation and penetration of the solid matrix by the liquid phase, diffusion and even worth permeation pathways for hydrogen are blocked. Hence, hydrogen has to diffuse either through the solid or liquid $LiBH_4$ to reach its target area, which leads to reduced

reaction kinetics. According to the results gained by Neutron Imaging data the temperature field is proposed as the main driving force for the observed symmetry and order: clustering of $LiBH_4$ and densification of the solid matrix follows the given symmetry of the temperature field, which is a crucial, ordering parameter for the evolving structure and phase separation.
This macroscopic phase separation that is inherent in the absorbed state raises the system to a further level of complexity. Considering kinetic barriers on atomic (e.g. diffusion), nano (e.g grain boundaries), micro (e.g. particle size) and now even macro-scale (phase separation), the improvement of the overall reaction kinetics and reversibility is a multi-scale problem. It is pointed out that as-performed cluster analysis can be addressed only due to isotope labeling of the liquid phase in combination with Neutron Tomography.

5.5.2.6 Solidification and cluster enhancement

The cluster analysis that has been performed for the post-sintering state is done now for the solid state after solidification of $LiBH_4$. By that, it is possible to analyze the effect of solidification on clustering in the sample. As the temperature field was already proposed as a crucial order parameter for the symmetry and clustering, solidification and corresponding temperature decrease is expected to have an effect on the observed clustering as well.
The cluster volume distribution for solid and liquid state is shown in Figure 5.47, where the liquid state is already known from the upper part of Figure 5.44. The same histogram parameters are used for the solid state in the lower part of Figure 5.47.

A clear enlargement of $LiBH_4$ clusters is observed, indicated by an increase of volume: the average volume in the solid state is 0.13 mm^3, which denotes an increase by a factor of 4.3 in comparison to the liquid state[33]. The absolute number of clusters in the liquid state is 90 for the used bin number of 50. After solidification, the number of clusters reduces to 70. Thus, in addition to the enlargement of existing clusters of $LiBH_4$ their absolute number is reduced, indicating a fusion of clusters. According to the histogram, the frequency of small clusters is reduced and at the same time the distribution shifts to higher cluster volumes. From this it can be deduced that small clusters which are located at close distance to each other merge to form larger clusters. In Figure 5.48 the histogram of the distances of the cluster centroids to the center of

[33]The histogram itself does not allow to draw the conclusion of growth of existing cluster since it contains no spatial information about the absolute cluster position. The identification of clusters in liquid and solid state was done using the information about the cluster centroid position provided by the particle analysis plugin of ImageJ [3], see appendix B.4. Hence, the volume increase can be assigned to an emergence of clusters.

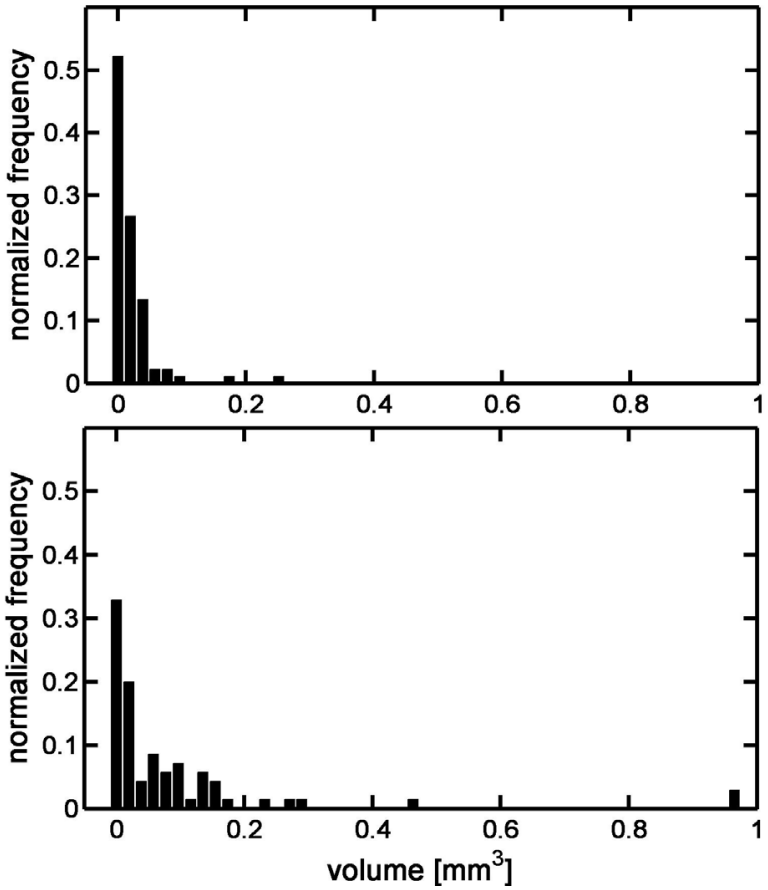

Figure 5.47: Cluster volume distribution in the natural sample composition for the liquid (top) and solid state (bottom) of $LiBH_4$. Frequencies are normalized to the absolute number of cluster, the applied binning is 50 for both histograms.

the sample, d_{CC}, is shown for both liquid (upper part) and solid state (lower part). The frequency distribution is normalized to the total number of clusters. Due to the binary representation of cluster volume data, the direction of cluster growth can be readily detected (see also appendix B.4). As visible, the histogram data is shifted to lower distances for the solid state. The average distance to the center is calculated to 0.91 mm. Hence, it can be deduced that the growth of clusters has a preferential direction, which is the center of the sample. Additionally, the histogram in Figure 5.48 shows no distances smaller than 0.5 mm, both for liquid and solid state. Thus, the solidification induces no cluster emergence in the sample center, though there is the presence of liquid $LiBH_4$ in the interface of the Magnesium Hydride matrix. This is in good agreement with the reduction of the total number of cluster in the overall sample and growth of existing cluster. The reason for this will be discussed later on.

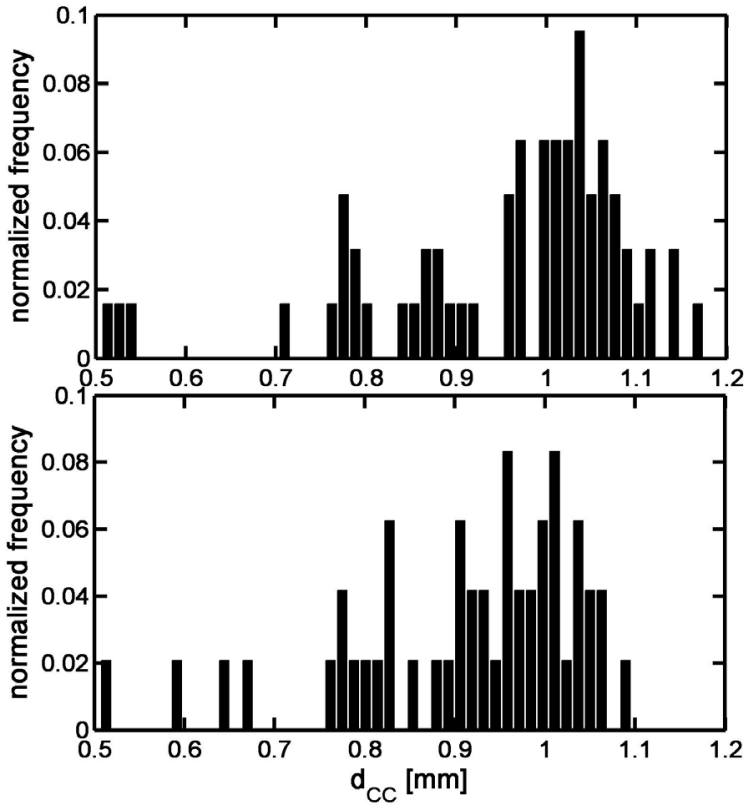

Figure 5.48: Distribution of distances of cluster centroids to the sample center in the natural sample composition for the liquid (top) and solid state (bottom) of $LiBH_4$. Frequencies are normalized to the absolute number of cluster, the applied binning is 50 for both histograms.

Combination of liquid and solid state - $LiBH_4$ material transfer

To investigate the cluster growth and to determine the source area of the observed growth, data sets of liquid and solid data are directly combined in terms of a difference image. By that, the material transfer of $LiBH_4$ can be tracked if it is assumed that any change in the attenuation coefficient of a voxel, $\Delta\mu$, can directly be assigned to a increase or decrease of the $LiBH_4$ content

$$\Delta\mu = \mu_l - \mu_s \begin{cases} < 0, & n(LiBH_4) \text{ growth} \\ > 0, & n(LiBH_4) \text{ decrease} \end{cases} \tag{5.36}$$

where $n(LiBH_4)$ is the amount of substance of $LiBH_4$ in that voxel. The validity of this assumption is discussed later on. To induce solidification of the latter, the temperature is reduced to 221.5 °C. The temperature difference corresponding to the liquid and solid state is 135.5 °C. In case of the liquid state, a thermal expansion of the

sample holder and sample cell is estimated to ≈ 0.07 mm [34]. This thermal expansion has to be considered for the calculation of the difference voxel data to avoid artifacts and identify cluster. The process of mapping two data sets by transformation of the coordinate systems is called registration [50], which is done with the software package *Avizo* [52] and described in appendix B.5. The data set corresponding to the solid state is used as reference, the transformation is applied on the liquid data set[35]. The registered liquid data set allows for a direct comparison of liquid and solid state by calculation of a difference data set as described above, where the term 'registered' is omitted in the following.

To analyze changes of the $LiBH_4$ content inside the solid matrix, the attenuation difference data set is subdivided into 5 (x,z)-slices for different y positions (depths) of the sample. This slicing is applied for both the natural as well as the isotope composition. For the sample with the natural composition, attenuation difference slices are shown in Figure 5.49. In the upper left an overview volume data set for the attenuation difference is shown with orientation and y-position of selected slices visualized by white rectangulars. They are sequenced as indicated by the arrow in the overview image with ascending y-position, starting from the upper left. The outer area of all slices and additionally the slice numbers 1 and 5 correspond to the sample boundary. In each slice, the attenuation difference is scaled by pseudo colors given to the right. As visible, positive $\Delta\mu$ are observed mainly in the center of the sample in particular pronounced for slice number 3, corresponding to a higher content of $LiBH_4$ within the solid matrix for the liquid state. For the sample boundary there exist mainly negative attenuation differences, hence the amount of $LiBH_4$ is increased at the sample boundary after solidification. Deviations from this general findings are concentrated in the upper sample area, where strong positive attenuation differences are also found at the sample boundary. This is due to a macroscopic change of the sample structure upon solidification, similar but less pronounced to the one that was already observed for initial sintering. Further informations are given in appendix B.3. The void areas that are frequent especially in the center slices 3, 4, 5 are due to a thresholding of $\Delta\mu$ to reduce artifacts at the sample boundary that are due to the registration of images (see appendix B.5 for further information). In the image center these voids correspond to low but positive $\Delta\mu$. From the difference attenuation slices it can be concluded that solidification causes a directed material transfer of $LiBH_4$ from the inner area (corresponding to the solid matrix) to the outer sample area (corresponding to $LiBH_4$ clusters according to the upper section, e.g. Figure 5.46). The increase of $LiBH_4$ at the

[34] The latter is an upper limit, derived by calculation of the linear thermal expansion of the aluminum sample holder (diameter 23 mm) for the given temperature difference.

[35] This is arbitrary and could be done vice versa without influencing the following results.

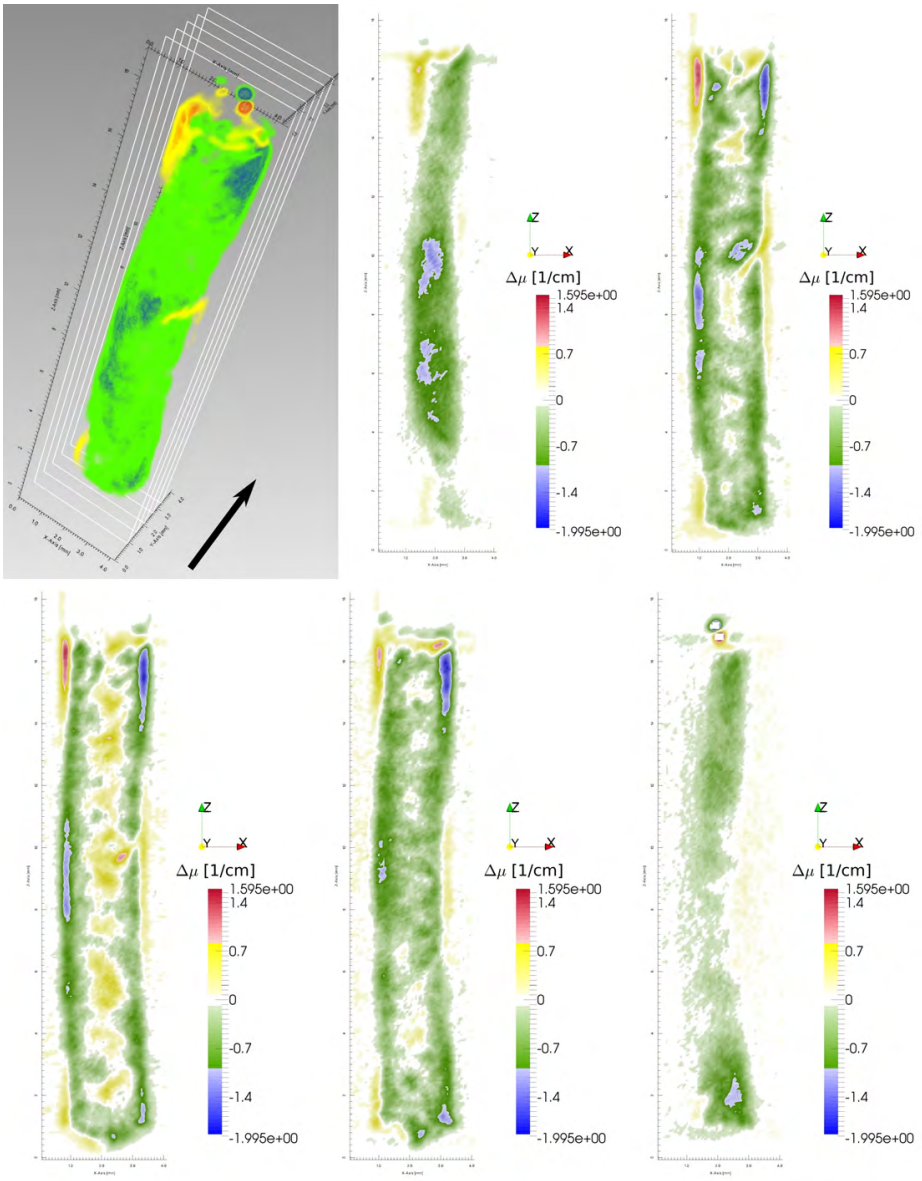

Figure 5.49: Volume data for the natural sample composition set showing the attenuation coefficient difference of liquid and solid state, obtained by registration. Upper left: Overview of the difference data set with positions of (x,z)-slices indicated by the white rectangulars. The attenuation coefficient difference for the slice data is shown row-wise, starting in the upper center and sequenced as indicated by the arrow in the overview image.

boundary of the solid matrix is homogeneous with no preferential areas except for a few distinct areas in the middle height for slices 1 and 2. This is probably due to reduction of pores or particle reorientation at the solid matrix boundary induced by material transfer. Another possible reason is the effect of temperature that will be discussed

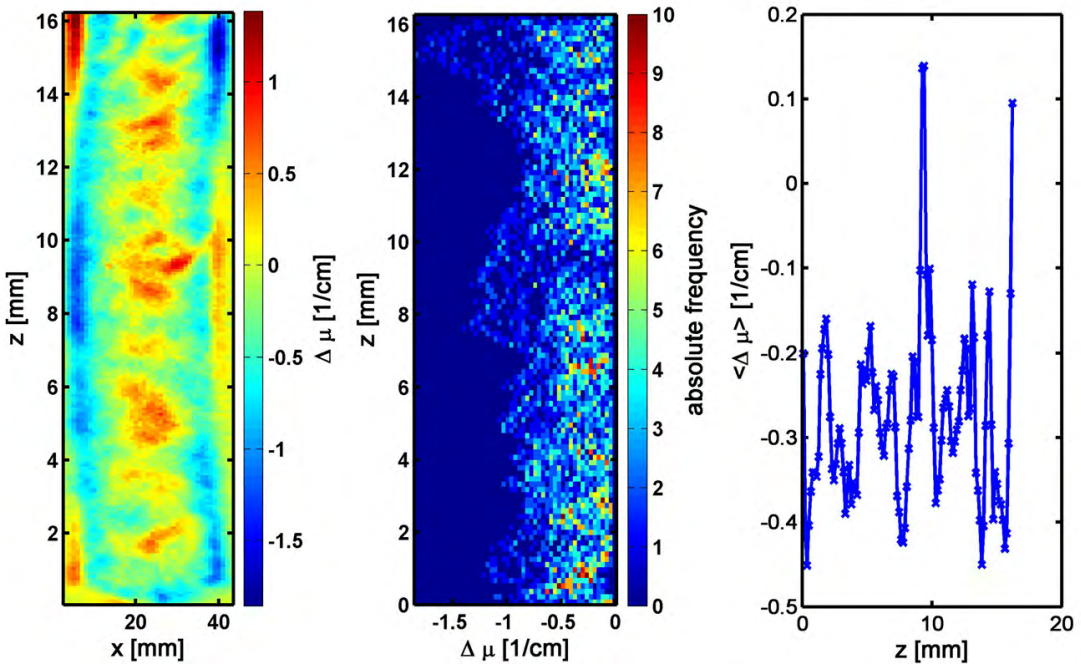

Figure 5.50: Analysis of the z-dependency for slice number 3 of the natural composition according to Figure 5.49. Left: Attenuation coefficient difference of slice 3. Center: 2D correlation map of $\Delta\mu$ and z-position. Right: Average attenuation coefficient difference depending on z.

later on. The z-distribution of changes in attenuation is shown in Figure 5.50 for slice 3. The left image shows the original difference slice, similar to Figure 5.49. In the center image, a 2D-correlation map as described in section 5.2.5.2 is calculated for the difference attenuation and z-position. The frequency of tuples is visualized by pseudo colors. In the right image the average attenuation difference, $< \Delta\mu >$, depending on the z-position is plotted. Only negative values for $< \Delta\mu >$ are considered since the sum over all $\Delta\mu$ should be zero due to conservation of mass. As visible, there is no evidence of z-position influence on the observed motion of $LiBH_4$: the correlation map is vertical without inclination and the average attenuation difference shows no z-dependency as well. Consequently, the influence of gravity on the material transfer of $LiBH_4$ induced by solidification is negligible.

An analogue investigation is done for the difference data set of the isotope composition, which is shown in Figure 5.51. Again, the orientation of slices is given in the overview image in the upper left of the Figure with their sequence indicated by the arrow, starting from the upper row. In general, the same results as for the natural composition are found. The artifacts are increased due to a worse distinguishability of sample boundary and sample cell wall. Thus, the initial and last slice are set closer

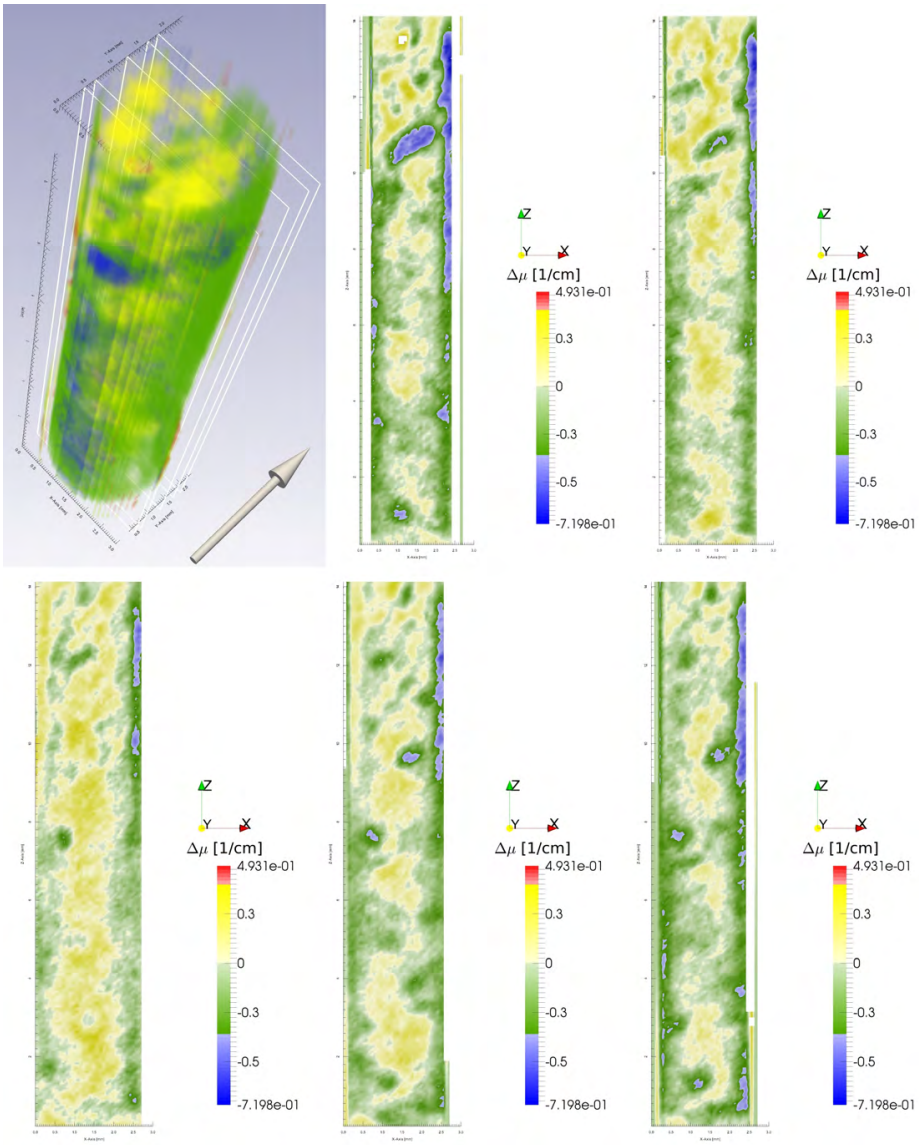

Figure 5.51: Volume data for the isotope sample composition set showing the attenuation coefficient difference of liquid and solid state, obtained by registration. Upper left: Overview of the difference data set with positions of the (x,z)-slices indicated by the white rectangulars. The attenuation coefficient difference for the slice data is shown row-wise, starting in the upper center and sequenced as indicated by the white arrow in the overview image.

to the sample center to reduce the influence of artifacts. Still, a general motion of $LiBH_4$ from the densified solid matrix to the outer boundary area is observed, showing similar characteristics as in case of the natural composition. The full data set histograms for both, the natural and the isotope composition, are shown in the inset of Figure 5.52 for positive $\Delta\mu$ for a number of 512 equidistant bins. To reduce the

influence of artifacts originating from image registration, a threshold of 0.26 cm^{-1} is applied[36]. The ratio of average attenuation differences is then calculated to 2.1. Scaling the histogram distribution for the isotope composition with this ratio, histogram curves agree well as visualized in the main plot of Figure 5.52. For the area density of

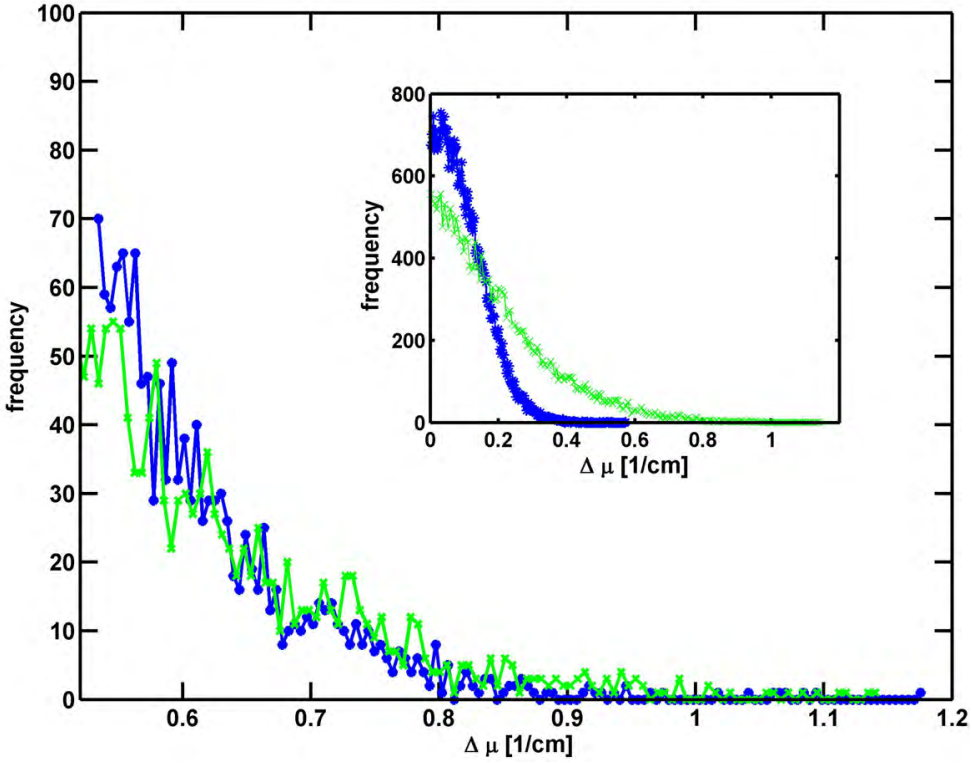

Figure 5.52: Histograms showing the distribution of the difference attenuation coefficients for the natural (green) and isotope (blue) sample composition. The latter is scaled by a factor of 2.1. The inset shows the original distribution of difference attenuation coefficients.

$\rho_A = 0.07$ g/cm^2 corresponding to the sample center of the natural composition the lower limit of the ratio of natural and isotope $LiBH_4$, $\tilde{r}$, is 3.5±0.8 (see Figure 5.18) and therewith slightly enhanced in comparison to the observed ratio of 2.1. Deviations are possibly due to an increased motion of $LiBH_4$ in the isotope composition, that is directed from the solid matrix located in the sample center to the boundary. Increased motion is originating of higher amounts of $LiBH_4$ in the less densified solid matrix in the liquid state. This is in agreement with an observed macroscopic densification for the isotope composition for the phase transition of $LiBH_4$ in terms of solidification, which is described in appendix B.3. Hence, it is proposed that the attenuation dif-

[36]It is derived from the standard deviation of $\Delta\mu$ corresponding to an area of the sample holder material, serving as a reference.

ferences are mainly due to motion of liquid $LiBH_4$ during the solidification process. Both, the direct cluster analysis of the liquid and solid state as well as the combination in terms of difference data, give a rather complete picture of the phase transformation of $LiBH_4$ from liquid to solid and of the effects on the Li-RHC system:

- The solidification of $LiBH_4$ induces a material transfer of the liquid phase out of the solid, center-located matrix to the outer boundary.
- The direction of material transfer is homogeneous and shows no dependency in z-direction (height).
- As part of the material transfer process to the boundary, existing clusters of $LiBH_4$ start to grow and smaller clusters merge together, reducing the absolute cluster number.
- The cluster growth is accompanied by the relocation of its centroid to the sample center, confirming the direction of material transfer and cluster growth.

The emergence of clusters and relocation of cluster centroids can be made visible by using the combined volume data set of the liquid and solid state. This is shown in Figure 5.53 for the natural sample composition, where clusters in the liquid state are visualized by a color gradient from red to yellow approaching the cluster boundary. Clusters corresponding to the solid state are shown as transparent, with only the surface colored in gray, which allows to directly reveal the cluster change induced by solidification. For the left and center image a cluster attenuation threshold of $\mu_{TC} = 10.7\ \mathrm{cm}^{-1}$ is applied for both liquid and solid data set. The left image shows the volume in vertical position and the center image a view from the top. For the right image the threshold is set to $11.5\ \mathrm{cm}^{-1}$. As visible, liquid state cluster are covered by corresponding solid state cluster, indicating a growth due to the as described motion of $LiBH_4$ from the solid matrix. The top view shows the relocation of cluster centroids to the sample center due to a corresponding directed cluster growth, indicated by non-symmetric covering for the solid state. This is as well visible in the right image, where the volume increase of the cluster is observed in agreement with the histogram shown in Figure 5.47. In the conclusions for sintering the temperature field was already identified as an order parameter for cluster symmetry and phase separation at the solid matrix boundary, the effects observed here for solidification of $LiBH_4$ are driven as well by the temperature field, which is discussed in the following:
If the temperature is reduced below the melting point of $LiBH_4$ to induce solidification, the time evolution of the phase transition carries a spatial dependency due to a spatial dependency of the temperature field: heat loss is occuring at the outer sample

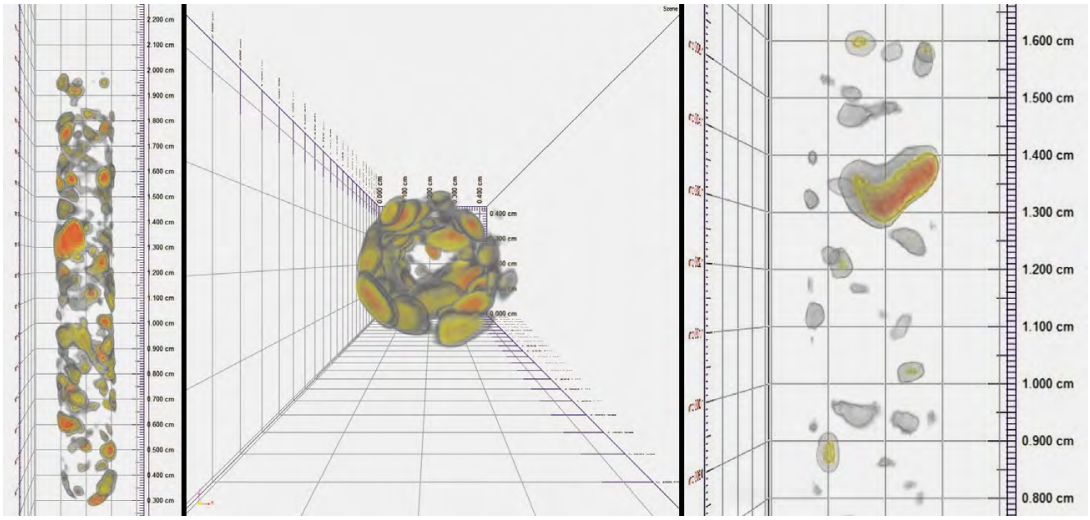

Figure 5.53: Visualization of the combined volume data set of liquid (colored) and solid (transparent gray) state. Left: View of the sample in vertical position, the cluster threshold for both states is $\mu_{TC} = 10.7$ cm^{-1}. Center: View from the top of the sample, same cluster threshold. Right: Zoomed center view in the vertical position and increased $\mu_{TC} = 11.5$ cm^{-1}.

cell boundary. Hence, there exists a temperature gradient from the sample center to the sample boundary, contrary to the case of liquefaction as discussed in the previous sections. The rotational symmetry of the temperature field causes a first solidification of $LiBH_4$ at the sample boundary, at the location of the $LiBH_4$ cluster. Since solidification is accompanied by a density increase of $LiBH_4$, cluster densify which is observed as an enhanced maximal attenuation coefficient for the solid state (histograms in Figure 5.39 and 5.41). Densification perturbs the liquid state equilibrium, occupied volume is reduced and solid $LiBH_4$ surfaces are preferably wetted by liquid $LiBH_4$, inducing a flow from the center to the outer boundary. As a consequence, the solid matrix can be further densified, which is observed here by a macroscopic density change for the isotope composition. It can be concluded that for the phase transition of $LiBH_4$[37] the temperature field is found to be a crucial parameter that induces material transfer, clustering and phase separation. The symmetry of the temperature field during temperature changes is conserved and reflected by the sample symmetry and cluster ordering even in the equilibrium state.

[37] As for both, liquefaction and solidification, the temperature field was found to have a tremendous effect.

5.5.2.7 Cycling - phase separation

Besides high operation temperatures and slow kinetics for scaled-up systems, one of the major drawbacks for the Li-RHC system is its capacity loss during cycling, which can be up to 0.17 wt% per cycle for a scaled-up storage tank containing a loose powder bed as reported by Jepsen [65]. A possible reason that is discussed is phase separation, though there is neither an experimental proof nor a comprehensive theoretical model so far since measurements are based on simple Sievert's-machines or powder diffraction that cannot reveal the spatial resolution of the sample structure. However, the use of Neutron Tomography gives first-time and detailed access to the spatial distribution of material and isotope labeling allows for the explicit analysis of the distribution and dynamics of $LiBH_4$, as shown in the previous sections. The above mentioned and discussed macroscopic phase separation and clustering of $LiBH_4$ is highly likely the reason for the observed capacity loss. To prove this prediction, a number of 6 cycles have been performed with the natural and isotope compositions between two different beamtimes at ANTARES. The Li-RHC system is investigated by Neutron Tomography in its desorbed state for temperatures corresponding to the solid, respectively liquid state of $LiBH_4$. In the fully desorbed state, the system composition is 2LiH-MgB_2+Mg, containing no $LiBH_4$ phase[38]. Hence, any change in the combined Tomography data sets can then be assigned to an existence of $LiBH_4$ due to the the induced phase transition in the case of the temperature increase, causing a change of density and material transfer. Consequently, an observed attenuation difference would prove a capacity loss due to phase separation. For reasons of comparability, the same temperature levels as for the investigation of sintering have been used: T= 357 °C for liquid, respectively 221.5 °C for the solid state. Measurements have been performed with ambient Argon gas pressure inside the sample cell. The same Neutron Tomography and image acquisition as well as data reconstruction parameters are used as for the measurements in the previous sections.

An overview image of the attenuation coefficients as result of the Neutron Tomography data reconstruction is given in Figure 5.54. It shows the natural composition sample at a temperature corresponding to the solid state of $LiBH_4$. The main sample is clearly indicated by its top surface at z-position of about 1.6 cm and cylindrical symmetry. In contrast to the initial state before sintering (see Figure5.39), material that is separated from the main sample is observed, located at higher z-positions. This is a first proof of macroscopic phase separation observed after cycling of the material. A detailed

[38]The standard composition is 2LiH+MgB_2 for a molar ration of 2:1 for $LiBH_4$ and MgH_2. In the present case there is an excess of Magnesium Hydride due the molar ratio of 1:1, which decomposes to Magnesium during desorption

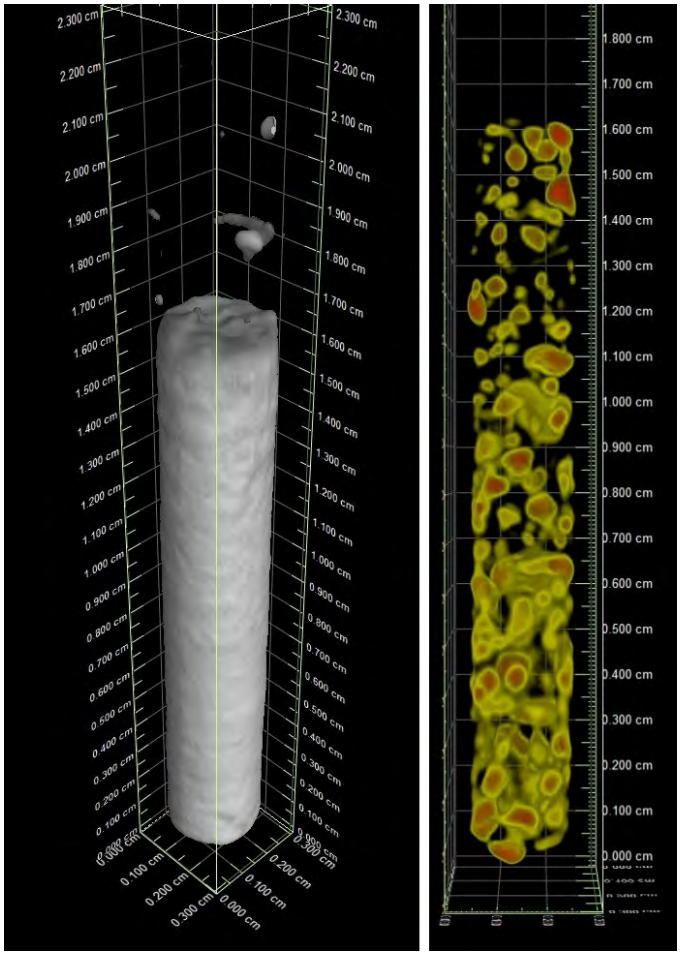

Figure 5.54: Left: Overview image showing the attenuation coefficient distribution in grayscale colors for the solid state of the natural sample composition. Right: Qualitative material packing density gradient visible by the increased amount of voxel with lower z-positions for the thresholded attenuation coefficient.

analysis of this evident separation is done at the end of this section. First, the main sample will be concentrated on with investigations related to the temperature increase and possible existence of $LiBH_4$ in this area. Analyses are constrained to the natural composition sample due to the higher significance for the $LiBH_4$ phase and related changes in attenuation for temperatures corresponding to the solid and liquid state.

Phase separation - main sample volume

For the main sample volume, already a qualitative visualization as given in the right part of Figure 5.54 reveals a distinct change in material packing density. A thresholding of attenuation coefficients is applied with $\mu_T = 9.72$ cm^{-1}. It is remarked, that thresholding for desorbed state data sets does not refer directly to clustering of

$LiBH_4$ and cannot resolve a potential long-range separation of Boron and Lithium: Although the beam attenuation is dominated by Boron since the absorption cross section for B-10 is significantly higher than for Li-6 and additionally the amount of B-10 is more than doubled to the respective amount of Li-6 in the natural sample composition (Figure 5.15 and table 5.1), there still is no phase sensitivity as in case of the absorbed state. Thus, a potential separation of LiH and MgB_2 cannot be stated nor investigated. Nevertheless, the material amount in the right part of Figure 5.54 shows a clear gradient with densification for lower z-positions. This might be due to influence of gravity at presence of liquid $LiBH_4$, since the density of the components of the Li-RHC system differs. However, after sintering no z-dependency of the packing density was observed in the liquid state. Thus, gravity seems to have an influence only during cycling and becomes more significant for longer time scales.

For detection of $LiBH_4$ present in the desorbed state a combination of reconstructed data sets corresponding to solid and liquid state of $LiBH_4$ is performed in analogy to the procedure introduced in the sections above. Again, the liquid state data set is registered and the solid state is used as reference. A difference data set is generated with $\Delta\mu = \mu_l - \mu_s$ according to equation 5.36. It is subdivided into 5 (x,z) slices for different y-positions along the sample to investigate a potential attenuation coefficient difference and its distribution. The slice data is shown in Figure 5.55. The distribution of attenuation differences is scaled by pseudo-colors. It shows a clear z-dependency, where negative $\Delta\mu$ of $\geq$-0.5 cm^{-1} are observed in the lower sample area for slices 2, 3 and 4 representing the inner part of the sample. In the upper sample half positive $\Delta\mu$ are found. The height-dependency of $\Delta\mu$ is shown quantitatively for the sample center slice (slice 3) in the upper row of Figure 5.56. In the left image, a different scaling for $\Delta\mu$ is applied to enhance differences corresponding to the z-position. Positive differences at the sample bottom for z = 0 mm are probably due to registration artifacts and not considered in the following. The middle and center image show a 2D correlation map of $\Delta\mu$ and z for $\Delta\mu < 0$. In comparison to the absorbed state given in Figure 5.50 the distribution of tuples shows a clear positive correlation of $\Delta\mu$ and z up to a height of about 11 mm. This is as well shown in the plot to the right, where $\Delta\mu$ is averaged for various height steps. For low z values it initially decreases due to the as-mentioned registration artifacts and converges into a plateau at about 11 mm. Fluctuations are caused by low data statistics. The evolution of $\Delta\mu$ is similar for the whole inner sample part as shown in the lower part of Figure 5.56. Here, averaged attenuation coefficient differences for slice numbers 3, 4 and 5 corresponding to y-positions of -0.4 mm, 0 mm and 0.4 mm depending on z are shown. The curves agree well, confirming the described positive correlation.

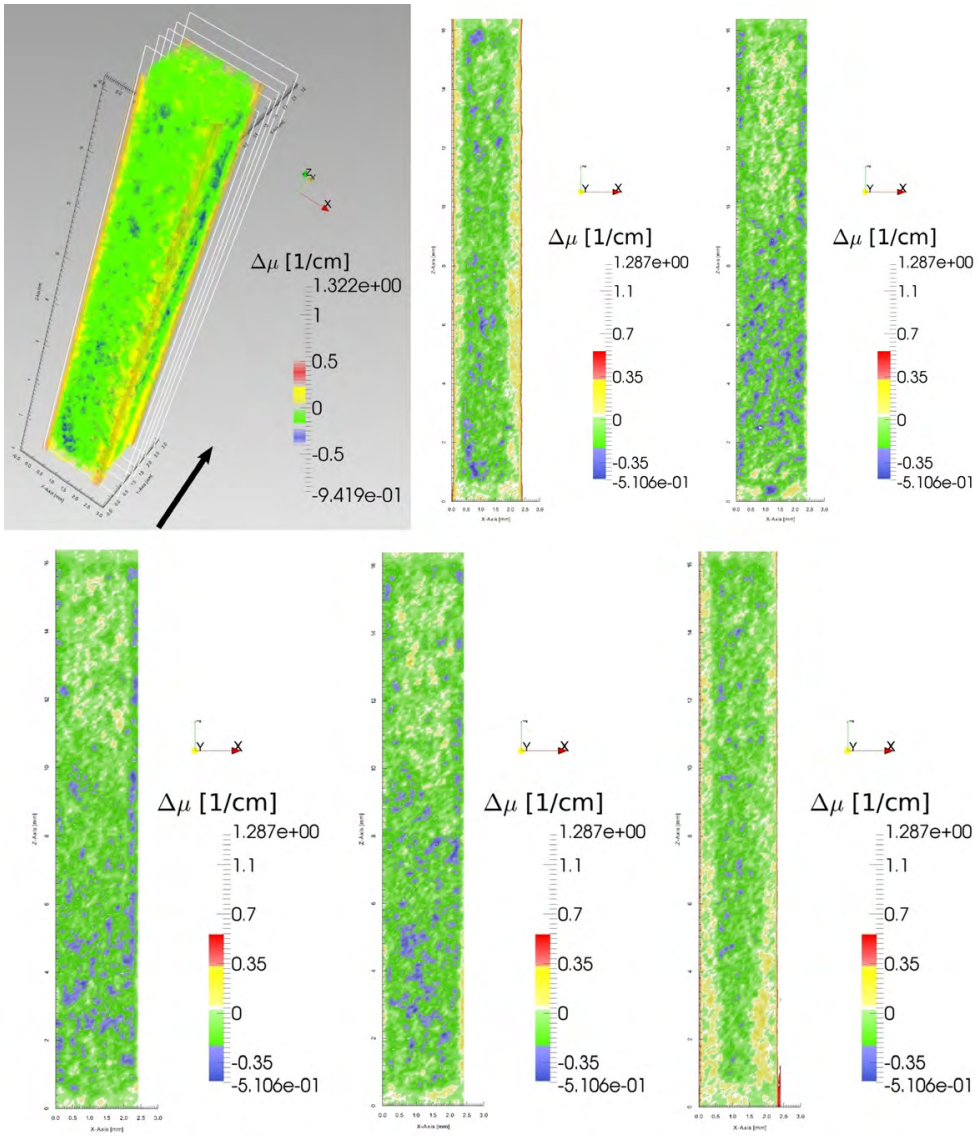

Figure 5.55: Volume data for the natural sample composition set showing the attenuation coefficient difference of liquid and solid state, obtained by registration fo data sets. Upper left: Overview of the difference data set with positions of (x,z)-slices indicated by the white rectangulars. The attenuation coefficient difference for the slice data is shown row-wise, starting in the upper center and sequenced as indicated by the arrow in the overview image.

From the combination of the solid and liquid data sets a number of conclusions can be drawn that are discussed in the following. The observed difference of attenuation coefficients in the combined data set indicates a still present $LiBH_4$ phase. It undergoes a density decrease upon melting resulting in expansion and material transfer, causing the difference attenuation that is discussed above for the combined data set. A remain-

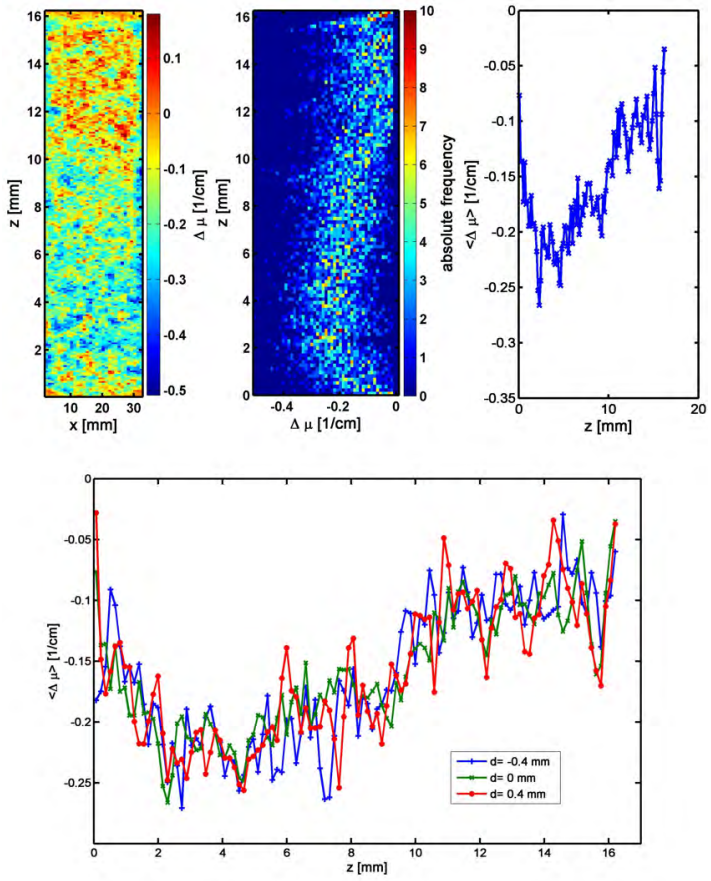

Figure 5.56: Analysis of z-dependency for slice number 3 of the natural composition according to Figure 5.49. Upper left: Attenuation coefficient difference of slice 3. Upper center: 2D correlation map of $\Delta\mu$ and z-position. Upper right: Equally distributed bins for z-position, a number of 50 bins is chosen. $\Delta\mu$ is averaged for the corresponding intervals. Bottom: Averaged attenuation coefficient differences for slice numbers 3 (blue), 4 (green) and 5 (red), the legend shows their distance to the center.

ing $LiBH_4$ phase in a desorbed sample is caused by an incomplete desorption reaction of $LiBH_4$ and MgH_2 due to non-sufficient contact od reaction partners. Hence, this is the proof of phase separation and incomplete reaction during cycling with remaining $LiBH_4$ in the desorbed state! As it is already known from the previous section, the phase transition of $LiBH_4$ from solid to liquid is accompanied by a reduction of density. According to the positive correlation of z and $\Delta\mu$ observed in Figures 5.55 and 5.56, liquefaction increases the amount of $LiBH_4$ in the upper sample area, accompanied by a decrease in the lower sample area. Hence, in the solid state $LiBH_4$ is present in the lower sample area, finely distributed within a dense matrix consisting of MgB_2 and LiH according to the packing density gradient of highly absorbing isotopes Li-6 and

B-10 indicated by Figure 5.54. By the increase of temperature and phase transition in terms of melting, $LiBH_4$ is 'expelled' out of the densified matrix and occupies volume in the upper sample area that exhibits a less densified structure. To quantitatively estimate the amount of $LiBH_4$ present in the desorbed state the first method described in section 5.3.2.2 is suitable, where the normalized attenuation of $LiBH_4$ that was calculated in section 5.3.2.1 is used to determine the amount of $LiBH_4$ that causes the observed difference data set for the attenuation coefficient. Since except for the thermal expansion of the sample cell no macroscopic structure change was observed, the assumption that attenuation coefficient differences can be exclusively addressed to motion and thereby the presence of $LiBH_4$ is valid. Still, thermal expansion of the sample cell and registration of the liquid state data set introduce artifacts into the combined difference volume data. Influences of registration and further artifacts are considered by thresholding the data set similar to the introduction of the environmental threshold in section 5.5.2.3. For the difference data set the threshold is derived from the average difference attenuation of the aluminum body inside the sample holder and determined to $\Delta\mu_E$ = -0.1 cm^{-1}. From the total histogram of attenuation coefficient differences shown in Figure 5.57, only voxel exhibiting $\Delta\mu$ lower than $\Delta\mu_E$ are considered in the following. The threshold is indicated by a vertical dashed line in Figure 5.57. The total difference attenuation is -2.8, which is the accumulated attenuation of all voxels in the data set. In the ideal case, the difference should be exactly zero due to conservation of mass. The deviation is due to artifacts originating of the registration of the liquid data set. Still, the overall attenuation difference is less than 0.5 % of the total attenuation and therefore neglected. With applied threshold the difference volume data set is visualized in Figure 5.58. It again shows the z-dependency of $LiBH_4$ by occurrence of voxels most dominantly in the lower sample area. All voxels shown in the Figure represent the amount of $LiBH_4$ that contributes to motion. For mass estimation of transferred $LiBH_4$ a normalized attenuation of $< \tilde{\Omega} > = 23 \pm 4$ cm^2/g is used, corresponding to an area density of $\rho_A = 0.092$ g/cm^2 for the sample center[39]. The amount of material motion is then given by

$$m_{mov} = \sum_{i=1}^{N} \frac{\Delta\mu_i \cdot V_{Voxel}}{< \tilde{\Omega} >} \cdot \Theta\left(\Delta\mu_i - \Delta\mu_E\right) \tag{5.37}$$

and calculated to $m_{mov} = 0.17 \pm 0.03$ mg, which is about 0.6 % of the total initial amount of $LiBH_4$ in the sample. However, if it is assumed that the observed motion

[39] A beam hardening effect by the sample holder is negligible, since the main element Fe shows no significant energy dependency in the concerned energy interval for the ANTARES instrument. Thus, a simple correction of the sample holder background is performed to determine the total sample attenuation of a projection and to derive the according area density as given in Figure 5.17.

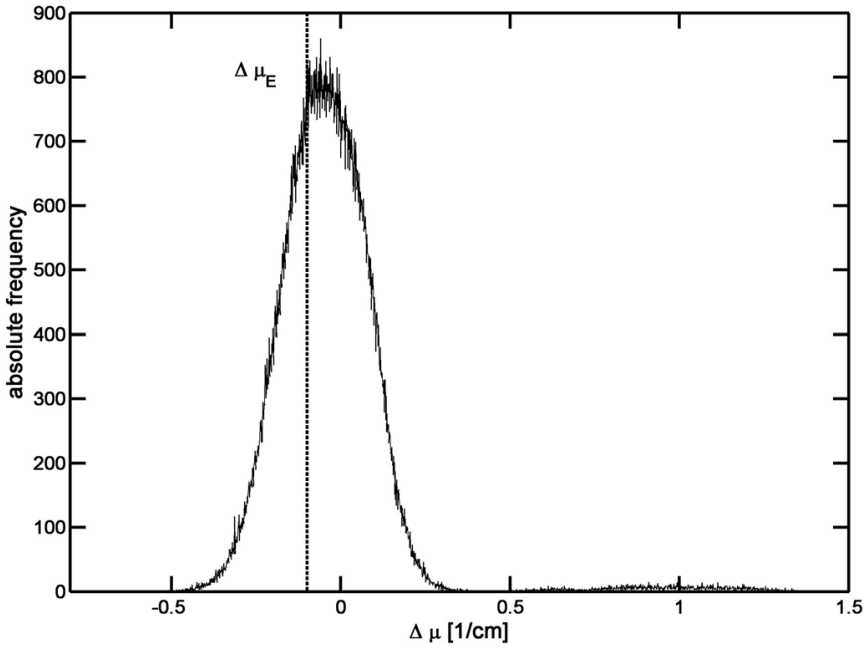

Figure 5.57: Histogram of attenuation coefficient difference, $\Delta\mu$, for the combined difference data set of liquid and solid state. For the generation of the frequency distribution, values are sorted into equally spaced bins, the number of bins is set to 2048. The vertical line shows the applied threshold, $\Delta\mu_E$ = -0.1 cm^{-1}, for consideration of artifacts.

of $LiBH_4$ is exclusively due to the phase transition and therewith the accompanied density decrease for liquefaction, the calculated amount of motion is only a fraction of the total present $LiBH_4$. With the density difference between solid and liquid state according to table 5.6, $\Delta\rho = \rho_s - \rho_l$, the total amount of $LiBH_4$ corresponding to the detected amount of motion is given by

$$m_{tot} = \rho_s \cdot \frac{m_{mov}}{\Delta\rho}$$

and calculated to m_{tot} = 2.3±0.7 mg. This is equivalent to 5-10 % of the initial amount of $LiBH_4$ in the absorbed state. Moreover, the calculated amount can be interpreted as the lower limit, since investigations are limited to the instrumental resolution with a pixel size of 73.2 μm. Hence, a significant phase separation of $LiBH_4$ and Magnesium Hydride in the Li-RHC system is proven! Since the samples have only been cycled 5 times, it can be concluded that already within the first cycle a partial and non-reversible phase separation is highly likely. Furthermore, the molar ratio of $LiBH_4$ and MgH_2 in the composition studied here is 1:1, but in the standard system it is 2:1 with an additional amount of liquid phase, further destabilizing the

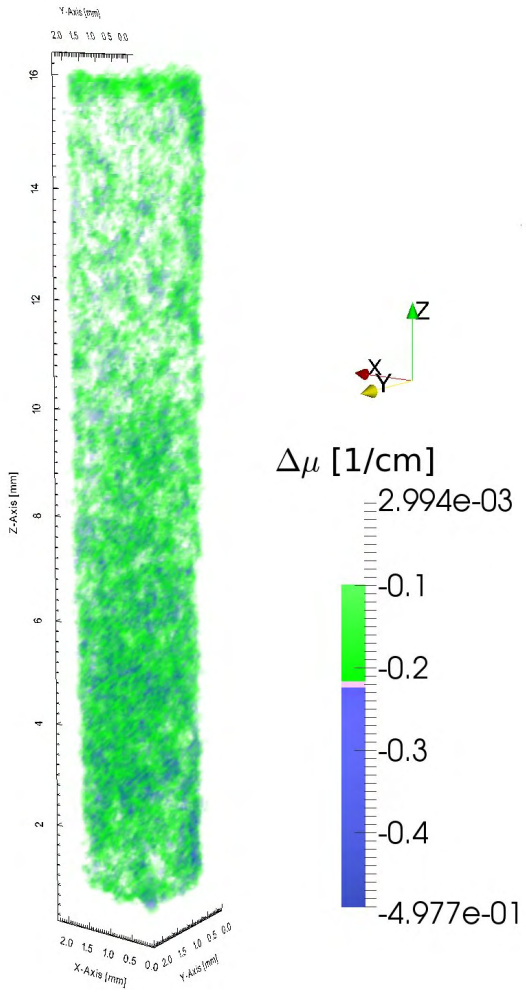

Figure 5.58: Volume data set of the difference attenuation coefficient with applied threshold $\Delta\mu_E$ = -0.1 cm^{-1}.

solid matrix and enhancing the clustering and macroscopic phase separation discussed in the upper section. There, the existence of macroscopic phase separation in terms of clustering of $LiBH_4$ was already proposed as a potential reason for the observed capacity loss of the Li-RHC system. Now it could be experimentally proven for the first-time that macroscopic phase separation of $LiBH_4$ and Magnesium Hydride is one important reason for the reported capacity loss during cycling in literature. It is highly probable that the observed clustering in case of initial phase transition and liquefaction of $LiBH_4$ persists during cycling. The initial stability of the macroscopic structure after liquefaction as found in e.g. Figure 5.40 was assumed to be due to a stable solid matrix and embedded hydrogen gas pores. During cycling, however, the sample structure is undergoing tremendous changes for nucleation and growth of new

phases for de- or absorption of hydrogen. This allows for a reordering and influence of gravity on the structure, causing a packing density gradient as found qualitatively in Figure 5.58.

Phase separation - upper sample volume Besides a phase separation resolved by the difference volume data set for the main sample volume there was deduced already a first indication of an additional macroscopic phase separation within the overview image in Figure 5.54: Above the main sample volume with its surface at about z = 1.6 cm the presence of additional material is detected, which is investigated in the following. In Figure 5.59 the attenuation coefficient distribution is shown for the solid state of the natural (upper row) and isotope composition (lower row). The

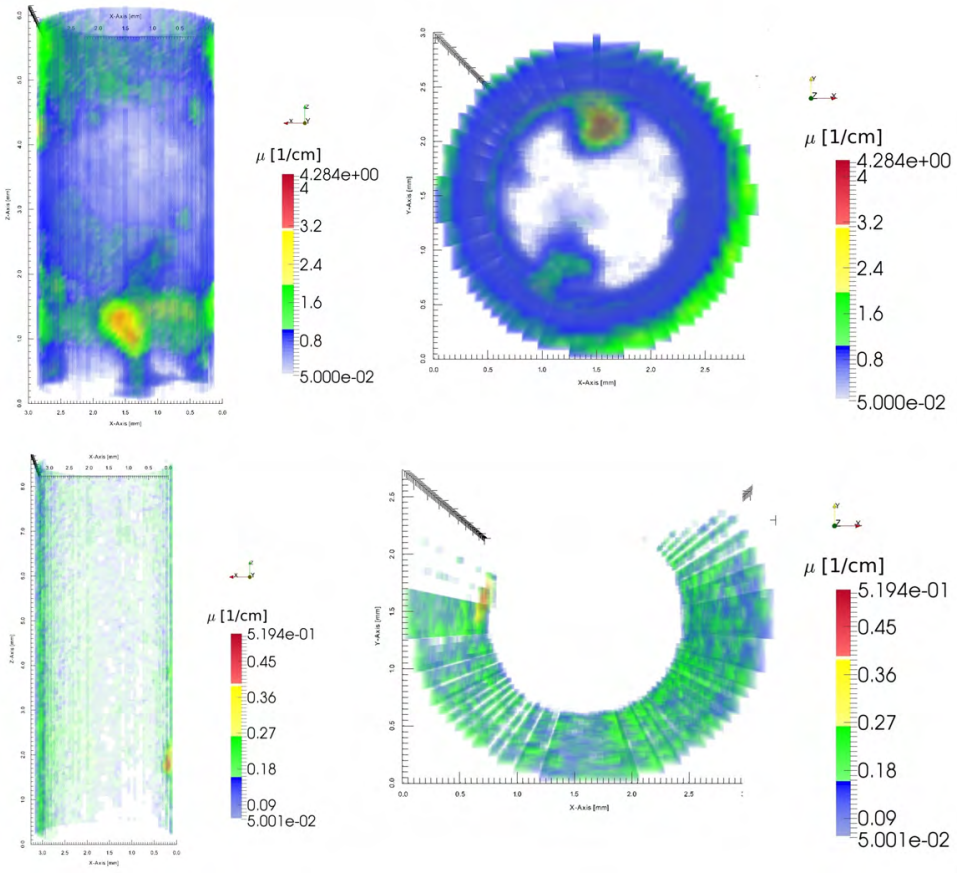

Figure 5.59: Long-range phase separation above the main sample volume for the solid state of $LiBH_4$. Upper row: Natural sample composition with vertical (left) sample position and top view in negative z-direction (right). Lower row: corresponding images for the isotope sample composition.

corresponding left is a front view in negative y-direction, the corresponding right shows

the view from the top in negative z-direction. The attenuation coefficient is scaled by pseudo-colors. For suppression of artifacts and noise, an environmental threshold of $\mu_E = 0.05$ cm^{-1} is applied. It corresponds to a suppression of attenuation coefficients within the inner free volume of the sample cell. As visible, for the natural composition the sample cell wall is wetted along the total z-distance. In addition, there are connected volumes/clusters reaching into the inner free volume of the sample cell, located in the lower and upper part of the visualized volume as shown in the top view. Within these clusters highest attenuation coefficient values of up to 4.28 cm^{-1} are observed. For the isotope composition in the lower row of Figure 5.59 wetting is less significant. According to the z-view to the right, the wetting is incomplete. In contrast to the natural composition, no clustering reaching into the inner volume of the sample cell is observed. The maximum attenuation coefficient value is 0.52 cm^{-1}. The full histogram of attenuation coefficients contributing to the volume data set given in Figure 5.59 is shown in Figure 5.60, with the environmental threshold indicated by the vertical dashed line at 0.05 cm^{-1}. Here, the normalized frequency distribu-

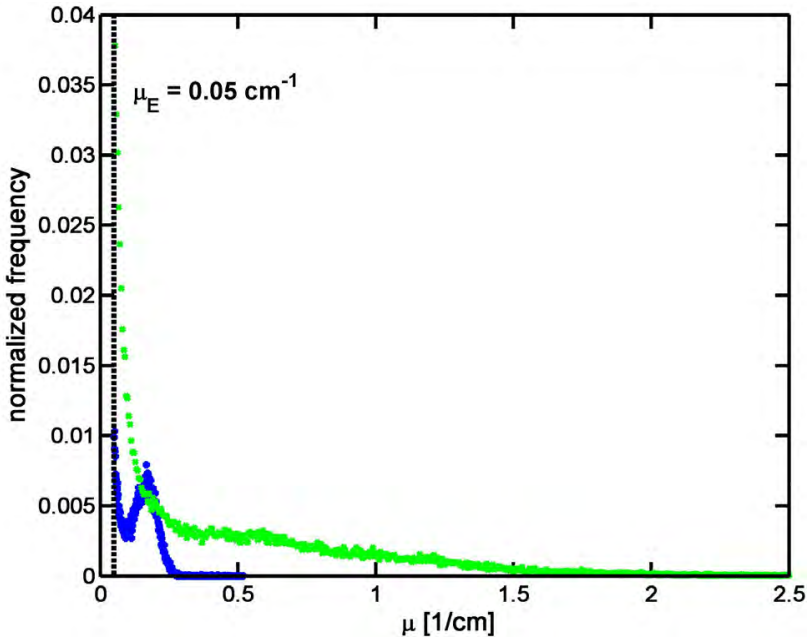

Figure 5.60: Histogram of attenuation coefficients for natural (green) and isotope (blue) composition. The frequency is normalized by the corresponding absolute amount of data points. Attenuation coefficient values from the volume data set are sorted into 1024 equally spaced bins from $\mu \in [0.05, \mu_{max}]$. The environmental threshold, μ_E, is indicated by a vertical dashed line.

tion for the natural composition is colored in green respectively blue for the isotope composition. The combination of natural and isotope sample composition allows to

determine the material that separated from the main sample and wets the sample cell wall. The ratio of the average attenuation coefficient for $\mu \in [0.8{\cdot}\mu_{max}, \mu_{max}]$ of natural and isotope composition is 8.2. This agrees approximately with the ratio of normalized attenuations for $LiBH_{4,nat}$ and $LiBH_{4,iso}$ given in Figure 5.18, which is 6.8±0.8 for the low area density and corresponding negligible beam hardening effect. In fact, beam hardening for the upper sample volume can be neglected due to the low absolute attenuation of $< \Omega > \approx 1.2$. It can be concluded that the material being macroscopically separated from the main sample volume consists of Lithium and Boron. Hence, most probably it is pure $LiBH_4$; deviations of ratios may originate of a slightly different amount of $LiBH_4$ in the two sample compositions. The reason for this phase separation and accumulation in the upper sample holder volume is assumed to be evaporation of liquid $LiBH_4$. Since the heating source is placed at the bottom part of the sample holder, a temperature gradient exists with lower temperatures for higher z-positions. Consequently, the saturation pressure of $LiBH_4$ has a similar z-dependency, which results in an effective material transport of $LiBH_4$ and condensation in the upper sample areas. This could also explain the well defined transition of separated material in the upper and the main sample volume. The different extent of phase separation for natural and isotope compositions is probably due to the different total sample amount and accordingly different surface area. The latter is directly proportional to the evaporation rate.

Using a normalized attenuation of $\tilde{\Omega} = 53{\pm}2$ cm^2/g for a negligible beam hardening according to the right part of Figure 5.17, the mass of $LiBH_4$ can be estimated in analogy to equation 5.37, but for the absolute attenuation coefficient and an environmental threshold of $\mu_E = 0.05$ cm^{-1}. This way, an amount of separated $LiBH_4$ of 0.23±0.01 mg is derived, which is about 0.7 % of the total amount of $LiBH_4$ in the initial sample composition. Originating from evaporation, it is inherent to the liquid phase of $LiBH_4$ and therewith to the absorbed state of the Li-RHC system at standard temperatures for ab- and desorption. From the small amount of separated material the saturation pressure can be assumed to be quite low, limiting evaporation and accordingly the rate of condensation and phase separation. Still, a cycling of material with well defined gas flow out of the sample volume in case of desorption enhances evaporation by induced molecule transport and separation from the main sample. This type of phase separation is clearly irreversible and inherent to a presence of a liquid phase.

5.5.3 Conclusions from Neutron Imaging studies for storage systems based on Li-RHC

From the measurement and results described and discussed in the above sections the following conclusions for storage systems based on Li-RHC can be drawn.

Loose powder samples exhibit a sintering-like densification of about 30 % upon first liquefaction of $LiBH_4$. The formation of a solid matrix is accompanied by a clustering of $LiBH_4$ at the outer boundaries of the densified solid matrix. Hereby, the gradient of the temperature field is crucial for the emergence of order and induced clustering. The latter denotes a partial phase separation of $LiBH_4$ and MgH_2. This process is system inherent, the formation of the densified solid matrix could only be avoided in case of an isothermal temperature field. Still, in real systems this cannot be realized as in particular in scaled-up samples the temperature field shows significant gradients. The structural repacking in case of first-time liquefaction of $LiBH_4$ is driven by capillary forces and minimization of surface energy. Material packing density in terms of providing a porous network, wettability and the temperature field have been identified as the most significant driving forces for motion and clustering of the liquid phase. During cycling there is an additional effect of gravity, causing a phase separation correlated to the z-position, which was present even for small sample sizes of a total height of 1.9 cm. For scaled-up samples with increased sample height, the influence of gravity is expected to be even more pronounced, adversely affecting the systems reversibility. From the results based on isotope labeling and the corresponding discussion in the above sections, the main reason for capacity degradations as reported in literature is the existence of phase separation and its persistence over cycling. A reduction of densification, structural repacking and accompanied clustering and phase separation induced by first-time liquefaction of $LiBH_4$ is achieved by pre-compaction of the metal hydride and use of pellets. It was shown that even after several cycles the main macroscopic geometry in a scaled-up pellet is preserved, though an internal motion of $LiBH_4$ over distances of 5 mm and more was observed. Against this background and with respect to the discussed mobility of the liquid phase together with the volume ratio of liquid and solid phase, the only probable reason for this macroscopic stability is a sufficient interconnection of solid particles and phases after the compaction process. In terms of the material packing density the latter has an important impact on the resulting distribution of the liquid phase. While an increased packing density and corresponding reduced average pore diameter lead to an increase of agglomeration and material transfer of $LiBH_4$ due to increased capillary forces, a sufficient free volume and porosity is necessary due to the density reduction of $LiBH_4$ in case of liquefaction,

which has been determined to 0.6-0.62 g/cm^3. Against this background, the optimum raw density in the desorbed state was found to be [0.75-0.95] g/cm^3. The temperature field is strongly impacting the final distribution of $LiBH_4$ in the absorbed state since it determines the time-sequence of liquefaction and hence the material transfer of the liquid phase. Thus, the homogeneity of the temperature field is of high importance for an equally distributed liquid phase and therewith for the reduction of phase separation. The temperature field might even be used for an improved reversibility: For the phase transition of $LiBH_4$ in terms of solidification the temperature field was identified as order parameter for the directed material transfer of the liquid phase. Hence, a particularly designed temperature field allows for a deliberate material transfer of $LiBH_4$ inside the solid matrix with the potential to reverse a present phase separation within a sample. Additionally, a long range phase separation is present due to evaporation of liquid $LiBH_4$. The evaporation rate was proposed to scale with the total sample surface and the saturation pressure of $LiBH_4$. With respect to the latter, a continuous pressure-discharging flow as part of a desorption setup increases the total amount of evaporated $LiBH_4$, so that time intervals for pressure ramps have to be minimized.

It is stressed again, that cold Neutron Imaging of isotope labeled lab-scale samples sizes has proven to be an ideal tool for the precise investigation of the distribution and fundamental dynamics of $LiBH_4$ inside the Li-RHC system. For the investigation of scaled-up samples, fission Neutron Imaging using fission neutrons was shown to give unique insights into macroscopic material transfer and sample structure, serving as the relevant characterization tool for scaled-up Li-RHC systems.

Chapter 6

Summary and conclusions

The following part is separated into summaries concerning method development respectively its application to metal hydride systems and according results for sodium alanate and Li-RHC.

6.1 Methods for Neutron Imaging

Within this work, methods for the precise quantification of the time and spatial resolved hydrogen distribution by combination of nuclear physics theory and thermodynamic quantities have been developed. A standard experimental setup of Neutron Imaging combined with monitoring of temperature, pressure and hydrogen flow to the metal hydride bed has been proposed. In the framework of data quantification, a method for the determination of the scattering field has been introduced. Scattering contributions are found to be non-significant for sufficient sample detector distances (about 15 cm), resulting in a linear correlation of beam attenuation by hydrogen and the corresponding absorbed hydrogen content and thereby confirming the validity of Lambert Beer's law. A linear correlation is the basic requirement for the quantification of the distribution of hydrogen in the metal hydride bed. The main advantage of the combination of thermodynamic data and macroscopic attenuation is its independence of the absolute neutron-hydrogen interaction cross section, which makes it superior to conventional quantification techniques that all rely on this very same absolute cross section. One of the highlights of this work is the development of a correlation analysis by the combination of multiple macroscopic fields. The associated transformation from real to correlation space allows for a unique investigation of the interdependency of driving forces in metal hydride systems by means of a multi-correlation analysis. This takes the investigation possibilities of Neutron Imaging much further than a sole and

classical 'imaging' of metal hydrides and paves the way for an optimization of hydrogen storage tanks and metal hydride systems: A single in situ Neutron Radiography investigation on metal hydride samples and sample environments that are designed for addressing a specific scientific question, e.g. by a well-defined material packing density or temperature gradient, can substitute several hundreds of classical ex situ or in situ Sieverts or compaction measurements to study the influence of e.g. the material packing density or the temperature field. Additionally, it reveals unique insights into the explicit hydrogen distribution in the metal hydride material inside a storage tank.

The methods have been developed by use of fission neutrons due to the associated investigation possibility of scaled-up samples and hydrogen storage tanks. The usage of fission neutrons bears the advantage of a reduced neutron-matter interaction cross section and accordingly higher transmission. Additionally, the lower energy dependency of interaction cross sections reduce effects of beam hardening, even for large samples with high area densities. Still, the developed methods are as well applicable for other neutron energy spectra, allowing for comprehensive analysis of metal hydride systems by means of Neutron Imaging. Hence, these methods are proposed as standard techniques for the investigation and optimization of scaled-up metal hydride systems.

While the above mentioned methods were developed for solid-state metal hydrides, liquid-solid mixtures as the Li-RHC require a different approach due a possible material transfer of the liquid phase throughout the reaction. A threshold condition was developed for the detection of material transfer by use of the maximum theoretical hydrogen content of the system. Even more, this allows for an estimation of the material mass involved in motion. It was shown that the lower limit of the material transfer distance can be determined by a selected binning of the image data. Another highlight of method development in this work is the first-ever use of isotope labeling for cold Neutron Imaging in combination with highly absorbing isotopes, which gives exclusive insights into their dynamics and spatial distribution. As a model system, Li-RHC was used with Li-6 and B-10 exhibiting a high neutron absorption cross section in the cold neutron energy regime. A calibration was performed with different mixtures of the natural sample composition and isotopically enriched Li-7 and B-11 within $LiBH_4$, showing a significant effect of beam hardening for the natural, highly absorbing sample. This is found to be in good agreement with the so-called 'bimodal energy model', originally developed by Van de Casteele et al. [124] for X-ray imaging techniques, and calibration curves have been derived for the attenuation by natural

$LiBH_4$ correlated to the area density of the latter. This allows for a mass estimation of $LiBH_4$ based on Neutron Imaging data. The introduced isotope labeling technique for Neutron Imaging is expected to heavily impact the general application of Neutron Imaging for material science. In particular, it bears a tremendous potential for the analysis of metal hydrides since a lot of promising systems contain either Lithium or Boron, which gives access to phase sensitive measurements without loss of the spatial resolution. In total, the developed methods in this thesis enlarge the analyses potentials provided by Neutron Imaging and support an intensified use of Neutron Imaging for research on metal hydride materials.

In the framework of the development of multi-correlation analysis, a new technique for determination of the temperature field of scaled-up metal hydride beds has been developed: The tank surface temperature field derived by IR-Thermography has been proven to agree well with the internal metal hydride bed temperature in thermal equilibrium. Additionally, the high potential also for in situ measurements is shown in section 7, facilitating the determination of temperature fields for metal hydride systems with respect to classical thermocouple-based measurement.

6.2 Application to metal hydrides

The developed methods have been applied to two different promising metal hydride systems. Techniques for solid-state metal hydrides have been applied to a scaled-up system of compacted sodium alanate by use of a fission neutron spectrum. In fact, this was the first-ever quantitative in-situ investigation of a complex hydride. Moreover, methods developed for liquid-solid systems have been applied to Li-RHC, which is the first Neutron Imaging study of a Reactive Hydride Composite material. A scaled-up Li-RHC pellet has been investigated again by use of a fission neutron spectrum while a lab-scale sample has been investigated using isotope labeling and a cold neutron spectrum.

For the scaled-up sodium alanate pellet the material packing density distribution could be calculated by means of the developed methods using a normalization procedure of the material attenuation to the total material mass. The packing density was found to be significantly non-homogeneous, resulting from an irregular bulk powder density before the compaction process. This shows, that a single Neutron Radiography experiment can be used as a quality check of metal hydride pellets. It further emphasizes the importance of a sufficient pre-processing of metal hydride powder by means

of a homogenized bulk powder density within the press matrix. The quantification of the hydrogen content by means of developed methods has revealed a non-homogeneous distribution and evolution of the hydrogen content inside the pellet, present even at the end of the absorption process. By multi-correlation analysis the reason for this kinetic differences was studied and a dominant effect of the material packing density was found for a homogeneous temperature field with differences less than 5 °C. The correlation analysis has been reduced in dimension from 3D to 2D, allowing for a quantification by the Pearson correlation coefficient. A significant negative correlation between packing density and hydrogen content has been found. For the first time, the detailed time-resolution of the correlation evolution reveals a dependency on the absorbed hydrogen content, hinting to a permeation and diffusion controlled limitation of kinetics in case of high packing densities. The particular time evolution is uniquely resolved by in situ Neutron Radiography and additional macroscopic fields of temperature and packing density. For optimized absorption processes of scaled-up metal hydride compacts, a homogeneous packing density is a basic requirement demanding an optimization of the compaction process. It emphasizes the necessity of a sufficient pre-processing of metal hydride powder to ensure a homogenized bulk powder density within the press matrix to hinder kinetic differences inside the pellet, aiming at the optimization of the whole storage tank.

For the scaled-up Li-RHC pellet investigated by fission Neutron Imaging, again a non-homogeneous material density distribution has been derived. The time-resolved and quantified hydrogen distribution reveal an initial negative correlation of packing density and kinetics as already determined for the solid-state sodium alanate system. Multi-correlation analysis additionally reveal a contributing effect of high temperatures on the reaction rate. Hence, the best kinetics are found for low material density and high temperatures of 380 °C. However, for the ongoing reaction this correlation does no longer hold: For the first time, motion could be detected in the Li-RHC system by hydrogen pseudo-contents exceeding the theoretical maximal capacity of this system of 11.2 wt.%. The detection of motion is a direct result of the application of developed methods for liquid-phase systems. The material transfer can be addressed to the liquid phase of $LiBH_4$. By selective radial binning, the lower limit of the motion distance has been estimated to 5-23 mm. The amount of $LiBH_4$ involved in motion is about 36-196 mg, which corresponds to 0.4 % to 2.3 % of the total amount of formed $LiBH_4$ in the system. This effect of motion is an important (if not the only) reason for the overall reduced hydrogen capacity of the Li-RHC system, where in this absorption study only 7.9 wt.% are achieved. By multi-correlation analysis, the desorbed state

packing density that corresponds to an attraction of $LiBH_4$ has been determined to be in the range of [0.75-0.95] g/cm^3 and is considered as the optimal packing density for the Li-RHC system. The evidence of motion and agglomeration of the liquid phase at the as-mentioned densities could be confirmed by a combined Neutron Tomography analysis of the ab- and desorbed state. Furthermore, it has been shown that motion and agglomeration is not a surface effect but involves the total pellet volume. Hence, for an optimization of scaled-up pellets the a priori material packing density should not exceed the as mentioned 0.95 g/cm^3 to prevent an expulsion of $LiBH_4$ of the solid matrix and in order to counteract a long-range material transfer and phase separation. As a driving force for material transfer an equilibrium of capillarity provided by the porous solid phase framework, surface energy and free volume is proposed. The model relies on the properties of $LiBH_4$ including its phase transformation and dynamics respectively mobility inside the solid framework provided by mainly Magnesium Hydride. These fundamental material properties have been investigated with high-resolution cold Neutron Imaging and use of the developed method of isotope labeling for an exclusive tracking and analysis of $LiBH_4$.

For an increased beam transmission a molar ratio of 1:1 of absorbed $LiBH_4$-MgH_2 with identically prepared samples has been used: a natural composition and an isotopically enriched composition by Li-7 and B-11 with low absorption cross sections. In situ Neutron Radiography measurements of the first-time liquefaction of $LiBH_4$ revealed a sintering-like densification of the whole sample of about 30 %. Another highlight of this work regarding material characterization is the Neutron Tomography analysis of the isotope labeled samples, both performed in the liquid and solid state of $LiBH_4$. The densification process was found to induce a clustering of $LiBH_4$ with large cluster volumes of up to 0.25 mm^3 at the boundary of the solid matrix, where the latter is a densified solid framework of MgH_2, in which $LiBH_4$ is dispersively distributed. The clustering is accompanied by an emergence of order of the initial homogeneous bulk powder density and denotes a partially macroscopic phase separation of $LiBH_4$, which could be shown in this work for the first time ever. The temperature field and its gradient along the sample symmetry axis was identified as an order parameter for the clustering of the liquid phase and the formation of the solid matrix. By combination of Neutron Tomography data sets for the liquid and solidified states, the density increase of $LiBH_4$ upon phase transformation from solid to liquid could be determined to 8-11 %, corresponding to a liquid density of 0.60-0.62 g/cm^3. Solidification of $LiBH_4$ caused an emergence of clustered material at the sample boundary and by registration of data sets this observation could be assigned to an effective motion of $LiBH_4$ from the solid matrix to the sample boundary. Again, the explicit radial temperature gradient

is proposed as the underlying driving force. The effects of clustering accompanied by a densification and emergence of a solid matrix in case of low contact angles as well as an induction of ordering with symmetry depending on the explicit temperature field (denoted as order parameter) can be generalized to any system exhibiting a mixture of solid and liquid phase. According to the results of microscopic and macroscopic phase separation (even in lab-scale samples) that superimpose with kinetic limitations referring to micro- (e.g. particle size distribution) and nanoscale (e.g. grain boundaries, additive distribution), the optimization of such a system is identified as a multi-scale problem! It sheds new light on strategies for system improvements by adding the macroscopic dimension as part of the rate limiting steps in terms of a necessity for reversibility of the phase separation by permeation and diffusion of species.
In addition to the effect of the initial liquefaction of $LiBH_4$, the effect of cycling has been investigated again by Neutron Tomography and isotope labeling using cold neutrons. For the first time, a macroscopic phase separation could be shown for a cycled Li-RHC system. $LiBH_4$ is identified in the desorbed state of Li-RHC by volume expansion due to phase transition induced by an increase of temperature. A significant dependency on the sample height was found, indicating the effect of gravity during cycling, which adversely affects the contact area of reaction partners. By use of the calibration curves derived within the method development, a phase-separated amount of 2 mg of $LiBH_4$ has been calculated, which corresponds to 5-10 % of the initial amount of $LiBH_4$ in the absorbed state. The results of phase separation analysis are of high scientific impact for optimization and tailoring of materials, since for the first time they give profound reasons for observed capacity degradation and kinetic limitations in the Li-RHC system. In addition to the phase separation within the main sample volume, a macroscopic and long-range phase separation of $LiBH_4$ has been identified in the upper part of the sample holder. This is explained by evaporation of liquid $LiBH_4$ and condensation in the upper sample holder part at corresponding temperatures below the melting point. A total evaporated amount of $LiBH_4$ of 0.23 mg has been calculated, corresponding to 0.7 % of the total initial amount. Besides the internal phase separation, the effect of long-range and irreversible phase separation due to evaporation of liquid $LiBH_4$ is crucial for the longterm cyclic stability and capacity of the sample. A probable solution to these effects is discussed in section 7.

It is finally remarked that the developed methods show a tremendous potential for investigation of metal hydride systems on the micro- **and** macroscale, where the chosen energy spectrum defines the possible dimension of investigation. Cold Neutron Tomography of isotope labeled samples of Li-RHC opens a new field of research due to

the observation of clustering and phase separation as summarized above. Such a kind of analysis is exclusively possible using Neutron Imaging and the developed methods of this work. This paves the way for an optimization of metal hydride systems - both concerning fundamental properties as well as concerning scale-up and development of storage tanks with respect to application.

Chapter 7

Outlook and perspectives

This section is subdivided into a methodical and a metal hydride related part.

7.1 Method development

7.1.1 IR-Thermography

In addition to the good agreement of the temperature field distribution measured within the storage tank FlexiStore and the tank surface temperature derived by IR-Thermography for the case of thermal equilibrium, there is a high potential for time-resolved measurements of ab- and desorption processes. Proof of principle in situ measurements of the hydrogen absorption of a sodium alanate pellet inside the FlexiStore tank have been performed. In the following, first preliminary results are given. The pellet was of 77 mm diameter with a thickness of 9 mm and mass of 49 g. The hydrogen absorption was started from thermal equilibrium at a temperature of 125 °C and ambient pressure. The latter was continuously increased up to a maximum of 85 bar with a constant hydrogen flow of 1 l_n/min. The temperature evolution due to the heat of reaction has been monitored by two thermocouples in the center: on the pellet surface respectively inside the tank wall according to Figure 4.3. Additionally, the tank surface temperature in the center was determined by in situ IR-Thermography. The obtained results show a promising time resolution of the two temperature peaks associated to the two reaction steps according to Figure 2.7 as shown in Figure 7.1. The red and the green curve correspond to the thermocouple in the storage tank placed on the metal hydride pellet respectively to the thermocouple in the tank wall. The black curve corresponds to the averaged temperature inside a region of interest on the tank surface center derived by IR-Thermography. As visible, both, magnitude as well as time-resolution of the surface temperature, agree well to the metal hydride

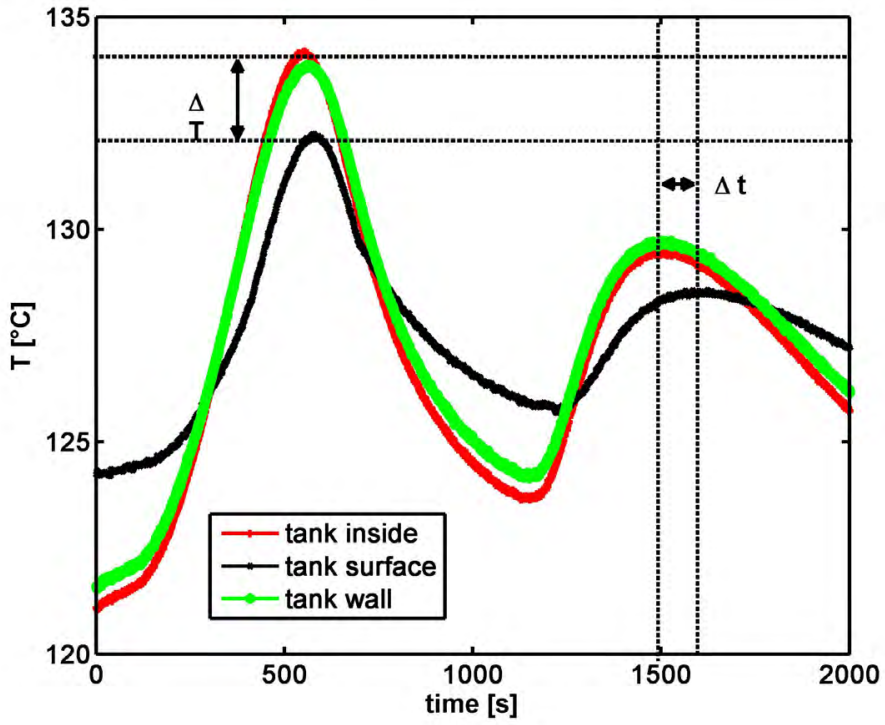

Figure 7.1: Temperature evolution for hydrogen absorption of a sodium alanate pellet. The plot shows temperatures of the pellet center (red), the tank wall center (green) and an averaged ROI on the tank surface center (black), where the latter has been derived by in situ IR-Thermography.

temperature: The difference of the temperature maxima of pellet and tank surface for the first absorption step is about 2 °C respectively 0.9 °C for the second absorption step. The corresponding time difference of temperature maxima is 25 s respectively 115 s. Further investigations have to be carried out to reveal the explicit correlation of time, amplitude and spatial resolution to the pellet-tank contact and the storage tank material. Still, a precise derivation of a time and spatial resolved temperature field is possible, highly improving the principle and methodical possibilities of storage tank temperature field measurements.

7.1.2 Neutron Imaging

With the above shown potential for in-situ resolution of the metal hydride temperature field, it is possible to combine in situ IR-Thermography with in situ Neutron Radiography for the study of fast sorption reactions. This would take the developed method of multi-correlation analysis one step further: additional multiple macroscopic

fields are then as well time-resolved, enabling access to the evolution of the heat of reaction and its complex correlation to the hydrogen distribution in the frame of the interdependency of the driving forces temperature and material packing density. The overall effect of scattering in case of thermal and cold neutron imaging has to be clarified as it has been done in the frame of this work for a fission neutron spectrum to ensure a linear correlation of the attenuation by hydrogen and the corresponding amount of absorbed hydrogen. Therewith the basis is set for a further application of the developed methods by use of thermal and cold neutron spectra with increased spatial resolution. Additionally, the corresponding wavelength of neutrons and their sensitivity for material structures can be used for a phase-sensitive investigation: the explicit use of Bragg-scattering on lattice structures has already been shown to be suitable for structural analysis by means of Neutron Imaging. However, within an in situ absorption process there is a superposition of attenuation change due to hydrogen concentration changes and structural changes without a possibility to distinguish between them within a direct imaging based on transmission intensity measurements. Still, it is possible to measure the coherently scattered signal originating from neutron-structure interaction with the use of a second detector as shown recently by proof-of-principle measurements by Peetermans et al. [89, 88]. Hence, a combined setup for imaging and diffraction measurements would allow to reveal the spatial distribution of hydrogen by means of Neutron Imaging and additionally give phase sensitiveness by the analysis of the scattered signal. The method of isotope labeling in Neutron Imaging and its high potential for tracking of specific phases has been shown within this work. A preparation of two samples is necessary to derive an absorption contrast between two isotopes of the same element. However, this demands the assumption of comparability of the two samples, which might not always be given, in particular for large metal hydride bed geometries. A possibility to overcome this measurement uncertainty is the combined use of cold/thermal and fission neutron spectra: due to the strong energy dependency of absorption cross sections of highly absorbing isotopes, the change of neutron energies towards the fission energy range has the same effect as a substitution with the low-absorbing isotope. It brings the advantage that only one sample is necessary and no assumption on comparability have to be taken. Due to the limited resolution of fission Neutron Imaging instruments, this dual-energy approach is in particular suitable for larger sample geometries. Against the background of the current development of powerful spallation sources like the ESS, the exclusive features of their corresponding spectra can as well be used for a phase sensitive analysis: Within the pulsed spectrum the energy resolution is related to the time domain between two pulses. Hence, this brings the same advantages as discussed above, but without the necessity to change

between instruments. Additionally, the continuous energy spectrum sets no constrains to the spatial resolution.

7.1.3 X-ray Tomography studies

Though Neutron Imaging gives unique insights into the distribution of hydrogen or phases addressable by isotope labeling, a precise investigation of the material structure on the micro- or nanoscale is not possible due to the limited spatial resolution. Changing the probe to photons and performing corresponding measurements at a synchrotron facility, a micro or even nano Tomography is possible due to the significantly higher L/D and the ability of beam focusing. Additionally, the photon flux is about 5 orders of magnitudes higher, allowing for a significantly better time-resolution for the study of in-situ processes. The imaging principles as well as image reconstruction as introduced in the theoretical section remain unchanged, though the interaction potential changes: in case of the neutron-matter interaction the relevant potential is the nuclear potential, resulting in a highly dependent interaction cross section on the explicit nucleus composition and differences among isotopes as in detail described in the theoretical section of this work. In case of photon-matter interaction the relevant potential is given by the electron density configuration of the element, resulting in an increasing total interaction cross section with the atomic number. Thus, in contrast to Neutron Imaging the cross section of hydrogen is low in comparison to heavier elements, allowing for a precise studies of the raw material structure. In the following, a brief analysis of an ex-situ micro Tomography of a fragment of a cycled sodium alanate pellet is shown to give an impression of the high analysis potential for material structure investigations of metal hydrides.

The measurement has been performed at the micro Tomography station at the beamline P05 at Petra III at DESY [51]. The photon energy was set to 15 keV. The used CCD camera has a pixel array of 3056×3056 pixel, the pixel size is 1.2 μm. The effective resolution by means of 10 % of the MTF (see appendix A.1.1) was determined to 1.31 μm. In total, 1700 projections have been acquired with an image exposure time of 200 ms. The image reconstruction was done with a backfiltered projection algorithm implemented within an IDL[1] routine. Volume data processing and analysis was done with *VGStudio* and *ImageJ*. For noise reduction, all images have been (2×2)-binned, resulting in a pixel size of 2.4 μm. The investigated pellet fragment was cutted from a 10-times cycled sodium alanate pellet of diameter 60 mm and 6 mm thickness with an initial material packing density of 1.4 g/cm^3. The sample holder, a standard glass capillary sealed with Plasticine, was glued onto the sample stage to ensure a fixed

[1] IDL - Interactive Data Language, Exelis Visual Information Solutions, Inc.

sample position on the rotation unit. In the left part of Figure 7.2 an overview of the attenuation coefficient distribution of the pellet fragment is given. The attached

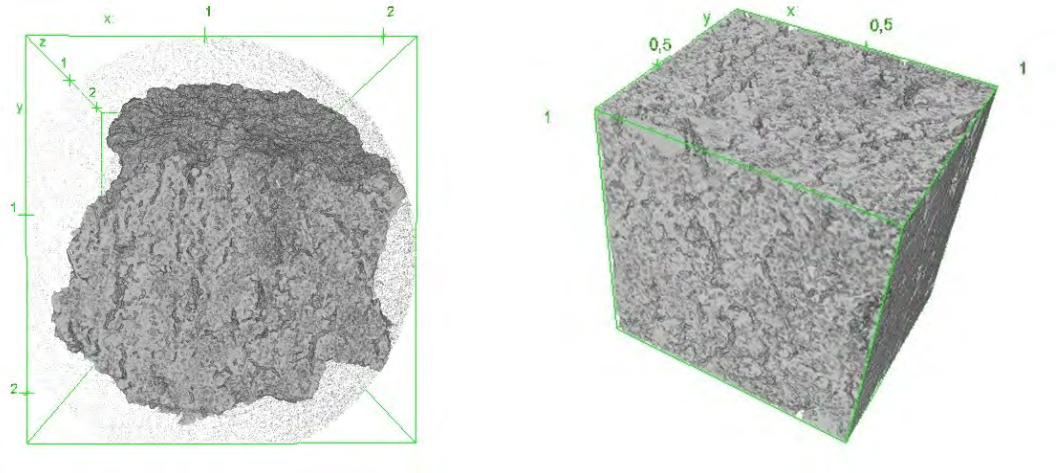

Figure 7.2: Left: Volume data set of attenuation coefficients from a sodium alanate pellet fragment, derived by X-ray micro Tomography. Axes are scaled in mm. Right: Inner sub-volume of the left total volume selected for pore analysis.

axes are scaled in millimeter. Higher gray values correspond to larger attenuation coefficients, referring to the metal hydride material. As visible, the fragment exhibits a large number of cracks and channels that can be further analyzed using the tools and methods already introduced within this work. To reduce the amount of data and exclude any influence of the fragment-cutting process, a center subset of the total volume is selected, shown in the right part of the Figure. An analysis of the pore-volume distribution has been performed. Therefore, the *Particle Analyser* plugin [3] has been used as shown in appendix B.4 for calculating the particle volume distribution, but here with an inversed threshold condition (equation B.1)[2]. The volume frequency distribution is normalized to the absolute number of pores and shown in the right part of Figure 7.3. Additionally, an exemplary (x,y)-slice of the sub-volume in Figure 7.2 is shown in the left part. The attenuation coefficient is scaled by pseudo-colors, with void areas colored in blue. The remaining voxel correspond to the metal hydride material. Since the pore-volume analysis is limited to *closed* pores only and the maximal pore volume is found to be in the order of 10^3-10^4 μm^3, the large voids visible in the slice image are interconnected cracks and *not* pores! Crack formation in compacts due to cycling was already reported in literature(e.g.[77, 66]), but so far limited to the surface analysis by optical microscopy. Here, a full three-dimensional analysis is possible, revealing the surprising interconnection of cracks accompanied by small and dispersed

[2]Thus, it is $\forall \mu_i \leq \mu_{TC}: \quad \mu_i := 1$, with $\mu_{TC} = 0$ cm^{-1}

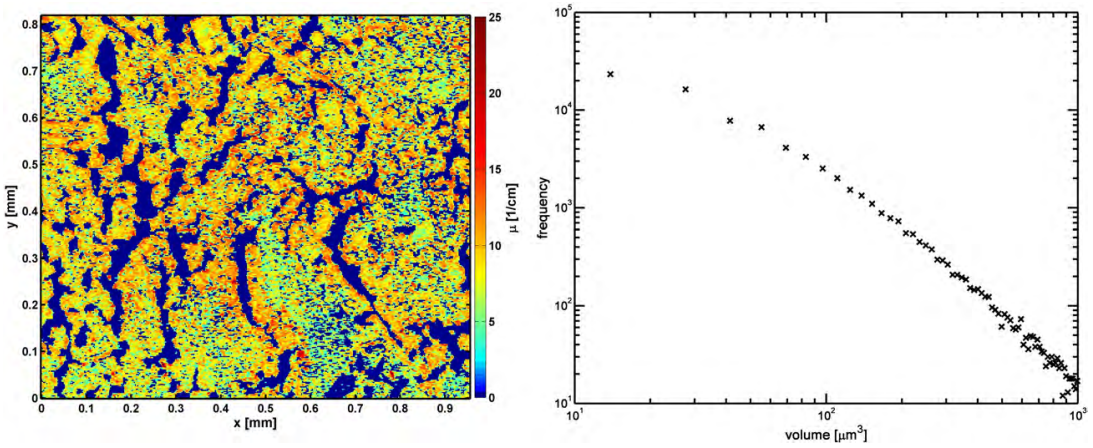

Figure 7.3: Left: Slice of the subvolume with the attenuation coefficient scaled by pseudo colors. Right: Log-log plot of the frequency distribution of the determined pore volumes.

closed pores with a volume of about 10 μm^3 according to the histogram. These closed pores probably emerge during phase-change and reordering of the lattice structure as part of a self-organized process. Though, the log-log plot of the corresponding histogram shows no power-law behavior. This is left without further discussion, emphasizing only the methodical power of micro Tomography investigations. Even more, the emergence of pores and cracks can be investigated in-situ due to the low image acquisition time, contributing to a fundamental understanding of sorption mechanism and accompanied structural changes.

However, it is stressed that the most comprehensive investigation of metal hydride materials (both fundamental and scaled-up), is realized by a complementary use of both probes: photons and neutrons. The combination of two unique investigation possibilities concerning structure and metal hydride matrix (photons) and hydrogen (neutrons) has the potential to give a fully and clarified understanding of the mechanism involved in metal hydride based hydrogen storage. Imaging techniques using photons and neutrons are wrongly underrepresented in current research of metal hydrides! In addition to new insights due to the spatial resolution, the introduced techniques for particle or pore volume analyses are at least highly complementary to small angle scattering studies. It is believed that they are even in favor since the true particle volume is imaged directly, without the need for model approaches due to the indirect measuring principle.

Concerning the investigation and optimization of hydrogen storage tanks and scaled-

up metal hydride systems, Neutron Imaging is outstanding in terms of its analysis capabilities relating to the distribution of hydrogen, in particular with respect to the methods developed within this work. Their application to further or optimized systems will greatly contribute to solve questions of tank and powder bed designs and their impact on hydrogen sorption kinetics. The method of isotope labeling for high absorbing isotopes that was first-time introduced into Neutron Imaging opens a new field of research: for metal hydrides, some of the most promising materials contain Lithium or Boron. Hence, their distribution, motion or dynamics throughout the reaction can uniquely be 'tracked'.

7.2 Metal hydride systems/ materials

Before addressing the two systems investigated within this work, it is stated that there is a general need for tank development and optimization in particular with respect to future applications of metal hydride systems. For that, an intensified use of Neutron Imaging in combination with the newly developed methods is highly recommended as it is at present the only comprehensive characterization tool for scaled-up systems.

7.2.1 Sodium alanate

As shown above, micro Tomography measurements can be used to investigate the distribution and emergence of pores and cracks. In situ measurements can reveal their correlation to the sorption process and thereby help for the optimization of the metal hydride bed structure. In additional to the fundamental properties, the sodium alanate system is already intensively characterized in terms of cyclic stability and kinetics as well. However, most of these studies are based on lab-scale measurements. Concerning scale-up and optimization, there is comparably litte effort. A possible reason might be the to date lack of as mentioned characterization techniques for storage tank systems. This work provides the basis for precise studies of in situ sorption measurements by time-resolved correlation analyses using Neutron Imaging. The challenges that have to be addressed are the interdependency of material packing density and temperature field concerning their impact on kinetics. The compaction process can be optimized by means of Neutron Imaging, where the resulting metal hydride bed has to be optimized for the explicit temperature field and heat transfer inside the storage tank. Though, right now sodium alanate appears to be the most promising metal hydride systems in terms of its use inside a scaled-up storage tank.

7.2.2 Li-RHC

The application of developed methods for the analyses of liquid-solid systems on the Li-RHC systems revealed a high mobility of the liquid phase in combination with material packing densification for the first-time liquefaction. The rearrangement and clustering of the liquid phase was accompanied by long-range phase separation. The dynamics and mobility of the liquid phase has to be further investigated since it was identified as one highly probable explanation for cyclic degradation of the hydrogen capacity. For this purpose, the introduced technique of isotope labeling in combination with Neutron Imaging gives unique insights and is the method of choice. In particular, there is the need for a more detailed analysis of the sintering process and its correlation to fundamental material or bulk powder properties. With respect to the latter, relevant quantities derived from this work are particle size distribution, wettability and temperature field. The effect of the particle size distribution can be well addressed by changed ball milling conditions since they influence the average size and shape of particles. Porosity can be affected by compaction. The wettability of solid compounds MgH_2, Mg, MgB_2 and LiH by $LiBH_4$ has a strong influence on the densification mechanism and therewith on the observed structure emergence. It can be changed by use of an adequate additive as shown by Parikh and Humenik for adding Mo to Ni in the TiC-Ni system [85]. By that, the sintering mechanism is expected to be significantly influenced!

Within the model that was developed for the densification process and structure emergence the existence of gas filled pores is of great importance. They are assumed to stabilize the solid matrix by changing the effective amount of liquid phase with respect to the overall volume. This hypothesis can be studied by means of X-ray micro or nano Tomography analogously to the study shown above for sodium alanate. According to the results derived from this work, the temperature field is supposed to have the highest impact on the phase changes of $LiBH_4$ and the accompanied effects of material transfer and emergence of an ordered structure. Thus, it is predicted that the change of the temperature field has a significant effect on the observed phase separation. Even more, it may be designed in such a way that phase separation can be reversed by cyclic phase transformations of $LiBH_4$ induced by according changes of the temperature field. It is stressed, that to address the multi-scale problem the material investigation should include Neutron Imaging (micro- and macroscale) and Xray-Imaging (nano-, micro- and macroscale) among the already used scattering techniques for a comprehensive analysis.

In addition to the sintering process itself and respective dynamics for the first-time liquefaction, the effect of cycling needs to be studied by the use of Neutron Imaging in

combination with isotope labeling to resolve the underlying mechanism and in order to optimize material properties. An in situ analysis of a complete cycle should clarify whether the observed phase separation is reversible. In situ studies of compacts are necessary, treating the effects of sintering, phase separation and cyclic degradation. A dependency of the phase separation on the material packing density is expected due to a possible expulsion of the liquid phase for high material packing densities in the desorbed state, driven by a volumetric increase upon hydride formation and liquefaction. As a general approach for the reduction of phase separation, scaffolding may be considered in future investigations.

Apart from the internal phase separation, the long-range macroscopic phase separation due to evaporation of $LiBH_4$ needs to be further investigated and reduced. Here, confinement by gas separating membranes or polymers might be a solution and need to be elucidated.

After clarification of the fundamental material properties and the associated dynamics upon the sorption reaction, the scale-up process needs to be investigated and optimized. The key issues are the effect of phase separation and its potential correlation and scaling with the sample size, the influence of gravity for large sample heights and the material transfer of $LiBH_4$ in systems with pellet stacks. Moreover, non-homogeneous temperature fields and material packing density distributions as present in scaled-up systems result in a high degree of complexity and a challenging task on the way to application.

Appendices

Appendix A

Experimental and Methods

A.1 Beamline setups

A.1.1 Determination of spatial resolution using ESF,LSF and MTF

A.1.1.1 Theoretical background

For quantification of the spatial resolution of an image it is necessary to introduce some general quantities first. In the description of imaging systems by linear response theory, a measured image is given by the convolution of the point spread function (PSF), $psf(x, y)$, and the object function, $o(x, y)$

$$I(x, y) = o(x, y) * *psf(x, y) = \int\int o(x - x', y - y') \cdot psf(x - x', y - y')dx'dy' \quad \text{(A.1)}$$

The point spread function is the system response to a point source, a delta-function. If a line object and and edge object are defined in parallel to the y-axis, the systems response to the line object is the so-called line spread function (LSF), the projection of the PSF in the direction of y and hence a one-dimensional function. The corresponding systems respond to the edge object gives the so-called edge-spread function (ESF). Its derivative in x gives the LSF

$$LSF(x) = \frac{d}{dx}ESF(x) \quad \text{(A.2)}$$

One definition of resolution is associated directly to the LSF. If the latter can be approximated by a Gaussian function, then the spatial resolution is given by the full width at the half maximum. Alternatively, resolution is defined by the full width that covers 50% or 90% of the integrated LSF according to Koch et al. [71]. In case of a non-Gaussian or non-symmetrical shape the modulation transfer function (MTF) can

be calculated. It is the Fourier transform of the LSF

$$MTF(\omega) = \mathcal{F}(LSF(x)) \tag{A.3}$$

and the resolution depends on the frequency, for which the MTF is equal to 10%, $r = 1/2\ f_{10}$.

A.1.1.2 Spatial resolution at NECTAR and effect of metal hydride material

In the following the concept of resolution measurement is applied to measurements of the FlexiStore storage tank for different sample-detector distances.

FlexiStore storage tank

For determination of the effective spatial resolution in an image of the empty FlexiStore storage tank, the edge spread function has to be calculated. Due to absence of a distinct and well-defined edge at the boundary of the tank body, the wall thickness reduction for the sinter metal filter in the center region of the tank is used (see technical drawing in Figure 4.3 in section 4.2). Before, an attenuation image is calculated according to equation 2.9 in section 2.1.1.2. A horizontal profile is computed and for increase of data statistics the tank is rotated around the center and various profiles are calculated for different rotation angles. The resulting set of profiles is shown in the left part of Figure A.1. For a more detailed description, see 'Step geometries' in

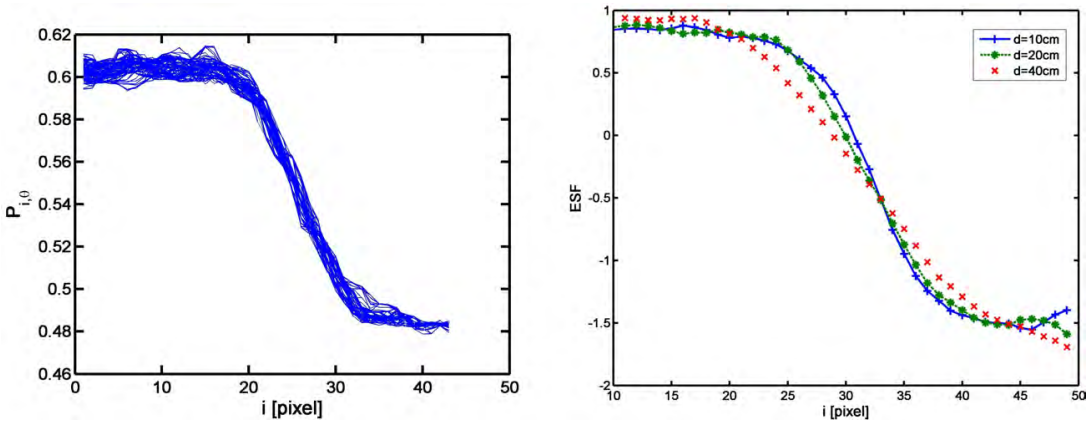

Figure A.1: Left: Set of profiles $P_{i,\theta}$ for different rotation angles θ. Right: ESF for three different sample-detector distances d=10 cm (blue), d=20 cm (green) and d=40 cm (red).

section 5.2.3.1. The profiles are averaged and a normalized ESF is calculated[1]

$$ESF(i) = \frac{P(i) - < P >}{\sqrt{Var(P)}} \tag{A.4}$$

where $P(i)$ is the average profile over the different rotation angles at position i. $< P >$ is the average attenuation of $P(i)$ and the denominator its standard deviation. In total, 6 different sample-detector distances (d = 10,15,20,25,40,60 cm) have been investigated to investigate the effect on the spatial resolution. The resulting ESF is shown for d = 10,20,40 cm in the right part of Figure A.1. As expected, the edge is significantly broadened with increasing sample-detector distance, in agreement with theoretical consideration according to the geometric unsharpness described in equation 2.10 in section 2.1.1.4. The derived LSF are shown in Figure A.2 for the different distances. All could be approximated by Gaussian, which are additionally shown in the Figure as

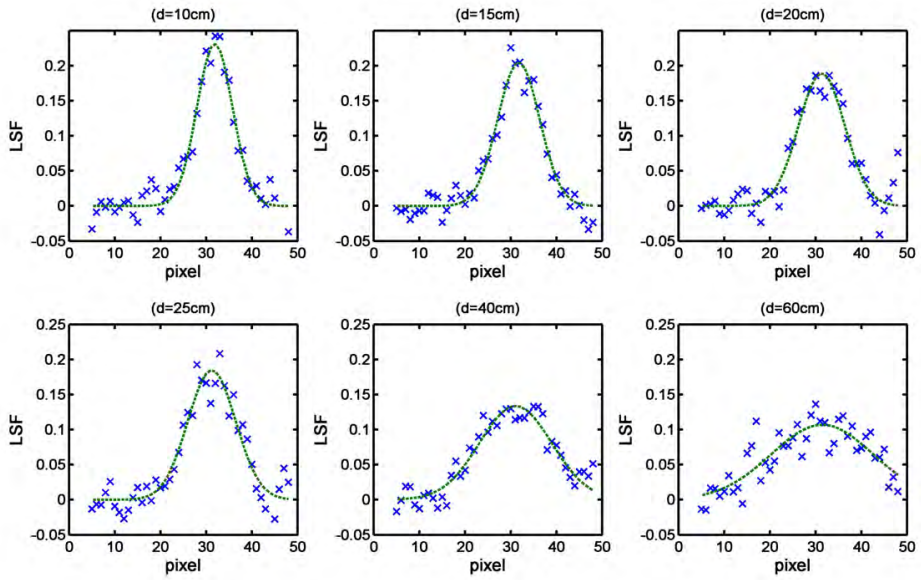

Figure A.2: LSF for different sample-detector distances (d = 10,15,20,25,40,60 cm) and Gaussian fit (dotted line).

dashed lines. Consequently, the full-width half maximum was used for calculation of the effective spatial resolution, shown in Figure A.3. At the standard sample-detector distance of 15 cm as used in the performed in-situ studies the resolution is about 3.1 mm. However, the derived dependency of resolution and distance does not totally reflect the decrease given by geometric unsharpness in terms of $d = l \cdot L/D$. According to the latter, the resolution should be significantly lower for low detector distances.

[1] Without an effect on the calculated resolution.

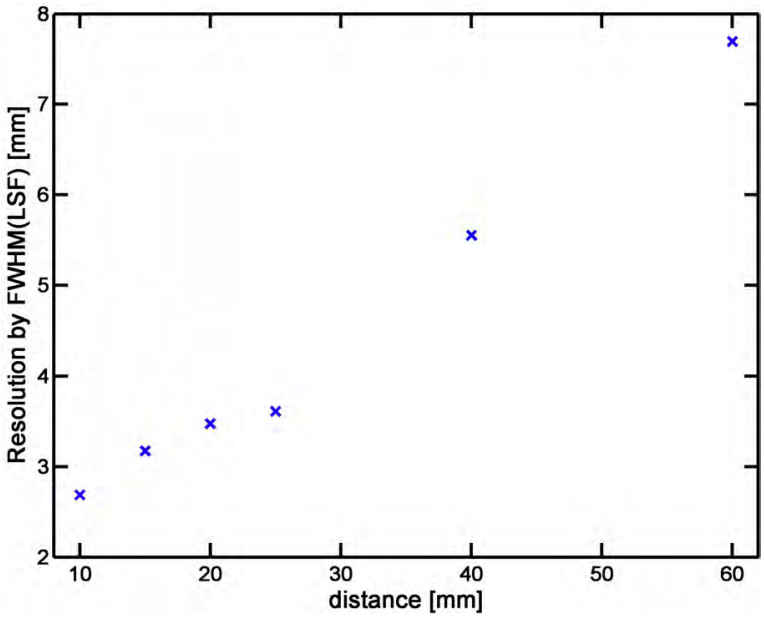

Figure A.3: Spatial resolution according to the FWHM of the LSF-fit for the different sample-detector distances (d = 10,15,20,25,40,60 cm).

Thus, for low distances a superposition of additional effects like scintillator thickness or scattering is reasonable, causing and effective lower resolution.

A.2 Loading station

To meet space requirements for sample environment at various Neutron Imaging instruments at different neutron sources the volume and design of the loading station is minimized, as can be seen in Figure A.4. In the left part a photo of the unit is shown, the corresponding schematic drawing of pipes, components and their interconnections are given in the right part of the Figure. A typical absorption process is performed with open valves V7, V9, V3 and V10 according to the schematic drawing in the right of Figure A.4. The hydrogen flow is controlled and measured by a mass flow controller (MFC) of type van Bronkhorst Maettich. Two controller types are available for different maximal hydrogen flows: a small MFC with range 1-50 ml_n/min and a larger MFC with range 100-5000 ml_n/min. A desorption measurement is performed with open valves V10, V3, V8 and V4. The internal pipe volume of the loading station was calculated by use of a reference volume and equation 4.1, it is 35 ml.

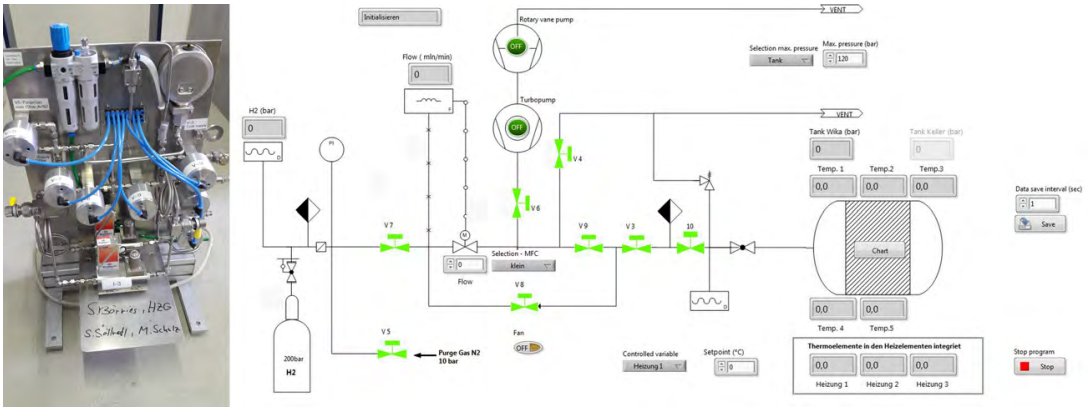

Figure A.4: Left: Photo of the loading station unit (without attached connection pipe to the hydrogen gas supply and the storage tank). Dimensions of the unit: W: 50 cm, D: 45 cm, H: 70 cm. Right: Schematic view of valves and components of the loading station.)

A.3 Aluminum Tank specifications

In the framework of this thesis a storage tank based on aluminum has been developed for maximal neutron beam transmission. Its dimensions exceed the FlexiStore tank dimensions to enable an investigation of even larger metal hydride sample sizes. The total inner volume is 0.318 dm^3, resulting of a width of approx. 90 mm, a depth of 35 mm and a height of 110 mm according to the right part of Figure A.5. The main tank body consists of $AlMg_1SiCu$ (EN AW 6061), the collar that hosts the metal expansion screws is made of steel (EN 1.4922) to provide a sufficient strength. The sealing is ensured by a FFKM polymer ring of type Perlast G92E with diameter of 85 mm and 5.33 mm thickness. The tank is heated by 4 heating cartridges at the tank corners, with a heating power of 250 W each. For temperature monitoring, 4 thermocouples can be attached, 2 on each of the large tank faces with variations in height. Due to to good thermal conductivity of aluminum, the temperature field can be precisely adjusted, e.g. to derive especially designed temperature fields exhibiting specific gradients. For a simple setup and connection of the storage tank system to the control box of the loading station, the electrical connections for the thermocouples are organized on a connector board in the lower front of the tank.
The tank can be operated at a temperature of maximal 180 °C at a pressure of 100 bar. Thus, it is limited to investigation of low and moderate temperature hydrides. The temperature and pressure range of operation was in particular chosen for operation with sodium alanate. In contrast to the FlexiStore design, the inner dimensions of the aluminum tank allow for a flexible metal hydride sample geometry and bed design.

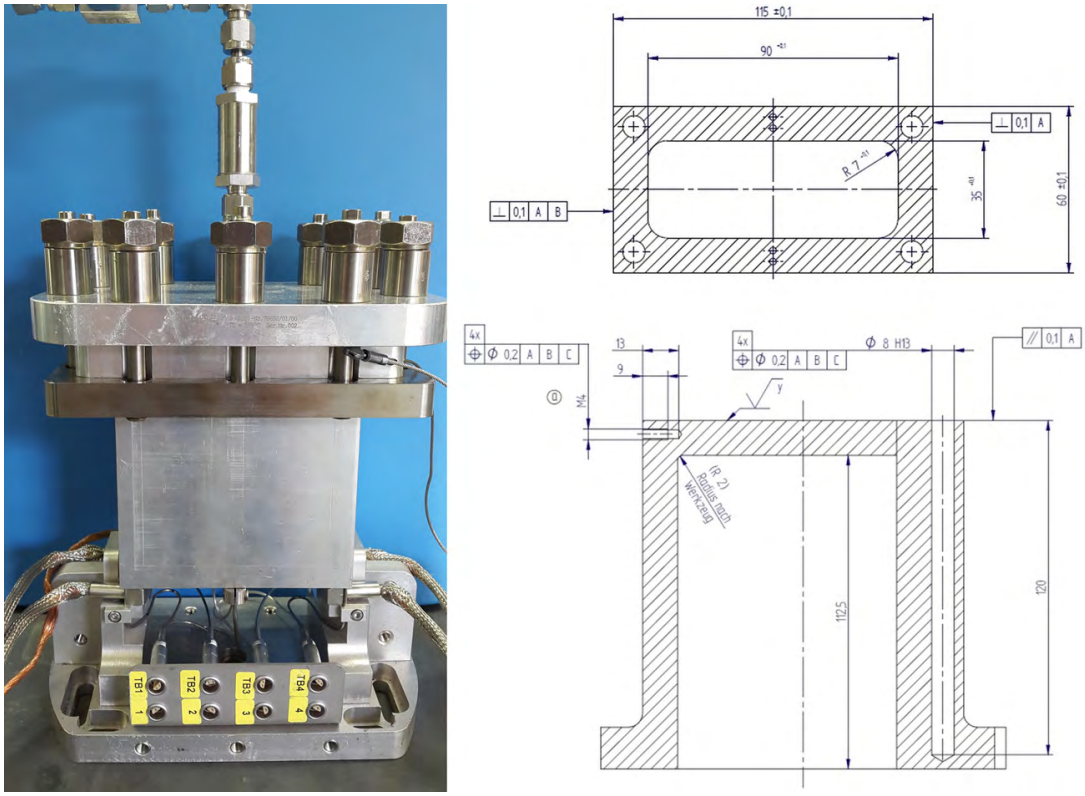

Figure A.5: Left: Frontal view of the aluminum tank with the connection board. Right: Technical drawing of the inner tank dimensions (top: top view, bottom: side cut).

For loose powder, a container made of aluminum ($AlMg_3$) can be inserted to prevent direct contact of the metal hydride material with the tank wall. For pellets, a special holder has been developed and built that allows for a centering of pellets of various diameter and again prevents direct contact of pellets and tank material[2].

A.4 Neutron Tomography data reconstruction

The Neutron Tomography data reconstruction is done with the commercial software package *Octopus* [26]. An adaptive filter is applied beforehand for reduction of image artifacts. A flat field correction based upon the intensity evolution over the different projection angles within a reference area without sample in the beam path is applied. This is to consider a potential variation of the neutron flux during the measurement. Additionally, the reference field allows to consider the influence of the scattering field

[2]In case of sodium alanate, this is to prevent a potential surface reaction of NaH or $TiCl_3$ with the aluminum tank material.

in analogy to the method described in detail in section 5.2.1. To correct for the effect of ring artifacts in the reconstructed data, a software-own ring filter (on default level 3) is applied. The software additionally offers the possibility to iteratively find the correct center of rotation. For further information the reader is referred to the software manual.

Appendix B

Results and Discussion

B.1 IR-Thermography measurements

For determination of the temperature inside the tank a metal body is used serving as a phantom. It has a diameter of 77 mm at a thickness of 10.5 mm. Two thermocouples are inserted into the tank inside through the hydrogen supply line and are placed on the surface of the phantom in different positions to record its surface temperature T_S as shown in the upper left part of Figure B.1. Accordingly, for a chosen target temperature two data points are derived from one temperature measurement in thermal equilibrium. To increase the data point density, the thermocouples are rotated within additional measurements for the same target temperature as shown in the lower part of the Figure. The corresponding positions of data points form two circles with different distance to the phantom center. This is visualized in the upper right image of Figure B.1. In total, 8 measurements are performed for one target temperature, resulting in 16 discrete data points. Due to variations of the heating power of the used cartridges for the same target temperature there is a potential small absolute temperature offset between the different measurement series, as e.g. the case in Figure 5.2 in section 5.1. For better comparison to an IR-Thermography image the data points of the internal temperature are interpolated to form a quasi-continuous field. This is shown exemplary for a target temperature of 100 °C in Figure B.2. Hence, the accuracy of IR-Thermography can readily be derived by subtracting the to images as shown and discussed in section 5.1.

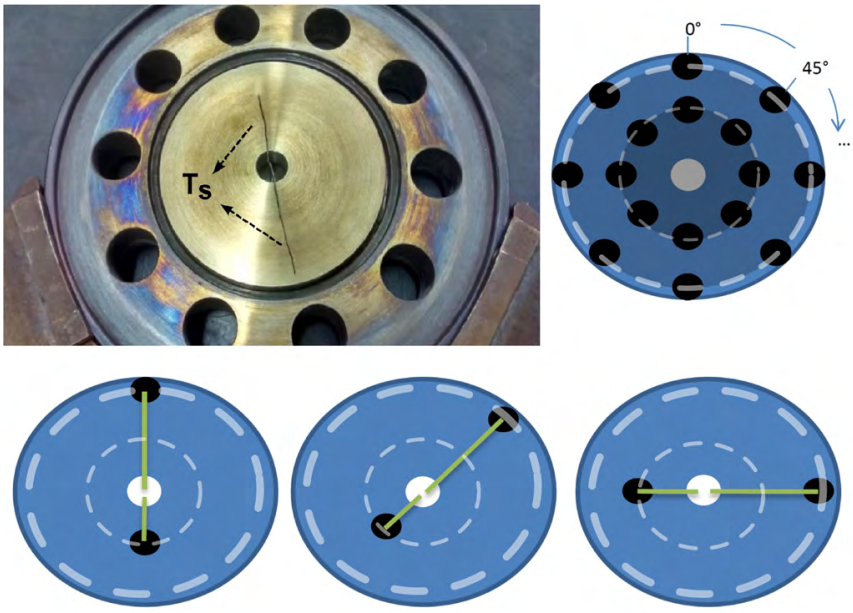

Figure B.1: Upper left: pellet phantom with exemplary position of two thermocouples at inner and outer radius for measurement of two data points contributing to the internal surface temperature T_S. Upper right: Inner and outer radii defined by subsequent rotation of single measurement positions according to the left image. Lower image: Illustration of the data acquisition principle. Each image corresponds to a single measurement.

B.2 Isotope labeling

B.2.1 Correlation of attenuation and area density for Magnesium Hydride

In analogy to the section 5.3.2, 'Isotope labling', the correlation of averaged attenuation and area density for MgH_2 as well as the normalized attenuation is calculated. For that purpose, a Neutron Radiography of a MgH_2 pellet was performed at the ANTARES instrument with the high resolution setup. The pellet has a density of $\rho = 1.071$ g/cm^3 with a mass of 239 mg, a diameter of 8.1 mm and height of 3.7 mm. It is placed with the press normal in parallel to the vertical axis. The exposure time was 55 s at a pixel size of 20.06 μm. The attenuation image is shown in the left part of Figure B.3 together with the energy dependent total neutron interaction cross sections for Magnesium-24 (green) and H-1 (blue curve). The energy spectrum at ANTARES is peaked around 36 meV [120].

In this magnitude, the energy dependency of Mg is negligible as visible in the right part of Figure B.3. This is different for hydrogen, which shows an energy dependency

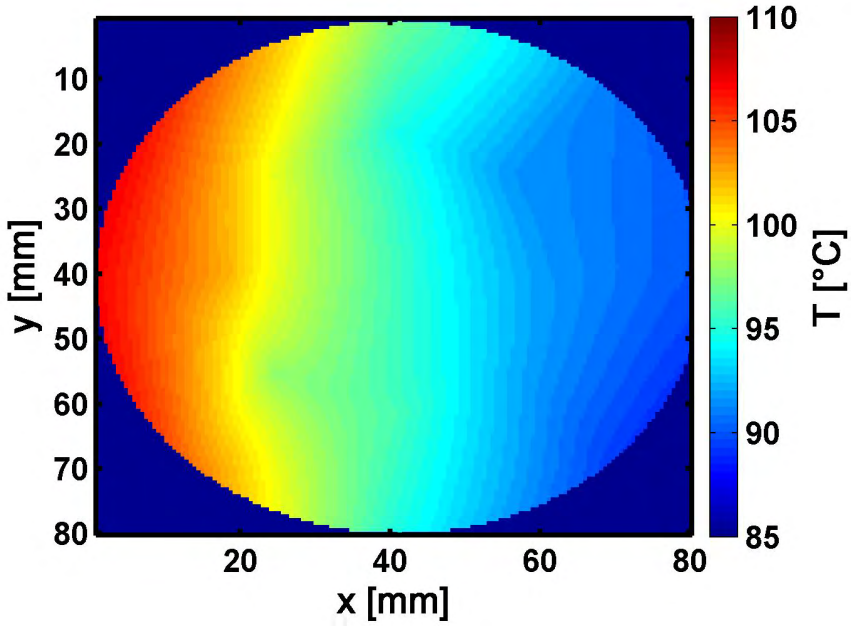

Figure B.2: Internal temperature field for a target temperature of 100 °C (reached at the center thermocouple in the tank wall of FlexiStore) after interpolation of the discrete data pairs resulting of 8 contributing measurement series.

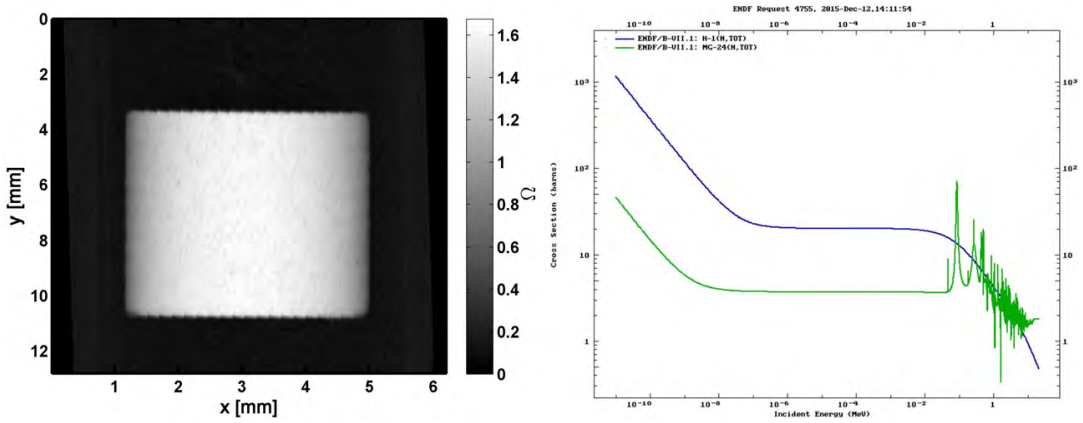

Figure B.3: Left: Attenuation image of the Magnesium Hydride pellet. Right: Total neutron interaction cross section of hydrogen (H-1, blue) and Magnesium (Mg-24, green) as a function of the neutron energy. The data is used from ENDF data base [42].

for energies in the meV range. With increasing energy there is a transition area in which the cross section converges into a plateau reaching until ≈ 10 eV. Thus, for the peak energy of 36 meV there still is an energy dependency in the cross section, allowing for a beam hardening effect by the neutron-hydrogen interaction. For the

analysis of its influence the same investigation as shown in the section 'Isotope labeling' is performed in the following.
The pellet is well aligned in the aluminum sample container. Thus, the sample thickness varies with x in the same way as it was for the Li-RHC powder samples in section 5.3.2 and a cylindrical symmetry of the area density is assumed. Since by compaction the inner porosity is reduced and the material distribution shows a higher homogeneity than in case of loose powder, the pellet is separated into subareas defined by single pixels with the y-range kept constant to cover the whole sample height. Thus, for each pixel along the x-axis a vertical data column is investigated. After correction of the sample holder background by a reference area above the pellet, the average attenuation and area density are calculated for each of the subareas. Their correlation is visualized by the lower curve in Figure B.4. The initial evolution up

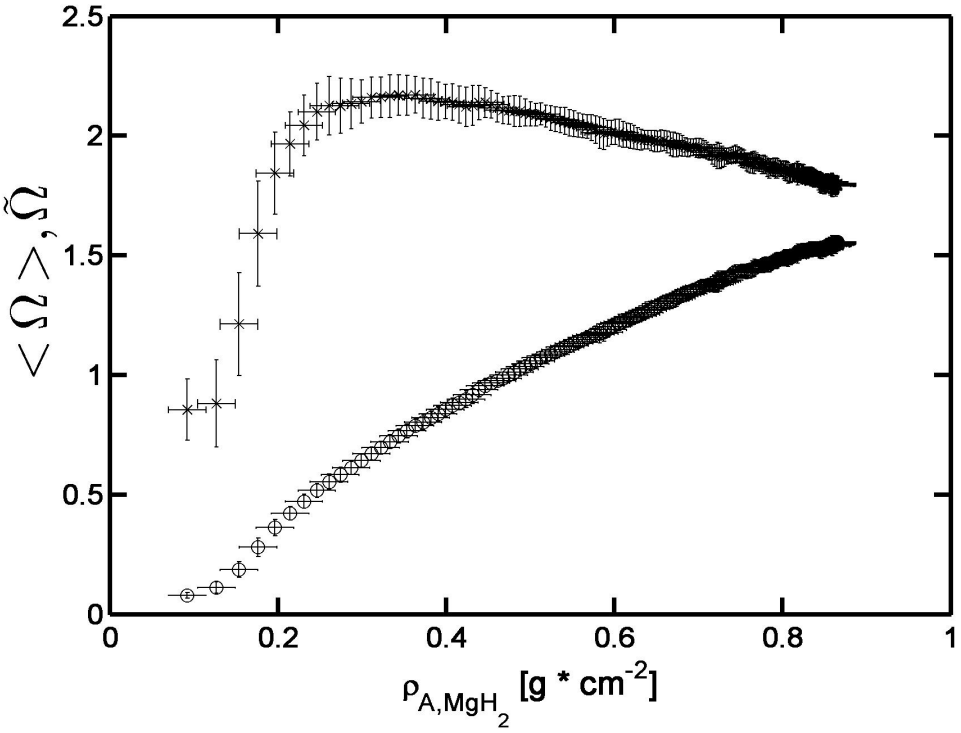

Figure B.4: Lower curve: Average attenuation by Mg-24 for different area densities ρ_{A,MgH_2}. Upper curve: Corresponding normalized attenuation, $\tilde{\Omega}$.

to an area density of $\rho_A \approx 0.25$ g/cm^2 is due to the the limited resolution and a resulting blurring of the pellet boundaries and not considered in the following. With increasing area density a reduced average attenuation $< \Omega >$ is observed, the evolution is non-linear. Consequently, the normalized attenuation decays with increasing area density. This is shown by the upper curve in Figure B.4. The reason for the

observed non-linear correlation is a beam hardening with increasing area density. The corresponding reduced interaction cross section of hydrogen leads to a reduced average attenuation. Since the energy dependency of the cross section for hydrogen (H-1) is much less pronounced than it is the case for Li-6 and B-11, the resulting hardening of the spectrum is reduced as well. The maximal normalized attenuation is found for area densities of 0.3-0.4 g/cm^2, it is $\tilde{\Omega} = 2.2 \pm 0.1$ cm^2/g. Since the variation of $\tilde{\Omega}(\rho_A)$ for ρ_A corresponding to loose powder is negligible in comparison to the one observed for $LiBH_4$, it is not considered for the correction of the overall attenuation by the influence of MgH_2 (see equation 5.31).

B.3 Neutron Radiography analysis of solidification of $LiBH_4$

The reduction of temperature to 221.5 °C in order to induce a solidification of $LiBH_4$ is accompanied by a further change of the material structure. Still, the magnitude of structure change is significantly lower than for the initial liquefaction. For the isotope sample, a slight densification of about 4.2% of the sample is observed with the cylindrical symmetry still being present after equilibrium is reached. The overall density in the final state is calculated to 0.52 g/cm^3 for the isotope sample. As it is the case for the initial liquefaction, the density change cannot be calculated for the natural sample composition due to a non-symmetric structure change. The kink that was observed in the liquid state is enhanced by solidification. This structure change is highly likely responsible for the observed attenuation changes in the upper sample area in the difference slices according to Figure 5.49. The non-symmetric structure change is due to the explicit a priori distribution of material and pores. Additionally, slight variations or symmetry deviations in the temperature field might contribute to this findings.

B.4 Selection of cluster from volume data set - particle analysis

The selection of cluster is done by using the *Particle Analyser* plugin of *ImageJ* [95, 3]. A thresholding is performed according to the cluster attenuation threshold, which generates a subset of the total voxel data set. Voxel within this subset are binarized, so that they fulfill the following condition:

$$\forall \mu_i \geq \mu_{TC} : \quad \mu_i \coloneqq 1 \tag{B.1}$$

Accordingly, the specific information about the attenuation coefficient for each voxel is lost. Neighboring voxel in the subset are allocated to cluster, denoted as particles within the *ImageJ* software. A list of all cluster in the sample volume is generated and fundamental properties are calculated. The most relevant for this thesis are the total cluster volume and the position of the cluster centroid. The latter can be used to identify cluster both in the liquid and solid state data set and track their potential motion. The binarization of the voxel data set provides spatial information about the growth of cluster in case of the solidification, which allows to draw further conclusions about the cluster changes accompanied by the solidification process: The performed binarization has the advantage that in case of cluster growth due to solidification the cluster centroid will be moved towards the direction of the new elements (voxel) of the cluster. This allows to determine whether the emergence of clustering has any preferential orientation.
The distance of the cluster centroid to the sample center is calculated as follows: The coordinates of the sample center are derived out of an arbitrary x-y slice of the sample volume. Thus, the distance of the cluster centroid to the center is calculated simply by

$$d_{CC} = \sqrt{(x_C - x_0)^2 + (y_C - y_0)^2}$$

where (x_C, y_C) is the position of the cluster centroid and (x_0, y_0) is the sample center position.

B.5 Registration of volume data sets

The process of alignment of two related data sets is referred to as registration. One data set is set as a reference system and the other data set is transformed in order to result in a minimal difference of data sets. The transformation possibilities reach from rigid/linear transformations to non-linear or elastic transformations. The studies in this work cover the case of sample cell displacement due to thermal expansion of the sample cell upon heating. It is emphasized that only the difference due to the sample cell displacement needs to be corrected. Any differences that are originating from the material structure itself are target of this investigation and any effect of registration on the structure itself has to be strongly avoided! To ensure a correct registration of the sample cell motion, a rigid transformation is applied with the software package *Avizo* [52]. After a resampling of the data, effects of thermal expansion are non-significant and the outer sample boundaries match well.

Bibliography

[1] http://www.mlz-garching.de/antares. last viewed: 03/2017.

[2] http://www.mlz-garching.de/englisch/neutron-research/neutron-source.html. last viewed: 03/2017.

[3] Particle analyser, plugin. http://bonej.org/particles; last viewed: 03/2017.

[4] *RADIOGRAPHY AND TOMOGRAPHY USING FISSION NEUTRONS AT FRM-II, Bücherl, Thomas and von Gostomski, Ch. Lierse, 16th WCNDT, Montreal Canada*, 2004. http://www.ndt.net/search/docs.php3?showForm=off&id=2443.

[5] M. Abdellaoui, D. Cracco, and A. Percheron-Guegan. Structural investigation and solid-h2 reaction of mg2ni rich nanocomposite materials elaborated by mechanical alloying. *Journal of Alloys and Compounds*, 293295:501 – 507, 1999.

[6] J. Ahrens, B. Geveci, C. Law, C. Hansen, and C. Johnson. 36-paraview: An end-user tool for large-data visualization, 2005.

[7] L. S. Andreas Zttel, Andreas Borgschulte, editor. *Hydrogen as a Future Energy Carrier*. WILEY-VCH Verlag GmbH, 2008.

[8] G. Barkhordarian, T. Klassen, and R. Bormann. Composite material storing hydrogen, and device for the reversible storage of hydrogen, 2009. US Patent App. 11/721,493.

[9] G. Barkhordarian, T. Klassen, M. Dornheim, and R. Bormann. Unexpected kinetic effect of mgb 2 in reactive hydride composites containing complex borohydrides. *Journal of Alloys and Compounds*, 440(1):L18–L21, 2007.

[10] J. F. Barrett and N. Keat. Artifacts in ct: recognition and avoidance 1. *Radiographics*, 24(6):1679–1691, 2004.

[11] G. K. Batchelor. *An introduction to fluid dynamics*. Cambridge university press, 2000.

[12] B. Bogdanovic, R. A. Brand, A. Marjanovic, M. Schwickardi, and J. Tolle. Metal-doped sodium aluminium hydrides as potential new hydrogen storage materials. *Journal of Alloys and Compounds*, 302(1-2):36–58, 2000.

[13] B. Bogdanovic, M. Felderhoff, A. Pommerin, F. Schth, N. Spielkamp, and A. Stark. Cycling properties of sc- and ce-doped naalh4 hydrogen storage materials prepared by the one-step direct synthesis method. *Journal of Alloys and Compounds*, 471(12):383 – 386, 2009.

[14] B. Bogdanovic and M. Schwickardi. Ti-doped alkali metal aluminium hydrides as potential novel reversible hydrogen storage materials. *Journal of Alloys and Compounds*, 253:1–9, 1997.

[15] M. Boin, R. Wimpory, A. Hilger, N. Kardjilov, S. Zhang, and M. Strobl. Monte carlo simulations for the analysis of texture and strain measured with bragg edge neutron transmission. In *Journal of Physics: Conference Series*, volume 340, page 012022. IOP Publishing, 2012.

[16] S. Börries, O. Metz, P. Pranzas, J. B. von Colbe, T. Bücherl, M. Dornheim, T. Klassen, and A. Schreyer. Optimization and comprehensive characterization of metal hydride based hydrogen storage systems using in-situ neutron radiography. *Journal of Power Sources*, 328:567 – 577, 2016.

[17] S. Börries, O. Metz, P. K. Pranzas, T. Bücherl, S. Söllradl, M. Dornheim, T. Klassen, and A. Schreyer. Scattering influences in quantitative fission neutron radiography for the in situ analysis of hydrogen distribution in metal hydrides. *Nuclear Instruments and Methods in Physics Research Section A: Accelerators, Spectrometers, Detectors and Associated Equipment*, 797:158–164, 2015.

[18] U. Bösenberg. *$LiBH_4MgH_2$ Composites for Hydrogen Storage*. PhD thesis, Technische Universitt Hamburg-Harburg, 2009.

[19] U. Bösenberg, J. W. Kim, D. Gosslar, N. Eigen, T. R. Jensen, J. B. Von Colbe, Y. Zhou, M. Dahms, D. Kim, R. Günther, et al. Role of additives in libh 4–mgh 2 reactive hydride composites for sorption kinetics. *Acta Materialia*, 58(9):3381–3389, 2010.

[20] U. Bösenberg, D. B. Ravnsbæk, H. Hagemann, V. DAnna, C. B. Minella, C. Pistidda, W. Van Beek, T. R. Jensen, R. Bormann, and M. Dornheim. Pressure and

temperature influence on the desorption pathway of the libh4- mgh2 composite system. *The Journal of Physical Chemistry C*, 114(35):15212–15217, 2010.

[21] H. Breitkreutz, F. M. Wagner, A. Röhrmoser, and W. Petry. Spectral fluence rates of the fast reactor neutron beam medapp at frm ii. *Nuclear Instruments and Methods in Physics Research Section A: Accelerators, Spectrometers, Detectors and Associated Equipment*, 593(3):466–471, 2008.

[22] R. A. Brooks and G. D. Chiro. Beam hardening in x-ray reconstructive tomography. *Physics in Medicine and Biology*, 21(3):390, 1976.

[23] R. A. Brooks and G. Di Chiro. Principles of computer assisted tomography (cat) in radiographic and radioisotopic imaging. *Physics in medicine and biology*, 21(5):689, 1976.

[24] T. Bücherl and C. L. von Gostomski. Radiography using fission neutrons. 2006.

[25] T. Bücherl, C. L. von Gostomski, H. Breitkreutz, M. Jungwirth, and F. M. Wagner. NECTAR-A fission neutron radiography and tomography facility. *Nuclear Instruments & Methods in Physics Research Section a-Accelerators Spectrometers Detectors and Associated Equipment*, 651(1):86–89, 2011.

[26] I. M. BVBA. Octopus reconstruction, octopus imaging software. https://octopusimaging.eu/octopus/octopus-reconstruction; last viewed: 03/2017.

[27] N. J. Carron. *An introduction to the passage of energetic particles through matter*. CRC Press, 2006.

[28] J. Chadwick. The existence of a neutron. *Proceedings of the Royal Society of London A: Mathematical, Physical and Engineering Sciences*, 136(830):692–708, 1932.

[29] M. Chadwick, M. Herman, P. Obložinský, M. Dunn, Y. Danon, A. Kahler, D. Smith, B. Pritychenko, G. Arbanas, R. Arcilla, R. Brewer, D. Brown, R. Capote, A. Carlson, Y. Cho, H. Derrien, K. Guber, G. Hale, S. Hoblit, S. Holloway, T. Johnson, T. Kawano, B. Kiedrowski, H. Kim, S. Kunieda, N. Larson, L. Leal, J. Lestone, R. Little, E. McCutchan, R. MacFarlane, M. MacInnes, C. Mattoon, R. McKnight, S. Mughabghab, G. Nobre, G. Palmiotti, A. Palumbo, M. Pigni, V. Pronyaev, R. Sayer, A. Sonzogni, N. Summers, P. Talou, I. Thompson, A. Trkov, R. Vogt, S. van der Marck, A. Wallner, M. White, D. Wiarda,

and P. Young. Endf/b-vii.1 nuclear data for science and technology: Cross sections, covariances, fission product yields and decay data. *Nuclear Data Sheets*, 112(12):2887–2996, Dec. 2011.

[30] S. Company. Swagelok. www.swagelok.com; last viewed: 03/2017.

[31] G. W. Crabtree, M. S. Dresselhaus, and M. V. Buchanan. The hydrogen economy. *Physics Today*, 57(12):39–44, 2004.

[32] R. de Paiva, J. Lynch, E. Rosenberg, and M. Bisiaux. A beam hardening correction for x-ray microtomography. *NDT and E International*, 31(1):17–22, 1998-02-01T00:00:00.

[33] E. Deprez, M. A. Muoz-Mrquez, M. A. Roldn, C. Prestipino, F. J. Palomares, C. B. Minella, U. Bsenberg, M. Dornheim, R. Bormann, and A. Fernndez. Oxidation state and local structure of ti-based additives in the reactive hydride composite 2libh4 + mgh2. *The Journal of Physical Chemistry C*, 114(7):3309–3317, 2010.

[34] M. Dornheim. Tailoring reaction enthalpies of hydrides. *Handbook of Hydrogen Storage*, pages 187–214, 2010.

[35] M. Dornheim. *Thermodynamics of metal hydrides: tailoring reaction enthalpies of hydrogen storage materials*. INTECH Open Access Publisher, 2011.

[36] M. Dornheim, S. Doppiu, G. Barkhordarian, U. Boesenberg, T. Klassen, O. Gutfleisch, and R. Bormann. Hydrogen storage in magnesium-based hydrides and hydride composites. *Scripta Materialia*, 56(10):841–846, 2007.

[37] N. Eigen, C. Keller, M. Dornheim, T. Klassen, and R. Bormann. Industrial production of light metal hydrides for hydrogen storage. *Scripta Materialia*, 56(10):847–851, 2007.

[38] N. Eigen, T. Klassen, E. Aust, R. Bormann, and F. Gärtner. Production of nanocrystalline cermet thermal spray powders for wear resistant coatings by high-energy milling. *Materials Science and Engineering: A*, 356(1):114–121, 2003.

[39] I. Elbakri and J. Fessler. Statistical image reconstruction for polyenergetic X-ray computed tomography. *IEEE TRANSACTIONS ON MEDICAL IMAGING*, 21(2):89–99, FEB 2002.

[40] J. D. Evans. *Straightforward statistics for the behavioral sciences*. Brooks/Cole, 1996.

[41] A. Fick. Ueber diffusion. *Annalen der Physik*, 170(1):59–86, 1855.

[42] E. N. D. File. https://www-nds.iaea.org/exfor/endf.htm.

[43] I. Gardner et al. A review of spallation neutron source accelerators. In *Proc. EPAC*, volume 98, 1998.

[44] R. German. *Sintering: from empirical observations to scientific principles*. Butterworth-Heinemann, 2014.

[45] R. M. German. Supersolidus liquid-phase sintering of prealloyed powders. *Metallurgical and materials transactions A*, 28(7):1553–1567, 1997.

[46] R. M. German. *Liquid phase sintering*. Springer Science & Business Media, 2013.

[47] H. Gerstenberg, E. Krähling, D. Päthe, K. Schreckenbach, and W. Gläser. The cold neutron source of the munich research reactor (frm). In *Advances in cryogenic engineering*, pages 613–620. Springer, 1998.

[48] V. G. GmbH. Vgstudio max. http://www.volumegraphics.com/de/produkte/vgstudio-max/grundfunktionen/.

[49] L. Gondek, N. B. Selvaraj, J. Czub, H. Figiel, D. Chapelle, N. Kardjilov, A. Hilger, and I. Manke. Imaging of an operating LaNi4.8Al0.2based hydrogen storage container. *International Journal of Hydrogen Energy*, 36(16):9751–9757, 2011.

[50] A. A. Goshtasby. *2-D and 3-D image registration: for medical, remote sensing, and industrial applications*. John Wiley & Sons, 2005.

[51] I. Greving, F. Wilde, M. Ogurreck, J. Herzen, J. U. Hammel, A. Hipp, F. Friedrich, L. Lottermoser, T. Dose, H. Burmester, et al. P05 imaging beamline at petra iii: first results. In *SPIE Optical Engineering+ Applications*, pages 92120O–92120O–8. International Society for Optics and Photonics, 2014.

[52] F. V. S. Group. Avizo 8. http://www.fei.com/software/avizo-3d; last view: 03/2017.

[53] C. Hall and W. D. Hoff. *Water transport in brick, stone and concrete*. CRC Press, 2011.

[54] P. Hammersberg and M. Måns. Correction for beam hardening artefacts in computerised tomography. *Journal of X-ray Science and Technology*, 8(1):75–93, 1998.

[55] K. Herbrig, C. Pohlmann, Ł. Gondek, H. Figiel, N. Kardjilov, A. Hilger, I. Manke, J. Banhart, B. Kieback, and L. Röntzsch. Investigations of the structural stability of metal hydride composites by in-situ neutron imaging. *Journal of Power Sources*, 293:109–118, 2015.

[56] T. Hibiki, K. Mishima, K. Yoneda, S. Fujine, A. Tsuruno, and M. Matsubayashi. Visualization of fluid phenomena using a high frame-rate neutron radiography with a steady thermal neutron beam. *Nuclear Instruments and Methods in Physics Research Section A: Accelerators, Spectrometers, Detectors and Associated Equipment*, 351(2):423 – 436, 1994.

[57] J. S. Higgins and H. Benoît. *Polymers and neutron scattering*. Clarendon press Oxford, 1994.

[58] M. Hirscher, editor. *Handbook of Hydrogen Storage*. WILEY-VCH Verlag GmBH, 2010.

[59] T. Hua, R. Ahluwalia, J.-K. Peng, M. Kromer, S. Lasher, K. McKenney, K. Law, and J. Sinha. Technical assessment of compressed hydrogen storage tank systems for automotive applications. *International Journal of Hydrogen Energy*, 36(4):3037–3049, 2011.

[60] W. Huppmann and H. Riegger. Modelling of rearrangement processes in liquid phase sintering. *Acta Metallurgica*, 23(8):965–971, 1975.

[61] H. Z. B. Ian S. Anderson, Robert L. McGreevy, editor. *Neutron Imaging and Applications: A Reference for the Imaging Community*. Springer, 2009.

[62] T. M. Inc. Matlab. http://de.mathworks.com/products/matlab; last view: 03/2017.

[63] D. L. Jacobson, D. S. Hussey, E. Baltic, T. J. Udovic, J. J. Rush, and R. C. Bowman Jr. Neutron imaging studies of metal-hydride storage beds. *International Journal of Hydrogen Energy*, 35(23):12837–12845, 2010.

[64] R. J. Jennings. A method for comparing beam-hardening filter materials for diagnostic radiology. *Medical Physics*, 15(4):588–599, 1988.

[65] J. Jepsen. *Technical and Economic Evaluation of Hydrogen Storage Systems based on Light Metal Hydrides*. PhD thesis, Helmut-Schmidt Universitt, Hamburg, 2013.

[66] J. Jepsen, C. Milanese, A. Girella, G. A. Lozano, C. Pistidda, J. M. Bellosta von Colbe, A. Marini, T. Klassen, and M. Dornheim. Compaction pressure influence on material properties and sorption behaviour of libh4mgh2 composite. *International Journal of Hydrogen Energy*, 38(20):8357–8366, 2013.

[67] J. L. Johnson, J. J. Brezovsky, and R. M. German. Effects of tungsten particle size and copper content on densification of liquid-phase-sintered w-cu. *Metallurgical and Materials Transactions A*, 36(10):2807–2814, 2005.

[68] A. C. Kak and M. Slaney. *Principles of computerized tomographic imaging*. IEEE press, 1988.

[69] W. Kingery. Densification during sintering in the presence of a liquid phase. i. theory. *Journal of Applied Physics*, 30(3):301–306, 1959.

[70] G. F. Knoll. *Radiation detection and measurement*. John Wiley & Sons, 2010.

[71] A. Koch, C. Raven, P. Spanne, and A. Snigirev. X-ray imaging with submicrometer resolution employing transparent luminescent screens. *JOSA A*, 15(7):1940–1951, 1998.

[72] O.-H. Kwon and G. L. Messing. Kinetic analysis of solution-precipitation during liquid-phase sintering of alumina. *Journal of the American Ceramic Society*, 73(2):275–281, 1990.

[73] S.-M. Lee and S.-J. L. Kang. Theoretical analysis of liquid-phase sintering: pore filling theory. *Acta Materialia*, 46(9):3191–3202, 1998.

[74] E. H. Lehmann, P. Vontobel, and N. Kardjilov. Hydrogen distribution measurements by neutrons. *Applied Radiation and Isotopes*, 61(4):503–509, 2004.

[75] P. Liu and J. Vajo. Thermodynamically tuned nanophase materials for reversible hydrogen storage. *Proceedings of the 2010 US DOE Hydrogen Program Annual Merit Review*, 2007.

[76] G. A. Lozano, N. Eigen, C. Keller, M. Dornheim, and R. Bormann. Effects of heat transfer on the sorption kinetics of complex hydride reacting systems. *International Journal of Hydrogen Energy*, 34(4):1896–1903, 2009.

[77] G. A. Lozano, J. M. B. von Colbe, R. Bormann, T. Klassen, and M. Dornheim. Enhanced volumetric hydrogen density in sodium alanate by compaction. *Journal of Power Sources*, 196(22):9254 – 9259, 2011.

[78] B. D. MacDonald and A. M. Rowe. Impacts of external heat transfer enhancements on metal hydride storage tanks. *International Journal of Hydrogen Energy*, 31(12):1721–1731, 2006.

[79] I. Manke, C. Hartnig, N. Kardjilov, M. Messerschmidt, A. Hilger, M. Strobl, W. Lehnert, and J. Banhart. Characterization of water exchange and two-phase flow in porous gas diffusion materials by hydrogen-deuterium contrast neutron radiography. *Applied physics letters*, 92(24):244101, 2008.

[80] G. A. L. Martinez. *Development of Hydrogen Storage Systems using Sodium Alanate*. PhD thesis, Technische Universitt Hamburg-Harburg, 2010.

[81] D. A. Mosher, S. Arsenault, X. Tang, and D. L. Anton. Design, fabrication and testing of NaAlH4 based hydrogen storage systems. *Journal of Alloys and Compounds*, 446-447:707–712, 2007.

[82] C. Na Ranong, M. Höhne, J. Franzen, J. Hapke, G. Fieg, M. Dornheim, N. Eigen, J. Bellosta von Colbe, and O. Metz. Concept, Design and Manufacture of a Prototype Hydrogen Storage Tank Based on Sodium Alanate. *Chemical Engineering & Technology*, 32(8):1154–1163, 2009.

[83] N. Niimura, Y. Karasawa, I. Tanaka, J. Miyahara, K. Takahashi, H. Saito, S. Koizumi, and M. Hidaka. An imaging plate neutron detector. *Nuclear Instruments and Methods in Physics Research Section A: Accelerators, Spectrometers, Detectors and Associated Equipment*, 349(2-3):521–525, 1994.

[84] K. Osterloh, T. Bücherl, C. Lierse von Gostomski, U. Zscherpel, U. Ewert, and S. Bock. Filtering algorithm for dotted interferences. *Nuclear Instruments and Methods in Physics Research Section A: Accelerators, Spectrometers, Detectors and Associated Equipment*, 651(1):171–174, 2011.

[85] N. Parikh and M. Humenik. Cermets: Ii, wettability and microstructure studies in liquid-phase sintering. *Journal of the American Ceramic Society*, 40(9):315–320, 1957.

[86] H.-H. Park, O.-J. Kwon, and D. N. Yoon. The critical grain size for liquid flow into pores during liquid phase sintering. *Metallurgical Transactions A*, 17(11):1915–1919, 1986.

[87] K. Pearson. Mathematical contributions to the theory of evolution. iii. regression, heredity, and panmixia. *Philosophical Transactions of the Royal Society of London A: Mathematical, Physical and Engineering Sciences*, 187:253–318, 1896.

[88] S. Peetermans, A. King, W. Ludwig, P. Reischig, and E. Lehmann. Cold neutron diffraction contrast tomography of polycrystalline material. *Analyst*, 139(22):5766–5772, 2014.

[89] S. Peetermans and E. Lehmann. Simultaneous neutron transmission and diffraction contrast tomography as a non-destructive 3d method for bulk single crystal quality investigations. *Journal of Applied Physics*, 114(12):124905, 2013.

[90] F. E. Pinkerton, M. S. Meyer, G. P. Meisner, M. P. Balogh, and J. J. Vajo. Phase boundaries and reversibility of libh4/mgh2 hydrogen storage material. *The Journal of Physical Chemistry C*, 111(35):12881–12885, 2007.

[91] F. E. Pinkerton, M. S. Meyer, G. P. Meisner, M. P. Balogh, and J. J. Vajo. Phase boundaries and reversibility of libh4/mgh2 hydrogen storage material. *The Journal of Physical Chemistry C*, 111(35):12881–12885, 2007.

[92] H. Pleinert, E. Lehmann, and S. Krner. Design of a new ccd-camera neutron radiography detector. *Nuclear Instruments and Methods in Physics Research Section A: Accelerators, Spectrometers, Detectors and Associated Equipment*, 399(23):382 – 390, 1997.

[93] C. Pohlmann, K. Herbrig, L. Gondek, N. Kardjilov, A. Hilger, H. Figiel, J. Banhart, B. Kieback, I. Manke, and L. Röntzsch. In operando visualization of hydride-graphite composites during cyclic hydrogenation by high-resolution neutron imaging. *Journal of Power Sources*, 277(0):360–369, 2015.

[94] P. K. Pranzas, U. Bösenberg, F. Karimi, M. Münning, O. Metz, C. B. Minella, H.-W. Schmitz, F. Beckmann, U. Vainio, D. Zajac, E. Welter, T. R. Jensen, Y. Cerenius, R. Bormann, T. Klassen, M. Dornheim, and A. Schreyer. Characterization of hydrogen storage materials and systems with photons and neutrons. *Advanced Engineering Materials*, 13(8):730–736, 2011.

[95] I. Processing and A. in Java. Imagej. http://imagej.nih.gov/ij/; last viewed: 03/2017.

[96] O. Reynolds. On the theory of lubrication and its application to mr. beauchamp tower's experiments, including an experimental determination of the viscosity of olive oil. *Proceedings of the Royal Society of London*, 40(242-245):191–203, 1886.

[97] P. Rinard. Neutron interactions with matter. *Passive Nondestructive Assay of Nuclear Materials*, pages 357–377, 1991.

[98] G. J. Russell. Spallation physics-an overview. *Proceedings of ICANS XI*, pages 22–26, 1991.

[99] H. Sakaguchi, A. Kohzai, K. Hatakeyama, S. Fujine, K. Yoneda, K. Kanda, and T. Esaka. Visualization of hydrogen in hydrogen storage alloys using neutron radiography. *International Journal of Hydrogen Energy*, 25(12):1205–1208, 2000.

[100] H. Sakaguchi, Y. Satake, K. Hatakeyama, S. Fujine, K. Yoneda, M. Matsubayashi, and T. Esaka. Analysis of hydrogen distribution in hydrogen storage alloy using neutron radiography. *Journal of Alloys and Compounds*, 354(12):208 – 215, 2003.

[101] G. Sandrock, K. Gross, and G. Thomas. Effect of ti-catalyst content on the reversible hydrogen storage properties of the sodium alanates. *Journal of alloys and compounds*, 339(1):299–308, 2002.

[102] J. Santisteban, L. Edwards, M. Fitzpatrick, A. Steuwer, P. Withers, M. Daymond, M. Johnson, N. Rhodes, and E. Schooneveld. Strain imaging by bragg edge neutron transmission. *Nuclear Instruments and Methods in Physics Research Section A: Accelerators, Spectrometers, Detectors and Associated Equipment*, 481(1):765–768, 2002.

[103] B. Schillinger, E. Calzada, F. Grünauer, and E. Steichele. The design of the neutron radiography and tomography facility at the new research reactor frm-ii at technical university munich. *Applied radiation and isotopes*, 61(4):653–657, 2004.

[104] L. Schlapbach and A. Züttel. Hydrogen-storage materials for mobile applications. *Nature*, 414(6861):353–358, 2001.

[105] L. Schlapbach and A. Züttel. Hydrogen-storage materials for mobile applications. *Nature*, 414(6861):353–358, 2001.

[106] M. Schulz and B. Schillinger. Antares: Cold neutron radiography and tomography facility. *Journal of large-scale research facilities JLSRF*, 1:17, 2015.

[107] M. Sedighi-Gilani, M. Griffa, D. Mannes, E. Lehmann, J. Carmeliet, and D. Derome. Visualization and quantification of liquid water transport in softwood by means of neutron radiography. *International Journal of Heat and Mass Transfer*, 55(2122):6211–6221, 2012.

[108] N. B. Selvaraj. *Thermal analysis and neutron imaging studies of the metal hydride storage tank*. PhD thesis, AGH University of Science and Technology, Krakow, Poland, 2011.

[109] L. Shu-Quan, L. Hang, Z. Yu-Bin, L. Yuan-Rong, G. Zhi-Yu, et al. Corrections on energy spectrum and scatterings for fast neutron radiography at nectar facility. *Chinese physics C*, 37(11):118201, 2013.

[110] K. Skold and D. L. Price. *Neutron scattering / edited by Kurt Skold, David L. Price*. Academic Press Orlando, 1986.

[111] A. Spowart. Measurement of the absolute scintillation efficiency of granular and glass neutron scintillators. *Nuclear Instruments and Methods*, 75(1):35–42, 1969.

[112] G. L. Squires. *Introduction to the theory of thermal neutron scattering*. Cambridge university press, 2012.

[113] W. M. Stacey. *Nuclear reactor physics*. John Wiley & Sons, 2007.

[114] M. Strobl, I. Manke, N. Kardjilov, A. Hilger, M. Dawson, and J. Banhart. Advances in neutron radiography and tomography. *Journal of Physics D: Applied Physics*, 42(24):243001, 2009.

[115] M. Sulic, M. Cai, and S. Kumar. Cycling and engineering properties of highly compacted sodium alanate pellets. *International Journal of Hydrogen Energy*, 37(20):15187–15195, 2012.

[116] C. Suryanarayana. *Mechanical alloying and milling*. CRC Press, 2004.

[117] Geesthacht researching boron for hydrogen storage: Bor4store. *Fuel Cells Bulletin*, 2012(6):13 –, 2012.

[118] B. Tatian. Method for obtaining the transfer function from the edge response function. *JOSA*, 55(8):1014–1019, 1965.

[119] W. Treimer, M. Strobl, N. Kardjilov, A. Hilger, and I. Manke. Wavelength tunable device for neutron radiography and tomography. *Applied Physics Letters*, 89(20), 2006.

[120] A. Tremsin, V. Dangendorf, K. Tittelmeier, B. Schillinger, M. Schulz, M. Lerche, and W. Feller. Time-resolved neutron imaging at antares cold neutron beamline. *Journal of Instrumentation*, 10(07):P07008, 2015. Energy spectrum of ANTARES.

[121] M. Utsuro and V. K. Ignatovich. *Handbook of Neutron Optics*. John Wiley & Sons, 2010.

[122] J. J. Vajo, S. L. Skeith, and F. Mertens. Reversible storage of hydrogen in destabilized libh4. *The Journal of Physical Chemistry B*, 109(9):3719–3722, 2005.

[123] E. Van de Casteele. *Model-based approach for beam hardening correction and resolution measurements in microtomography*. Citeseer, 2004.

[124] E. Van de Casteele, D. Van Dyck, J. Sijbers, and E. Raman. An energy-based beam hardening model in tomography. *Physics in medicine and biology*, 47(23):4181, 2002.

[125] E. Van de Casteele, D. Van Dyck, J. Sijbers, and E. Raman. A model-based correction method for beam hardening artefacts in x-ray microtomography. *Journal of X-ray science and technology*, 12(1):43–57, 2004.

[126] B. Van Hassel, D. Mosher, J. Pasini, M. Gorbounov, J. Holowczak, X. Tang, R. Brown, B. Laube, and L. Pryor. Engineering improvement of naalh 4 system. *International Journal of hydrogen energy*, 37(3):2756–2766, 2012.

[127] J. M. B. von Colbe, G. Lozano, O. Metz, T. Bücherl, R. Bormann, T. Klassen, and M. Dornheim. Design, sorption behaviour and energy management in a sodium alanate-based lightweight hydrogen storage tank. *International Journal of Hydrogen Energy*, 40(7):2984–2988, 2015.

[128] J. M. B. von Colbe, O. Metz, G. A. Lozano, P. K. Pranzas, H. W. Schmitz, F. Beckmann, A. Schreyer, T. Klassen, and M. Dornheim. Behavior of scaled-up sodium alanate hydrogen storage tanks during sorption. *International Journal of Hydrogen Energy*, 37(3):2807 – 2811, 2012.

[129] L. W. Wang, Z. Tamainot-Telto, S. J. Metcalf, R. E. Critoph, and R. Z. Wang. Anisotropic thermal conductivity and permeability of compacted expanded natural graphite. *Applied Thermal Engineering*, 30(13):1805–1811, 2010.

[130] C.-J. Winter and J. Nitsch. *Hydrogen as an energy carrier: technologies, systems, economy*. Springer Science & Business Media, 2012.

[131] B. M. Wood, K. Ham, D. S. Hussey, D. L. Jacobson, A. Faridani, A. Kaestner, J. J. Vajo, P. Liu, T. A. Dobbins, and L. G. Butler. Real-time observation of hydrogen absorption by lani 5 with quasi-dynamic neutron tomography. *Nuclear*

Instruments and Methods in Physics Research Section B: Beam Interactions with Materials and Atoms, 324:95–101, 2014.

[132] K. Yoshii and K. Miya. A study on the mechanism model of luminescence in fast neutron television converter. *Nuclear Instruments and Methods in Physics Research Section A: Accelerators, Spectrometers, Detectors and Associated Equipment*, 346:253 – 258, 1994.

[133] A. Zaluska, L. Zaluski, and J. Strm-Olsen. Structure, catalysis and atomic reactions on the nano-scale: a systematic approach to metal hydrides for hydrogen storage. *Applied Physics A*, 72(2):157–165, 2001.

[134] A. Züttel, P. Wenger, S. Rentsch, P. Sudan, P. Mauron, and C. Emmenegger. Libh 4 a new hydrogen storage material. *Journal of Power Sources*, 118(1):1–7, 2003.

List of publications

S. Börries, O. Metz, P. K. Pranzas, T. Bücherl, S. Söllradl, M. Dornheim, T. Klassen and A. Schreyer. Scattering influences in quantitative fission neutron radiography for the in situ analysis of hydrogen distribution in metal hydrides. *Nuclear Instruments and Methods in Physics Research Section A: Accelerators, Spectrometers, Detectors and Associated Equipment*, 797:158-164, 2015.

S. Börries, O. Metz, P. K. Pranzas, J. M. Bellosta von Colbe, T. Bücherl, M. Dornheim, T. Klassen and A. Schreyer. Optimization and comprehensive characterization of metal hydride based hydrogen storage systems using in-situ neutron radiography. *Journal of Power Sources*, 328:567-577, 2016.

Danksagung/Acknowledgements

Zunächst möchte ich meinen Betreuern, Prof. Dr. Andreas Schreyer und Prof. Dr. Thomas Klassen, danken, mir die Möglichkeit für diese Arbeit an der Schnittstelle zweier Arbeitsgruppen gegeben zu haben. Darüber hinaus danke ich Ihnen für die fortwährende Unterstützung bei der Umsetzung meiner Ideen und Vorhaben. Weiterhin danke ich Dr. Martin Dornheim für seine Unterstützung, die hilfreichen Diskussionen und die Möglichkeit, Räumlichkeiten und Austattung seiner Abteilung für diese Arbeit nutzen zu können. In diesem Zusammenhang gilt mein ganz besonderer Dank auch Dr. Philipp Klaus Pranzas für sein Engagement und die tolle Unterstützung und Hilfe während meiner gesamten Zeit am HZG. Viele Kollegen, sowohl aus der Gruppe Nanotechnologie als auch aus der Imaging-Gruppe an der Außenstelle am DESY, haben zum Gelingen dieser Arbeit beigetragen. Ein besonderer Dank gilt Dr. Julia Herzen für ihre Hilfe beim Start in das Themenfeld 'Imaging'. Ebenfalls bedanken möchte ich mich bei Dr. Jörg Hammel für die großartige Unterstützung bei der Daten-Rekonstruktion. Den Kollegen aus der Imaging-Gruppe am FRM II in Garching gilt mein großer Dank für den Support während der Messzeiten. Hier möchte ich den tollen Einsatz von Dr. Stefan Söllradl hervorheben, der viele Messungen erst möglich gemacht hat. Fahim Karimi hat anfangs das Büro in Geesthacht mit mir geteilt und ich danke Ihm für die schöne gemeinsame Zeit. Mein ganz besonderer Dank gilt auch meinem späteren Bürokollegen Nils Bergemann: die Fahrten von Hamburg nach Geesthacht, den Büroalltag, die Bandbreite der Diskussionen und auch die schöne Zeit neben der Arbeit habe ich sehr geschätzt und werde sie gewiss vermissen! Besonders hervorheben möchte ich auch die großartige Zusammenarbeit mit Oliver Metz. Ohne seine tatkräftige und technische Unterstützung während der Messzeiten und ihrer Vorbereitungen wäre diese Arbeit nicht möglich gewesen. Die Beamline-Zeiten in München und auch in der Schweiz werde ich vermutlich immer in sehr positiver Erinnerung behalten. Abschließend möchte ich meiner Familie, meinen Eltern und meinem Bruder, danken. Die Gewissheit Eurer permanenten Unterstützung ist von unschätzbarem Wert. Der größte Dank gilt meiner Partnerin Rieke Bruns: Danke für Deine immerwährende Geduld, Unterstützung und Deinen Glauben an mich.